Theoretical Modelling of Non-contact Atomic Force Microscopy on Insulators

The PhD Thesis of Adam Foster

Supervisors: Alexander L. Shluger and Lev N. Kantorovich

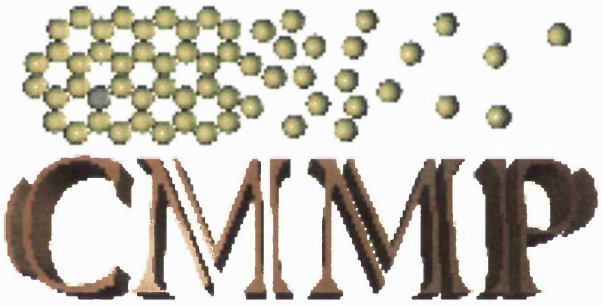

Condensed Matter and Materials Physics Group
University College London

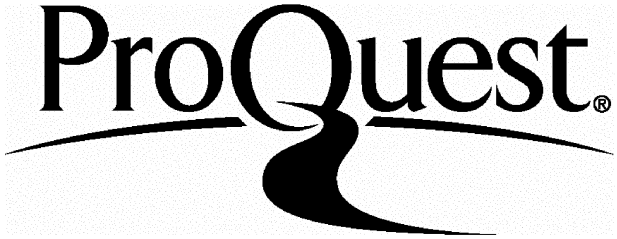

Abstract

The Non-contact Atomic Force Microscope (NC-AFM) now offers the surface scientist the ability to resolve individual atoms on the surfaces of insulators. Atomically resolved NC-AFM images have now been demonstrated on insulating surfaces such as sodium chloride, calcium difluoride and nickel oxide, as well as many metallic and semi-conducting surfaces. However, in nearly all experiments the amount of information that can be extracted from these images alone is limited, and usually the identity of the resolved features is unknown. A great deal more information and understanding can be achieved if experimental data is combined with theoretical modelling of NC-AFM.

A theoretical model was developed to reproduce the real NC-AFM tip-surface interactions and to simulate the behaviour of the oscillating cantilever under the influence of these interactions. A general study of the components of the tip-surface interaction has been performed, with special regard to the complex electrostatic interactions which are relevant to NC-AFM both at the microscopic and macroscopic scale. This study was used to produce a physical model of a NC-AFM tip which could be used in further modelling. In an attempt to characterize some of the important processes in NC-AFM, the model was first used to analyze the role of the tip, atomic relaxation and image forces in NC-AFM imaging.

The model was then applied to NC-AFM imaging of the 1x1 reconstruction of the (110) surface of titanium dioxide, a classic benchmark in surface science. Theoretical scanlines of the surface compared well with experimental results, but it was found that image forces were important in imaging of TiO_2. The model, including image forces, was then applied to two characteristic systems which have been atomically resolved in NC-AFM: (i) a thin film of NaCl on a copper substrate and (ii) the (111) surface of CaF_2. In both cases the theoretical results compared well with experiment and extracted a lot more information about the tip, surface and tip-surface interactions than was previously available. In particular, for the first time in NC-AFM imaging of insulators, comparison of theory and experiment on the CaF_2 surface allowed the sublattice imaged in experiments to be identified. Finally, the possibility of detecting the exchange force on a magnetic surface with a metal coated NC-AFM tip has been studied theoretically and compared with experimental results on the antiferromagnetic NiO (001) surface.

The importance of theoretical modelling of NC-AFM in improving understanding of experimental results has been demonstrated. The model developed here has proved successful in simulating a wide variety of surfaces and interactions, and has greatly increased the amount of physical information available on the tip and surface structure, and tip-surface interactions compared to experiment alone.

Contents

List of Figures

List of Tables

0.1 Acknowledgements

I warn anyone of a sober and sensible disposition to avoid this section entirely, it is likely to be unpleasant reading.

In no particular order, I would first like to thank the NC-AFM community in general for their general good humour and helpful suggestions. I am especially grateful for the welcoming and warm attitude I experienced at conferences and while visiting groups, even when people disagreed with me. The most satisfying and successful parts of this work came directly from collaboration with NC-AFM experimentalists, and it was a great learning experience to discuss with them. In this regard, special thanks go to Chi Pang, Hibbat Raza and Geoff Thornton from Manchester for the work on TiO_2, Wolf Allers and Roland Wiesendanger for the work on NiO, Roland Bennewitz and Ernst Meyer for the work on NaCl/metals and cakes, and Clemens Barth and Michael Reichling for the work on CaF_2 and weisse beer. I would also like to thank Andrew Rohl for his essential advice and for letting me use the brilliant MARVIN code, which I regard as one of the best pieces of physics software around.

99.9 % of this work was done while I was in the Condensed Matter and Materials Group in University College London, so many thanks go to all the people there. More or less everyone there helped me in some way over the last three years and I wish them all well. Special mention must go to Alex Livshits who began most of the work on AFM and aided me greatly in continuing his excellent initial work. I would also like to thank all the people in CMMP who kept me (most of the time ;-) smiling, even when the stress of finishing started to wear on me. In the category of entertainment, special regards to Peter Sushko for his puzzled amusement and laughter, Stephen Shevlin for his hair and potatoes and peas, Johnathon Wasse for Fifa, *'Allo 'Allo* and Sheffield Wednesday, Louise Dash for outraged looks and telling me not to be so miserable, Andy Gormanly for taking it easy and comics, and Francisco Lopez for red wine, spanish omelettes and mariachi.

I owe a huge debt of gratitude (which they won't accept) to my supervisors Alex Shluger and Lev Kantorovich. Lev has proved an invaluable source of knowledge, ideas and most of all fun. He has contributed to every part of this work and has greatly supported me with his relentless enthusiasm for science and life in general. The fact that this work has proved (in my ever so humble opinion ;-) successful is mainly due to the encouragement and advice of Alex Shluger. His guidance and ideas are fundamental to this study, as was his drive to find the *physics* in NC-AFM. I also very grateful to him for the environment he created in our 'mini-group', which greatly encouraged the sharing of ideas and teamwork.

Finally, I would like to thank all the people outside physics who supported me during my PhD. I know most of you will just look at the pictures, but at least you can see that I didn't just surf the net for 3 years. Special thanks to my parents for their complete support and encouragement, even though you thought I should be at MIT. Massive and eternal thanks (specifically because she asked to be omitted) to Hanna, my ultimate motivation and reward.

Don't complain, I did warn you.

0.2 Companion Publications

The following publications were produced in the course of this study and they are listed along with the chapters that they are relevant to:

1. Model of noncontact atomic force microscopy on ionic surfaces - *A. I. Livshits, A. L. Shluger, A. L. Rohl and A. S. Foster*, Phys. Rev. **B** 59 (1999) 2436 - chapter 4.

2. Investigating the effects of silicon tip contamination in noncontact scanning force microscopy (SFM) - *P. V. Sushko, A. S. Foster, L. N. Kantorovich and A. L. Shluger*, Applied Surface Sci. **144 - 145** (1999) 608 - chapter 4.

3. Models of image contrast in scanning force microscopy on insulators - *A. L. Shluger, A. I. Livshits, A. S. Foster and C. R. A. Catlow*, J. Phys.: Condens. Matter **11** (1999) R295 - chapters 4 and 6.

4. Role of Image Forces in NC-AFM of Ionic Surfaces - *L. N. Kantorovich, A. S. Foster, A. L. Shluger and A. M. Stoneham*, Surface Sci. **445** (2000) 283 - chapter 5.

5. Atomically Resolved Edges and Kinks of NaCl islands on Cu(111): Experiment and Theory - *R. Bennewitz, A. S. Foster, L. N. Kantorovich, M. Bammerlin, Ch. Loppacher, S. Schär, M. Guggisberg, E. Meyer and A. L. Shluger*, Phys. Rev. B **62** (2000) 2074 - chapter 7.

6. Tip and Surface Properties from the Distance Dependence of Tip-Surface Interaction - *A. S. Foster, L. N. Kantorovich and A. L. Shluger*, Appl. Phys. A (2000) Accepted - chapters 5 and 8.

7. Imaging Problems on Insulators: What can be learnt from NC-AFM modelling on CaF_2? - *A. S. Foster, A. L. Rohl and A. L. Shluger*, Appl. Phys. A (2000) Accepted - chapter 8.

8. Unambiguous Interpretation of Atomically Resolved Force Microscopy Images of an Insulator - *A. S. Foster, C. Barth, A. L. Shluger and M. Reichling*, Phys. Rev. Lett. (2001) Submitted - chapter 8.

9. Contrast Formation in Atomic Resolution Scanning Force Microscopy on CaF_2 (111): Experiment and Theory - *C. Barth, A. S. Foster, M. Reichling and A. L. Shluger*, J. Phys.: Condens. Matter (2001) Submitted - chapter 8.

0.3 Conventions

Some standard conventions used in this study have been listed in this section.

- Length Scale - Angstroms (Å) and nanometres (nm) are the standard length units, where 10 Å is equal to 1 nm.

- Energy Scale - ElectronVolts (eV) and atomic units are the standard energy units, where 27.2114 eV is equal to 1 a.u.

- Force Scale - ElectronVolts per Angstrom (eV/Å) and nanoNewtons (nN) are the standard force units, where 1.62 eV/Å is equal to 1 nN.
- Surface Nomenclature - surfaces are referenced by their Miller Index, where the (001) surface is the plane normal to the x-axis in cartesian coordinates. Surface reconstructions are referred to by their extension of the primitive surface unit cell, so the 2×2 reconstruction is four times the area of the primitive surface unit cell.

Chapter 1

Introduction

The surface was invented by the devil. *Wolfgang Pauli.*

The study of surfaces has long held great importance in terms of technological applications. Many of the important properties of materials depend critically on the structure of their surfaces and how these surfaces interact with their environment. These surface properties dominate in such diverse applications as catalysis, microelectronics, electrochemistry, corrosion, photography, lubrication, adhesion, biology etc. The difficulties of producing and maintaining a clean, uncontaminated surface, limited surface science to the study of 'real' surfaces in the early part of the 20th century [1]. However, many important discoveries in surface science were still made in this period, such as the photo-electric effect by Einstein and the invention of the transistor by Bardeen and Brattain. Nevertheless the problems associated with contamination of surfaces after normal preparation meant that almost nothing was learnt about surfaces on the atomic scale. In 1937 Davisson and Germer were aware that their electron diffraction techniques probed the surface layer, yet the science community would have to wait a further 30 years before Photoemission Spectroscopy and Low Energy Electron Diffraction (LEED) were standard laboratory probes. This was mainly due to the nature of the experimental techniques available. For example, LEED gives information about the long-range order of the surface and studies require atomically flat areas of the order of tens of nanometres to give reliable data. Preparation of this type of controlled surface was impossible in the first half of the 20th century.

After the commercial development of Ultra-High Vacuum (UHV) chambers as an offshoot of the sixties space program, the study of surfaces expanded rapidly. It was now possible to prepare well-characterized solid surfaces, on which experimental results could be usefully compared with theoretical predictions. This experimental expansion coincided with the explosion of computer power and now, defected surfaces can be studied theoretically on the atomic scale with very high accuracy. However, these experimental techniques are limited in the type and scale of information that can be gathered. For example, Reflection High Energy Electron Diffraction (RHEED) and LEED, techniques commonly used for surface studies, cannot tell you anything about the local atomic geometric structure or local defects. Surface preparation is also much more difficult for many insulating surfaces compared to metals and semiconductors [2], difficulties in cleaving lead to very rough surfaces which are unsuited to the usual delocalized experimental techniques. To really

understand processes at surfaces, it is necessary to have information on the local atomic scale. Defects themselves also play a crucial role in many surface processes and statistical information about a large area of the surface cannot answer questions related to local surface features. The development of Scanning Probe Microscopy (SPM) finally offers the surface scientist the possibility to see surfaces on the atomic scale. SPM techniques measure the interaction between a probing tip and the surface on the atomic scale, so that, in principle, **individual** atoms on the surface can be imaged, an unprecedented ability. Combined with the power of recent theoretical treatments of surfaces, SPM techniques offer a possible solution to a great many of the questions which limit the development of surface applications.

As with any experimental technique, it is important to develop theoretical models of SPM which can be used to interpret the experimental data into information about the atomic structure of the surface studied. This study attempts to develop a model for one of the most recent SPM techniques, the Non-Contact Atomic Force Microscope (NC-AFM). The NC-AFM measures the change in frequency of an oscillating cantilever due to the interaction between tip and surface. Contrast in an NC-AFM image is usually generated by plotting the change in cantilever height necessary to keep the frequency change constant. It has demonstrated phenomenal success in imaging surfaces on the atomic scale, with many studies clearly resolving sites with atomic periodicity and atomic-sized defects. However, the chemical identity of the sites and defects resolved in images is usually not available from experiment alone, in fact it is not possible to say whether atoms are imaged at all from experiment alone. A combination of LEED/RHEED data and NC-AFM images can be used to identify the periodicity of the lattice imaged, but only a comparison of experimental data with a theoretical model can establish whether 'atomic resolution' has been achieved and identify the features imaged. The main motivation of this study is to produce a reliable model of NC-AFM imaging of insulating surfaces and use it to extract more information about the tip, surface and tip-surface interaction from experimental data on imaged surfaces, and also to make predictions about NC-AFM imaging of surfaces which are yet to be studied experimentally.

The first part of the study details the methods used and begins in chapter 2 with a detailed discussion of the NC-AFM technique itself and the specific interpretation problems associated with it. An 'ideal model' of those factors which must be represented in any theoretical treatment is then outlined. Since the NC-AFM effectively measures the tip-surface force across the surface studied, the first stage of the theoretical modelling process is to establish the components of the tip-surface interaction and the most effective way to calculate them. Chapter 3 discusses the components of the tip-surface interaction which are relevant to this study and also gives the details of how their contribution is calculated. A clear distinction between the forces important in atomic resolution and background forces is made. Chapter 4 uses these tip-surface components to establish a good model of the tip and surface. The tip itself must be represented at the macroscopic and microscopic scale, so that the macroscopic background forces and atomically sensitive chemical forces can both be included. The final part of the model simulates the behaviour of the cantilever oscillations under the influence of the tip-surface interactions. A discussion of tip chemical structure was published in ref. [3] and the basic model of NC-AFM was detailed in ref. [4]. A review published in ref. [5] also discussed many of the issues important to modelling and interpretting NC-AFM experiments.

Chapter 5 uses the model to try to characterize some important processes in NC-AFM imaging. Firstly, the model is used to characterize real NC-AFM tips by studying their interactions over a

metal surface and comparing with experimental results. This showed the importance of frequency change vs. distance curves taken after atomic resolution in getting more information on the tip and tip-surface interactions from NC-AFM experiments. This was published in ref. [6]. Then the importance of atomic displacements due to the interaction with the tip is discussed. Finally, the role of image forces in various characteristic systems based on a Sodium Chloride cluster on a metal substrate is studied. The model demonstrates that for charged steps and charged vacancies, the image force dominates the tip-surface interaction. The role of image forces in NC-AFM imaging was published in ref. [7].

The second part of this study is devoted to specific examples of systems studied by NC-AFM and the information that can be extracted by NC-AFM using a combination of theory and experiment. The systems studied demonstrate a wide variety of physical and chemical properties, and also demonstrate clearly how different tip-surface forces can dominate in different systems. Chapter 6 focuses on the titanium dioxide 1×1 (110) surface, a wide gap semiconducting material which has been well-characterized structurally by several experimental and theoretical techniques. The surface has also been atomically resolved in several experiments and represents a good benchmark for theoretical comparison. The model reproduces experimentally observed contrast on the TiO_2 surface with experimental parameters and predicts that for a tip with a negative electrostatic potential, the titanium atoms would be imaged as bright. However, the conductivity of TiO_2 means that image forces due to polarization could be significant in NC-AFM imaging of the TiO_2 and their introduction to the modelling reverses the predicted contrast. This chapter is organized in order to clearly outline each stage of applying the modelling process to a real system. Further chapters will focus more on the results rather than the method.

Chapter 7 is devoted to a comparison of theoretical modelling with experiments on NaCl thin films on a copper substrate. NC-AFM experiments on this system demonstrated atomic resolution of kinks and step-edges of islands of NaCl on top of the substrate. The experimental images showed a clear increase in contrast or brightness at these edges and kinks compared to resolution over the flat terraces. Modelling of this system demonstrated that this increase in contrast is due to the low-coordination of these sites. The low-coordination increases the electrostatic potential gradient at kinks and edges, and also increases the susceptibility of kink and edge ions to displacement when the tip is in close proximity. Both these effects cause an increase in attractive forces at low-coordinated sites and a corresponding increase in contrast. The model also demonstrated the importance of the microscopic chemical structure of the tip on atomic resolution. Simulated images with a negative potential tip were reversed compared to images with a positive potential tip and it was not possible to establish completely which sublattice was imaged as bright in the experiments. The combined experimental and theoretical study of NC-AFM imaging of NaCl thin films was published in ref. [8].

Chapter 8 focuses on a classic insulating system, calcium difluoride. As a wide gap insulator CaF_2 represents a good example of insulating systems in general. The 1×1 (111) surface of CaF_2 has been imaged in atomic resolution by NC-AFM successfully and atomic sized defects have also been observed after exposure to oxygen. The first stage of modelling on CaF_2 focused on using the system is an example to study why other insulating surfaces, such as magnesium oxide and alumina, have yet to be imaged in atomic resolution. The calculations predict that the main source of imaging difficulties is the roughness of these surfaces after cleavage. Simulated scanlines

across the CaF_2 surface show that its complexity produces secondary features, which in principle could be used to establish which sublattice is imaged in experiments and give a great deal of information about the chemical structure of the tip. In the second stage of modelling on CaF_2, the possibility of sublattice identification is studied by comparing directly with experimental evidence. The macroscopic properties of the tip were characterized by comparison between theoretical and experimental frequency change vs. distance curves, and then used to generate simulated scanlines and images with experimental parameters. These simulated results demonstrated very good agreement with experimental data and even reproduced directly the change in images observed experimentally as the tip moves close to the surface. A comparison of observed secondary features in theory and experiment predicts that the tip used in the experiment had a positive potential, and that the images showed the protruding F sublattice as bright with a deeper F sublattice producing a characteristic triangular contrast pattern. The study of the source of imaging difficulties in NC-AFM was published in ref. [9] and the combined experimental and theoretical study of NC-AFM imaging of CaF_2 was published in ref. [10] and ref. [11].

Chapter 9 moves to the more complex physics of the (001) surface of nickel oxide. Although the chemical structure of this system is quite simple and has the same lattice as MgO, NiO is a magnetic system. It's most stable surface is anti-ferromagnetic and this has motivated experimentalists to try to use NC-AFM with an iron coated tip to measure the exchange force on this surface. This would correspond to a clear difference in contrast over spin up and spin down Ni ions at the surface. An initial estimate of the size of this exchange force and the corresponding change in contrast is made using a advanced model of NC-AFM with a full *ab-initio* treatment of atomic interactions, electron and spin density. The role of ion jumps in limiting measurement of the exchange force was also studied.

Finally, in chapter 10 general conclusions from the study as a whole are discussed, drawing on the results from all the other chapters. These are then used to make some suggestions for future directions of both theoretical and experimental work in NC-AFM.

Part I

Methods

Introduction

The first part of this study focuses on the methods used to model NC-AFM. This begins with a description of the relevant forces and how they are calculated. Then the model itself is detailed and the NC-AFM simulation process is described. Finally, the model is applied to characterize some of the important processes in NC-AFM imaging.

Chapter 2

The Non-contact Atomic Force Microscope

2.1 Introduction

This work aimed to model one of the newest techniques in the toolkit of the experimental surface scientist, the dynamic or non-contact atomic force microscope (NC-AFM). The original AFM was developed in 1986 by Binnig, Quate and Gerber [12], in the same year that Binnig and Rohrer shared the Nobel Prize for their earlier invention in 1982 of probably the most successful of the SPM family, the scanning tunneling microscope (STM) [13].

The STM utilizes an atomically sharp tip which is placed sufficiently close to the sample so that tunneling of electrons between the two is possible. The tunneling current as a function of the tip-surface separation across the sample provides an image that reflects the local density of electronic states at the Fermi level of the uppermost atoms at the surface of the sample [14]. This technique has proved extremely successful in imaging metallic and semi-conducting surfaces with 'atomic resolution' in recent years [15, 16], but suffers from several drawbacks due to the mechanism of imaging. Most obviously, the STM can only image conducting surfaces or insulating films on top of conducting substrates [17]. Secondly, as discussed above, the STM does not directly image surface topography, but images the electronic structure of the sample. This can lead to ambiguities and inconsistencies in image interpretation and analysis. The AFM was developed to try and provide an experimental technique which could image a wide-range of conducting and insulating materials without these problems.

2.2 Experimental Setup

In AFM the probing tip is attached to a cantilever, and tip-surface forces, as opposed to current, are detected from microscopic deflections of the cantilever. Figure 2.1 shows a general picture of the experimental setup of an atomic force microscope. The whole system is suspended by four springs to damp any external vibrations and is also within an Ultra-High Vacuum (UHV) chamber to minimize environmental contaminants. The whole chamber is normally at room temperature,

but very recently low temperature NC-AFM [18] has been introduced, where the chamber is kept at less than 15 K and thermal noise is greatly reduced. The deflections of the cantilever (3) are measured using a laser (1) detected via a photodiode (5). The position of the sample (directly opposite the cantilever at (3)) is controlled by piezo-electric devices at (6) and (8).

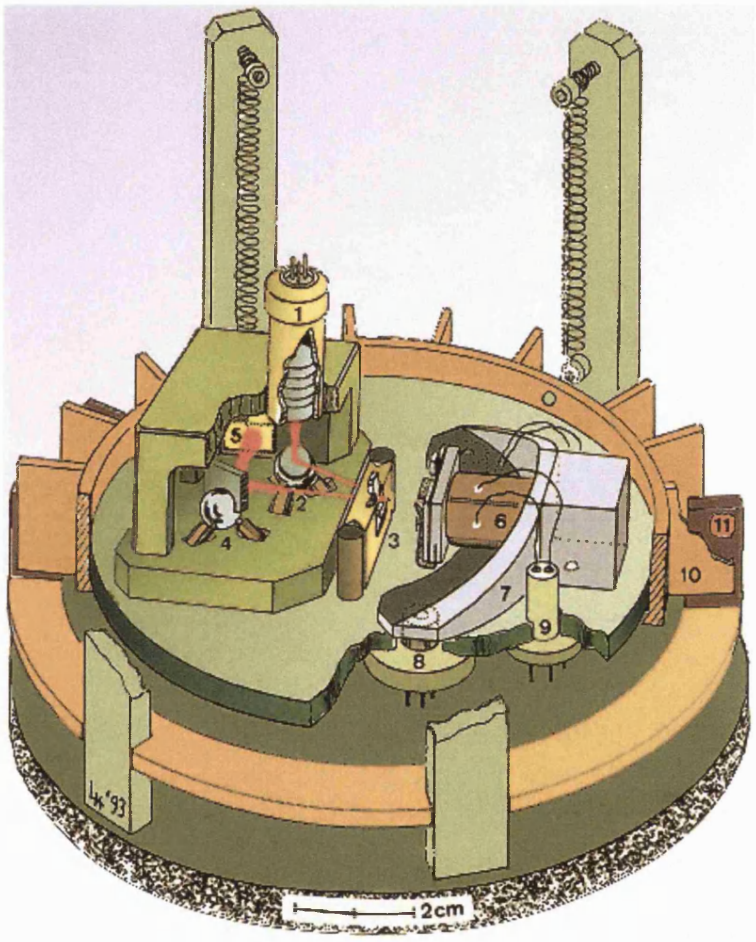

Figure 2.1: Experimental Setup of an AFM [19]

Unlike the STM, the AFM is not restricted to conducting tips and samples. There is also no restriction to tip-surface separations of the order of atomic separation, meaning tip-surface interactions of various decay lengths can be probed. The AFM has become a widely used, and trusted, technique for imaging of surfaces at large scale (nm$\Rightarrow$ μm), especially in the fields of materials engineering [20] and biology [21]. However, one of the most exciting and challenging aims of this technique, and all SPM techniques in general, is imaging of surfaces at the atomic scale. This requires probing the tip-surface interaction at close range, so that the differences in forces over specific atoms can be detected. The 'contact' mode of AFM (C-AFM) operation probes the surface at atomically close separations (< 2 Å) where the interactions are dominated by short-range attractive and repulsive interatomic forces. This mode of operation has proved to be unreliable for stable imaging in atomic resolution. Although early C-AFM studies demonstrated images with atomic periodicity, it soon became clear that the images produced were really a convolution of the

tip and the surface [22, 23, 24]. The small tip-surface separation in C-AFM meant that the atoms at and under the tip apex were extremely unstable, and likely to jump from the tip to surface and vice versa. These instabilities meant that it was impossible to determine whether images were really showing atoms or just showing how the properties of the tip and surface change while scanning. The tip itself was also likely to crash into the surface due to instability, damaging the surface and completely changing the imaging properties of the tip. In an effort to remove the destructive effects of instabilities from AFM imaging, the non-contact mode of AFM operation was developed. The specifics of this mode of operation are discussed in the next few sections, but it is important to first emphasize the experimental success already shown by this technique. After the first atomically resolved images of semiconductor surfaces [25], the technique soon expanded to successfully image halide [26, 27] and oxide surfaces [28, 29]. However, the technique still remains unreliable and although many groups have imaged a variety of surfaces with NC-AFM [30, 31], atomic resolution still remains rare and for most insulating systems, unobtained.

2.2.1 Electrical Setup

Figure 2.2 shows a circuit diagram of the standard electrical setup of a NC-AFM. In this diagram it is clear that voltages U_{dc} and U_{ac} are applied to the back of the sample beneath the tip (there is a metal plate beneath the sample being imaged) . Usually this effective *bias* is applied to the sample to minimize the electrostatic forces between the tip and surface [32, 33]. The general idea behind this process is that if electrons are allowed to flow between two different conducting materials (in this case tip and sample/substrate connected by an effective wire) there will be a contact potential U between them, as the electrons must pay energy to travel from the material with the smaller work function to the material with the higher one. The resultant difference in surface potential of the two materials produces an electrostatic force between them of the form:

$$F(x,y,z) = \frac{1}{2}\frac{dC}{dz}U^2(x,y) \tag{2.1}$$

where C is the tip-sample capacitance. By applying combined a.c. and d.c voltage to the system this force can be locally minimized (effectively removed from the tip-surface interactions). This electrostatic minimization is very similar to performing kelvin probe microscopy (KPM) [33], but in KPM the whole purpose of the experiment is to find this U and use it to infer properties of the sample. However, in KPM the sample is always conductive and electrons flow from tip to sample via a wire, whereas in AFM most samples are insulating and the electrons flow from tip to the conducting substrate under the sample.

However, there remain some inconsistencies in applying this minimization procedure. In NC-AFM it is normally performed at only one point (x,y,z) and it is assumed that the potential is uniform. Also in some NC-AFM setups it is not clear whether there is a direct electrical connection between the tip and sample. In later sections the effect of applied bias and electrostatic minimization in NC-AFM imaging will be discussed.

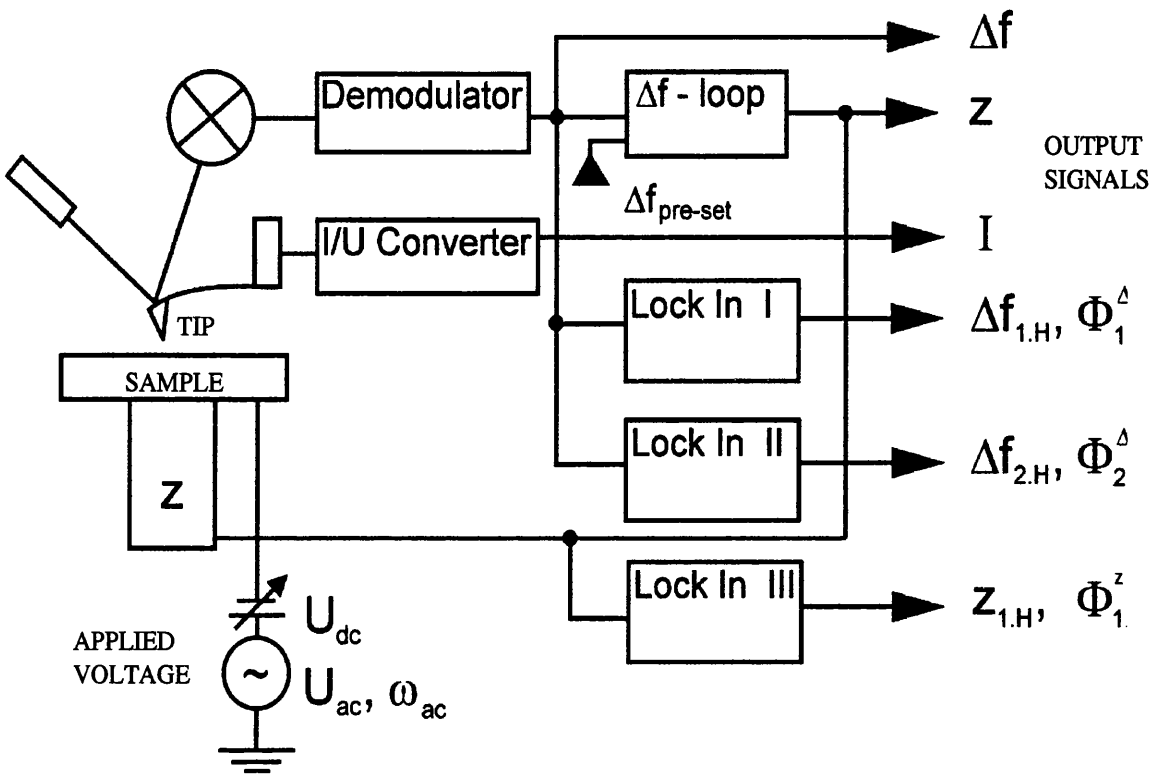

Figure 2.2: Circuit Diagram for standard NC-AFM operation

2.3 NC-AFM Operation

Figure 2.3 shows a schematic drawing of the actual operation of an atomic force microscope in non-contact mode. The whole tip-cantilever system is oscillated as it scans over the surface. As the tip is moved across the surface the interaction between the tip and the surface causes a change in the frequency of the oscillations. In most experimental setups the microscope scans the surface at constant frequency change and at a constant amplitude. This means that two electronic feedback loops are required. The first loop regulates the equilibrium height of the tip above the surface so that the frequency change remains constant, obviously this process is not instantaneous and there is some finite time between a change in the frequency and the deflection of the cantilever to compensate. The second loop attempts to keep the amplitude constant, this is necessary because the cantilever oscillations are damped and the amplitude of the cantilever will decay if a compensating excitation amplitude is not applied. Again there is a finite time between decay of the amplitude and compensation. A topographic image is generated by measuring the height of the tip at constant frequency change as a function of its position over the surface. Contrast in images is normally calibrated so that bright represents strong attraction and bigger tip-surface separation, and dark represents weaker attraction and smaller tip-surface separation. An example image can be seen in figure 2.4. Another possible mode of operation is the 'constant-height' mode, where only the amplitude is regulated and the frequency change, not cantilever height, produces image contrast. This mode of operation generally reduces noise in images, but it requires the tip to be scanned at higher speeds to avoid crashing and this can introduce image artifacts (see chapter 8).

Atomically resolved images have also been produced using damping, but a theoretical treatment of Non-Contact Dissipation Force Microscopy [34] and the damping mechanism is beyond the scope of this study. Examples of damping images can be seen in chapter 7.

The cantilever is usually oscillated at a frequency, f_0, of about 100-200 kHz and an amplitude, A_1, of 100-200 Å. The tip is moved very slowly across the surface (10 - 50 nm s^{-1}) and each pixel in an image is an average from several hundred oscillations (about 100 oscillations in 0.01 nm for a frequency of 100 kHz at scanning speed 10 nms^{-1}). The exact parameters depend on the cantilevers used and can vary widely [35]. The cantilevers are produced with a certain stiffness, k, which is usually in the range 1 - 50 N/m. The elastic force in the cantilever due to the oscillations, along with sensitive control over the frequency and amplitude allows the tip to be held in a net attractive tip-surface interaction at all times, which greatly reduces the probability of the tip crashing into the surface. This also means that the tip-surface separation during atomically resolved scanning will be of the order of 4 - 5 Å (based on theoretical predictions, for example see chapter 6), much further than in the contact regime. The greater separation when scanning means that the probability of ions jumping between tip and surface is reduced, although this remains an issue in NC-AFM and its role in imaging will be discussed later.

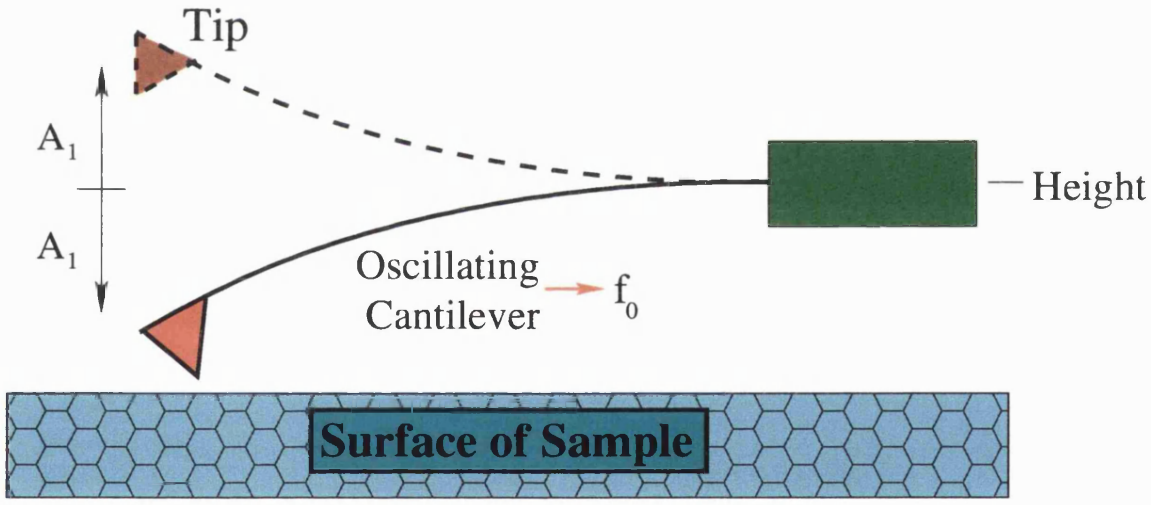

Figure 2.3: Schematic of Non-Contact AFM Operation. A_1 is oscillation amplitude and f_0 is the frequency of oscillations.

2.3.1 Normalized Frequency Shift

At this stage it is useful to introduce the Normalized Frequency Shift (γ_0) [36], as a representation of the magnitude of the force in an NC-AFM experiment which is independent of the parameters used. The frequency shift itself is dependent on the amplitude, frequency etc. of the cantilever oscillations, so is not a good measure of the force. Assuming that the force between tip and sample can be well represented by an inverse power law:

$$F(z) = -Cz^{-n} \tag{2.2}$$

where C is a tip-surface force constant and n is the order of the power, the frequency shift is given by [36]:

$$\Delta f\,(d,k,A_1,f_0,n) = \frac{1}{2\pi}\frac{f_0}{kA_1}\frac{C}{d^n}\int_0^{2\pi}\frac{\cos x}{\{1+(A_1/d)\,(\cos x+1)\}^n}dx \tag{2.3}$$

where d is the tip-surface closest approach and $x = f_0 t$. For large amplitudes, such that $A_1 \gg d$, a Taylor series expansion of the denominator of eq. 2.3 around $x_0 = \pi$ ($x' = x-\pi, cosx \simeq -1+x_2'/2$) and substitution ($y = \sqrt{A_1/2dx'}$) gives:

$$\Delta f(d,k,A_1,f_0,n) \cong -\frac{1}{\sqrt{2}\pi}\frac{f_0}{kA_0^{\frac{3}{2}}}\frac{C}{d^{n-1/2}}I_1(n) \tag{2.4}$$

with:

$$I_1(n) = \int_{-\infty}^{\infty}\frac{1}{(1+y^2)^n}dy \tag{2.5}$$

since $\Delta f \propto f_0/kA_1^{3/2}$ for large amplitudes for all inverse power forces independent of the exponent n, the set of parameters that is currently needed for a full description of a NC-AFM experiment can be condensed into a single parameter, the normalized frequency shift γ_0:

$$\gamma_0 = \frac{\Delta f k A_1^{\frac{3}{2}}}{f_0} \tag{2.6}$$

where Δf here is the frequency shift at imaging. This allows a comparison to be made between the magnitude of forces seen in various experiments. Table 2.1 gives a comparison of γ_0 for different materials imaged in atomic resolution. Clearly atomic resolution can be achieved for a wide variety of γ_0, although studies [35] have suggested that certain parameter sets will minimize the noise in experiments. It should be emphasized that γ_0 tells nothing about the components of the tip-surface force, but indicates the relative magnitude between different experiments.

Sample	γ_0 (fN$\sqrt{m}$)	Ref.
Si(111)	-65.4	[25]
NaCl(001)	-21.2	[26]
TiO_2(110)	-15.2	[37]
InP(110)	-3.8	[38]

Table 2.1: Comparison of normalized frequency shift for different surfaces imaged in atomic resolution by NC-AFM.

2.4 Image Analysis

Figure 2.4 shows four experimentally produced images of the sodium chloride surface with atomic resolution. This represents the final result of the imaging process, although this may have also undergone several stages of data filtering and Fourier analysis to reduce noise. It is at this stage that several of the problems associated with NC-AFM imaging become evident. Unlike the STM and Tersoff-Hamann theory [14], there as yet does not exist a reliable model for interpretting NC-AFM images. If we take figure 2.4 as an example, although by calculating the distances between

bright (or dark) parts of an image, strong conclusions about the periodicity of the lattice imaged can be made, it is not possible to distinguish which of the two sublattices (Na or Cl) is being imaged as bright or even if interstitials are being imaged.

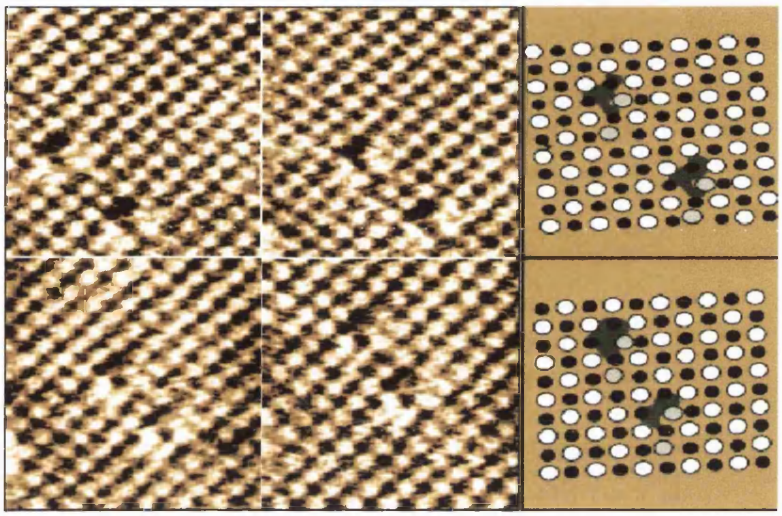

Figure 2.4: NC-AFM image of NaCl Surface [39].

Figure 2.4 also shows two point defects on the surface and how they move across the surface over a period of about two hours, with schematic drawings to the right of the figure showing the experimentalists' interpretation of what is happening. However, there is no way to determine the nature of the defect from these images alone, in fact it is difficult to obtain much real physical information at all from NC-AFM images. This is really the motivation behind the theoretical efforts to understand the interactions involved in imaging, and it is also the thread which will connect all the research presented in this study. By developing a reliable model for understanding the mechanism of contrast in NC-AFM, theory can then increase greatly the amount of physical information that can be extracted from images.

2.5 Ideal Model

Before discussing the interactions important in NC-AFM and how they can be modelled, it is useful to develop an 'idealized' model which demonstrates those properties which must be modelled in a good simulation of NC-AFM. These properties can be effectively categorized into 3 different areas: (i) tip, (ii) surface and (iii) experimental setup.

- Tip - macroscopic size and shape; conductivity; microscopic chemical structure; charging.
- Surface - macroscopic thickness; conductivity; microscopic chemical structure; charging.
- Experimental Setup - cantilever oscillations; conducting substrate; applied bias between tip and surface.

Fig. 2.5 shows a schematic diagram of this ideal setup.

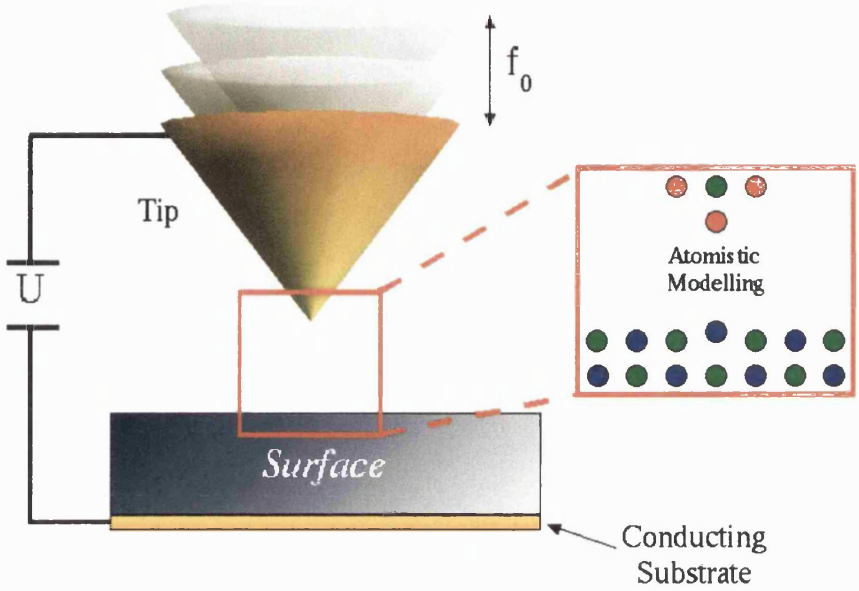

Figure 2.5: Idealized schematic of the setup needed to model an NC-AFM experiment. f_0 is the frequency of cantilever oscillations and U is the applied bias between conducting substrate and tip.

Most of these properties are self-explanatory and it is easy to see why it is important to model them and their effect on the tip-surface interaction. For example, the van der Waals interaction between tip and surface is almost totally dominated by the macroscopic size and shape of the tip. Also, since the NC-AFM is designed to measure atomic force, it is important to represent the microscopic tip and surface at an atomistic level so that the interactions over different atoms can be calculated. Finally, the whole system must model the dynamic effects introduced by the oscillations of the cantilever. This setup assumes that the conductivity of the tip and surface in real experiments is enough to keep their surfaces at constant potential at each point of slow cantilever oscillations.

Although fig. 2.5 shows a direct electrical connection between tip and surface, other possibilities may exist. For example, a setup where the tip and substrate are decoupled and their potentials are changed independently is equivalent, since only the absolute magnitude of the potential difference between the tip and the metal substrate matters.

In the next chapter the role of these properties in the tip-surface interaction will be discussed in detail, as will the components of the tip-surface interaction itself and the methods used to calculate it.

Chapter 3

Methods of Calculating the Tip-Surface Forces

3.1 Components of the Tip-Surface Interaction

The tip-surface interaction defines those forces which play a role in non-contact AFM imaging. It is impossible to discuss every possible interaction that occurs during an experiment, however it is clear that for a technique to be reliable a consistent set of significant interactions must exist. If the interactions varied wildly between experiments then no useful comparisons or conclusions could be made. In this chapter the significant interactions in NC-AFM will be explained, along with the methods used to calculate their contribution in modelling and discussion of when they are important.

As suggested in chapter 2, accurately representing the interactions between tip and surface while scanning means that the tip must be modelled on both the macroscopic and microscopic level. For example, knowledge of the tip structure on the macroscopic scale is required for calculation of the van der Waals interaction between the tip and surface. However, the tip-surface separation is not well defined on an atomic scale, so to avoid errors at short distances the van der Waals interaction between the tip and surface atoms in the contact area should be considered atomistically. Many studies [40, 41] of scanning force microscopy have demonstrated that it is important to model the tip-surface interaction at an atomistic level because surface relaxation and tip contamination [24] by surface and/or ambient atoms has a significant effect on contrast in SFM images. Therefore a complete model must include not only an accurate description of these forces, but also an accurate description of the behaviour of tip and surface atoms under the influence of these forces.

Representing the macroscopic and microscopic properties of the tip-surface interactions is achieved by dividing the tip model into two parts i) a macroscopic part and ii) an atomistic 'nano-tip' at the end of the macroscopic part. Figure 3.1 shows a schematic of an example tip-surface model. NC-AFM tips' macroscopic shape has been experimentally determined as a pyramidal by scanning the AFM tip across a surface of sharp pins [42] and by Scanning Transmission Electron Microscopy (STEM) images [43]. This pyramidal shape is represented by a conical macroscopic

tip of angle γ with a sphere of radius R at the end and the atomistic nano-tip is embedded at the base of the sphere. Representation of the nano-tip will be discussed in chapter 4.

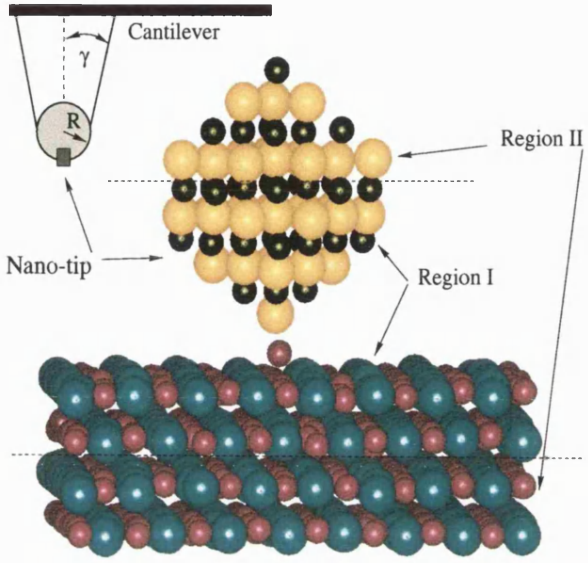

Figure 3.1: Schematic of integration of macroscopic and microscopic tip.

In this chapter it is important to remember the standard experimental conditions for NC-AFM imaging, UHV and room temperature. This means that certain forces, for example capillary forces, which were relevant for C-AFM in air will not be discussed here. An excellent review of the forces which are relevant to AFM in general can be found in ref. [44], however this study focuses on NC-AFM and the relevant forces are as follows:

- Chemical Forces - forces due to atomistic interactions in the nano-tip and surface. Relevant in all systems.
- Van der Waals Force - force due to interaction of fluctuating dipoles in the macroscopic tip and surface. Relevant in all systems.
- Image Force - due to polarization of conducting materials. Relevant if tip and/or surface is conducting.
- Capacitance Force - due to potential difference between tip and surface/substrate. Relevant if bias is applied or there is a significant contact potential between tip and surface.
- Forces due to Tip and Surface Charging - relevant if tip and/or surface is charged.
- Magnetic Forces - due to the interaction of a magnetic tip and surface. Relevant if tip and/or surface are magnetic.

In the following sections, each of these components will be discussed in detail and the method for calculating their contribution to the tip-surface interaction will be described.

3.2 Chemical Forces

Chemical forces really represent the atomistic interactions, the forces which are calculated for each pair of atoms in the system. Although in reality all the forces discussed in this chapter are the result of atomic interactions, most of the other forces can be accurately approximated by a macroscopic interaction. Excepting chemical forces, only the image force depends on the atomic configuration of the tip and surface, and still that is only dependent on the charge of atoms and not their identity. Chemical forces in atomistic simulations are generated from charge-charge electrostatic interactions, very short-range repulsive interactions due to electron orbital overlap and atom-atom van der Waals interactions. This description still holds for *ab initio* simulation, but then discrete charge interactions with separate attractive and repulsive components are replaced by more physical electron-electron, nuclear-electron and nuclear-nuclear interactions.

The chemical forces are the most important interaction in NC-AFM, they are the only interactions which can really distinguish atomic identities and are therefore responsible for atomic resolution in images (further discussion in chapter 4). They also define the atomic structure of the tip and surface, and are responsible for atomic displacements when the tip is close to the surface. Since they are so crucial to understanding NC-AFM imaging, it is important to check the interactions with as many experimental and theoretical benchmarks as possible for each system studied.

3.2.1 Calculating Atomistic Interactions

The level of complexity needed to calculate the atomistic interactions in NC-AFM depends on the properties of the system being studied. The various methods are discussed in detail below, but first it is important to establish the criteria for choosing a method. For the interactions of ionic systems, where the electron charge density is localized on the atomic cores and there is no significant charge transfer, it is sufficient to use a pair-potential treatment via the Shell Model (SM). Shell model calculations are very computationally cheap and systems of several hundred atoms can be calculated on a PC. However, the interactions in SM calculations must be parametrized for each pair of atoms and this leads to problems in overall accuracy - although very high accuracy can be achieved for specific physical properties. It should be noted that the parameters for the SM interactions are always checked by comparison to experiment or quantum mechanical calculations. Examples of this can be seen in chapters 6 and 8, in the studies of TiO_2 and CaF_2 respectively.

For semi-conducting or metallic systems it is important to represent the delocalized electron density correctly and therefore a more rigorous quantum mechanical treatment should be used throughout. In this case *ab initio* Hartree Fock Theory (HF) or Density Functional Theory (DFT) is used. An example of this can be seen in the study of silicon clusters in chapter 4. *Ab initio* calculations occupy the opposite end of the computational physics spectrum, they are very expensive and calculations of a hundred atoms requires the use of a supercomputer. In contrast to SM calculations, *ab initio* techniques, in principle, do not need any parameterization and provide very high levels of overall accuracy.

3.2.2 The Shell Model

In the Shell model, atomic interactions are represented by potentials between each pair of atoms in the system. Electronic polarization of the atoms is implemented via the Dick-Overhauser model [45], in which an atom is considered as a charged core connected by a harmonic spring to a massless charged shell (see figure 3.2). The equilibrium distance between the core and shell is a representation of the electronic polarization of that atom. This is important, as there are *no* electrons in the SM, all atoms are effectively represented by point charges and the shells approximate the effects of electron density flow on the atomic interactions.

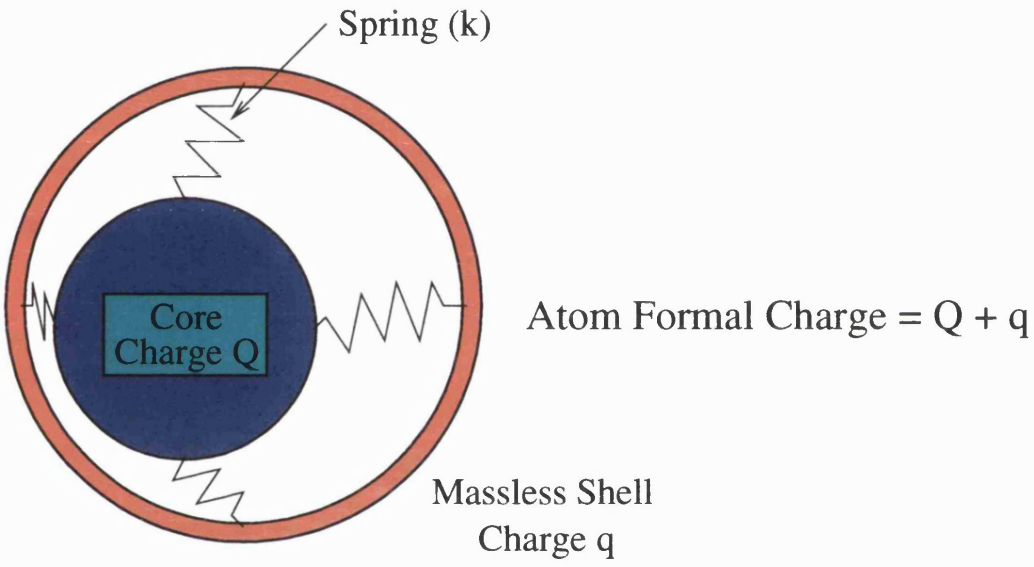

Figure 3.2: Schematic diagram of core and shell atomic representation.

The interactions between cores and shells are controlled by empirical potentials whose parameters are fitted to achieve the best possible comparison with experiment or *ab initio* techniques. The potentials are usually derived from three interactions: (i) electrostatic coulomb interactions between the atoms (cores and shells), (ii) van der Waals interactions and (iii) short-range repulsive interactions. The charge-charge electrostatic interaction between atoms i and j is given as the sum of four terms:

$$V_i^{elec} = \sum_j^n \frac{q_i q_j}{4\pi\varepsilon_0 |\mathbf{r}_{si} - \mathbf{r}_{sj}|} + \sum_j^n \frac{Q_i Q_j}{4\pi\varepsilon_0 |\mathbf{r}_{ci} - \mathbf{r}_{cj}|} + \sum_j^n \frac{Q_i q_j}{4\pi\varepsilon_0 |\mathbf{r}_{ci} - \mathbf{r}_{sj}|} + \sum_j^n \frac{q_i Q_j}{4\pi\varepsilon_0 |\mathbf{r}_{si} - \mathbf{r}_{cj}|} \quad (3.1)$$

where $i \neq j$, n is the number of atoms, q_i is the shell charge of atom i, Q_i the core charge of atom i, $\mathbf{r}_{si}$ is the position vector of the shell of atom i and $\mathbf{r}_{ci}$ is the position vector of the core of atom i. Buckingham two-body potentials were used throughout this study to represent the non-coulombic short-range interactions between the shells. These potentials have the following form:

$$V_i^{short} = \sum_j^n \left(-C |\mathbf{r}_{si} - \mathbf{r}_{sj}|^{-6} + Ae^{-\frac{|\mathbf{r}_{si} - \mathbf{r}_{sj}|}{\rho}} \right) \quad (3.2)$$

where C, A and ρ are parametrized constants specific to each pair of shells i and j, and $i \neq j$. Note that for some atoms there is no shell and all references to distance apply to the position of the core instead. The first term in equation (3.2) represents the attractive van der Waals interaction and the second term the short-range repulsion due to electron cloud overlap. For shells there is also an additional contribution to the interaction due to the elastic force in the spring connecting core and shell. This force is equal to $k\delta r_i$, where k is the parametrized spring constant between a core-shell pair and δr_i is the distance between the centres of core and shell for atom i. The spring interaction between the cores and shells is given by:

$$V_i^{spring} = \frac{1}{2} k \delta r_i^2 \tag{3.3}$$

Combining equations (3.1), (3.2) and (3.3)gives the total energy of the system as:

$$E = \frac{1}{2} \sum_i^n \left[V_i^{elec} + V_i^{short} + 2V_i^{spring} \right] \tag{3.4}$$

This can then be minimized with respect to core and shell positions to find the equilibrium geometry of relaxed atoms in the system. Usually certain atoms within the tip-surface unit cell remain frozen to represent the interface between the macroscopic and microscopic features, e.g. in fig. 3.1 region I would be relaxed and region II would be frozen. For infinite systems the unit cell is repeated, according to the system lattice vectors, across space until the atomic interactions converge to the desired accuracy. For bulk samples the cell is repeated in three dimensions, but for surfaces two possibilities exist. One method for calculating surfaces is by cutting the infinite bulk system and creating a series of slabs which are infinite in two dimensions, but separated in the third dimension by a large vacuum gap. These slabs are a good model of a surface if the gap is large enough that there is no significant interaction between the slabs. Another method for calculating surfaces is just to repeat the cell in two dimensions, directly generating a real infinite surface. Note that the electrostatic interaction converges conditionally for an infinite system and methods, such as Ewald summation [46], must be used to calculate this contribution.

3.2.3 Density Functional Theory

The following derivation and discussion is based on that given by Ohno *et al* [46] and is by no means a comprehensive treatment. For more details of the derivation and a deeper discussion of its significance please consult that text.

Density Functional Theory is one of many *ab initio* techniques which attempt to solve the many-body Schrödinger equation:

$$H\Psi_i(1, 2, ...N) = E_i\Psi_i(1, 2, ...N) \tag{3.5}$$

where H is the Hamiltonian of a quantum mechanical system composed of N particles, Ψ_i is its ith wavefunction and E_i is the energy eigenvalue of the ith state. The particle coordinates $(1, 2, ...N)$ are usually associated with a spin and a position coordinate. For electronic systems with non-relativistic velocities the Hamiltonian for an N-electron system is:

$$H = -\frac{1}{2}\sum_{i=1}^{N}\nabla_i^2 + \sum_{i>j}^{N}\frac{1}{|\mathbf{r}_i - \mathbf{r}_j|} + \sum_{i=1}^{N} v(\mathbf{r}_i) \tag{3.6}$$

where the first term of equation (3.6) represents the electron kinetic energy, the second term the electron-electron Coulomb interactions and the third term is the coulomb potential generated by the nuclei. This equation also assumes that the nuclei are effectively stationary with respect to electron motion (Born-Oppenheimer approximation).

Initial approaches to this problem attempted to transform the full N-body equation into N single-body equations by using the Hartree-Fock (HF) approximation (see section 3.2.4). This approximation basically affects the accuracy with which the 'exchange-correlation' contribution to the total energy is calculated. The exchange contribution is a direct consequence of Pauli's exclusion principle, which prohibits two fermions from occupying the same quantum state. This reduces the probability of one electron being near another electron of the same spin. The correlation contribution is due to the reduction in probability of an electron being near another electron due to strong electron-electron Coulomb repulsion. HF only includes the correlation contribution for similar spin electrons, but neglects entirely the contribution for opposite spin electrons. Traditionally (and confusingly....) the part of exchange-correlation included in HF is known as 'Exchange' and that neglected is known as 'Correlation'.

In contrast to these methods which try to determine approximations of the electron density or many-electron wavefunction, DFT can "exactly" calculate any ground-state property from the electron density. In 1964, Hohenberg and Kohn [47] considered the ground state of the electron-gas system in an external potential $v(\mathbf{r})$, and proved that the following density functional theorem holds exactly: There is a universal functional $F[\rho(\mathbf{r})]$ of the electron charge density $\rho(\mathbf{r})$ that defines the total energy of the electronic system as:

$$E = \int v(\mathbf{r})\rho(\mathbf{r})d\mathbf{r} + F[\rho(\mathbf{r})] \tag{3.7}$$

The energy of the system can be minimized to find the true electron charge density in the external potential. This theory is exact for a non-degenerate ground state. Unfortunately, as yet an exact general form of the functional $F[\rho(\mathbf{r})]$ has not been found, so approximations must be used.

Local Density Approximation

The most commonly used and successful approximation is the Local Density Approximation (LDA), first formulated by Kohn and Sham [48] in 1965. If the electron kinetic energy is written as $T[\rho(\mathbf{r})]$ then in the LDA the universal functional is given by (note that atomic units are used throughout this section):

$$F[\rho(\mathbf{r})] = T[\rho(\mathbf{r})] + \frac{1}{2}\int \frac{\rho(\mathbf{r})\rho(\mathbf{r}')}{|\mathbf{r} - \mathbf{r}'|}d\mathbf{r}d\mathbf{r}' + E_{xc}[\rho(\mathbf{r})] \tag{3.8}$$

where $E_{xc}[\rho(\mathbf{r})]$ is the exchange-correlation energy functional and is given as:

$$E_{xc}[\rho] = \int \rho(\mathbf{r})\,\epsilon_{xc}(\rho)\,d\mathbf{r} \tag{3.9}$$

where $\epsilon_{xc}(\mathbf{r})$ is the exchange and correlation energy per particle of a uniform electron gas of density ρ. The LDA uses the exchange-correlation energy of the homogeneous electron gas, evaluated from the charge density at the point $\mathbf{r}$ under consideration. Effectively at $\mathbf{r}$, $\rho = \rho(\mathbf{r})$ and E_{xc} is equal to the exchange-correlation energy for the electron-gas system which has a homogeneous charge density ρ. This is valid if the inhomogeneity of $\rho(\mathbf{r})$ is small, but the main approximation of LDA is that this is applied even if the inhomogeneity is large. By applying the variational principle to equation (3.7), with the constraint that for an N electron system $\int \rho(\mathbf{r})d\mathbf{r} = N$, the following equation is obtained:

$$\int \delta\rho(\mathbf{r}) \left\{ \frac{\delta T[\rho]}{\delta\rho(\mathbf{r})} + v(\mathbf{r}) + \int \frac{\rho(\mathbf{r}')}{|\mathbf{r}-\mathbf{r}'|} d\mathbf{r}' + \frac{\delta E_{xc}}{\delta\rho(\mathbf{r})} - \mu \right\} d\mathbf{r} = 0 \tag{3.10}$$

where μ is the Lagrangian multiplier equivalent to the chemical potential. Using the wavefunction $\psi_\lambda(\mathbf{r})$ of the λth level, the charge density is defined as :

$$\rho(\mathbf{r}) = \sum_{\lambda=1}^{N} |\psi_\lambda(\mathbf{r})|^2 \tag{3.11}$$

which allows the kinetic energy to be defined as:

$$T[\rho(\mathbf{r})] = -\frac{1}{2} \sum_{\lambda=1}^{N} \int \psi_\lambda^*(\mathbf{r}) \nabla^2 \psi_\lambda(\mathbf{r}) d\mathbf{r} \tag{3.12}$$

The solution of equation (3.10) is then given by solving the following effective one-electron Schrödinger equation for ψ_λ:

$$\left\{ -\frac{1}{2}\nabla^2 + v(\mathbf{r}) + \int \frac{\rho(\mathbf{r}')}{|\mathbf{r}-\mathbf{r}'|} d\mathbf{r}' + \frac{\delta E_{xc}}{\delta\rho(\mathbf{r})} \right\} \psi_\lambda(\mathbf{r}) = \epsilon_\lambda \psi_\lambda(\mathbf{r}) \tag{3.13}$$

where ϵ_λ is the energy eigenvalue of the λth state. This equation is called the Kohn-Sham equation and the eigenvalues are usually identified as the one-electron energy levels (this is an approximation due to LDA's deviation from the real result for states far below the Fermi level [46]). If equation (3.13) is solved self-consistently then the solutions, ψ_λ, will be related to the electron charge density and kinetic energy density via equations (3.11) and (3.12), but the Slater determinant constructed from ψ_λ is not the true many-electron HF wavefunction. ψ_λ are not the same as the one-electron wavefunctions in the Hartree-Fock approximation, but are more directly related to the true electronic charge density.

Generalized Gradient Approximation

Many modern codes using DFT now use more advanced approximations to improve accuracy for certain physical properties. The DFT calculations in this study have been made using the Generalized Gradient Approximation (GGA) [49, 50, 51, 52]. As stated above, the LDA uses the exchange-correlation energy for the uniform electron gas at every point in the system regardless of the homogeneity of the real charge density. For nonuniform charge densities the exchange-correlation energy can deviate significantly from the uniform result. This deviation can be expressed in terms of the gradient and higher spatial derivatives of the total charge density. The GGA uses the gradient of the charge density to correct for this deviation. For systems where the

charge density is slowly varying, the GGA has proved to be an improvement over LDA.

3.2.4 Hartree-Fock Theory

Another *ab initio* method for solving the many-body Schrödinger equation (equation (3.5)), is Hartree-Fock theory. As discussed in section 3.2.3, this method attempts to transform the full N-body equation into N single-body equations. According to quantum mechanics, one can determine the ground state of the Hamiltonian, H, by means of the variational principle for the normalized wavefunction $\Psi(1,2,\cdots,N)$:

$$\langle \Psi | H | \Psi \rangle = \sum_{s_1}\sum_{s_2}\cdots\sum_{s_N}\int \Psi^*(1,2,\cdots,N) H \Psi(1,2,\cdots,N) dr_1 dr_2 \cdots dr_N = minimum = E_0 \tag{3.14}$$

where s_i is the spin direction of the ith electron. According to this variational principle, an approximate wavefunction $\Psi(1,2,\cdots,N)$ can be found which minimizes the expectation value $\langle \Psi | H | \Psi \rangle$, since the expectation value is always greater than the true ground state energy. Assuming that the electrons are independent, then $\Psi(1,2,\cdots N)$ is a Slater determinant of single-particle wavefunctions such that:

$$\Psi(1,2,\cdots N) = \frac{1}{\sqrt{N!}} \begin{vmatrix} \psi_1(1) & \psi_2(1) & \cdots & \psi_N(1) \\ \psi_1(2) & \psi_2(2) & \cdots & \psi_N(2) \\ \vdots & \vdots & & \vdots \\ \psi_1(N) & \psi_2(N) & \cdots & \psi_N(N) \end{vmatrix} \tag{3.15}$$

where $\psi_\lambda(i)$ is the one-electron wavefunction of the λth level, which depends on the position, $\mathbf{r}_i$, and spin direction, s_i, of the ith electron, and forms an orthonormal set:

$$\langle \psi_\lambda \mid \psi_\nu \rangle = \sum_{s_i} \int \psi_\lambda^*(i) \psi_\nu(i) d\mathbf{r}_i = \delta_{\lambda\nu} \tag{3.16}$$

Using equation (3.15) as a trial solution, the expectation value can be evaluated as:

$$\langle \Psi | H | \Psi \rangle = \sum_{\lambda=1}^{N} \langle \psi_\lambda | H_0 | \psi_\lambda \rangle + \frac{1}{2}\sum_{\lambda,\nu} \langle \psi_\lambda \psi_\nu | U | \psi_\lambda \psi_\nu \rangle - \frac{1}{2}\sum_{\lambda,\nu} \langle \psi_\lambda \psi_\nu | U | \psi_\nu \psi_\lambda \rangle \tag{3.17}$$

where the Hamiltonian is divided into the one-electron part H_0 and the electron-electron Coulomb interaction U. H_0 represents the 1st and 3rd terms of equation (3.6) and U the remaining term. Using Lagrangian multipliers to keep the normalization condition, equation (3.16), the variational problem of equation (3.17) is solved:

$$\sum_{\lambda=1}^{N} \langle \delta\psi_\lambda | H_0 | \psi_\lambda \rangle + \sum_{\lambda,\nu} \langle \delta\psi_\lambda \psi_\nu | U | \psi_\lambda \psi_\nu \rangle - \sum_{\lambda,\nu} \langle \delta\psi_\lambda \psi_\nu | U | \psi_\nu \psi_\lambda \rangle - \sum_{\lambda} \epsilon_\lambda \langle \delta\psi_\lambda \mid \psi_\lambda \rangle = 0 \tag{3.18}$$

where ϵ_λ denotes the Lagrangian multiplier. To satisfy equation (3.18) for an arbitrary variation

$\langle \delta\psi_\lambda |$, the one-electron wavefunction ψ_λ should satisfy:

$$H_0\psi_\lambda(i)+\left[\sum_{\nu=1}^{N}\sum_{s_j}\int \psi_\nu^*(j)U(i,j)\psi_\nu(j)d\mathbf{r}_j\right]\psi_\lambda(i)-\left[\sum_{\nu=1}^{N}\sum_{s_j}\int \psi_\nu^*(j)U(i,j)\psi_\lambda(j)d\mathbf{r}_j\right]\psi_\nu(i)=\epsilon_\lambda\psi_\lambda(i) \tag{3.19}$$

Equation (3.19) is known as the Hartree-Fock equation and the use of the single Slater determinant, equation (3.15), to express the many-electron wavefunction is known as the Hartree-Fock approximation. The Hartree-Fock equation represents the one-electron approximation for interacting fermions which includes the anti-symmetry of the wavefunction or exchange interaction. If this contribution is ignored, then it is called the Hartree approximation.

3.2.5 Periodic Systems

For calculations of real crystals, both the *ab initio* techniques discussed previously must be implemented for infinite systems. This section outlines the methods used to represent the interactions of an infinite system with an *ab initio* treatment.

The atomic positions of a pure bulk crystal are invariant when they are translated by any sum $\mathbf{R}$, called the lattice vector, of integer multiples of three primitive translation vectors $\mathbf{a}_1, \mathbf{a}_2, \mathbf{a}_3$. This means that the potential of an infinite crystal system $V(\mathbf{r})$ has perfect periodicity and translational invariance such that $V(\mathbf{r}+\mathbf{R}) = V(\mathbf{r})$. Since the Hamiltonian of the one-electron problem is translationary invariant, the effective one-electron wavefunctions can be written as a product of an exponential and a periodic function, $u_{\mathbf{k}\lambda}(\mathbf{r}+\mathbf{R}) = u_{\mathbf{k}\lambda}(\mathbf{r})$ for the λth level , such that:

$$\psi_{\mathbf{k}\lambda}(\mathbf{r}) = e^{i\mathbf{k}.\mathbf{r}}u_{\mathbf{k}\lambda}(\mathbf{r}) \tag{3.20}$$

where $\mathbf{k}$ is the wave vector. This is called the Bloch Theorem and it satisfies:

$$\psi_{\mathbf{k}\lambda}(\mathbf{r}+\mathbf{R}) = e^{i\mathbf{k}.\mathbf{r}}\psi_{\mathbf{k}\lambda}(\mathbf{r}), \tag{3.21}$$

which is known as the Bloch function, and the orthonormality condition:

$$\int \psi_{\mathbf{k}\lambda}^*(\mathbf{r})\psi_{\mathbf{k}'\lambda'}(\mathbf{r})d\mathbf{r} = \delta_{\mathbf{k}\mathbf{k}'}\delta_{\lambda\lambda'} \tag{3.22}$$

where the integral is over the whole system. Then it is easy to verify that $\psi_{\mathbf{k}\lambda}(\mathbf{r})$ and $u_{\mathbf{k}\lambda}(\mathbf{r})$ satisfy the eigenvalue equation for the effective one-electron problem:

$$H\psi_{\mathbf{k}\lambda}(\mathbf{r}) = \left[-\frac{1}{2}\nabla^2 + V(\mathbf{r})\right]\psi_{\mathbf{k}\lambda}(\mathbf{r}) = \epsilon_{\mathbf{k}\lambda}\psi_{\mathbf{k}\lambda}(\mathbf{r}) \tag{3.23}$$

and

$$H_{\mathbf{k}}u_{\mathbf{k}\lambda}(\mathbf{r}) = \left[\frac{1}{2}(\mathbf{k}-i\nabla)^2 + V(\mathbf{r})\right]u_{\mathbf{k}\lambda}(\mathbf{r}) = \epsilon_{\mathbf{k}\lambda}u_{\mathbf{k}\lambda}(\mathbf{r}) \tag{3.24}$$

for the wavevector $\mathbf{k}$. The energy eigenvalue $\epsilon_{\mathbf{k}\lambda}$ of each level λ changes smoothly as a function of $\mathbf{k}$ and forms a curve along one direction of $\mathbf{k}$ in $\epsilon - \mathbf{k}$ space. Plots of these curves in different $\mathbf{k}$ directions are called the band structure of the crystal.

Now, by using reciprocal lattice vectors $\mathbf{b}_1, \mathbf{b}_2, \mathbf{b}_3$ such that $\mathbf{a}_i.\mathbf{b}_j = 2\pi\delta_{ij}$ and $\mathbf{G}$ as the reciprocal space equivalent of $\mathbf{R}$, the periodic function can be expanded as a Fourier series:

$$u_{\mathbf{k}\lambda}(\mathbf{r}) = \frac{1}{\sqrt{\Omega}} \sum_{\mathbf{G}} \widetilde{u}_{\mathbf{k}\lambda}(\mathbf{G}) e^{i\mathbf{G}.\mathbf{r}} \tag{3.25}$$

$$\widetilde{u}_{\mathbf{k}\lambda}(\mathbf{G}) = \frac{1}{\sqrt{\Omega}} \int_{cell} u_{\mathbf{k}\lambda}(\mathbf{r}) e^{-i\mathbf{G}.\mathbf{r}} d\mathbf{r} \tag{3.26}$$

where Ω is the volume of the unit cell. Substituting equation (3.25) into the Bloch theorem, equation (3.20), gives:

$$\psi_{\mathbf{k}\lambda} = \frac{1}{\sqrt{\Omega}} \sum_{\mathbf{G}} \widetilde{u}_{\mathbf{k}\lambda}(\mathbf{G}) e^{i(\mathbf{k}+\mathbf{G}).\mathbf{r}} \tag{3.27}$$

The basis function

$$|\mathbf{k}+\mathbf{G}\rangle = \frac{1}{\sqrt{\Omega}} e^{i(\mathbf{k}+\mathbf{G}).\mathbf{r}}, \tag{3.28}$$

normalized across the unit cell volume, is called a plane wave and the representation of the one-electron wavefunction in a periodic potential by equation (3.27) is called a plane wave expansion. The maximum value of the kinetic energy, $\frac{1}{2}\mathbf{G}^2$, of the plane waves is limited in real calculations and is usually referred to as the cutoff energy.

It is also possible to represent the effective one-electron wavefunction in the periodic potential as a superposition of localized orbitals, $\phi_\lambda(\mathbf{r})$, centred at each unit cell:

$$\psi_{\mathbf{k}\lambda}(\mathbf{r}) = \frac{1}{\sqrt{\eta}} \sum_{\mathbf{R}} e^{i\mathbf{k}.\mathbf{r}} \phi_\lambda(\mathbf{r}-\mathbf{R}) \tag{3.29}$$

Again equation (3.29) satisfies the Bloch theorem.

Using the fact that the wavefunction does not change if an arbitrary $\mathbf{G}$ is added to the wavevector i.e. $\psi_{\mathbf{k}\lambda}(\mathbf{r}) = \psi_{(\mathbf{k}+\mathbf{G})\lambda}(\mathbf{r})$, the wavevector can be confined within a minimum region bounded by the planes bisecting perpendicularly the lines from the origin to the neighbouring reciprocal lattice points. This region is called the first Brillouin zone (1st BZ) and the ground-state charge density is a sum over the occupied levels of Bloch functions within the 1st BZ:

$$\rho(\mathbf{r}) = \sum_{\lambda_{occ}} \sum_{\mathbf{k} \in 1st\,BZ} |\psi_{\mathbf{k}\lambda}(\mathbf{r})|^2 \tag{3.30}$$

where $\psi_{\mathbf{k}\lambda}(\mathbf{r})$ is an eigenstate of equation (3.23). Furthermore, due to translational symmetry:

$$\langle \psi_{\mathbf{k}\lambda} | H | \psi_{\mathbf{k}'\lambda'} \rangle = \epsilon_{\mathbf{k}\lambda} \delta_{\mathbf{k}\mathbf{k}'} \delta_{\lambda\lambda'} \tag{3.31}$$

if $\mathbf{k}$ and $\mathbf{k}'$ belong to the 1st BZ. For calculations of insulators and semiconductors, which have an energy band gap between valence and conduction states, the density can be accurately defined by an appropriate small $\mathbf{k}$-point sampling of the 1st BZ. For metals a much larger density of $\mathbf{k}$-points is required in the 1st BZ, as some of the bands are only partially filled and the Fermi energy is unknown before the calculation.

3.2.6 Programs for Calculating Chemical Forces

MARVIN

Nearly all Shell model calculations presented in this study were performed with the MARVIN computer code [53, 54, 55]. This code implements the full SM for 2D periodic systems i.e. it reproduces the interactions of an infinite surface without the need for calculating the interactions of an infinite number of atoms. MARVIN achieves this by repeating a unit cell of atoms in 2 dimensions by specified lattice vectors. For tip-surface calculations this unit cell includes the whole tip and a large block of the surface (see fig. 3.1), but for surface-only calculations the unit cell may contain only a few atoms. Only the full interactions for this unit cell are calculated explicitly and an Ewald summation is used to calculate the long-range electrostatic contribution of the infinite system to the total energy. MARVIN uses the Conjugate Gradient algorithm and a hybrid Newton algorithm to minimize the total energy with respect to the geometry of the unit cell.

VASP

In this study the VASP [56, 57] code was used to perform Density Functional Theory calculations. In this code the effective one-electron wavefunctions, ψ_λ, are expanded by plane wave basis functions. This method is based on the Car-Parrinello technique [58], in which the total energy of the system is minimized with respect to the plane wave coefficients of the occupied orbitals. As with MARVIN, VASP is a periodic code and it generates an infinite 3D system from a specified unit cell and lattice vectors. Surfaces can be studied with VASP by using the slab method discussed previously. For all calculations the generalized Gradient Approximation (GGA) functional of Perdew and Wang [59, 60] known as GGA-II has been used.

VASP also implements ultrasoft Vanderbilt pseudopotentials [61, 62], so that the core electrons are not treated explicitly and the effective one-electron potential is given by the sum of atomic pseudopotentials, the Coulomb potential due to the average valence electron density and the exchange-correlation potential. For some atoms, 'soft' and 'hard' ultrasoft pseudopotentials were available, but in this study only the safer 'hard' potentials were used.

CRYSTAL98

In this study the CRYSTAL98 [63] code was used to perform Hartree-Fock calculations. This approximates the one-electron wavefunctions by a linear combination of Gaussian localized atomic orbitals ($e^{-\alpha r^2}$). As with VASP, CRYSTAL98 is a periodic code and it generates an infinite 3D system from a specified unit cell and lattice vectors. Surfaces can be studied with CRYSTAL98 by using the slab method discussed previously. All calculations were performed without pseudopotentials (i.e. all-electron) and using Unrestricted Hartree-Fock (UHF) where the overall spin of the electrons on each atom is not restricted to zero. There is no geometry optimization in CRYSTAL98, so all calculations were performed with experimentally determined geometries.

3.3 Van der Waals Force

The van der Waals force represents the electromagnetic interaction of fluctuating dipoles in the atoms of the tip and surface. Basically, fluctuations of the electronic structure in one component induces dipoles in the other, the dipoles in both interact and a force between them is generated. This force is always attractive i.e. tip and surface are attracted to one another, and is present regardless of the tip/surface setup used or the environmental conditions of the experiment (excepting AFM experiments in liquids [64]). This is the same interaction mentioned in section 3.2, but in that case the number of atoms is small enough that the van der Waals force can be calculated explicitly by summing the interaction of all pairs of atoms. The full tip contains billions of atoms and it is impossible to sum all the interactions, therefore an approximation must be made based on the material and structure of the tip.

Assuming that the potential, $V(r)$, between two atoms separated by a distance r is known, then the force between them is defined by the gradient of that potential:

$$f(r) = -\nabla V(r) \tag{3.32}$$

For the van der Waals interaction the potential is of the form:

$$V(r) = -\frac{C_6}{r^6} \tag{3.33}$$

where C_6 is the interaction constant as defined by London [65] and is specific to the identity of the interacting atoms. Hamaker [66] then performed the integration of the interaction potential to calculate the total interaction between two macroscopic bodies. Hamaker used the following hypotheses in his derivation:

- additivity - the total interaction can be obtained by the pairwise summation of the individual contributions.
- continuous medium - the summation can be replaced by an integration over the volumes of the interacting bodies assuming that each atom occupies a volume dV with a number density ρ.
- uniform material properties - ρ and C_6 are uniform over the volume of the bodies.

This then allows the total force between two arbitrarily shaped bodies to be given by:

$$F_{vdw} = \rho_1 \rho_2 \int_{v_2} \int_{v_1} f(r) dV_1 dV_2 \tag{3.34}$$

where ρ_1 and ρ_2 are the number densities and V_1 and V_2 are the volumes of bodies 1 and 2 respectively. The Hamaker constant for the interaction is then:

$$H = \pi^2 C_6 \rho_1 \rho_2 \tag{3.35}$$

This study uses the derivation of Argento and French [67] for the total van der Waals force between a conical tip of angle γ and radius R (see fig. 3.1) and a plane. The total force is given by:

$$F_{vdw} = \frac{HR^2(1-\sin\gamma)(R\sin\gamma - z_0\sin\gamma - R - z_0)}{6z_0^2(R+z_0-R\sin\gamma)^2} - \frac{H\tan\gamma[z_0\sin\gamma + R\sin\gamma + R\cos(2\gamma)]}{6\cos\gamma(z_0+R-R\sin\gamma)^2} \tag{3.36}$$

where z_0 is the tip-surface separation. Calculation of the van der Waals contribution to the total tip-surface force requires only knowledge of γ, R and H. γ and R depend only on the tip-shape, and this can be estimated from experimental studies of NC-AFM tip properties (see section 4). The Hamaker constant, H, depends on the geometry and materials of the tip and surface. However, the NC-AFM system is assumed to be well represented by a conical tip and a planar surface, so H effectively depends only on the material of the tip and surface.

3.4 Image Force

The image force is the interaction due to the polarization of the conducting electrodes (i.e. of the conducting tip and the substrate) by the charged atoms of the sample. This is important for any tip-surface (or just surface) setup containing conducting materials e.g. interaction of a conducting tip with an insulating surface or studying the properties of an insulating thin film on top of a metal substrate.

The potential on conducting electrodes is maintained by external sources (i.e. by the "battery"). From the point of view of classical electrostatics the polarization of the conductors by external charges is caused by the additional potential on the conductors due to the charges. This extra potential is compensated by a charge flow from one electrode to another to keep the potential on the conductors fixed. This work is done by the battery. As a result, there will be some distribution of the net charge on the surfaces of conductors induced by the point charges situated in the free space between them. The net charge on each conducting electrode would interact with the total charge on other conductors and with the point charges. Hereafter this interaction is called the *image interaction.*

3.4.1 Electrostatic energy of a system of metals and charges

The derivation of the electrostatic energy given here is taken from ref. [68] and that should be consulted for a more thorough discussion. Consider a set of *finite* metallic conductors of arbitrary shape and an arbitrary distribution of point charges $\{q_i\}$ at the points $\{\mathbf{r}_i\}$ anywhere in the free space outside the conductors. Assume that the conductors, which will hereafter be designated by indices m, m', are kept at some *fixed* potentials ϕ_m. These potentials are provided by the batteries.

It is known from the standard textbooks (e.g. Refs. [69], [70], [71]) how to calculate the energy accumulated in the electrostatic field $\mathbf{E}$ created by point charges and metals. Using the total energy of the field, $U_{tot} = \frac{1}{8\pi}\int_\sigma \mathbf{E}^2 d\mathbf{r}$ (the integral is taken over the volume σ outside the metals since inside those the field $\mathbf{E} = 0$) and applying the Poisson equation for the field, one gets:

$$U_{tot} = \frac{1}{2}\sum_i q_i\phi(\mathbf{r}_i) + \frac{1}{2}\sum_m Q_m\phi_m \tag{3.37}$$

where the first sum is taken over all point charges and the second one over all conductors. $Q_m =$

$-\frac{1}{4\pi}\int\int_{S_m}\frac{\partial\phi}{\partial n}ds$ is the charge on the metal m, where the integral is performed over the surface S_m of the metal. Note that the surface integral over a remote surface at infinity (which is surrounding all the metals and the point charges) vanishes due to rapid decrease of the potential to zero there [70]. Therefore, this derivation is not valid for infinite metals for which this assumption is not correct (e.g. a charged infinite metal conductor). It should also be noted that according to classical theory, the charge is distributed at the surface, i.e. it does not penetrate into the bulk of the metal; quantum theory [72], [73], [74] gives a certain distribution of the surface charge in the direction to the bulk.

The result of Eq. (3.37) has a very simple physical meaning: every charge q at the point $\mathbf{r}_q$ (either a point charge outside the metals or the distributed charge on a metal surface) gets energy $\frac{1}{2}q\phi(\mathbf{r}_q)$, where the factor $\frac{1}{2}$ is needed to avoid double counting. Note that the potential $\phi(\mathbf{r})$ is produced both by the metals (i.e. by the distributed charges on their surfaces) and by the point charges. Note also that both the potential $\phi(\mathbf{r}_i)$ on point charges and the charges Q_m on the metals are unknown and should be calculated by solving the Poisson equation. The effect of the metals comes into play via the boundary conditions and the charges Q_m.

In order to calculate the electrostatic force imposed on any of the conductors, a method essentially similar to the one of Ref. [70] was used. In this method an arbitrary distribution of metals is considered without point charges. The force is obtained by differentiating the energy with respect to the corresponding position of the metal of interest. It is shown in Ref. [70] that the same expression for the force is obtained in the cases of fixed potentials or fixed charges on the metals. This, however, is not the case if the point charges are present. Indeed, if some metal is moved by the vector $\delta\mathbf{r}$, work $\delta A = -\mathbf{F}\delta\mathbf{r}$ is done by the external force against the force $\mathbf{F}$ imposed on the conductor. When the conductor is moved to the new position, the potential $\phi(\mathbf{r})$ in the system will change by $\delta\phi(\mathbf{r})$. The potential on any metal m will no longer be equal to the fixed value ϕ_m so that there should be some charge flow between the connected conductors to maintain the potential on them. Therefore, some work δA will be spent in changing the potential energy of the field (given by Eq. (3.37)) by the amount

$$\delta U_{tot} = \frac{1}{2}\sum_i q_i\delta\phi(\mathbf{r}_i) + \frac{1}{2}\sum_m \phi_m\delta Q_m$$

and some work δA_b is done in transferring charge *between* the conductors. The latter work δA_b is done by the batteries (as the charge flows via the battery from one conductor to another) and so should be taken with the minus sign: $\delta A = -\delta A_b + \delta U_{tot}$. Alternatively, one could think of the batteries being incorporated into the system; in that case it would mean that the work done by the batteries would reduce the total potential energy of the whole system.

Let δQ_m be the change of the charge on the conductor m, then the work $\delta A_b = \sum_m \phi_m\delta Q_m$ (cf. Eq. (2.5) in Ref. [70]). Since $\sum_m \delta Q_m = 0$, this is the work needed to distribute the zero charge initially stored at infinity (where the potential is zero) between different metals by transferring the amounts δQ_m to the each metal m. Using the above given expressions, we obtain:

$$\delta A \equiv -\mathbf{F}\delta\mathbf{r} = -\sum_m \phi_m\delta Q_m + \delta U_{tot}$$

so that the final expression for the force imposed on the displaced metal becomes

$$\mathbf{F} = -\frac{\partial U_{eff}}{\partial \mathbf{r}} \tag{3.38}$$

with the *effective energy* (or the total potential energy of the whole system which includes the batteries as well) defined as:

$$U_{eff} = \frac{1}{2}\sum_i q_i\phi(\mathbf{r}_i) - \frac{1}{2}\sum_m Q_m\phi_m \tag{3.39}$$

3.4.2 Tip-surface Image Interaction

In order to calculate the force imposed on the tip the following expression for the total energy of the system was used:

$$U_{tot} = \frac{1}{2}\sum_{ij,i\neq j} v_{ij} + U_{el} \tag{3.40}$$

where v_{ij} is the interatomic potential between atoms i, j. This total energy is a function of both the tip position z_s and the coordinates $\mathbf{r}_i$ of all atoms (and shells see section 3.2.1) involved.

The last term in Eq. (3.40) represents the total electrostatic energy of the whole system. It is assumed that the Coulomb interaction between all atoms is included in the first term in Eq. (3.40) and hence should be excluded from U_{el}. Therefore, the energy U_{el} includes the interaction of the atoms in the system with the macroscopic tip and substrate. As has been demonstrated, the correct electrostatic energy should incorporate the work done by the battery to maintain the constant potential on the electrodes. Following the derivation in ref. [68] the electrostatic component of the total energy can be written as:

$$U_{el} = -\frac{1}{2}Q^{(0)}V + \sum_i q_i\phi^{(0)}(\mathbf{r}_i) + \frac{1}{2}\sum_{i,j} q_iq_j\phi_{ind}(\mathbf{r}_i,\mathbf{r}_j) \tag{3.41}$$

Here V is the potential difference applied to the metal electrodes. Without loss of generality, one can choose the potential ϕ on the metal plane to be zero, so that the potential on the macroscopic part of the tip will be $\phi = V$. It should be noted that the substrate is considered in the limit of a sphere of a very big radius $R' \gg R$ since the metal electrodes formally cannot be infinite. The charge on the tip *without* charges outside the metals (i.e. when there are only bare electrodes and the polarization effects can be neglected) is $Q^{(0)}$ and the electrostatic potential of the bare electrodes anywhere outside the metals is $\phi^{(0)}(\mathbf{r})$. The charge $Q^{(0)}$ and the potential $\phi^{(0)}(\mathbf{r})$ depend only on the geometry of the capacitor formed by the two electrodes and on the bias V. The charge $Q^{(0)}$ can be calculated from the potential $\phi^{(0)}(\mathbf{r})$ as follows [70]: $Q^{(0)} = -\frac{1}{4\pi}\int\int \frac{\partial\phi^{(0)}}{\partial n}ds$ where the integration is performed over the entire surface of the macroscopic part of the tip with the integrand being the normal derivative of the potential $\phi^{(0)}(\mathbf{r})$; the normal $\mathbf{n}$ is directed outside the metal. Summation in the second term of Eq. (3.41) is performed over the atoms and shells of the sample and those of the tip apex which are represented by point charges q_i at positions $\mathbf{r}_i$.

Finally, $\phi_{ind}(\mathbf{r},\mathbf{r}')$ in Eq. (3.41) is the potential at $\mathbf{r}$ due to image charges *induced* on the metals by a unit point charge at $\mathbf{r}'$. This function is directly related to the Green function $G(\mathbf{r},\mathbf{r}')$ of the Laplace equation, $\phi_{ind}(\mathbf{r},\mathbf{r}') = G(\mathbf{r},\mathbf{r}') - \frac{1}{|\mathbf{r}-\mathbf{r}'|}$, and is symmetric, i.e. $\phi_{ind}(\mathbf{r},\mathbf{r}') = \phi_{ind}(\mathbf{r}',\mathbf{r})$,

due to the symmetry of the Green function itself [71]. The total potential at $\mathbf{r}$ due to a net charge induced on all conductors present in the system by all the point charges $\{q_i\}$,

$$\phi_{ind}(\mathbf{r}) = \sum_i q_i \phi_{ind}(\mathbf{r}, \mathbf{r}_i) \tag{3.42}$$

is the *image potential*. Note that the last double summation in Eq. (3.41) includes the $i = j$ term as well. This term corresponds to the interaction of the charge q_i with its own polarization.

The function $\phi_{ind}(\mathbf{r}, \mathbf{r}')$ and, therefore, the image potential, $\phi_{ind}(\mathbf{r})$, together with the potential $\phi^{(0)}(\mathbf{r})$ of the bare electrodes could be calculated if the exact Green function of the electrostatic problem is known

$$\Delta_{\mathbf{r}'} G(\mathbf{r}, \mathbf{r}') = -4\pi\delta(\mathbf{r} - \mathbf{r}') \tag{3.43}$$

with the corresponding boundary conditions ($G(\mathbf{r}, \mathbf{r}') = 0$ when $\mathbf{r}$ or $\mathbf{r}'$ belong to either the substrate or the tip surface) [71]. Therefore, given the applied bias V, the geometric characteristics of the capacitor and the positions $\{\mathbf{r}_j\}$ of the point charges $\{q_i\}$ between the tip and sample, one can calculate the electrostatic energy U_{el}. The problem is that the Green function for real tip-sample shapes and arrangements is difficult to calculate. In this study a planar-spherical geometry of the junction, as depicted in fig. 3.3, is used.

3.4.3 Solution of the electrostatic problem of point charges inside the sphere-plane capacitor

First, the calculation of the potential $\phi^{(0)}(\mathbf{r})$ of the bare electrodes is considered, i.e. the capacitor problem. It should be noted that the potential $\phi^{(0)}(\mathbf{r})$ satisfies the same boundary conditions as the original problem, i.e. $\phi^{(0)} = 0$ and $\phi^{(0)} = V$ at the lower and upper electrodes, respectively. The solution for the plane-spherical capacitor is well known [75] and can be given using the method of image charges. Since this solution is needed for calculating forces later on, it is given here in detail. It is convenient to choose the coordinate system as shown in fig. 3.3. Note, however, that the positions of the image charges in fig. 3.3 are only relevant for the later discussion of the induced potential. It is easy to check that the following two *infinite* sequences of image charges give the potential at the sphere and the metal plane as V and zero respectively. The first sequence is given by the image charges $\varsigma_1 = RV$ and then $\varsigma_{k+1} = \frac{\varsigma_k}{D_k}$ for all $k = 1, 2, \ldots$, where the dimensionless constants D_k are defined by the recurrence relation $D_{k+1} = 2\lambda - \frac{1}{D_k}$ with $D_1 = 2\lambda$ and $\lambda = \frac{z_s}{R} > 1$, z_s being the distance between the sphere centre and the plane (fig. 3.3). The point charges $\{\varsigma_k\}$ are all inside the sphere along the line normal to the surface passing through the sphere centre. Their z-coordinates are as follows: $z_1 = z_s$ and $z_{k+1} = R\left(\lambda - \frac{1}{D_k}\right) = R(D_{k+1} - \lambda)$ for all $k = 1, 2, \ldots$. The second sequence of charges $\{\varsigma'_k\}$ is formed by the images of the first sequence with respect to the metal plane, i.e. $\varsigma'_k = -\varsigma_k$ and $z'_k = -z_k$. An interesting point about the image charges $\{\varsigma_k\}$ is that they converge very quickly at the point $z_\infty = R\sqrt{\lambda^2 - 1}$ (i.e. $z_k \to z_\infty$ with $k \to \infty$) and that $z_{k+1} < z_k$ for all k. This is because the numbers D_k converge rapidly to the limiting value $D_\infty = \lambda + \sqrt{\lambda^2 - 1}$ which follows from the original recurrent relation above, $D_\infty = 2\lambda - \frac{1}{D_\infty}$. Therefore, while calculating the potential $\phi^{(0)}(\mathbf{r})$, one can consider the charges $\{\varsigma_k\}$ and $\{\varsigma'_k\}$ explicitly only up to some $k = k_0 - 1$ and then sum up the rest of the charges to infinity analytically to obtain the effective charge $\varsigma_\infty = \sum_{k=k_0}^{\infty} \varsigma_k = \sum_{n=0}^{\infty} \frac{\varsigma_{k_0}}{D_\infty^n} = \frac{\varsigma_{k_0} D_\infty}{D_\infty - 1}$ to be

placed at z_∞. This can be used *instead* of the rest of the series:

$$\phi^{(0)}(\mathbf{r}) = \sum_{k=1}^{k_0} \bar{\varsigma}_k \left(\frac{1}{|\mathbf{r} - \mathbf{r}_{\varsigma_k}|} - \frac{1}{|\mathbf{r} - \widehat{\sigma}\mathbf{r}_{\varsigma_k}|} \right) \tag{3.44}$$

where $\bar{\varsigma}_k = \varsigma_k$ for $k < k_0$ and $\bar{\varsigma}_{k_0} = \varsigma_\infty$; then, $\mathbf{r}_{\varsigma_k} = (0, 0, z_k)$ is the position vector of the charge ς_k and $\mathbf{r}_{\varsigma'_k} = \widehat{\sigma}\mathbf{r}_{\varsigma_k} = (0, 0, -z_k)$ is the position of the charge ς'_k ($\widehat{\sigma}$ means reflection with respect to the substrate surface $z = 0$). To find the charge $Q^{(0)}$ which is also needed for the calculation of the electrostatic energy, eq. (3.41), the normal derivative of the potential $\phi^{(0)}(\mathbf{r})$ on the sphere should be calculated and then the corresponding surface integral should be solved (see above). However, it is useful to recall that the total charge induced on the metal sphere due to an external charge is equal exactly to the image charge inside the sphere [70], [71]. Therefore, the following can be immediately obtained:

$$Q^{(0)} = \sum_{k=1}^{k_0} \bar{\varsigma}_k \tag{3.45}$$

Note that the potential $\phi^{(0)}(\mathbf{r})$ and the charge $Q^{(0)}$ depend on the position z_s of the sphere *indirectly* via the charges ς_k and their positions $\mathbf{r}_{\varsigma_k}$ according to the recurrent expressions above. Therefore, care has to be taken when calculating the contribution to the force imposed on the tip due to bias V (i.e. when differentiating $\phi^{(0)}(\mathbf{r})$ and $Q^{(0)}$ in Eq. (3.41)).

Next is the calculation of the function $\phi_{ind}(\mathbf{r}, \mathbf{r}')$ in Eq. (3.41). This function corresponds to the image potential at a point $\mathbf{r}$ due to a unit charge at $\mathbf{r}'$. This potential is to be defined in such a way that together with the direct potential of the unit point charge, it should be zero on both electrodes (the boundary condition for the Green function). Thus, a unit charge $q = 1$ at $\mathbf{r}_q$ somewhere outside the metal electrodes must be considered, as shown in fig. 3.3. First, a direct image $-q$ of this charge is created with respect to the plane at the point $\mathbf{r}'_q = \widehat{\sigma}\mathbf{r}_q$ to maintain zero potential at the plane. Then, images of the two charges, $q = 1$ and $-q = -1$, are created with respect to the sphere to get two image charges $\xi_1 = -\frac{R}{|\mathbf{r}_q - \mathbf{R}_s|}$ and $\zeta_1 = \frac{R}{|\widehat{\sigma}\mathbf{r}_q - \mathbf{R}_s|}$, as shown in fig. 3.3 where $\mathbf{R}_s = (0, 0, z_s)$. These image charges are both inside the sphere by construction and their positions can be written down using a vector function $\mathbf{f}(\mathbf{r}) = \mathbf{R}_s + R^2 \frac{\mathbf{r} - \mathbf{R}_s}{|\mathbf{r} - \mathbf{R}_s|^2}$ as follows: $\mathbf{r}_{\xi_1} = \mathbf{f}(\mathbf{r}_q)$ and $\mathbf{r}_{\zeta_1} = \mathbf{f}(\widehat{\sigma}\mathbf{r}_q)$. Now the potential at the surface will be zero. At the next step the images $\xi'_1 = -\xi_1$ and $\zeta'_1 = -\zeta_1$ of the charges ξ_1 and ζ_1 are created in the plane at points $\widehat{\sigma}\mathbf{r}_{\xi_1}$ and $\widehat{\sigma}\mathbf{r}_{\zeta_1}$ respectively, to get the potential at the plane also zero. This process is continued and in this way two infinite sequences of image charges are constructed, which are given by the following recurrence relations:

$$\begin{cases} \xi_{k+1} = \xi_k \frac{R}{|\widehat{\sigma}\mathbf{r}_{\xi_k} - \mathbf{R}_s|} \\ \mathbf{r}_{\zeta_{k+1}} = \mathbf{f}(\widehat{\sigma}\mathbf{r}_{\xi_k}) = \mathbf{R}_s + R^2 \frac{\widehat{\sigma}\mathbf{r}_{\xi_k} - \mathbf{R}_s}{|\widehat{\sigma}\mathbf{r}_{\xi_k} - \mathbf{R}_s|^2} \end{cases} \tag{3.46}$$

where $k = 1, 2, \ldots$ and similarly for the ζ-sequence. Note, however, that the two sequences start from different initial charges. Namely, the ξ-sequence starts from the original charge q while the ζ-sequence from its image in the plane $-q$. The two sequences $\{\xi_k\}$ and $\{\zeta_k\}$ are to be accompanied by the other two sequences $\{\xi'_k\}$ and $\{\zeta'_k\}$ which are the images of the former charges with respect to the plane. The four sequences of the image charges and the charges q and $-q$ provide the correct solution for the problem formulated above since they produce the potential which is the

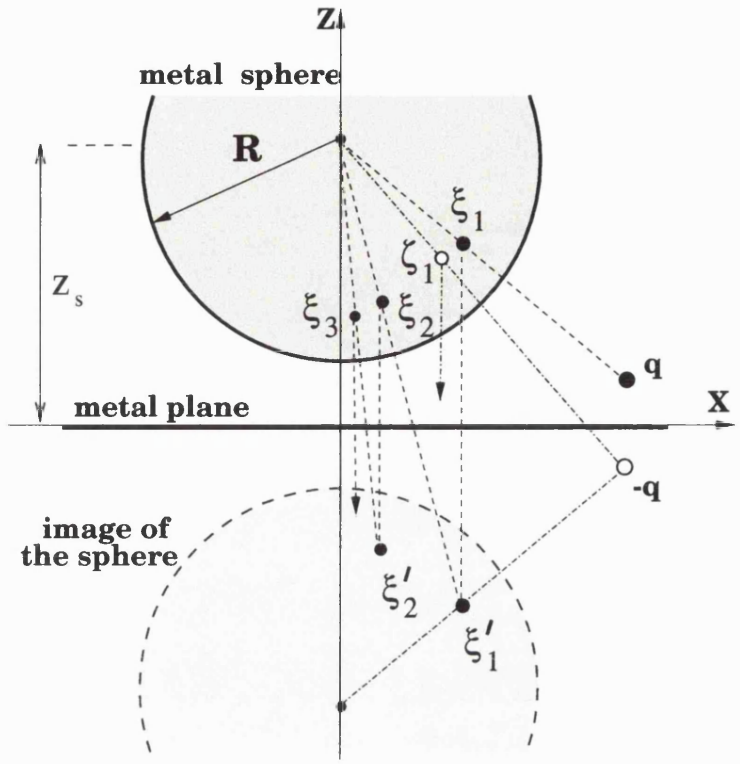

Figure 3.3: Construction of image charges in the sphere-plane capacitor system due to one charge q outside the metals.

solution of the corresponding Poisson equation and, at the same time, is zero both on the metal sphere and the metal plane.

It is useful to study the convergence properties of the sequences of image charges. To simplify the notations, it can be assumed that the original charge is in the xz-plane. Then it follows from Eq. (3.46) that $x_{\xi_{k+1}} < x_{\xi_k}$. It is also seen that $x_{\xi_k} \to 0$ and $z_{\xi_k} \to z_\infty = R\sqrt{\lambda^2 - 1}$ (see above) as $k \to \infty$ and the same for the ζ-sequence. This means that the image charges inside the sphere move towards the vertical line passing through the centre of the sphere and finally converge at the same point z_∞. This is the same behaviour observed for charges in the capacitor problem at the beginning of this subsection (see fig. 3.3). In fact, the calculation clearly shows a very fast convergence so that the series of charges can be summed up from some $k = k_0$. Thus, the image potential at a point $\mathbf{r}$ due to the unit charge at $\mathbf{r}_q$ is:

$$\phi_{ind}(\mathbf{r}, \mathbf{r}_q) = -\frac{1}{\mathbf{r} - \widehat{\sigma}\mathbf{r}_q} + \sum_{k=1}^{k_0} \left[\overline{\xi}_k \left(\frac{1}{|\mathbf{r} - \mathbf{r}_{\xi_k}|} - \frac{1}{|\mathbf{r} - \widehat{\sigma}\mathbf{r}_{\xi_k}|} \right) + \overline{\zeta}_k \left(\frac{1}{|\mathbf{r} - \mathbf{r}_{\zeta_k}|} - \frac{1}{|\mathbf{r} - \widehat{\sigma}\mathbf{r}_{\zeta_k}|} \right) \right] \quad (3.47)$$

where $\overline{\xi}_k = \xi_k$ for $k < k_0$ and $\overline{\xi}_{k_0} = \xi_\infty = \xi_{k_0} \frac{D_\infty}{D_\infty - 1}$, and similarly for the ζ-sequence. Here D_∞ is the geometrical characteristic of the capacitor introduced at the beginning of this subsection.

3.4.4 The calculation of the total image force acting on the tip

In order to calculate the total force acting on the tip, the total energy has to be differentiated, eq. (3.40), with respect to the position of the sphere, $\mathbf{R}_s$. Since only the force acting in the z-direction has interest, it is sufficient to study the dependence of the energy on z_s. There will be two contributions to the force. The interatomic interactions between all atoms between the conducting sphere and plane lead to a force which is calculated by differentiating the shell-model energy (the first term in eq. (3.40)). Therefore,

$$F_{tip} = -\frac{dU_{sh}}{dz_s} - \frac{dU_{el}}{dz_s} \tag{3.48}$$

where $U_{sh} = \frac{1}{2}\sum_{ij}{}' v_{ij}$ is the shell model energy. The summation here is performed over all atoms in between the electrodes. Only positions of the frozen atoms in the nano-tip depend directly on z_s. However, the equilibrium positions, $\mathbf{r}_i^{(0)}$, of the other atoms, determined by the minimisation of the energy of Eq. (3.40), will depend *indirectly* on z_s at equilibrium, $\mathbf{r}_i^{(0)} = \mathbf{r}_i^{(0)}(z_s)$. The electrostatic energy, U_{el}, depends on the positions of atoms and the tip position z_s.

The positions of atoms can be denoted by a vector $\mathbf{x} = (\mathbf{r}_1, \mathbf{r}_2, \ldots)$. The total energy $U_{tot} = U_{tot}(\mathbf{x}, z_s)$, where the direct dependence on z_s comes from relaxed tip atoms of the shell model energy, U_{sh}, and from the electrostatic energy, U_{el}. In equilibrium the total energy is a minimum:

$$\left(\frac{\partial U_{tot}}{\partial \mathbf{x}}\right)_{z_s} = 0 \tag{3.49}$$

where the derivatives are calculated at a given fixed tip position z_s. Let $\mathbf{x}_0 = (\mathbf{r}_1^{(0)}, \mathbf{r}_2^{(0)}, \ldots)$ be the solution of Eq. (3.49). Then, since $\mathbf{x}_0 = \mathbf{x}_0(z_s)$, the force is given as:

$$F_{tip} = -\frac{dU_{tot}(\mathbf{x}_0(z_s), z_s)}{dz_s} = -\left(\frac{\partial U_{tot}}{\partial \mathbf{x}_0}\right)_{z_s}\frac{\partial \mathbf{x}_0}{\partial z_s} - \left(\frac{\partial U_{tot}}{\partial z_s}\right)_{\mathbf{x}_0} = -\left(\frac{\partial U_{tot}}{\partial z_s}\right)_{\mathbf{x}_0} \tag{3.50}$$

where Eq. (3.49) has been used. This result can be simplified further, the partial derivative of the shell-model energy, $-\frac{\partial U_{sh}}{\partial z_s}$, is equal to the sum of all z-forces acting on fixed atoms in the tip due to all shell-model interactions, since only these atoms are responsible for the dependence on z_s in the energy U_{sh}. Therefore, finally the force is:

$$F_{tip} = \sum_{fix}\left(F_{iz}^{(sh)}\right)_{\mathbf{x}_0} - \left(\frac{\partial U_{el}}{\partial z_s}\right)_{\mathbf{x}_0} \tag{3.51}$$

where the first summation runs only over fixed tip atoms. Thus, in order to calculate the force imposed on the tip at a given tip position z_s, one has to relax the positions of atoms with respect to the *total energy* of the system, $U_{sh} + U_{el}$. Then calculate the shell-model force, $F_{iz}^{(sh)}$, acting on every fixed tip atom in the z-direction as well as the electrostatic contribution to the force given by the last term in Eq. (3.51).

3.4.5 SCIFI

The Self-Consistent Image Force Interaction (SCIFI) code has been developed to calculate self-consistently the equilibrium atomic structure under the influence of microscopic and image forces,

as well as bias. This code implements the Shell-Model for atomistic interactions as described in section 3.2.1, but differs from the MARVIN code in that it also relaxes the system with respect to image forces and is non-periodic. Interactions with infinite systems, e.g. surfaces, can be represented accurately with this method since tip-surface interactions converge rapidly with respect to sample size. The non-periodicity means that it is also capable of studying charged systems, as it does not suffer from the convergence problems associated with charged periodic systems.

3.5 Capacitance Force

As mentioned in chapter 2, if electrons are allowed to flow between two different conducting materials (in this case tip and sample/substrate connected directly by a wire) there will be a contact potential U between them, as the electrons must pay energy to travel from the material with the smaller work function to the material with the higher one. This effect is exactly the same as that discussed in the previous section for the image force, but now the difference in potential between the tip and surface is due to the contact potential, U, not the applied bias, V. In effect, when calculating the image force with an applied bias, capacitance force is included as a component of the overall force and therefore this capacitance force is present in all calculations which include the image force component. However, it will prove useful later (see chapter 5) to be able to compare the magnitude of the image force with an independently calculated capacitance force to demonstrate that they have the same components. It is important to note that for electrons to flow there must be some direct electrical connection between the tip and surface. Although in principle, electrons can transfer between the end of tip and the surface, at the scanning ranges used in NC-AFM this effect is negligible and contact potential will only be significant if there is a direct electrical connection.

The difference in surface potential of the two materials produces an electrostatic energy of the form:

$$E_{elec} = \frac{1}{2} C U^2(x, y) \tag{3.52}$$

where C is the tip-sample capacitance. This can be differentiated with respect to tip-surface separation, z, to give the capacitance force between them:

$$F(x, y, z) = \frac{1}{2} \frac{dC}{dz} U^2(x, y) \tag{3.53}$$

The main difficulty in evaluating this expression is in finding a physical expression for $C(z)$ for the real tip-shape. Numerical methods can give an exact value for the force, but do not allow variations of tip size and curvature to be studied. An approximate analytical method [76] has been developed which allows the capacitance of an axisymmetrical tip to be given as [77]:

$$C(z) = \frac{1}{U} \int_{tip} 2\pi \rho_s'(z') \sigma_s(z') dz' \tag{3.54}$$

where ρ_s is the analytical surface equation of the tip and σ_s is the surface charge density. For a conical tip (see fig. 3.1) of radius R and sharpness γ, the capacitance force is given by:

$$F_c(z) = \pi\varepsilon_0 U^2 \left\{ \frac{R^2(1-\sin\gamma)}{z[z+R(1-\sin\gamma)]} + \frac{1}{\{\ln[\tan(\gamma/2)]\}^2} \left[-\ln\frac{z+R(1-\sin\gamma)}{H_{tip}} + \frac{R\cos^2\gamma}{\sin\gamma[z+R(1-\sin\gamma)]} - 1 \right] \right\} \tag{3.55}$$

where ε_0 is the dielectric constant of a vacuum and H_{tip} is the height of the tip (effectively distance from end of the tip to electrical contact with tip).

The importance of the capacitance force due to the tip-surface interaction depends critically on the tip/surface properties and experimental setup. If there is a significant potential difference between the tip and surface, then the capacitance force is an important contribution to the interactions. As stated above, a large potential difference could exist if there is a significant difference between the work functions of the tip and surface material or a large bias is applied in the experiment. However, as discussed in chapter 2, bias is normally applied to minimize the effect of work function differences, so capacitance forces due to contact potential and applied bias should in principle cancel each other. This electrostatic minimization process is not well defined and its success in cancelling the capacitance force due to work function differences is not clear. In light of this it is important to understand how the capacitance force compares with other interactions. For a metal surface and a silicon tip, with a potential difference of about 1 V, the capacitance force will dominate tip-surface interactions beyond a separation of about 6 - 7 nm and is comparable to the van der Waals force at about 5 nm.

3.5.1 Work Function Anisotropies

The discussion of capacitance force above makes an assumption about surfaces that is not always valid. By calculating the capacitance force as a function of z alone, it is assumed that the work function is uniform across the surface. On real surfaces, inequivalencies in the work function across the surface can arise due to surface preparation, adsorbates, crystallographic orientation and variations in local geometry [44, 78]. Real surfaces of any material are not perfectly smooth, as is suggested by the very small scale NC-AFM images usually seen. As can be seen in fig. 3.4, real surfaces are very rough on the micro-scale and this roughness can lead to inhomogeneities in the surface charge density and work function.

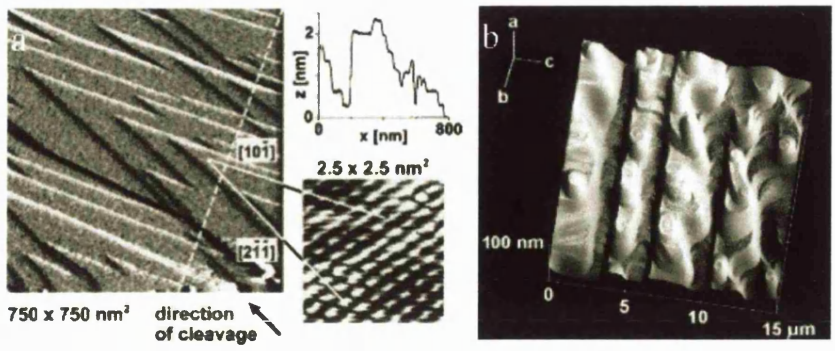

Figure 3.4: Microscale Images of (a) CaF_2 [79] and (b) MgO [80] surfaces.

This is especially relevant for the electrostatic minimization procedure used in experiments

(see chapter 2), as this minimizes at a single point on the surface before scanning. Variations in the work function over the region scanned could render the minimization process invalid, or at least approximate. Other studies [44] have already suggested that work function anisotropies are the most likely source of the long-range interactions observed in force microscopy of graphite with diamond tips.

The contribution of work function anisotropies to the tip-surface interaction cannot be calculated explicitly, however they can be represented by increased surface charge density or increased/decreased applied bias when calculating the image force contribution [44].

3.6 Forces due to Tip and Surface Charging

Many processes in NC-AFM imaging can introduce charge onto the tip and surface. Surface preparation by cleavage is known to induce very large charges on insulating surfaces [79, 81, 82, 83], although these can be reduced by annealing. Tip and surface sputtering can also cause charging, as can ion exchange between tip and surface during scanning (tribo-charging). On the microscopic scale, these charge defects can appear as strange artifacts in images or as unexpected interactions close to the surface. On the macroscopic scale, tip and surface charging can dominate the interactions, and in some cases even prevent stable imaging. It is commonly assumed that the very large attractive forces which prevent stable imaging of some insulating oxides e.g. MgO, alumina, are due to significant surface charging after cleavage. The significance of tip and surface charging to NC-AFM imaging of CaF_2 and other insulating surfaces will be discussed in chapter 8.

Charging is limited to insulating materials, where the charge density is localized around ion positions and the added charge cannot conduct away. This means it is not relevant for imaging of metal surfaces, nor for tips which are pure conductors. However, most NC-AFM experiments use silicon tips which are likely to be coated by a thin oxide layer which could be charged. In principle charging just adds a contribution to the charge-charge chemical interaction discussed previously, but this interaction can be large if the tip and surface are oppositely charged. The charge-charge interaction for a neutral surface, where all the charged defects have been compensated without atomic displacement, decays exponentially into the vacuum and would introduce a contribution to the tip-surface force only at small tip-surface separations. However, usually charged defects in the surface cause atoms to move from their ideal lattice sites creating dipoles within the surface. Charge-dipole and dipole-dipole interactions [44] have much longer range than charge-charge interactions, and can introduce very long-range electrostatic contributions to the tip-surface interactions. It should also be noted that for systems with conducting materials, any charging will also change the image force. Charging of the tip will greatly increase the magnitude of image charges produced in the conductors and hence the image force. The influence of tip-charging on the image force is discussed explicitly in chapter 5.

3.7 Magnetic Forces

Magnetic forces are really only important when both the tip and sample demonstrate magnetic behaviour e.g. both are ferromagnets. This situation is not encountered in normal NC-AFM,

but modifications of the standard setup have been performed so that the magnetic properties of materials can be probed on the nano-scale. These Magnetic Force Microscopes (MFM) [84] have proved successful in imaging magnetic domains at very small scales, and offer a great deal of potential for nano-scale magnetic recording.

For a ferromagnetic tip and sample the magnetic force contribution can be calculated by first estimating, theoretically or experimentally, the magnetic moment of the tip and then applying

$$F = \nabla(m.B)$$

where m is the magnetic moment and B the magnetic flux density. For a setup with a ferromagnetic tip and a paramagnetic/diamagnetic sample the force will be due to the interaction of the induced moment in the sample and the diverging field of the tip. For standard silicon tips and insulating/semiconducting surfaces commonly studied in NC-AFM, this interaction will not be significant.

3.7.1 Atomic Scale Magnetic Imaging

The force sensitivity of the NC-AFM technique on the atomic scale has encouraged studies of the atomic scale magnetic properties of surfaces. For example, several insulating oxide surfaces are anti-ferromagnetic and it is hoped that NC-AFM with a spin-polarized tip could detect the difference in force over spin up and spin down metal ions. This would represent a direct measurement of the exchange force between the spin of the tip and the spins of the metal ions. Characterizing the spin of the tip and getting close enough to the surface to measure the exchange force without crashing are the main obstacles to this kind of study, and as yet no experimental attempts have been successful.

Chapter 4

Modelling the NC-AFM

Modelling the NC-AFM is a process of several stages and as such this chapter is split into four sections. The four sections can be summarized as follows:

- The Surface - establishing a realistic model of the surface from experiment and theory.
- The Tip - establishing a realistic model of a NC-AFM tip using properties known experimentally and properties inferred from theory.
- Tip-Surface Interaction - explicitly modelling the macroscopic and microscopic interactions between the tip and surface.
- Modelling Oscillations - modelling the oscillations of the cantilever under the influence of these interactions.

4.1 The Surface

The first stage of the modelling process is establishing a good representation of the surface being studied. However, this process is obviously very specific to the system studied and this section will only outline some of the general issues. For specific details on modelling of different surfaces see chapters 6, 7, 8 and 9.

In an experiment the surface is prepared by cleavage along a specific direction, so the miller index, or plane, of the surface is known. However, to simulate atomic resolution in an NC-AFM experiment, knowledge of the surface atomic structure scanned by the tip is also needed. Most surfaces will relax significantly from their ideal bulk termination after cleavage and some even reconstruct to form very different atomic structures, therefore it is important to find the what the tip will really 'see'. This can usually be found in the literature from a combination of other experimental techniques and theoretical methods. If a clear consensus on the surface structure has been established previously then this can be used directly, e.g. TiO_2 in chapter 6. If there is no clear consensus, then an accurate structure can be found by *ab initio* calculations of the surface, e.g. CaF_2 in chapter 8. The final stage of the surface modelling is checking that the empirical methods usually used in the NC-AFM simulation to calculate the atomistic interactions also reproduce the same surface structure. Note that if empirical methods fail to reproduce the

surface structure to a sufficient accuracy or neglect interactions of interest, then more advanced methods must be used to represent the atomistic interactions, e.g. NiO in chapter 9.

4.2 The Tip

Unfortunately there is very little information on the properties of NC-AFM tips, effectively only the most basic qualities are known. The tips are micro-fabricated from silicon in much the same way as computer chips. As stated in chapter 3 their macroscopic shape has been experimentally determined as a pyramidal. This only gives its structure on the micrometre scale, and there is no method for imaging the nano-tip. It is also known that the tips are oxidized due to exposure to the atmosphere, and although this can be removed by argon ion sputtering, some recent atomically resolved images use untreated tips [85].

This limited information must be used as the basis for modelling of the nano-tip. It is known that the tip is fabricated from silicon, so one direction of modelling would be to try and find the most realistic silicon based model possible. This is the method used in some recent ab initio studies of NC-AFM [40, 41, 86], and it is a good basis for beginning the tip modelling process. However, it is also known that the tip is oxidized before scanning so its properties may be better represented by an oxide based model. Before studying either of these models, it is important to study the effect of sputtering of the tip to see if there will be any significant difference between treated and untreated tips.

4.2.1 Argon Ion Bombardment of Silicon Surfaces

Methods

There seem to be only two basic methods which can be applied to this preparation procedure. The main process for Ultra High Vacuum (UHV) applications involves initial argon sputtering at a specific temperature to remove the oxide, followed by an anneal to regrow the resultant amorphized silicon region. Previous research [87] has indicated that the optimum conditions for this procedure are room temperature for the sputtering and 800°C for the anneal. This idea works on the basis that the surface damage produced by the sputtering is a strong function of the sputtering temperature and that damage from high temperature bombardment cannot be repaired.

Comfort *et al* [88], [89] challenge this method and claim to have developed a technique relying on high temperature sputtering. They suggest that the efficiency of sputtering is enhanced at 750°C and that by using specific ion energies and doses, the oxide can be removed without damage to the substrate. They suggest that the success of this method is because the rate of self-annealing at the elevated temperature is greater than the rate of damage production induced by the ion bombardment. Low ion energies insure that damage production is restricted to the near surface region and is removed by self-annealing. Low doses avoid the excessive removal of silicon atoms from the surface which is usually the main cause of roughness. This technique also avoids the need of UHV conditions and is carried out at a pressure below 1×10^{-2} torr.

In spite of the possible benefits of this newer preparation technique, or problems [90], this report must focus on the method which is actually applied to the preparation of AFM tips. The specific preparation conditions of interest are usually initial bombardment by 1 keV argon ions at room

temperature and pressures below 10^{-10} mbar [30]. Although the preparation of silicon surfaces involves an annealing process after the argon sputter, this is not the case for tip preparation. Under UHV conditions heating causes problems with released gases and interaction with dust, either of these would prove a major unknown when focusing on the microscopic nature of an AFM tip.

Surface Effects of Ion Bombardment and Annealing

Ironically one of the most thorough studies [91] into the surface effects of ion bombardment and annealing involved the use of AFM to study the resultant surfaces. They used a slightly different method of cleaning the surface, making use of a microwave multipolar plasma reactor instead of the normal ion sources (ion gun). Their results focused mainly on the difference between room temperature and high temperature ion bombardment, but they do show clearly the effects of the bombardment on the surface. Although they use very low ion energies (75, 135 eV) impacting on a (100) surface, they find that even this perturbs the surface significantly and the damage cannot be repaired by annealing at 700 ^{o}C. They conclude that although clean surfaces can be produced, clean and smooth surfaces cannot be. The reconstructed surfaces show (2×1) patterns for energies less then 200 eV. They find no change in damage depth with respect to the treatment time.

Another experiment [92] uses Scanning Tunneling Microscopy (STM) to study the surfaces. They bombarded a Si(001)-(2×1) surface with 3 keV argon ions at an impact angle of 30^{o} and then annealed it from 245 - 600 ^{o}C under UHV. After bombardment STM showed that the surface consisted of granular grains of diameter $\sim$ 1 nm and various steplike structures along the [110] direction. This at first seems in direct contrast to the results produced by other experiments, but the very high ion energies seem a likely candidate for the reduction of the size of the grains found on the surface. At annealing of 245 ^{o}C the grains begin to coalesce to form clusters of size $\sim$ 3 nm. Prolonged annealing of about 10 min. promotes crystallization of the amorphous layers, producing (2×1) reconstructions surrounded by amorphous layers. As the temperature increases, the reconstructed regions increase and a mixture of (2×1) and (1×2) regions appear. At 445 ^{o}C many monatomic height islands of (2×1) reconstruction appear on the surface, these are slowly smoothed out by annealing at 500 ^{o}C. As the temperature is increased further to 600 ^{o}C the point defects on the surface are removed, leaving only the line defects. Unfortunately the very high ion energy used in this experiment casts significant doubt over the amount of damage below the surface. Hu *et al* [93], [94] carried out spectroscopic ellipsometry studies of the effects of bombardment with ion energies in the range 100 - 1500 eV. They found that the sample was damaged to a depth of $\sim$ 13 nm with an ion energy of 1500 eV, however they made no attempt to investigate the resultant surface, nor did they attempt to anneal it.

Some low pressure studies $(2 - 5 \times 10^{-10}$ mbar) [95] of silicon (111) were also conducted via x-ray photoelectron spectra. They found that although argon sputtering removed the surface oxide, sputtered oxygen from higher oxidation states was knocked into the bulk crystal and the oxygen concentration, although reduced, remained finite ($\sim$ 5%).

Tip Charging

One aspect of sputtering which is not considered thoroughly in the studies discussed above is charging of the tip due to ion bombardment. In principle the tip is a conductor and any charge generated by sputtering is removed when the tip is grounded. In fact experimentalists claim to see a temporary current produced when the tip is grounded, indicating that any charge is dissipated. However, as discussed in the previous section, it is not at all obvious that the whole tip is conducting silicon. An oxide layer will remain and it is possible that this layer could be charged by the sputtering process [96, 97]. In recent NC-AFM experiments [98] it was found that sputtered tips required a much higher bias to minimize the electrostatic forces (see chapter 2 for discussion of this process), implying that sputtering the tip introduces a much larger force to the system. The possible effects and implications for NC-AFM of tip charging will be discussed later, but for the moment it is important to recognize that sputtering is one possible source of this effect.

Summary

While looking at the data produced in these experiments it is always important to remember the conditions of relevance to the preparation of an AFM tip. These are: UHV - pressure less than 10^{-10} mbar and room temperature bombardment with Ar^+ ions of energy 1 keV. The ion energies used in the AFM experiment [91] initially seem too low in comparison with the conditions for AFM tips, but their conclusions on the inevitability of roughness are important. This seems to indicate that any model of the tip must account for this non-uniformity. The STM experiment [92] backs up this claim of (2×1) reconstructions on the surface, and the islands and steps found demonstrate the roughness of the surface. It is clear that the tip surfaces will be very rough due to the evidence of extensive damage even at low ion energies and the lack of annealing after bombardment. The results of Uesugi *et al* [92] suggest that the surface is covered in grains of ~ 1 nm diameter, about the size of the intermediate clusters discussed in the next section. Although this gives support to a cluster model of the tip, none of the experiments really give any insight into the possible microscopic structure of the surfaces they investigate. They almost exclusively focus on the macroscopic nature of the surfaces after bombardment and annealing, and therefore do not support any discrimination between the various clusters. Also the low-energy of the bombarding ions means that sputtering is unlikely to clean the tips of oxide at the microscopic scale. This is supported by the fact that some recent atomically resolved experiments were performed without tip-sputtering, indicating that whether sputtered or not, the tip still has an effective oxide coating at the scales important for imaging. More recent studies on CaF_2 surfaces [99] have shown that adding oxygen to the tip-surface system during scanning actually improves contrast (reduces noise) in NC-AFM images.

In conclusion, although it is clear that sputtering increases the tip roughness, it is probable that the tip is rough on the microscopic scale anyway and sputtering does not change anything physically that would affect imaging. However, it is also possible that sputtering may charge the tip and a residual of this charge remains when imaging. It is therefore important to understand whether this will have any significant effect on the tip-surface interactions.

4.2.2 A Cluster as a Nano-Tip

In the previous section it was demonstrated that tips are rough on the microscopic scale, whether they are sputtered or not. This means that contact between the bottom of the tip and the sample surface will not be between two smooth, regular surfaces. Due to preparation the sample surface will be quite smooth, but the bottom of the tip will contain many asperities and one of these asperities will serve as the probe. To accurately model an AFM tip, a nano-tip must be found which best represents the possible asperities found on the tip surface. Experiment can tell us little of their properties directly, therefore theory must be used to study them.

A study of different possible nano-tip models was performed to try and determine which most closely matches experimental behaviour. Firstly, it was found that if the bottom of the tip was flat i.e. no nano-tip, then the interaction with the surface was averaged over several tip ions and no contrast was produced. When a nano-tip is included, it must extend significantly beyond the main part of the tip to reproduce the interaction observed in experiment. Specifically a nano-tip of only a few atoms would not atomically resolve lower terraces of stepped surfaces, which contradicts experiments on the NaCl surface (see fig. 7.4).

In conclusion, the theoretical study, in combination with some experimental results, show that the surface probe or nano-tip in NC-AFM can be well represented by a microscopic protrusion or cluster extending beyond the terminating surface of the macroscopic part of the tip. The importance of a nano-asperity in NC-AFM reliable imaging has also recently been discussed in experimental images of a MgO surface [100].

Investigation of Silicon Clusters

Since the tip surface is silicon, silicon clusters are the most likely candidate to reproduce the properties of the microscopic protrusion discussed in the previous subsection. Again assuming the tip is terminated by a rough silicon surface, the cluster must effectively model the important properties of that surface i.e. microscopic physical structure, charge distribution, bonding. The next few subsections contain a review of the literature on silicon clusters and their properties, with detailed discussion of those properties important to NC-AFM. In section 4.2.3 this information is used to determine a cluster model which best represents the properties of a silicon NC-AFM tip.

Stability

Most of the studies on silicon clusters investigate the varying stability of the clusters, in fact this property is the focus of references [101], [102] and [103]. Kaxiras [101] looked at the occurrence of 'Magic Numbers' in the size of silicon clusters i.e. cluster sizes that are particularly stable. He proposed that, at least for intermediate sizes, these 'Magic Numbers' are due to the possibility of forming a cluster surface which closely resembles a stable reconstruction of the crystal. This surface simulating fullerene cage surrounds a core of 5 bulk-like tetrahedrally bonded atoms. He used Si_{33} and Si_{45} clusters to demonstrate this. They are experimentally observed to have very low reactivity and they also accommodate the two most stable surface reconstructions of bulk silicon.

Kaxiras' later work [104] investigated the relation between the size and shape of medium sized ($20 \leq N \leq 40$) silicon clusters. He found that a transition occurred between size-specific behaviour

and bulk-like behaviour somewhere around N=25. Unsurprisingly this is about the size of cluster where it becomes possible for a full tetrahedral system to develop. Rothlisberger *et al* [105] realized this and calculated the geometries of stable structures based on the tetrahedral system. Lee *et al* [106] used molecular dynamics to study the properties of some smaller clusters with less than 19 atoms. They found that once 15 atoms are used for a cluster, it begins to have some internal structure and a large gap develops between the highest occupied molecular orbital (HOMO) and the lowest unoccupied molecular orbital (LUMO).

Jug and Krack [102] conducted a much more widespread study of the stability of different clusters, from 12 to 61 atoms, including several different symmetries. They found that the stability does not vary that severely with cluster size. Although they found Si_{44} was the most stable with a binding energy (BE) of 3.49 (eV)/atom, other cluster sizes were comparable e.g. Si_{33} 3.35 and Si_{45} 3.39. They suggested that for clusters with less than 40 atoms, the central tetrahedrally bonded atom (tetra) is important for stability. Beyond 40 atoms more than one central atom is required within the cage to stabilize the cluster. These central atoms attract bonds from the surface atoms, reducing the number of dangling bonds. In the case where the charge of the highest occupied molecular orbital is almost equally distributed over the surface, it cannot generate any special reactive sites. Gong [103] supports the idea of the importance of the central tetrahedral system to the stability of the cluster. He investigates Si_{28}, without the central tetra, and Si_{33}, which does have the central tetrahedrally bonded 5-atom system. Again it is seen that the addition of the tetra-system saturates four dangling bonds on the surface. The covalent bonding between the Si_5 cluster and the Si_{28} fullerene cage introduces a gap between the HOMO and the LUMO, making Si_{33} more inert, as predicted by experiment.

As a counter to this general consensus on the most stable structures of silicon clusters, Menon and Subbaswamy [107] found low energy structures of Si_{45} which did not contain a central tetrahedrally bonded atom. They suggest that the transition from size-like to bulk-like behaviour occurs in much larger clusters than originally predicted by Kaxiras, possibly when the ratio of surface to bulk atoms approaches unity. Curiously, however, they re-iterate the importance of the translation of the core atoms to tetrahedral symmetry, contradicting their own results.

Correlation

On a slightly different tangent it is necessary to discuss the importance of correlation in determining the most stable structures for silicon clusters. Grossman and Mitas [108] used variational and fixed-node diffusion Monte Carlo methods to investigate the structural and valence electron properties of silicon clusters. They compared the binding energies (eV/atom) of small clusters ($2 \leq N \leq 20$) as calculated by the Hartree-Fock, Local Density Approximation and Quantum Monte Carlo methods, along with experimental data. They found that HF consistently underestimates the binding energy and that the LDA consistently overestimates it, with QMC providing much better accuracy overall. For example HF predicts 1.91 eV/atom for Si_7 , LDA 4.14, QMC 3.43 and the experimental value is 3.60. This demonstrates the importance of accurately calculating the correlation energy in determining the stability hierarchy of silicon clusters.

Reactivity

Initially it was assumed that the stability of a cluster is closely related to the reactivity of the cluster. The studies mentioned in the previous section were trying to explain the unreactivity of specific clusters found in experiments, the so-called 'Magic Numbers'. They did find that the 5-atom tetrahedron placed at the centre of cluster fullerene cages plays an important role in stability. Ramakrishna and Pan [109] used this as a basis to find structures which have the maximum number of 4-fold coordinated atoms and no surface dangling bonds. Their model only applies to Si_{33}, Si_{39} and Si_{45}, but these clusters have been shown experimentally to be the least reactive towards reagents with closed shell electronic structure e.g. water, ammonia. They also suggest that on the most stable silicon surface, the (111) 7×7 reconstruction, surface chemisorption occurs preferentially on rest atom sites and less on crown atom sites. It is the absence of rest atoms in silicon clusters that is the main cause of the unreactivity. Furthermore, it is the close proximity of the rest and crown atom sites that causes ammonia to chemisorb dissociatively. This configuration is absent from clusters, and ammonia usually undergoes molecular adsorption.

Two patterns of reactivity with cluster size emerge from these studies. The reactivities of closed shell reagents depends critically on the number of dangling bonds on the cluster, whereas open shell reagents carry the dangling bonds with them and react almost independently of cluster size. This explains why only the closed shell reagents are sensitive to cluster size, structure and annealing, and exhibit the highly oscillatory pattern of reactivities as a function of cluster size. This was confirmed by the work of Krack and Jug [110] who studied the adsorption of ammonia on Si_5 and Si_{10} clusters. They also found that it was important to investigate the cumulative atomic dipole moments, as well as the net charges, of possible reactive atoms.

Jelski *et al* [111] focused their attention solely on the Si_{45} cluster in an effort to understand its properties. After finding a stable structure in line with Kaxiras' original predictions, they found evidence to support the importance of the coordination of the surface atoms in determining the reactivity of the cluster. Their choice of clusters were almost entirely tetra-coordinated, eliminating dangling bonds from the surface. The clusters also had well defined energy gaps, a common property of the more inert systems. A more thorough investigation [112] into this self-passivation of the surface dangling bonds using HF and configuration interaction, found that the charge density tends to move from the two- and three-coordinated sites at the surface to the central four-coordinated atoms. The distribution of charge within the cluster, however, does not follow any clear pattern. In Si_{29} the electron depletion is delocalized almost uniformly across the surface, whereas in Si_{23} and Si_{33} the electron depletion is localized on a few distinctive surface atoms. Nevertheless they confirm the correlation between the stable clusters and a core which passivates the surface dangling bonds. They also discuss the transition from metallic and covalent bonding at the surface to purely covalent bonding in the bulk-like core.

As a final note on the lack of a simple correlation between stability and reactivity in silicon clusters, work by Gong *et al* [113] found that it is very difficult to explain the reactivity of the Si_{13} cluster, and in fact they found that the energetically stable structure was more reactive than the experimentally observed Si_{13} cluster.

4.2.3 Model of the Nano-Tip

The most stable silicon surface is the (7×7) reconstruction of the (111) surface [114], so intuitively it makes sense to use this as a basis for the model of the tip. As is clear from the previous section, the properties of silicon clusters have been thoroughly explored, with most authors agreeing on the fundamental issues. The stability of the cluster is controlled by its structure and all the literature supports the fullerene cage and tetrahedral centre system as the most stable form. Reactivity of the clusters depends on the coordination of the external atoms and associated dangling bonds, with adsorbates much more likely to bond with the lowest coordinated atoms. This information can be used to select a stable cluster and compare its physical and chemical properties with those of the silicon surface.

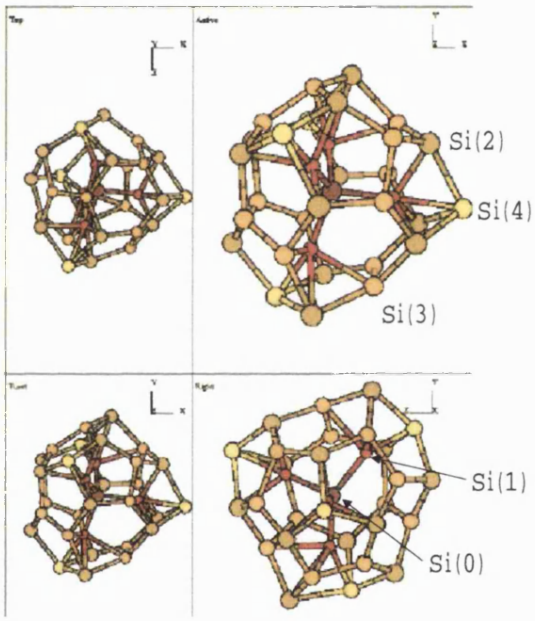

Figure 4.1: Structure of 33 atom silicon cluster. Different colours represent equivalent atoms, Si(0) - maroon, Si(1) - red, Si(2) - bronze, Si(3) - orange and Si(4) - yellow.

The Si_{33} cluster, figure 4.1, has a surface consisting of a series of interlocking pentagons and hexagons, with the stabilizing 5 atom tetrahedral system in the core. The cluster consists of five different equivalent atom positions, specified by a number from 0 to 4. The four-fold coordinated Si(0) atom is at the centre of the tetra system, bonded to 4 Si(1) atoms. These are four-fold coordinated with bonds to the central atom and 3 four-fold coordinated Si(2) atoms. The remaining atom types are both three-fold coordinated, Si(3) types bonded to two Si(2) and another Si(3), and the adatom Si(4) bonded to three Si(2). Although the lower coordination of the Si(3) and Si(4) atom types would initially seem to suggest the existence of dangling bonds at the surface, silicon's propensity for forming local $\pi - bonds$ eliminates this problem.

The Si_{33} cluster shares several structural properties with the (7×7) surface. The semi-hexagonal surface of the cluster matches with the hexagonal structure of the (7×7) surface. The Si(4) atoms on the cluster surface are also consistent with the adatoms on the (7×7) surface,

both form a tetrahedral pyramid extending out from the surface. The adatoms in the cluster are flanked by 3 dimer pairs of Si(3), compared to 2 dimer pairs for the Si(7 × 7) corner adatoms. The relaxation required to form the Si(3)-Si(3) dimer is also very similar to the atomic displacement required to form the dimer pairs in the surface. The cluster therefore simulates the two most important characteristics of the dimer-adatom-stacking-fault (DAS) [114] model of the (7 × 7) surface, the adatoms and the dimers.

Structurally there seems little doubt that the Si_{33} cluster is the best model of the physical features of the Si(111) (7 × 7) reconstructed surface. However, the literature on silicon clusters demonstrates that there are considerable differences between the chemical properties of clusters and surfaces. A thorough investigation of an appropriate tip model requires that a comparison is made between the electronic properties of the cluster and the surface. This will reveal whether the cluster can be expected to demonstrate similar chemical behaviour.

4.2.4 Electronic Properties of Tip Models

This study focuses on non-contact AFM imaging of insulating surfaces and these are principally ionic in nature. For these surfaces electrostatics will dominate the short-range interaction between tip and surface, hence it is important to represent the electrostatic properties of the silicon surface. Figure 4.2 shows the (5 × 5) reconstruction of the (111) silicon surface which contains all the main features of the (7 × 7) reconstruction. This surface was used in calculations due to the computational expenses of using the full (7 × 7) reconstruction. Figure 4.2 also shows two silicon clusters, the 33 atom cluster discussed previously and a smaller 10 atom silicon cluster which is introduced as the simplest possible silicon tip model.

The calculations of the geometries and electrostatic potentials in this section were performed using DFT and the VASP code, as described in section 3.2.1. For the clusters, the calculations were performed at a single k-point, the gamma point, only, but for the surface the total energy was converged to within 0.1 meV using 4 k-points (specifically $(\pm 0.25, \pm 0.25, 0)$). The clusters in the unit cell were separated by large enough vacuum gaps to converge the total energy of the system. The total energy was also converged with respect to the cutoff energy. The fully relaxed geometries of the clusters were then calculated. The fully relaxed geometry of the Si(5 × 5) reconstruction was provided by R. Perez and the 192 atom surface unit cell is shown in full in fig. 4.2, the forces on the atoms were re-calculated in the VASP code and found to be less than 0.01 eV/Å. These forces were also converged with respect to the vacuum gap between periodic slabs. It should be noted at this point that since the electrostatic potential was calculated using DFT, it is only defined up to a constant which is different for different systems and periodic cells. This means that effective comparisons can only be made between the gradients of the potentials in different systems. In NC-AFM, changes in the oscillating frequency are caused by the forces on the tip due to its interaction with surface, hence the gradient is the best criteria for comparison.

It can be clearly seen that the most protruding feature on the silicon surface is the adatom sites, and as such these would represent the most likely imaging feature of a tip. The adatoms of each system have been highlighted in figure 4.2, the Si_{10} cluster is the smallest cluster which contains an adatom. Using DFT the total electrostatic potential was calculated for each system on a grid. This was then interpolated to produce a 3D plot of the electrostatic potential for the

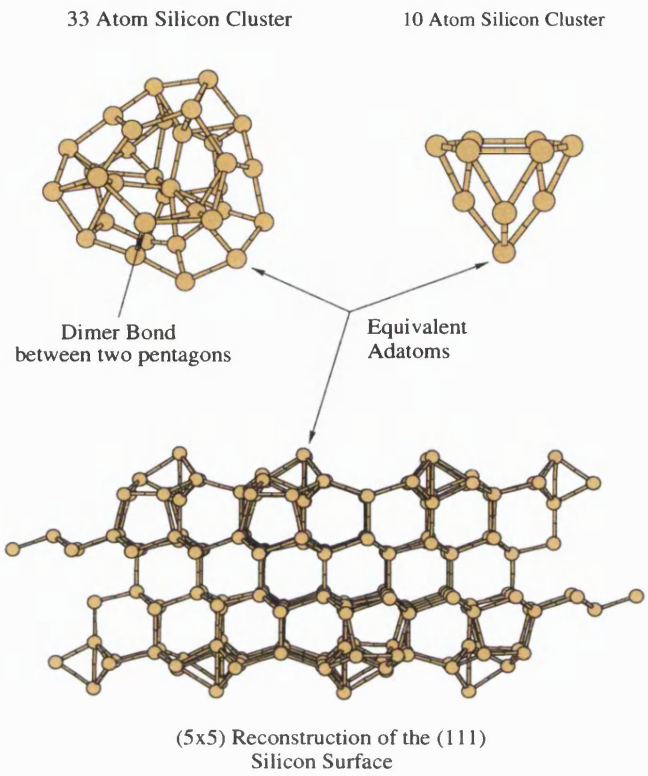

Figure 4.2: Geometries of Studied Silicon Systems

system over the unit cell. 2D slices of the 3D plot through the adatoms are shown in figure 4.3.

Figure 4.3 shows clearly that the gradient of the potential from each adatom is very similar, with the potentials decaying to zero within 1 Å of the adatom. Although there is some slight difference in the absolute values of the potential near the adatom (comparing the Si_{10} and Si_{33} clusters), the rapid decay to zero away from the adatom is seen in all the plots. This demonstrates that even though the Si_{10} cluster is a much poorer physical representation of the surface than the Si_{33} cluster, it reproduces the electrostatic properties of the adatom. Since the electrostatic potential is the most crucial property of the nano-tip, the Si_{10} cluster is a good model of a microscopic protrusion from a silicon surface. Effectively the over 200 atom unit cell (7×7) (111) infinite silicon surface has been reduced to a much more manageable ten atom cluster.

Dangling Bonds

In section 4.2.2 the dependence of the adsorption properties of silicon clusters on the number of dangling bonds on the surface of the cluster was discussed. However, for studies of imaging of ionic surfaces, there are no dangling bonds on the surface and therefore only their contribution to the tip potential is relevant. If the interaction of tips with covalent surfaces is studied then the effects of dangling bonds becomes much more critical, as the dangling bond on the tip adatom interacts strongly with the dangling bonds on the surface. Perez *et al* [86] have used DFT to

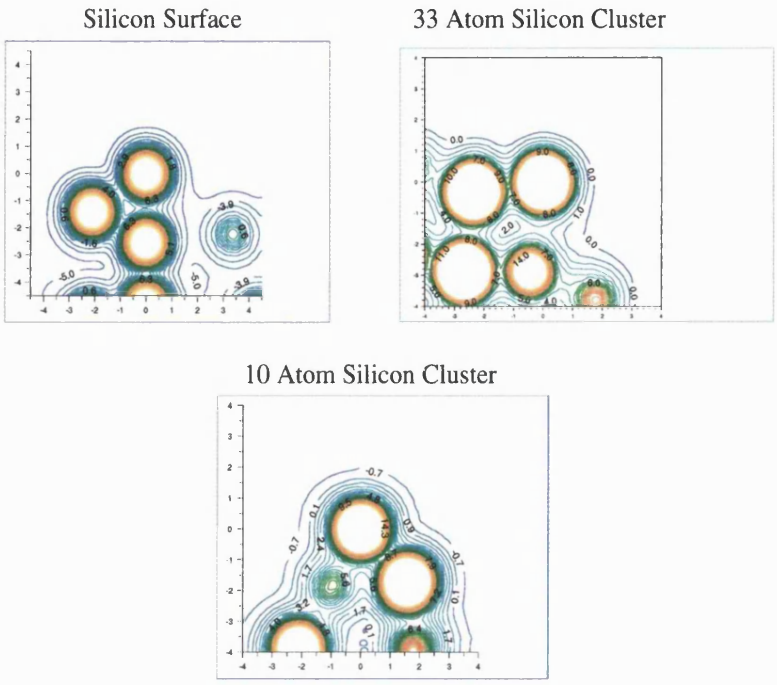

Figure 4.3: Electrostatic potentials of adatoms on silicon clusters. Axes are in Å.

calculate the interactions between silicon tips and a silicon surface, and also have calculated force lines across the surface. They stated that clusters that are terminated by hydrogen will have strong dangling bonds at the adatom of the cluster, they then showed that hydrogen terminated Si_4 and Si_{10} clusters have much stronger attraction to the silicon surface than an unterminated Si_4 cluster. To investigate the effect of dangling bonds on the tip potential, the Si_{10} cluster from fig. 4.2 was taken and 6 hydrogens were added to its base reproducing the tip used in the Perez study. The electrostatic potential was then re-calculated in the same way as previously. This had no significant effect on the electrostatic potential gradient produced at the tip apex.

4.2.5 Tip Contamination

Tip contamination due to oxygen in the atmosphere has already been discussed, but other environmental contaminants may change the interaction properties of the tip. Water vapour is always present in air and experiments [115] have shown that dissociation occurs across the adatom-rest atom pair, forming silanol on the adatom and hydride on the rest atom. All these discussions are appropriate to low coverage - the important conditions for tip modelling. To investigate the effects of these possible tip contaminants, the electrostatic potentials of Si_{10} clusters with adsorbed contaminant species were calculated using DFT. These calculations were performed in exactly the same way as the previous cluster calculations, with the total energy converged with respect to cutoff energy and vacuum gaps.

Comparison between figure 4.3 and figure 4.4 clearly shows that the adsorbed hydrogen has no effect on the potential from the uncontaminated silicon cluster. However, the adsorbed oxygen and hydroxyl group causes a significant change in the potential gradient from the adatom. Both

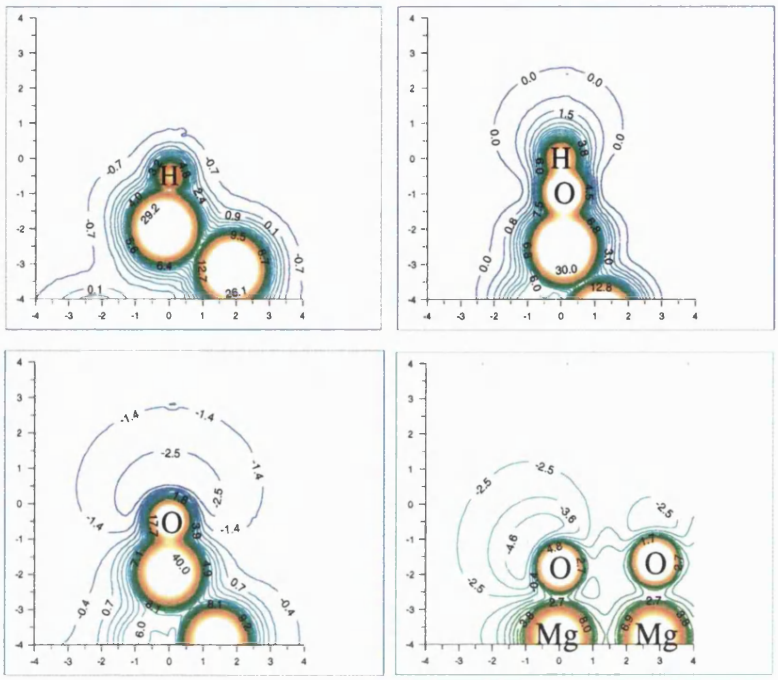

Figure 4.4: Electrostatic potentials of contaminated silicon tips. Axes are in Å.

potentials decay over a much longer range than the uncontaminated cluster, and their stronger gradients suggest they would interact much more strongly with the surface.

At this point the limited information we have on NC-AFM must be used as a basis for choosing the most appropriate cluster model for a silicon tip. It is known that the tips are oxidized, and therefore we can assume that the cluster with the adsorbed oxygen would represent the best silicon-based model of a tip. As a final check, some calculations were performed on the Si_{33} cluster with the same adsorbed species, and there was no significant difference in the electrostatic properties relative to the contaminated Si_{10} cluster.

The final picture in figure 4.4 shows the potential from the corner oxygen of a 64 atom MgO cube. A picture of this tip is shown in fig. 4.5, the cube is orientated so that it is symmetric about the z-axis with a single oxygen ion at the lowest point. Here, we have returned to the second possible direction of modelling - a simple oxide model. Although a realistic silicon-based tip model has been established, as a semi-conductor, silicon represents a very difficult species to model accurately. Any serious attempt to model silicon must include the effects of electron density to represent the covalent bonding between the silicon atoms. This type of modelling is computationally expensive, and very undesirable for the large systems needed to model NC-AFM effectively. Other studies [86] have used this approach, but they are then restricted to unrealistically small tips and semi-conducting surfaces. Figure 4.4 shows that the gradient from the MgO corner is very similar to that of the oxygen contaminated silicon cluster, hence the MgO system gives a good representation of the electrostatic properties of the silicon tip. This MgO or generic oxide tip gives the best compromise between modelling a real oxygen contaminated silicon tip and computational expense. It reproduces the properties of the silicon tip most important to NC-AFM imaging on the microscopic scale i.e. the electrostatic potential, while allowing the use

of the large tip-surface unit cells necessary for modelling. The fact that the *total* tip model is separated into two components, the microscopic and macroscopic, means that the properties of a silicon tip missing in an MgO/oxide microscopic model can be introduced in the macroscopic model of the tip.

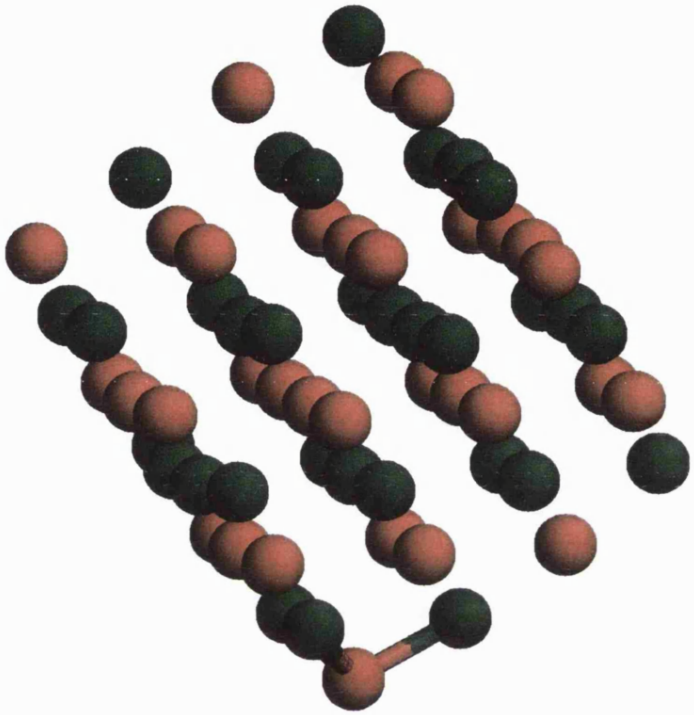

Figure 4.5: MgO cube used as generic oxide nano-tip.

4.3 Tip-Surface Interaction

As discussed at the beginning of chapter 3, the force can be split into two general components: (i) the *microscopic* chemical force between atoms in the tip and surface, which includes the van der Waals force between ions and (ii) the *macroscopic* force between the tip and surface. This macroscopic force consists of the various interactions depending on the specific tip/surface combination studied. Chapter 3 discussed the different contributions to the macroscopic force in detail, but here the exact sources of this force will not be discussed.

It has been shown in previous studies [24, 116], and in chapter 3, that for a locally neutral system (the interactions of charged systems will be discussed in chapter 5), the short-range chemical forces are responsible for atomic resolution. This means that the macroscopic forces can be treated as a *background attractive force* which is important in terms of reproducing experimentally observed frequency changes, but is independent of the identity of the atom under the tip and does not play a role in atomic displacements. In terms of modelling, this means that the interactions can be calculated separately and just combined for the final stages of modelling. The macroscopic force is included by calculating the force and and then adding it to the microscopic force as a

function of tip-surface distance to give the total force.

4.3.1 Tip-Surface Model

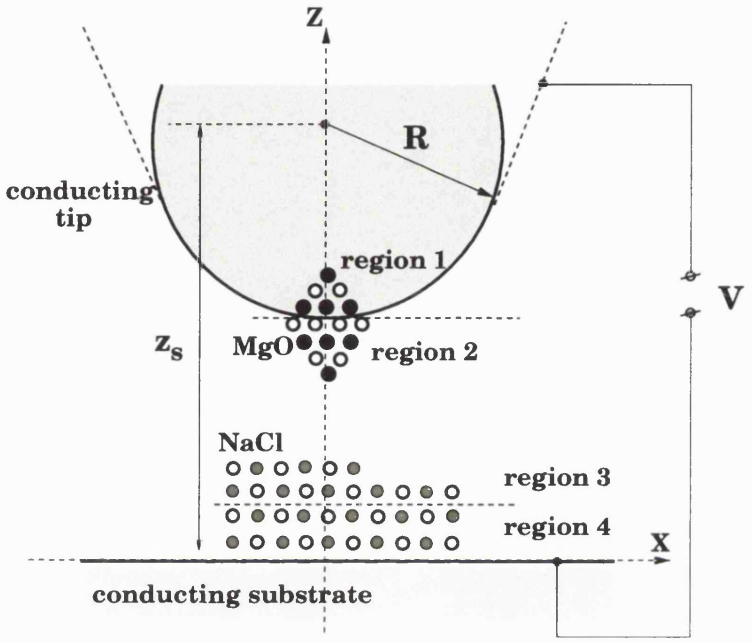

Figure 4.6: Schematic picture of the microscopic model used here to simulate the interaction between the tip and the sample. The coordinate axes are aligned with respect to the sphere centre (at $x = y = 0$, $z = z_s$) and the metal plane (at $z = 0$) for convenience.

Figure 4.6 shows a schematic diagram of the model used to simulate NC-AFM in this study. A NaCl cluster is used as an example surface, but this can be replaced by an atomistic sample of any size. The model contains all the features discussed in the 'idealized' model in chapter 2 and can include all the interactions discussed in chapter 3. This model is consistent throughout all systems studied.

Microscopic Forces

The interaction between ions in the tip-surface system is calculated using a static atomistic simulation technique and the MARVIN code as discussed in section 3.2.2. Figure 4.6 shows how the tip-surface is represented within the atomistic simulation. The nano-tip and the upper surface layers are divided into two regions, I and II. In terms of fig. 4.6 region I consists of regions 2 and 3, and region II consists of regions 1 and 4. The region I ions are relaxed explicitly, whilst the region II ions are kept fixed to reproduce the potential of the bulk lattice and the remaining tip ions on the relaxed ions. The calculation is periodic so that the infinite surface is represented, however this means large surface unit cells must be used to avoid interactions between tip images in different cells. This is not a problem as atomistic calculations are very cheap and large systems do not represent a significant problem.

The atomistic simulations, although cheap, do not account for electronic effects caused by the

tip-surface interaction, such as electron density redistribution between ions or electron transfer between tip and surface ions. It is assumed that at the tip-surface separations usual for NC-AFM these effects can be neglected. It should be noted that the accuracy of this type of simulation depends critically on the quality of the parameters used to represent the interactions. The parameters for the interactions of the tip ions are well tested and are fully described in ref. [117]. The parameters for the surfaces studied will be discussed in the appropriate chapters.

The total relaxed shell-model energy and the tip-surface force is calculated at a range of tip-surface separations, producing curves as function of tip-surface separation for both energy and force. The shell-model contribution to the force is completely converged with respect to the size of the periodically translated simulation cell. By calculating these curves over many surface positions, a map of the microscopic tip-surface interaction is generated. This can then be combined with the surface position independent macroscopic force to give the total tip-surface force as a function of tip-surface relative position, $F(x,y,z)$. Note here that a slight 'double-counting' occurs when the microscopic and macroscopic forces are combined. The frozen atoms of the nano-tip are in effect already part of the macroscopic tip and their van der Waals contribution to the force is effectively counted twice. However, this effect is very small and it is more important to include a large enough tip so that a significant number of atoms at the apex can be relaxed and also that the nano-tip is kept neutral.

4.4 Modelling Oscillations

The complete tip-surface system has now been established and the method for calculating the microscopic tip-surface interaction discussed. This leaves only a model of the cantilever oscillations as the final part of the non-contact AFM modelling process. As described in chapter 2 the tip oscillates with large constant amplitude above the surface, and the tip deflection is measured at constant frequency change. The oscillations of a cantilever over a surface point (x,y) driven by an external force, F_{ext}, in a force field $F(z)$ can be described by the equation of motion:

$$\ddot{z} + \frac{\omega_0^2}{k}\alpha\dot{z} + \omega_0^2 z - \frac{\omega_0^2}{k}F(z+h) = \frac{\omega_0^2}{k}F_{ext} \tag{4.1}$$

where ω_0 is the oscillating frequency of the cantilever in the absence of any interaction with the surface, k is the spring constant of the cantilever, α is the damping coefficient and h is the equilibrium height of the cantilever above the surface in the absence of interaction. At constant amplitude and frequency change we can assume that any damping is completely cancelled by the external force and that $F(z)$ does not depend on time. This simplifies equation (4.1) to the following:

$$\ddot{z} + \omega_0^2 z - \frac{\omega_0^2}{k}F(z+h) = 0 \tag{4.2}$$

As the cantilever motion is periodic, we can search for a solution of eq. (4.2) in the form of a Fourier series for the oscillator coordinate z:

$$z(t) = \sum_{n=0}^{\infty} A_n \cos(n\omega t) \tag{4.3}$$

Substituting equation (4.3) into equation (4.2) gives the following equation of motion:

$$\sum_{n=0}^{\infty}(1-(n\Omega)^2)A_n\cos(n\tau)+A_0-\frac{1}{k}F(z+h)=0 \tag{4.4}$$

where dimensionless time $\tau=\omega t$ has been used and $\Omega=\omega/\omega_0$. To find Ω, A_n, $n=0,2,...\infty$, for a given oscillation amplitude, A_1, h and $F(z)$, we multiply eq. 4.4 by $\cos(j\tau)$ and integrate the result over the period of main frequency $\tau=[0,2\pi]$. This produces a system of non-linear equations for $A_n, n=0,2,3,...m$, which is approximate for finite m:

$$A_0-\frac{1}{2\pi k}\int_0^{2\pi}F(z+h)d\tau=0 \tag{4.5}$$

$$A_n-\frac{\int_0^{2\pi}F(z+h)\cos(n\tau)d\tau}{\pi k-\pi kn^2+\frac{n^2}{A_1}\int_0^{2\pi}F(z+h)\cos(\tau)d\tau}=0 \tag{4.6}$$

If we designate the left-hand side of equations (4.5) and (4.6) as $\phi_n(A_0,A_2,...)$, one can re-write this system of equations more compactly i.e. $\phi_n(A_0,A_2,...)=0, n=0,2,3,...,m$, and solve it using a modified Newton method. As an initial step, we set all A_i except A_1 to zero. For each iteration afterwards the values of the amplitude increments (ΔA_i) can be obtained by solving the set of equations:

$$\frac{d\phi_n}{dA_0}\Delta A_0+\sum_{j=2}^{m}\frac{d\phi_n}{dA_j}\Delta A_j=-\phi_n \tag{4.7}$$

Unfortunately using equation (4.7) as the foundation of the iterative procedure often leads to divergent results, and ΔA_i from this are only used to find a search direction. The absolute values of the increments are calculated by minimizing the residual function

$$\Phi(\lambda)=\sum_{i=0}^{m}\phi_i^2((A_i)_k) \tag{4.8}$$

with respect to the parameter λ, where

$$(A_i)_k=(A_i)_{k-1}+\lambda\Delta(A_i)_{k-1} \tag{4.9}$$

and k is the iteration number and i is the index of the unknown coefficient. Finally the frequency of cantilever oscillations in the presence of the interaction, Ω, is obtained as

$$\Omega^2=1-\frac{1}{\pi kA_1}\int_0^{2\pi}F(z+h)\cos(\tau)d\tau \tag{4.10}$$

A similar result was derived by Giessibl [25] using perturbation theory and a more specific force expression, although equation 4.10 represents a more general form of the equation.

4.5 Generating a Theoretical Surface Image

Using the above mechanism produces a map of the change in frequency of the oscillations of the cantilever due to the influence of the tip-surface interaction. This can be interpolated to find the cantilever deflections to keep the cantilever oscillating at a constant frequency change (or constant modified frequency). The deflections can then be plotted as a function of surface position (x, y) to give the theoretical NC-AFM image. At this point, the theoretical image and data can be compared with the experimental equivalents. It should be noted that the theoretical image is generated using experimental values for all known parameters such as frequency ω_0, amplitude A_1, elastic constant k and frequency change $(\omega - \omega_0)$. All parameters which are not known from experiment, such as tip radius, are taken from the best experimental or theoretical estimate as appropriate. The specific parameters used for each system studied will be discussed in later chapters.

4.6 Conclusions

A theoretical model of NC-AFM has now been developed. It simulates all the features which were identified as important in NC-AFM in chapter 2 and can include all of the components of the tip-surface interaction discussed in chapter 3. As a first step, the full model can now be used to try and characterize some of the important processes in NC-AFM.

Chapter 5

System Characterization

This chapter attempts to use the model described in chapter 4 to characterize some of the important processes in NC-AFM. It focuses on the role of the tip, atomic relaxation and image forces in NC-AFM imaging. In the first section the tip-surface interaction over a metal surface is used to try and characterize NC-AFM tips. Then the role of atomic displacements due to interaction with the tip is discussed. Finally, the role of image forces in NC-AFM of several generic surface features and defects is discussed. Although all of these processes are intrinsically useful to study, they also have important implications for the application of the model to real experimental surfaces in later chapters.

5.1 Tip Characterization

As discussed previously, many interpretation problems in NC-AFM experiments are due to the lack of physical information about the tip. Nearly all the forces discussed in chapter 3 depend on the properties of the tip as well as the surface. However, for an 'ideal' conducting or metallic surface the tip would become the dominant factor in the tip-surface interaction - the tip is effectively mirrored in the surface. This means that the model discussed in chapter 4 can be used to try and characterize different NC-AFM tips by comparing the 'fingerprints' of their tip-surface interactions over a metal surface.

Clearly 'fingerprints' is a subjective term and a quantitative measure of the tip-surface interaction is required. The best method for analyzing the tip-surface interaction is by analysing the distance dependence of the forces [44]. There has been a number of previous studies of force vs. distance curves. Recent theoretical and experimental studies on semi-conductors [40, 41, 118, 119] and insulators [4] have used short-range force vs. distance curves to analyze the mechanism of contrast and the changes in interactions over different surface sites. Analysis of the tip-surface interaction at longer-range has also been performed [36, 120], but the possible components of the long-range interaction were not studied in detail. Recent experimental studies [98, 121] have tried to separate out the tip-surface interaction components. These studies assume that any electrostatic interaction has been compensated for by applied bias and the tip-surface interaction is van der Waals alone. However, they were unable to explain the unphysically long-range chemical forces needed to fit the strength of interaction at medium-range. As discussed in chapter 3 and in refs.

[44, 122, 123], many other interactions can be significant in AFM and van der Waals is rarely the sole component of the long-range tip-surface interaction. In fact, it is the other components of the tip-surface interaction which often hold the most information about the tip and surface structure. The image force, for example, depends crucially on the conduction and oxidation of the tip, whereas the van der Waals interaction is dominated by the tip radius.

5.1.1 Setup

The same setup as shown in fig. 4.6 is used for the calculations over a metal, but now the conducting substrate is effectively the surface being studied. However, the metal atoms are not included explicitly in the model and the metal is treated as an ideal conductor where polarization due to the tip-surface interaction is represented by point image charges. This means that the tip-surface interaction is not physical close to the metal surface (< 0.5 nm), but for this study only longer-range interactions are of interest.

The macroscopic part of the van der Waals force is calculated using a Hamaker constant (H) of 2.5 eV and the method described section in 3.3. The microscopic and image force are calculated using a static atomistic simulation technique and the SCIFI code, as described in section 3.4.5. The SCIFI code was used since it allows us to self-consistently study the image force, a significant interaction when the surface is conducting, and it also allows the properties of a charged tip to be simulated.

Since experimentally the frequency change, not force, is measured as a function of distance, this study converts the calculated force vs. distance curves into frequency change vs. distance curves using the method described in section 4.4. The metal frequency curves were calculated with a cantilever amplitude of 6.5 nm, eigenfrequency of 168 kHz and spring constant of 31.2 N/m, as in experiments on copper [98].

5.1.2 Interactions over a Metal Surface

In this section the possibility of using metal substrates as standard systems for tip characterisation has been explored. Four tips are considered. These could be produced by appropriate preparation, such as doping, oxidation, sputtering etc. Each of the tip types include a macroscopic tip of radius 10 nm and no bias. The four tip types are: (i) "insulator" - this represents the situation where the macroscopic tip is insulating (Hamaker constant reduced to 1 eV) and the nano-tip is neutral, (ii) "conductor" - the macroscopic tip is conducting and there is no nano-tip, (iii) "neutral tip" - the macroscopic tip is conducting and there is a neutral nano-tip, and (iv) "charged tip" - the macroscopic tip is conducting and there is a charged nano-tip. To simulate tip charging, two oxygen ions were removed from the original nano-tip so that its net charge became $+4e$. Fig. 5.1 shows frequency change vs. distance curves for each of the tip types.

Fig. 5.1 demonstrates that the different tips give different long-range tip-surface interactions. The weakest interaction is for the insulating tip, where the force is dominated by the van der Waals interaction. In this case the image force is insignificant, as the polarization that occurs within the metal is not mirrored in the insulating tip. For the conducting tip, the interaction at long-range is solely van der Waals as there is no oxide nano-tip to polarize the metal surface. The force is greater than for the insulating tip even though the radii are the same, as the conducting

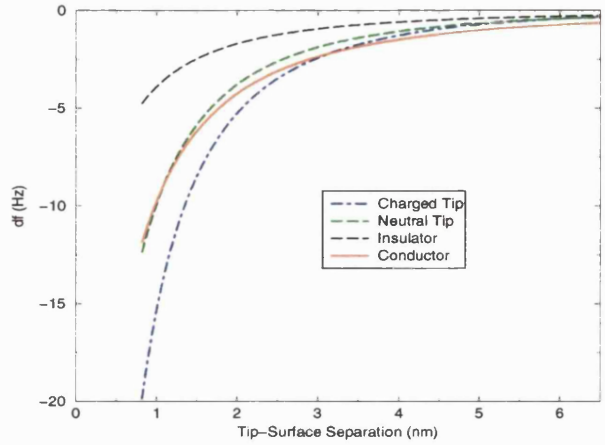

Figure 5.1: Frequency change vs. distance curves over a metal surface.

tip has a greater Hamaker constant (2.5 eV compared to 1.0 eV) for the macroscopic van der Waals interaction with the metal. When the neutral oxide nano-tip is added to the conducting tip, a deviation from the pure van der Waals behaviour can be seen. This is due to the image force between the tip and surface, produced when the oxide nano-tip polarizes the tip and the metal. Beyond about 1 nm the image force is actually repulsive, but this is an unphysical result due to the finite accuracy of the force on the ions in the simulation. By increasing the convergence criteria for force gradients this can be reduced, but this does not affect any of the conclusions here and the extra expense did not seem necessary for this study. In any case, the image force for the neutral tip is a small contribution to the overall interaction as the tip approaches the metal surface. At very close-range the image force is significant, but this study is concerned only with the more long-range interactions. In the final charged tip curve, the nano-tip has an effective charge of +4e. This increases the magnitude of the polarization of the metal and the image force increases by an order of magnitude. In previous curves with a neutral nano-tip, the equal positive and negative ions of the oxide compensate each other's polarizing of the metal and the image force is small. However, with the charged tip the uncompensated interaction produces a large image force, which is comparable to van der Waals force at tip-surface separations of less than 2 nm.

5.1.3 Comparison with Experiment

These results predict the ability of frequency change vs. distance curves to differentiate between different tip models. To demonstrate how this analysis can work for real systems, it is important to compare the theoretical predictions with experimental results. Fig. 5.2 shows a comparison between an experimental frequency change vs. distance curve over a copper surface [98] and theoretical curves calculated using only the van der Waals background interaction. Since there is no reference for the distance scale in experiments, the experimental curve has been set so that the minimum of the curve is at 0.2 nm, which is a reasonable estimate of where repulsion due to electron orbital overlap would begin. The van der Waals curves are calculated using macroscopic tip radii in the range 4 to 32 nm. Fig. 5.2 shows clearly that none of the theoretical curves can match the experimental behaviour at both short and long-range. This demonstrates that the

interaction is not due to pure van der Waals and that other interaction components are significant.

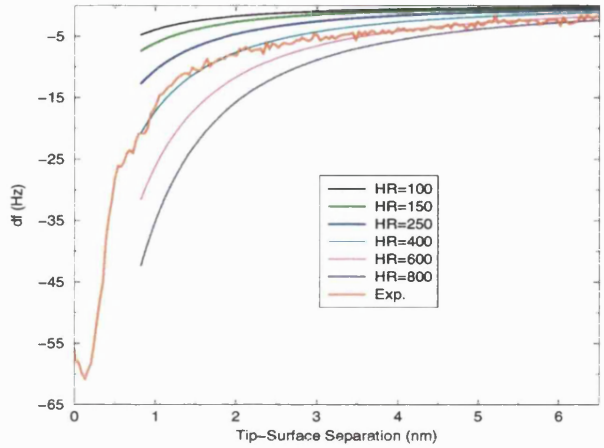

Figure 5.2: Comparison of van der Waals interaction for different tip radii with experimental frequency change vs. distance curve over a copper surface. Note that the legend is given in terms of the product of the Hamaker constant (H) and radius (R), but H is always 2.5 eV and only the radius changes.

Fig. 5.3 shows a comparison of two different models of the tip-surface interaction with the same experimental curve as in fig. 5.2. The two theoretical interaction models used in fig. 5.3 are: (i) conductor - conducting macroscopic tip with no nano-tip, the same as in fig. 5.1; (ii) conducting macroscopic tip with a neutral nano-tip, simulating an oxide coating and an applied bias, which is named model_1. Model_1 was fitted to the experimental results by varying the macroscopic tip radius and applied bias. The best fit was found with a tip radius of 4 nm and a bias of 1.2 V.

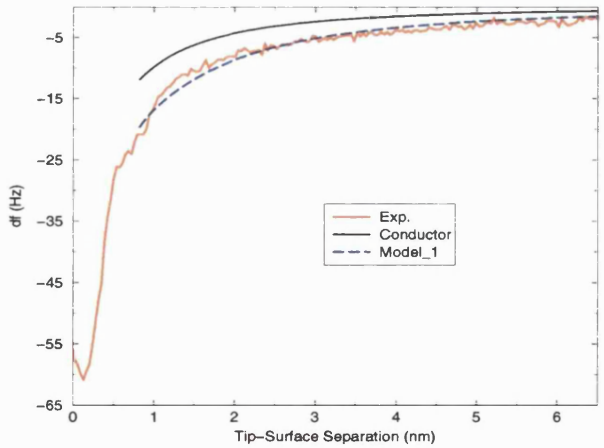

Figure 5.3: Comparison of theoretical curves over an ideally conducting metal surface and a experimental frequency change vs. distance over a copper surface.

Fig. 5.3 shows that in the conductor model the tip-surface interaction is much weaker than that observed in experiment. The bias applied in the model_1 increases the overall electrostatic interaction by adding a long-range capacitance force to the system. The magnitude of the bias needed for the fit is a parameter dependent on the model chosen. Although slight variations

of the radius and bias would produce similar curves to model_1 in fig. 5.3, the ratio between electrostatic and van der Waals is important. Using widely different parameters produces curves matching experiment only at short or long-range, and not both. This implies that the tip radius in the experiments was about 4 nm and an electrostatic force, corresponding to a bias of 1.2 V in this model, was present. A phenomelogical model [122] of the capacitance force was also compared with model_1 and results were found to be similar.

5.2 Atomic Relaxation due to Tip Proximity

One important effect in SPM is the relaxation of surface ions when the tip is close to the surface. In contact AFM this is a significant problem [24], as the surface atoms would have such large displacements that they would actually jump onto the tip and contaminate it (see section 4.2.5), effectively ruining the image. NC-AFM does not suffer so acutely from this problem as the tip's closest approach is greater than in C-AFM (4-5 Å cf. 2 Å). However, surface relaxation can be apparent even in NC-AFM and it is important to understand how this affects the tip-surface interaction and imaging.

In order to investigate the effects of surface relaxation, the MgO surface was modelled with *ab initio* calculations performed using the VASP code as discussed in section 3.2.1. First, calculations on bulk MgO were performed and the total energy of the bulk unit cell was converged with respect to cut-off energy and k-point mesh. The Monkhorst-Pack [56] k-point generation scheme was used and the total energy was converged to 1 meV with a $9 \times 9 \times 9$ mesh. Then the unit cell was relaxed giving a lattice constant of 4.24 Å, which compares well with the experimental value [124] of 4.21 Å. The relaxed bulk unit cell was then used to generate a (001) surface unit cell and the total energy of this system was converged with respect to k-points, cell depth and vacuum gap. 4 k-points ($(\pm 0.25, \pm 0.25, 0)$) converged the total energy to 0.1 meV. A 3 layer MgO slab separated by a vacuum gap of 6 Å was found to be sufficient to converge the total energy (and the forces on atoms). The surface was then relaxed and it demonstrated characteristic rumpling of the top (and bottom for slab calculation) layer seen in experiments. This rumpling had a magnitude of about 0.03 Å with oxygens displacing out and magnesiums displacing into the surface.

The relaxed surface was then taken and re-calculated with one Mg ion displaced out of the surface by 0.15 Å (a relaxation which is quite realistic for NC-AFM on MgO [4]). In this calculation the displaced ion is frozen and all other ions are allowed to relax. Fig. 5.4 shows the electrostatic potential from the displaced ion and the surrounding surface. It is immediately evident that there is much longer range potential from the displaced Mg in the centre of the figure than from the other two Mg atoms in the image. Effectively the same electrostatic gradient is experienced a further 1 Å from the surface than in the unperturbed system. This is because by displacing the ion, a dipole is produced at the surface which has a much longer-ranged interaction. Since the electrostatic tip-surface interaction is one of the dominant forces in NC-AFM imaging, this means that surface relaxation will increase the tip-surface force. This effect could be especially important for 'soft' ionic surfaces where the atomic displacements when the tip is close could be much larger than in MgO, producing a larger dipole.

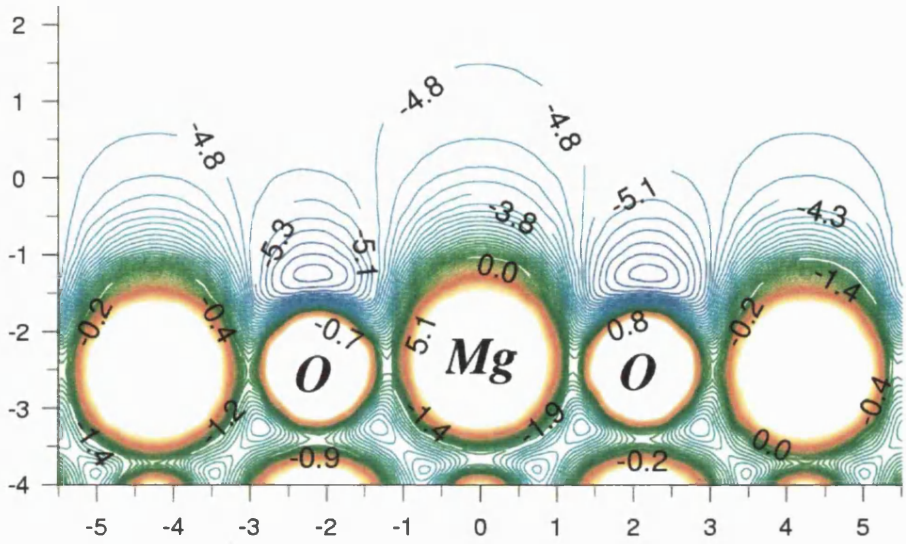

Figure 5.4: Electrostatic potential from Mg atom displaced by 0.15 Å from its relaxed surface position. Axes are in Å.

5.3 Role of Image Forces in NC-AFM

In chapter 3 the different possible contributions to the macroscopic force were discussed in some detail. However, the image force interaction has been neglected as a significant interaction in NC-AFM studies so far and it is important to establish in what systems they are relevant. Although their relevance has long been recognised in metal-insulator interfaces, electro-chemistry and other areas, their role in image formation in Scanning Force Microscopy (SFM) has not been analysed in detail [44]. The reasons are mainly related to the small number of experimental situations where these forces were evidently important, e.g. where an ionic insulator would make a contact with a conducting tip. In particular, most of the early SFM applications on insulators used either insulating tips or strongly oxidised tips. However, recent combined applications of STM and NC-AFM (for example, refs. [29, 30, 125]) bring these interactions to the front. Although these experiments use the same tips as in normal NC-AFM experiments, the ability to image in tunnelling mode demonstrates that the tips are effective conductors.

In these applications conducting tips are interacting with thin polar films grown on metal substrates or with conducting oxides. This means that both the interactions of the tip with the film and of the film with the substrate involve the image force and it should be taken into account in analysis and interpretation of SFM images. To study the role of image forces in NC-AFM image formation an example of a finite cluster of NaCl adsorbed on a metallic substrate has been modelled. This system has been studied in recent STM [126] and NC-SFM experiments [127], [128] and is representative of a common case of an insulating film grown on a metal.

5.3.1 Theoretical Model

The image interaction is calculated as is shown in chapter 3, with the total force between tip and surface given by equation 3.51. Although the expression for the force obtained is exact

for the model used in this study, such a calculation is quite demanding since it requires using the electrostatic energy, U_{el}, alongside the shell model (short-range chemical interaction) energy, U_{sh}, in the optimisation process. Most time is spent in the calculation of the forces imposed on atoms due to the energy U_{el}. Therefore, in this study the following approximate strategy has been adopted. For every tip position all non-frozen atoms were allowed to relax to mechanical equilibrium in accordance with the shell model interactions only and the effect of the image charges on their geometry was neglected. To investigate the effect of this, some fully self-consistent calculations on the NaCl step system were performed. In these calculations, all non-frozen ions are allowed to relax completely with respect to microscopic *and image forces.* The displacements of ions in the system due to image forces was less than 0.01 Å and would not affect our results. The expression for the tip surface force using this approximation becomes:

$$F_{tip} \simeq \sum_{fix} \left(F_{iz}^{(sh)}\right)_{\mathbf{x}_0} + \sum_{relax} \left(F_{iz}^{(el)}\right)_{\mathbf{x}_0} - \frac{dU_{vdW}}{dz_s} - \left(\frac{\partial U_{el}}{\partial z_s}\right)_{\mathbf{x}_0} \tag{5.1}$$

where in the first summation we sum all z-forces acting on fixed atoms (region 1 in fig. 4.6) in the tip due to the electrostatic energy U_{el} and in the second summation we sum all z-forces acting on all relaxed atoms (region 2 in fig. 4.6) of the tip due to the electrostatic energy U_{el}.

The setup shown in fig. 4.6 was used to model the interactions of the NaCl cluster absorbed on a metallic substrate with a conducting tip of radius R. Note that quantum effects in metal polarisation [72], [73], [74], [129] are neglected here and theoretical consideration is based entirely on classical electrostatics. According to this model, the image charge does not penetrate into the bulk of the metal. In reality, however, there is some distribution of the charge inside the metals [72], [73], [74]. However, this effect is not important for processes which occur at distances of the order of several Å outside the metal and therefore will be neglected in this study.

5.3.2 Details of the calculations

Setup

The systems used to calculate the forces are all setup as shown in fig. 4.6, with only the exact structure of the NaCl cluster changing between systems. For these calculations the tip consists of a sphere of radius 100 Å with a 64-atom MgO cube embedded at the apex. The cube is orientated so that it is symmetric about the z-axis with a single oxygen ion at the lowest point of the tip. The top three layers of the cube fall within the sphere's radius and constitute region 1 as shown in fig. 4.6. The exact number of ions in region 1 is set so as to keep the nano-tip attached to the sphere neutral. The remaining ions of the cube constitute region 2. The clusters used consist of four layers of NaCl with the top two layers designated region 3 and the bottom two layers region 4, as in fig. 4.6. The metal plate is 2 Å below the bottom of the cluster and the bias is held at 1.0 V in all calculations. This setup is consistent through all systems calculated and, where appropriate, for all interactions calculated. This allows a reasonable comparison to be made between the relative values of forces in the same system and between different systems.

Microscopic Interaction

The shell-model contribution to the tip-surface force is calculated using a periodic static atomistic simulation as implemented in the MARVIN code and described in section 3.2.2. The nano-tip and the NaCl cluster are each divided into two regions, I and II. In terms of fig. 4.6, region I consists of region 2 and the top two layers of the cluster (region 3), and region II consists of region 1 and the remaining bottom two layers of the cluster (region 4). The region I ions are relaxed explicitly, whilst the region II ions are kept fixed.

Image Interaction

The image force is calculated by taking the relaxed geometry from the shell-model calculation at each tip-surface separation. Any ions within the metal sphere (i.e. region 1) are not considered in the image force calculation, as it is impossible to have ions within the conducting sphere. The force on each atom in the system due to the image interaction is then calculated, and the force on the tip atoms is summed to find the contribution of the image force to the tip-surface force, cf. eq. (5.1). This calculation is not periodic, the NaCl cluster is now a finite body. However, since the NaCl periodic cell is large enough that the interaction between the tip images can be neglected, the NaCl sample can be effectively considered to be a finite cluster at all stages of the calculation. The only difference is that the periodic boundary conditions in atomistic simulations do not allow the atoms at the cluster border to relax as in a free cluster. However, this effect is small and does not affect the results. The described approach ensures the consistency of the model shown in fig. 4.6 throughout the whole modelling process.

Van der Waals Interaction

The final contribution to the force is the van der Waals interaction. It includes the following contributions: i) between the macroscopic Si tip of conical shape with the sphere of radius R at the end and semi-infinite substrate; ii) the dispersion forces between the atoms in the sample; and iii) the interaction between the macroscopic part of the tip and the sample atoms. The first contribution is calculated analytically as discussed in chapter 3. In fact, the macroscopic contribution to the van der Waals force is the same in each of the three systems described below, as it depends only on the tip-surface separation, macroscopic sphere radius, cone-angle and Hamaker constant of the system. All these quantities are identical in each system we look at, so that the van der Waals force acts as a background attractive force independent of the microscopic properties of the system. The Hamaker constant needed for the calculation of the macroscopic van der Waals force is estimated to be 0.5 eV [130]. The second contribution is calculated directly in the atomistic simulation of the surface.

To estimate the importance of the third contribution, the dispersion interaction between one atom and a spherical block of atoms has been calculated explicitly. This interaction converges to a constant value when the radius of the sphere exceeds about 30 Å. The force exerted on one atom due to this interaction at characteristic tip-sample distances is several orders of magnitude smaller than the force between macroscopic tip and substrate. Also the force decays with distance as r^{-4}. This effectively means that only the top layer of the sample contributes to the van der Waals force, and there are not enough ions in that layer for it to be significant. Therefore this

interaction was neglected in further calculations. However, for much larger clusters (such as those discussed in chapter 7) this contribution could be significant.

5.3.3 NaCl Step

The first system studied was a stepped NaCl cluster produced by placing a $5 \times 3 \times 2$ (in terms of an 8 atom cubic unit cell) block on top of a $5 \times 5 \times 2$ block so that two corners are aligned. A schematic for the calculation cell of this system is shown in fig. 5.5. The upper terrace of the step is a good representation of the ideal (001) surface of NaCl, as long as the studied row remains at least 3 rows from the edge the forces are converged with respect to row choice. This system also allows the study of interactions over sites of different coordination. The ions at the step-edge have a coordination of 4, as compared to a coordination of 5 for the terrace ions. To study the difference between these types of sites the interactions over a Na ion in the terrace and a Cl ion at the step edge were calculated, as shown in fig. 5.5. This allows comparison of the effects of coordination and chemical identity to the forces between tip and surface.

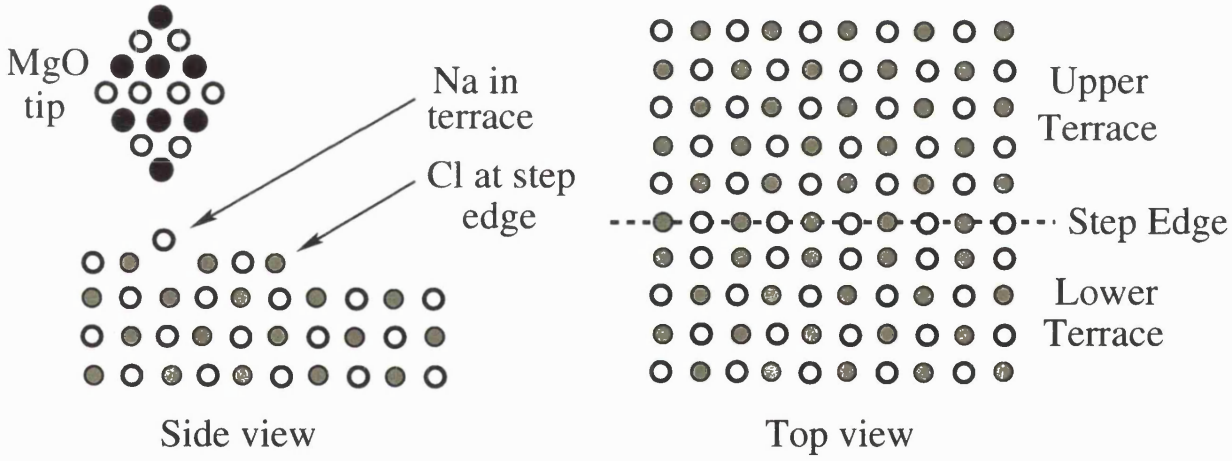

Figure 5.5: System schematic for NaCl step.

The first point to note is that the macroscopic van der Waals force is the same for both anion and cation, this is an obvious effect from the way in which this interaction is calculated. It is also the least significant force at tip-surface separations less than 6 Å as can be seen in fig. 5.6.

The behaviour of the microscopic force is as would be expected for the interaction of an oxygen ion (which simulates the end of the tip apex) with the ions in the surface. The force is attractive over the positive Na in the terrace and repulsive over the negative Cl at the step edge. The microscopic force becomes the dominant interaction in the system at around 5.5 Å. As the tip gets very close to the Na ion in the terrace the ion begins to displace towards the tip oxygen, greatly increasing the attractive force. When the separation is closer than around 4.7 Å the displacement of the Na ion towards the tip exceeds 1 Å. This ion instability can be seen clearly both in the microscopic and image force curves for Na in fig. 5.6 and has been already described in the literature in the context of AFM [131].

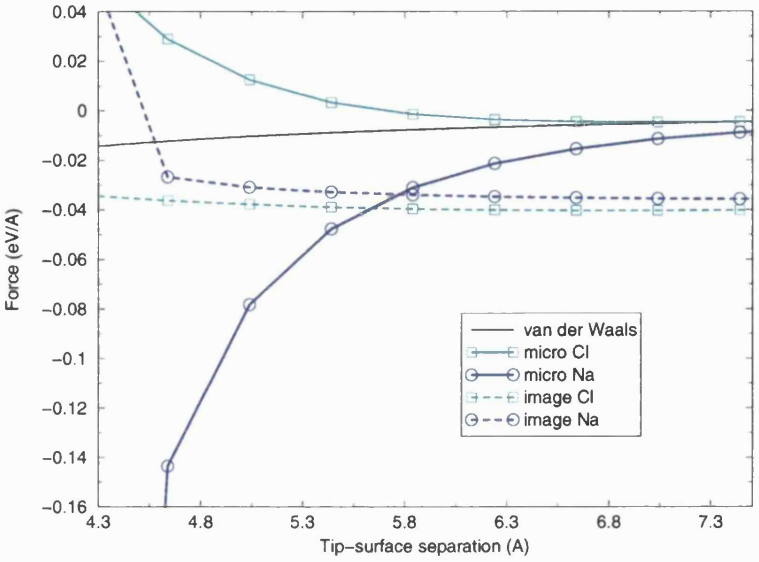

Figure 5.6: Forces over NaCl step

The image force itself is the dominant interaction at longer ranges, but it is fairly consistent over cation and anion in the NaCl terrace. The difference in image force over the Cl and Na ions is less than 0.01 eV/Å until the instability at 4.7 Å. This means that for this system the image force acts in a similar way to the macroscopic van der Waals force, i.e. as an attractive background force which is blind to atomic identity and therefore does not contribute to the NC-AFM image contrast.

5.3.4 Pair Vacancy

The second system studied is formed by taking the NaCl step from the previous section and removing a Na-Cl pair of nearest-neighbour ions from the upper terrace, as shown in fig. 5.7. This effectively creates a dipole on the upper terrace of the step, but does not greatly affect the original geometry of the step.

In this system the total force contributions were calculated over the ions at the edge of the pair vacancy, the Na ion labelled 1 in fig. 5.7 and the Cl ion labelled 2. The force contributions as a function of tip-surface separation are shown in fig. 5.8. The macroscopic van der Waals force is obviously identical to the previous example, and is here only for comparison. The microscopic force is also very similar to the previous example. This is expected, as we are still looking at the interaction over the same ions and the double vacancy of oppositely charged ions has little significant effect on this force. The removal of the vacancy ions does change the local coordination of the ions at the edge of the vacancy, but this is compensated by relaxation of these ions away from the vacancy. This compensation means that the microscopic van der Waals and electrostatic force directly over the edge ions is similar to the force over the ions in the defect free terrace. This is seen clearly by the onset of Na ion instability at the same tip-surface separation, about 4.7 Å.

The image force over the edge ions demonstrates very different behaviour to the plain step system studied in the previous Subsection. The only similarity is that the microscopic force

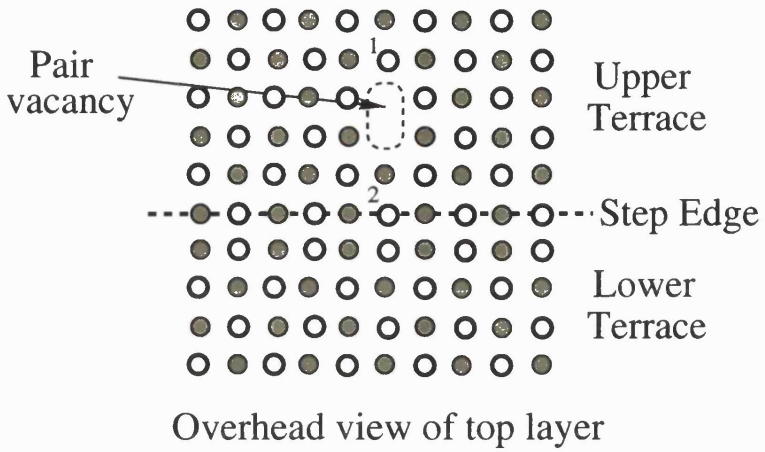

Figure 5.7: System schematic for pair vacancy on NaCl terrace

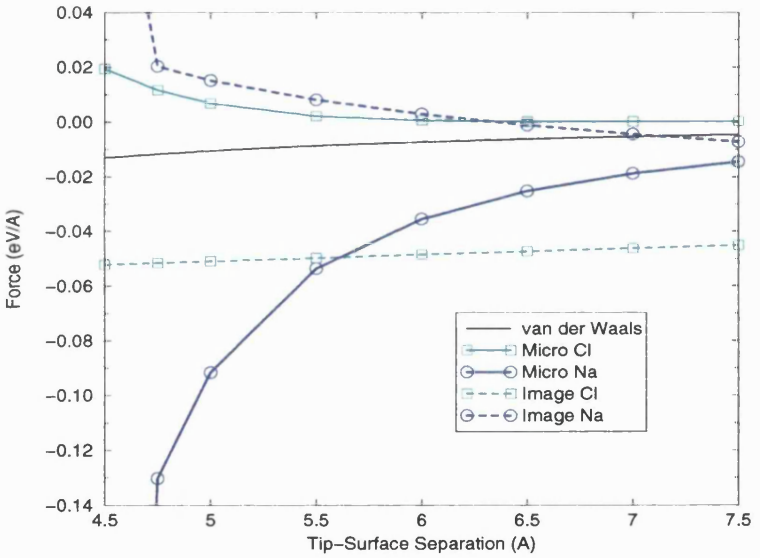

Figure 5.8: Forces over pair vacancy in NaCl step

becomes the dominant interaction at the same distance of 5.5 Å. The image force over the Cl vacancy edge ion is attractive and almost twice as large (-0.05 eV/Å) as the force over the Cl at the plain step edge (-0.03 eV/Å). The image force clearly feels the defect in the terrace and the increase in force reflects the change in the local charge environment of the Cl ion. This is even more clearly shown by the image force over the Na ion at the vacancy edge. The force is much smaller than the microscopic force at all separations and actually becomes repulsive at around 6.2 Å. This means that the induced potential in the conducting tip reflects the change in local charge environment produced by the vacancy. The net interaction over the Cl ion is attractive and repulsive over the Na ion. The difference in magnitude of the image force over the two ions is due to the asymmetry of the nano-tip ions at the end of the conducting tip. Although this result implies that the image force is somewhat sensitive to the geometry of the interacting feature, it does demonstrate that the image force would feel a defect in the surface.

5.3.5 Charged Step

In the final system studied, a charged step where *similar* ions run along each edge of the step was modelled. Fig. 5.9 shows a schematic of the calculation cell used. The system is created by taking the neutral step setup from section 5.3.3 and just removing ions from four rows of the upper terrace. This charged row of ions is similar to the bridging oxygen rows seen in the TiO_2 (110) surface (see chapter 6).

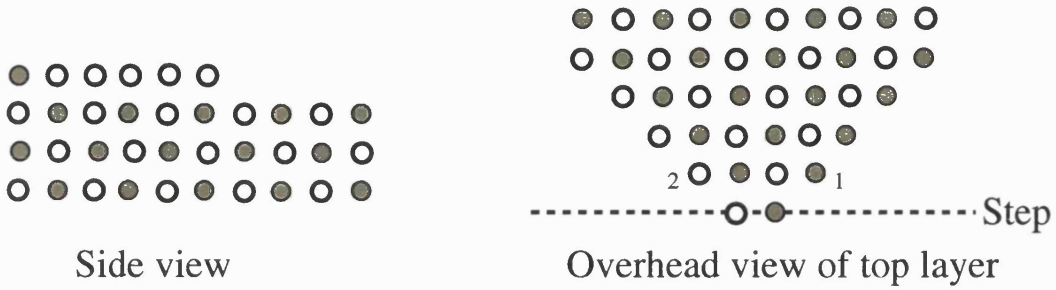

Figure 5.9: System schematic for charged NaCl step

The contributions to the total force were calculated over a Cl ion at one edge of the step, labelled 1 in fig. 5.9, and over a Na ion at the other edge, labelled 2. The force contributions are shown in fig. 5.10.

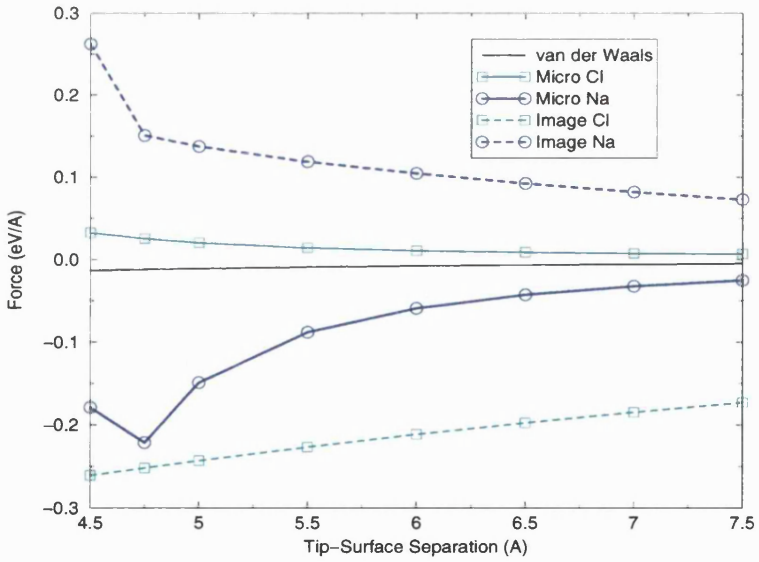

Figure 5.10: Forces over charged NaCl step

The macroscopic van der Waals force for the charged step is again identical to previous examples and plotted only for comparison. The microscopic van der Waals and electrostatic forces over both the ions are increased as compared to the previous two systems. Over the Na ion at the step edge the force is -0.1 eV/Å at 5.5 Å compared to -0.05 eV/Å at 5.5 Å for the Na ion in the terrace of the plain step. This doubling of the force is also seen over the Cl ion where the force at 5.5 Å is 0.025 eV/Å over the charged step and 0.012 eV/Å over the plain step. This is a consequence of

the change of geometry of the charged step system, both ions have lower coordination than the ions in the plain step system. Lowering the coordination increases the gradient of the electrostatic potential around these ions and therefore increases the microscopic force between tip and surface.

The image force dominates the interactions over the charged step at nearly all tip-surface separations, only after the onset of Na ion instability at 4.7 Å does the microscopic attraction between the tip and the step Na overcome the image force. Over the Cl ion the image force is completely dominant, and is approximately an order of magnitude larger than the microscopic force. At the edge of the charged step, the row of similar ions produces a row of similar image charges of opposite sign in the conducting tip. In the other systems this effect is effectively compensated by the alternating ion species. As in the previous system the image force does feel the difference between one side of the step and the other, and this is manifested in the opposition of the interactions at either side of the step. Over the Cl ion the image force is attractive and over the Na ion the force is repulsive. This is a refiection of the image charge distribution produced in the tip by the charged step system, an exaggerated version of the effect seen over the vacancy. The significance of the image force above the ions of the charged step is in agreement with other results [68], where it was found the the image force is very sensitive to the charge of the system between the electrodes.

5.3.6 Tip Charging

For consistency, throughout this study a neutral nano-tip was used. As discussed in section 4.2.3, it is known that the tips used in real experiments can be highly contaminated by external material, which may lead to tip charging. Therefore, it is relevant to study the effect of a charged tip (i.e. a nano-tip with a different number of anions and cations) on the image force. To simulate this, four uncompensated oxygen ions were added to the top of the nano-tip so that its net charge became $-8e$. Using this modified tip, the interaction over the three systems above was re-calculated. For the charged step, the image force more than doubles. This system is an extreme example of this effect, but an increase in image force can be seen when using a charged tip in all the systems.

The effects of tip contamination could be even more significant in the case of contact SFM. In previous studies of contact SFM imaging [24], the importance of ion displacements and ion exchange between tip and surface has been demonstrated. Our results here show that displacement of ions causes a large increase in the image force between the tip and surface. Ion exchange may also charge the tip, again changing the image force. This means that the image force could exaggerate the effects of ion displacement on imaging of conducting materials or thin films with contact AFM.

5.3.7 Cluster Size

A limitation of the present model is that for the calculation of the image interaction, finite clusters of a particular shape were studied. However, it is important to understand how the result of the calculation would depend on the size of the cluster if any general conclusions about image forces in these systems are to be made. As has been mentioned in the previous sections, the image force over a particular ion is somewhat dependent on the geometry of the system being studied. Note that we cannot increase the cluster size indefinitely since it is limited to roughly twice the radius

of the sphere used to model the tip. Beyond this limit the top of the sphere affects the interaction with the surface, which is an unphysical result as in reality the tip has essentially infinite height at this scale.

In order to investigate the effect of the size of the cluster, the image force over the same terrace Na ion as in the first system studied was calculated, but the size of the cluster was increased by several hundred atoms (being still within the limit of the maximum cluster size). This effectively means that the local geometry and charge environment of the ion under the tip apex remains the same, but the total number of charges in the system changes significantly. The calculations show that the image force over the cluster does increase as the number of atoms is increased, but then converges. The increase in image force is due to the interactions of the extra charges in the system, but the difference is an order of magnitude smaller than the image force itself, so it would not affect the results significantly.

5.4 Conclusions

The study of the tip-surface interaction over a metal surface has demonstrated the ability of frequency change vs. distance curves to differentiate between different tips. The importance of the properties of the tip to NC-AFM imaging has long been known, but no systematic method for characterising the tip in a *specific experiment* has been developed. Comparison of theoretical and experimental frequency change vs. distance curves allows predictions to be made about the tip and tip-surface interactions in experiments. The theoretical results demonstrate that van der Waals cannot be the only interaction in NC-AFM experiments on copper. The importance of an electrostatic interaction at medium-range (1 - 2 nm) implies that the tip is a conductor at the macroscopic scale and has a thin oxide coating which provides a nano-tip. Both these elements are crucial in providing the magnitude of image force needed to match experimental results. At longer range, the introduction of a bias is required to match the experimental results. This means it is very likely that the electrostatic minimization procedure used in experiments does not fully compensate for the contact potential difference and some residual capacitance force remains. As the minimization process is only performed at one point on the surface, this residual could be due to inhomogeneities in the contact potential or 'patch charges'. Ref. [44] also predicted that patch charges were responsible for deviations from a pure van der Waals interaction in experiments. To summarize, these results suggest that frequency change vs. distance curves obtained on standard substrates and on real samples can provide fingerprints of the tip properties vital for interpretation of images.

Atomic relaxation due to interaction with the tip has been shown to have a significant effect on the tip-surface force. Displacements of the surface atoms cause an extension of the electrostatic potential due to the formation of a dipole and this increases the short-range electrostatic force on the tip compared to the interaction over an undisplaced atom. This effect will be especially important for 'soft' or low-coordinated surface ions which are more weakly bound.

The significance of the image interaction in NC-AFM contrast formation has been demonstrated. Over neutral systems the image force acts as a background attractive force which is blind to the identity of the atom under the tip apex. Over locally charged systems the image force becomes the dominant interaction in contrast formation. It was able to resolve (in terms of force

changes) the charged di-vacancy and charged step. This shows that the image force could be the dominant source of contrast in NC-AFM images of charged features. Even for neutral systems, it is clear that for systems which include conducting materials it is important to include the image contribution in the tip-surface interactions.

Part II

Applications

Introduction

In the following chapters, the application of the model described previously to several NC-AFM experimentally studied systems will be described. These systems represent examples of different surfaces, such as oxides, a thin insulating film on metal and a bulk insulator, as well as different types of problem. The choice of surfaces presented here is also strongly affected by our experimental collaborations. In each case experimentalists approached us directly to try and aid them in understanding the results they were getting or attempting to get.

The first system is Titanium Dioxide (chapter 6), this is wide band gap semi-conducting oxide, which has been thoroughly studied by many other surface techniques including STM and NC-AFM, but interpretation in NC-AFM still remains difficult. The second system is a Sodium Chloride thin film on a copper substrate (chapter 7). NaCl is a classic ionic insulating system and it has been studied in bulk experimentally and theoretically via NC-AFM previously [4], however thin films are known to have different properties [132] and the effect of the copper substrate on the tip-surface interaction is unknown. Also, the nature of the growth of the NaCl thin films means that it allows a detailed study of the properties of low-coordinated sites. Next studied is Calcium Difluoride (chapter 8), a wide band gap insulating system which represents the class of materials for which NC-AFM was originally designed. Again, image interpretation problems are the main motivation behind studying this system. Finally, the possibility of measuring the exchange force directly using a metal coated NC-AFM tip scanning the anti-ferromagnetic NiO surface is investigated theoretically (chapter 9).

Chapter 6

Titanium Dioxide

6.1 Original Motivation

This study was funded by a joint EPSRC project with an experimental group in Manchester led by Geoff Thornton. The original aim of the work was to study oxide surfaces experimentally and theoretically in collaboration. Initially, most effort was focused in studying the TiO_2 (110) surface, which is why this part of the study begins with that system. The original plan was to move to other oxide surfaces after TiO_2, such as MgO and Alumina, but no other oxide surfaces could be atomically resolved experimentally. This means that TiO_2 stands slightly alone and is the reason why this study moved to insulating surfaces in general rather than just focusing on oxides.

6.2 Introduction

Due to its many applications and their dependence on surface properties, TiO_2 is easily the most widely studied oxide surface in surface science. This popularity also makes it a very attractive candidate for comparing different and developing new experimental techniques. A comprehensive review of these techniques was undertaken by Henrich [133] in 1985, where the stoichiometric (110) 1×1 surface was established as the most stable. A section of this surface can be seen in figure 6.1.

This surface was more recently studied by surface X-ray diffraction [134], medium-energy back-scattering electron diffraction [135], STM [136, 137, 138], non-contact AFM [85] and a combination of both STM and NC-AFM techniques [28]. An example of a NC-AFM image of TiO_2 is given in figure 6.2. These experimental results are well supported by theoretical calculations of the surface structure and properties, using various techniques. Comprehensive surface atomistic calculations [139] confirmed the experimental stability predictions. Ramamoorthy *et al* [140, 141] investigated several surfaces using DFT + LDA and predicted surface stabilities which corresponded with experiment. More advanced calculations using DFT + GGA [142] and spin-polarized GGA [143] also support the experimentally found simple 1×1 unit cell, although all the theoretical calculations underestimate the large relaxation of the surface bridging oxygen predicted by surface X-ray diffraction [134]. Very recently Harrison *et al* [144] undertook a comprehensive theoretical study of the TiO_2 surface using DFT and discovered that the bridging oxygen on the (110) surface is very

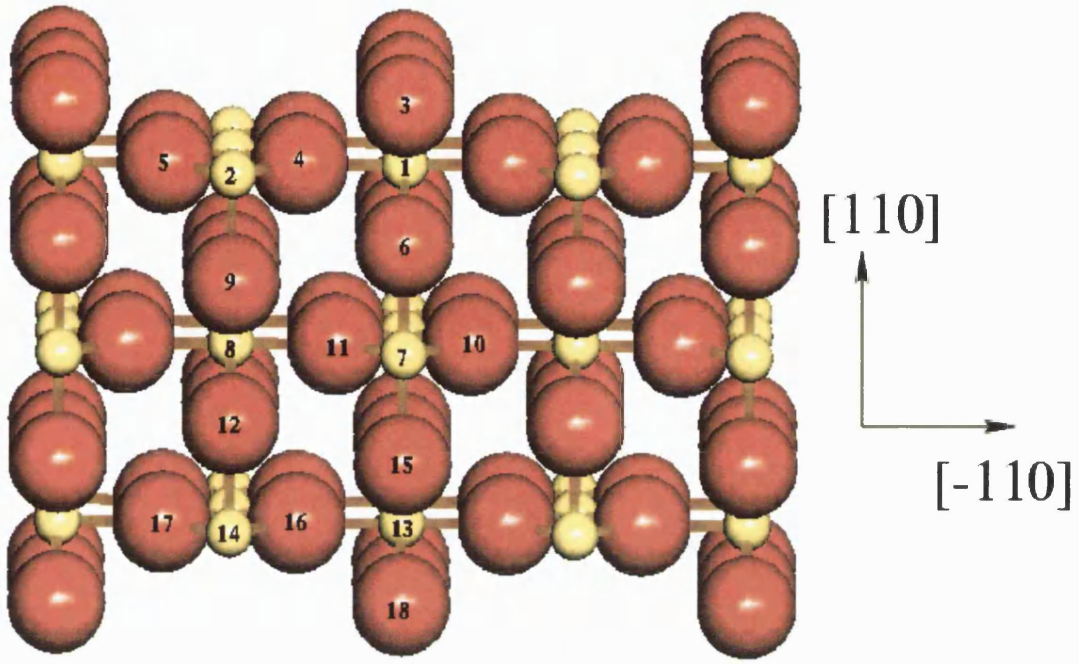

Figure 6.1: TiO_2 110 (1 × 1) Surface (Courtesy of J. Muscat)

soft with respect to displacements in the (110) direction. This means that at room temperature it vibrates along an axis perpendendicular to the surface plane by about 0.15 Å, and this must be accounted for in any comparison of experiment and theory.

Each of the probe microscopy studies came to the conclusion that they imaged the familiar 1×1 surface unit cell, though via different sub-lattices. The STM experiments use Tersoff-Hamann theory [14] as a model to understand the images they produce, hence, with positive bias, the electrons should tunnel into unoccupied surface states. Several theoretical studies [140, 141, 145] have shown that the fivefold coordinated titanium^{4+} ions are the source of the unoccupied states, and therefore STM images these Ti ions. Non-contact AFM does not have the luxury of a reliable model to identify the imaged ions, and therefore more specific analysis must be used for each case. Iwasawa [28] just makes the assumption that the imaged contrast is due to the physical corrugation of the surface, and that the protruding bridging oxygen rows are being imaged. Unfortunately the mechanism of contrast is not such a simple phenomenon. As discussed in chapter 4, contrast is due to an interplay of short-range microscopic forces and long-range macroscopic forces, and a simple argument based on physical corrugation cannot be used arbitrarily.

However, it is possible to investigate the nature of the image contrast indirectly by adsorbing ions to the surface. Iwasawa adsorbed formate anions onto the TiO_2 surface and then imaged them using STM. The adsorbed formate ions can interact primarily with the accessible Ti^{4+} cations. His images show clearly bright spots on the resolved titanium rows as expected. This adsorption-image process was also undertaken for non-contact AFM [146], and formate ions were observed as bright spots between bright rows with periodicity of about 0.65 nm, in contrast to the STM

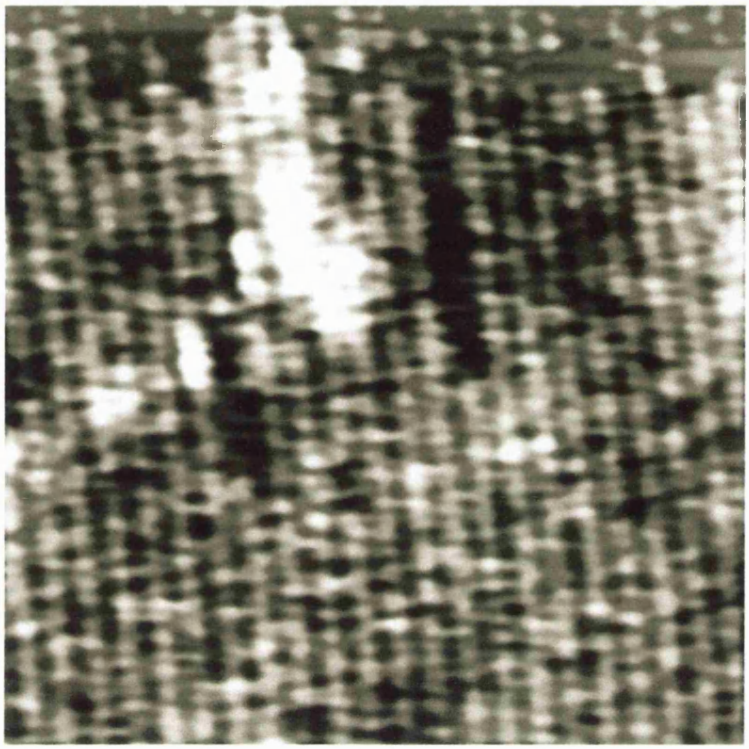

Figure 6.2: Experimental NC-AFM Image of (110) Surface of TiO_2. (Courtesy of H. Raza, Manchester University)

image. Fukui *et al* [146] argue that as it is clear that the formate ions are adsorbed onto the titanium ions and that STM images the Ti ions, non-contact AFM must therefore be imaging the bridging oxygen rows. However, the AFM image is very poor and the periodic rows are barely resolved. Again they assume that the observed contrast is due to the physical corrugation of the surface, yet the periodic rows are brighter than the formate ions even though the hydrogen of the formate extends a further 0.25 nm beyond the bridging oxygens. This confirms that contrast cannot be a measure of the surface's physical corrugation and a more thorough analysis of the interactions involved must be undertaken. Nevertheless, there is a strong case for the bridging oxygens as the source of contrast in NC-AFM images of the TiO_2 surface. Since, as yet, there are no other atomically resolved surfaces which have any evidence for imaged sub-lattice identity, the TiO_2 surface represents an excellent candidate for theoretical modelling.

6.3 Parameters for TiO_2 Interactions

The first stage of modelling any surface is to obtain a set of reliable parameters for the microscopic interactions (see chapter 4) of that surface with the tip. For TiO_2 this is a difficult task, as the few parameter sets around [147, 148, 149] are mainly optimized for the bulk properties of TiO_2. The one set, by Matsui *et al* [147], which has been optimized for surface properties has not been tested thoroughly. Since this is the only set of parameters which can be used reliably for surface calculations they have been used for all the atomistic calculations discussed in the next section.

However, it is the lack of testing of these parameters which motivated the following extensive *ab initio* study for the purpose of establishing their physical reliability.

6.3.1 *Ab Initio* Modelling of the TiO_2 Surface

Ab initio calculations of the TiO_2 surface were performed using the VASP code as discussed in section 3.2.1. Specifically, calculations were performed on bulk TiO_2 to converge the total energy of the system with respect to k-point sampling of the Brillouin zone and energy cut-off of the plane waves. The Monkhorst-Pack [56] k-point generation scheme was used and the total energy was converged to 0.1 meV with a 63 k-point $5 \times 5 \times 5$ mesh. The 6 atom bulk unit cell is equivalent to atoms 1-6 in fig. 6.1. This bulk cell was fully relaxed. A comparison of calculated and experimental bulk properties is shown in table 6.1.

Property (Å)	Calc.	Exp. [150]	Diff. (%)
Ti-O (flat)	2.00	1.98	1.1
Ti-O (bridge)	1.97	1.95	1.0
Volume ($Å^3$)	64.38	62.43	3.1
a	4.64	4.60	1.0
c	2.99	2.96	1.0
c/a	0.64	0.64	0.0

Table 6.1: Comparison of calculated and experimental bulk TiO_2 properties. a is the lattice constant in the (100) direction and c in the (001) direction.

The relaxed bulk unit cell from the fully converged calculation was then used to generate the surface unit cell.. The total energy of the surface was then converged with respect to the number of surface layers, k-points and the vacuum gap between the periodic slabs. 4 k-points ($(\pm 0.25, \pm 0.25, 0)$) converged the total energy to 0.1 meV. It was found that a 36 atom surface unit cell with 6 surface layers and a vacuum gap of 6 Å between slabs was sufficient, consistent with previous studies by Lindan *et al* [142]. This surface unit cell is equivalent to repeating atoms 1-12 in fig. 6.1 three times in the (110) direction. The relaxed surface geometry was taken from the final fully converged calculation and is used in all further discussion.

Table 6.2 gives a comparison of the surface relaxations in the x ($\bar{1}10$) and z (110) directions of atoms in the TiO_2 (110) surface taken from various sources. The atom number refers to the numbers in figure 6.1. GGA refers to calculations undertaken in this study using the VASP code. Muscat [151] refers to DFT + LDA calculations using a unit cell with eleven surface layers. MARVIN refers to calculations using atomistic simulation of the surface with the MARVIN code, as described in section 3.2.2 using the Matsui [147] parameters. The atomistic simulation uses the same surface unit cell as the VASP calculations. Finally, the experimental results are taken from surface x-ray diffraction data [134].

The first thing to note from this comparison, is that there is general agreement between the methods on the direction and magnitude of relaxations for atoms in the top surface layer (atoms 1 - 6). These atoms are the ones critical to NC-AFM imaging, so their properties must be reproduced well. Secondly, all the theoretical methods give a much smaller relaxation of the bridging oxygen (atom 3) than observed in experiment. As mentioned at the beginning of the chapter, this is due to the softness of the bridging oxygen to displacements perpendicular to the surface. This causes it

Atom	*Ab Initio*		Muscat		Atomistic		Experiment	
	x	z	x	z	x	z	x	z
1	0.01	0.19	0.0	0.23	0.0	0.07	0.0	0.12±0.05
2	0.01	-0.14	0.0	-0.17	0.0	-0.15	0.0	-0.16±0.05
3	0.02	-0.04	0.0	-0.02	0.0	-0.01	0.0	-0.27±0.08
4	-0.05	0.15	-0.05	0.13	-0.05	0.06	-0.16±0.08	0.05±0.05
5	0.06	0.14	0.05	0.13	0.05	0.06	0.16±0.08	0.05±0.05
6	0.0	0.0	0.0	0.02	0.0	-0.04	0.0	0.05±0.08
7	-0.01	-0.06	0.0	0.14	0.0	-0.05	0.0	0.07±0.04
8	-0.01	0.09	0.0	-0.10	0.0	0.05	0.0	-0.09±0.04
9	0.01	0.01	0.0	0.0	0.0	-0.04	0.0	0.0±0.08
10	-0.02	-0.01	0.03	0.03	0.0	0.01	-0.07±0.06	0.02±0.06
11	0.02	0.01	-0.03	0.03	0.0	0.01	0.07±0.06	0.02±0.06
12	0.0	0.02	0.0	-0.01	0.0	-0.03	0.0	-0.09±0.08

Table 6.2: Relaxations of the 110 TiO_2 surface calculated by (i) *Ab initio* - DFT using GGA (VASP), (ii) Muscat - DFT using LDA [151] and (iii) Atomistic - pair potentials (MARVIN). Experimental results taken from surface X-ray diffraction [134]. Atoms are numbered according to fig. 6.1.

to vibrate at room temperatures with an amplitude of about 0.15 Å, a process which is completely missing from the theoretical treatments. The calculations by Muscat are better than the other theoretical methods for atoms in the second layer, but this is as expected for a deeper unit cell. For the purposes of modelling NC-AFM, the extra expense of a deeper cell is unnecessary.

In terms of a direct comparison between the atomistic values produced by the MARVIN calculations and those produced by the DFT calculations, the agreement is good. The atomistic simulation using the Matsui [147] parameters produced relaxations of the surface ions in the same direction and to within around 0.1 Å of the values calculated with density functional theory. As a further test of the Matsui parameters, the electrostatic potential of the TiO_2 surface calculated with pair potentials and DFT was compared. Figure 6.3 shows that the form and the gradients of the potentials are very similar. In combination with the relaxation comparison above, this demonstrates that the Matsui parameters reproduce the interactions of the TiO_2 (110) surface important to modelling of the microscopic tip-surface interactions.

At this point we have a set of parameters which describes the interactions within the tip (see chapter 4) and the interactions within the surface, but nothing which describes the interaction between the tip and the surface. To get parameters for the interaction potentials between the surface and tip ions, it was assumed that the metal-metal ion interactions are purely coulombic and that the metal-oxygen interactions are the same for each metal (Ti and Mg) throughout the system. The geometric average of the C_6 parameters was derived for the interaction between oxygens in the tip and oxygens in the surface. Note that the oxygens in the tip and the oxygens in the surface are effectively treated as different atom types in the atomistic simulation.

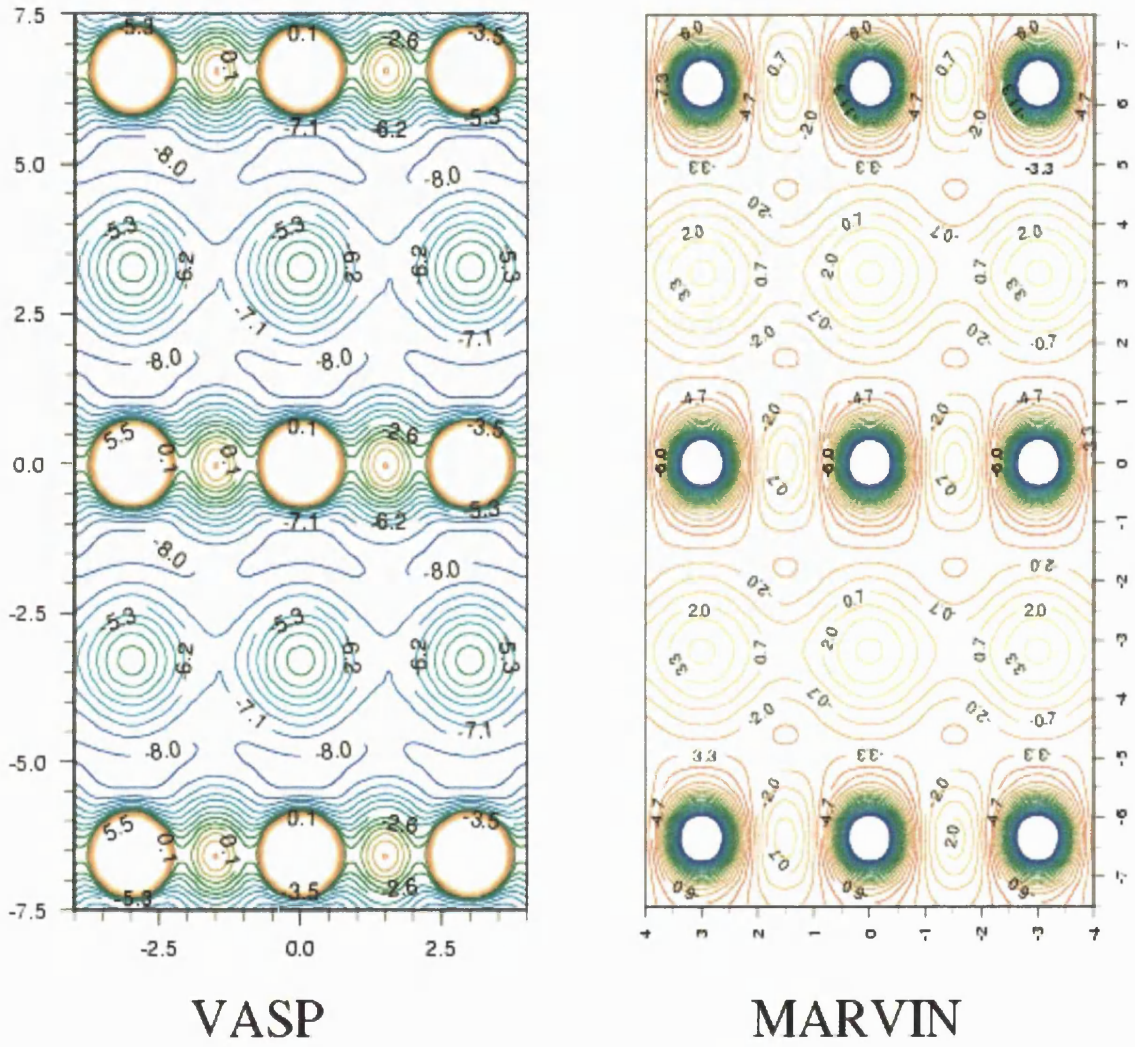

Figure 6.3: Electrostatic Potentials of the TiO_2 110 (1 × 1) Surface. Axes are in Å.

6.4 Method

6.4.1 Setup

The setup for the calculations is the same as in fig. 4.6, with the NaCl cluster replaced by the TiO_2 surface unit cell. Stoichiometric TiO_2 is a wide-gap semiconductor with large dielectric constant caused by soft phonon modes, hence the initial part of this study will focus on a thick insulating system. The only macroscopic force introduced at this stage of modelling of the TiO_2 surface was the van der Waals force. It is assumed that the thickness of the TiO_2 sample (order of mm) is large enough that there is effectively no interaction between the tip and conducting substrate and the image force is negligible. The van der Waals interaction between the macroscopic part of the tip and the surface was calculated using a model of a conical tip, as shown in figure 3.1, with $\gamma = 30^o$

and a sphere of radius R embedded at the end. The expression for calculating the force between this type of tip and a semi-infinite surface is as discussed in chapter 3. A Hamaker constant of 0.9085 eV [130] was used. The radius of the sphere is effectively an empirical parameter since there is no experimental data which gives the radius of the tip, although estimates of the radii are in the range 10 - 20 nm.

6.4.2 Generating an Interaction Map

To calculate an interaction 'map' across the surface, the relaxed total energy and tip-surface force of the system is calculated via atomistic simulation at different heights over the main features of the surface. Figure 6.4 shows the force curves through the surface points, it also clearly shows the repulsive interaction over the bridging oxygen (atom 3 in figure 6.1) and the attractive interaction over the 4-coordinated titanium ion (atom 2 in figure 6.1). The other curves fill the range between these two extremes, suggesting that each curve is due to composite interactions with the electrostatic potential from several ions.

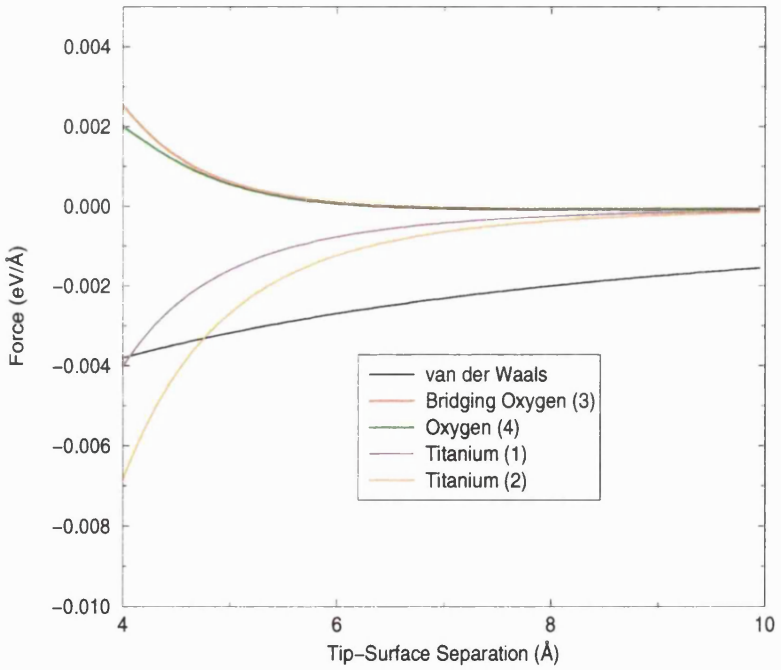

Figure 6.4: Force vs. Tip-Surface Separation for TiO_2 Surface. Numbers in the legend refer to atom numbers in fig. 6.1. The van der Waals force is uniform over all atoms.

These force curves were then fitted to an analytical curve, which for this system was of the form

$$F(x,y,z) = \frac{C_1}{z^2} + \frac{C_2}{z^4} + \frac{C_3}{z^7} + \frac{C_4}{z^{10}} + \frac{C_5}{z^{13}} \tag{6.1}$$

where z is the tip-surface separation and C_n are the fitting coefficients. For the TiO_2 surface, 17 height points, in the range 1.6 - 8.0 Å, at 26 surface points were required to cover all the possible scan features and directions, a total of 442 force points. Producing this many points with an *ab*

initio technique like DFT would be very time consuming, with pair potentials this many points can be calculated on a PC in a few days.

The atomic relaxations of the TiO_2 surface due to tip-proximity can be directly taken from the MARVIN simulation of tip-surface scanning. At tip-surface distances of around 3 Å the bridging oxygens are pushed into the surface by 0.24 Å and the surface oxygens by 0.08 Å. At the same separations the titanium ions jump to the tip, but at around a separation of 3.5 Å the 5-coordinated titaniums move out by 0.25 Å and the 6-coordinated by 0.1 Å. However, in section 6.5 we will see that a simulated image is produced by scanning the surface at distances greater than 4 Å. At this distance the atomic relaxations due to tip proximity are an order of magnitude smaller, nevertheless they can still have a significant effect on the surface electrostatic potential (see section 5.2).

6.5 Theoretical NC-AFM Image of TiO_2

Using the force map across the surface and the method described in chapter 4, the frequency of the cantilever oscillations for a given height above a given position on the surface can be calculated. At this point experimental parameters for the tip-cantilever setup must be included in the model.

The values of parameters describing the tip-cantilever used in modelling the TiO_2 surface are taken directly from an experimental NC-AFM study of the TiO_2 surface. The cantilever eigenfrequency, ω_0, was 280 kHz, the cantilever amplitude was 15 nm, the cantilever stiffness was 30 N/m and all calculations were performed at a frequency change of 40 Hz. γ_0 (see section 2.3) for these parameters is -7.87. The height of the cantilever above the surface at a given frequency change can then be calculated using linear interpolation. This cantilever deflection as a function of surface position is the **theoretical surface image**, although for the purposes of quantitative comparison with experiment it is more convenient to plot scanlines over the surface. Figure 6.5 shows scanlines across the TiO_2 surface with three different tip radii, each maximum corresponds to a 5-coordinated surface titanium and each minimum to a bridging oxygen. Note that the geometric nature of the scanlines is due to the limited number of surface points taken in the scanline direction. Increasing the number of points would produce a more realistic shape, but this is not important in the following discussion.

The most obvious result from this model is a definite prediction for the source of contrast in experimental NC-AFM images of the TiO_2 surface. The attractive interaction between the negatively charged oxygen on the tip apex and the positively charged surface titanium dominates the interactions. The scanline shows one periodic strongly attractive interaction and one periodic weaker attractive interaction at the 5-coordinated titanium and the bridging oxygen respectively. Note that the net force between the tip and surface is always *attractive* and the repulsive microscopic interaction between the bridging oxygens and the oxygen at the tip apex merely reduces the magnitude of the overall attractive interaction.

This also demonstrates that the potential from the 6-coordinated titaniums is screened by the potential from the bridging oxygens, and similarly the potential from the surface oxygens is screened by the 5-coordinated titanium ions. The contrast of the scanlines decreases as the effective macroscopic radius of the tip is increased. It is about 0.8 Å for a radius of 350 Å, 0.5 Å for 400 Å and 0.25 Å for 450 Å. This decrease in contrast is due to the increase in van der

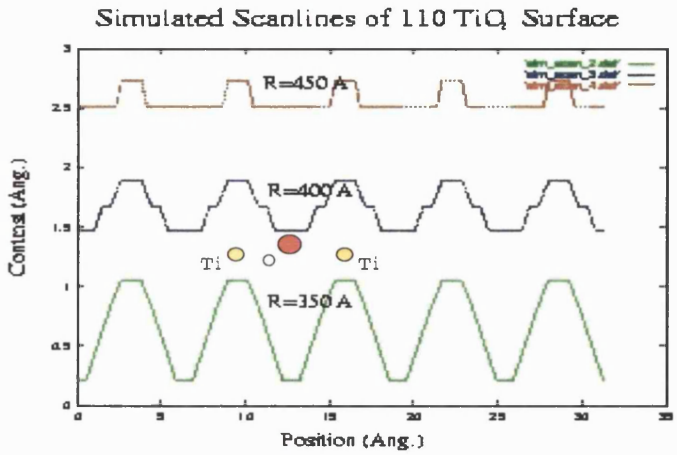

Figure 6.5: Simulated scanlines taken across the TiO_2 (110) surface in the (-110) direction with different macroscopic tip radii (R). The tip-surface separation of the scanlines is scaled so that zero on the contrast scale represents a tip-surface separation of 4 Å.

Waals attraction as the tip radius is increased. The general increase in attractive force means that there is larger frequency changes for a given height about the surface, hence for constant frequency change the tip will scan further from the surface for larger tip radii. At these larger distances the microscopic forces from the ions are weaker, and therefore contrast is lower. It should be noted that these scanlines are produced at tip-surface separations of greater than 4 Å, and at these distances surface ionic relaxation is very small as discussed previously. This means that surface relaxation due to tip proximity does not play a large role, but the enhancement effect described in section 5.2 will cause even small relaxations to produce extended electrostatic potentials.

Experimental scanlines produced using the same parameters gave an average contrast over a large section of surface of 0.6 - 0.8 Å, matching predictions from this model for the 350 Å tip radius. Experiments also show that contrast decreases as the scanning height above the surface is increased.

However, experimental opinion strongly supports the bridging oxygens as the source of contrast in images of the TiO_2 surface. As discussed at the beginning of this chapter, even though the evidence supporting this assertion is not perfect, it cannot be ignored and suggests that there is some factor which plays a significant role in contrast formation which has been neglected in this theoretical treatment of the TiO_2 surface. One possible explanation is that a real NC-AFM is not terminated by a anion, but by a cation such as the hydrogen of an adsorbed hydroxyl group. However, experiments have been performed where the tip-surface system is dosed with oxygen and this has no effect on the resultant images, suggesting that the tip is well oxidized after preparation, as the model assumes. In light of this it seems more practical to focus on properties of the tip-surface system which are well defined and try to understand what interactions should be present.

6.6 Role of Image Forces in NC-AFM Imaging of TiO_2

In the previous modelling of TiO_2 it was assumed that the thickness of the sample was large enough to neglect the interaction between the tip and conducting substrate. This would be an entirely fair assumption if TiO_2 was an ideal wide gap (3.1 eV) semi-conductor. However, the real surface is always non-stoichiometric and the oxygen vacancies trap electrons making the surface even more conducting [143]. As discussed in chapter 3, for conducting materials it becomes important to model their polarization by charges in the system. The effect of the conductivity of the TiO_2 surface in NC-AFM imaging can be represented approximately by moving the metal substrate (see fig. 4.6) much closer to the surface. This effectively produces a thin film of TiO_2 on top of a conducting substrate and should give some indication of the role of conductivity in imaging.

6.6.1 Setup

The setup remains exactly as described in the first part of this chapter, but now the metal substrate is placed at 0.25 nm from the bottom of the TiO_2 surface unit cell, as opposed to being effectively at infinity. The image force is calculated non-self-consistently using the approximation discussed in section 5.3, so that atoms do not relax with respect to image forces. The parameters for the cantilever oscillations are the same as previously, but now the tip has a radius of only 100 Å. This radius was chosen so that the scanline produced with image forces included is at about the same minimum distance range as the previous scanlines without image forces i.e. 4 - 6 Å.

6.6.2 Simulated Scanline

Fig. 6.6 shows a simulated scanline across the bridging oxygen rows of the surface using the modified setup and an oxygen terminated nano-tip. Note again that the rather unusual shapes of the features in the scanlines is due to the limited number points used in the scanline direction, but this does not affect the following discussion. The contrast over the surface has now reversed in comparison with fig. 6.5, it is dominated by the *image force* interaction between the tip and the bridging oxygens. Contrast over the oxygens is about 8 Å, an order of magnitude larger than in the previous scanlines where the contrast maximum was over the titanium ions. This increase in contrast is despite the fact that the tip is scanning further from the surface (in terms of minimum tip-surface separation), than for the 350 Å radius tip without image forces (5.3 Å compared to 4.2 Å). Fig. 6.5 shows that contrast due to microscopic forces should decrease as tip-surface separation increases, but the large contrast seen in fig. 6.6 at a greater tip-surface separation demonstrates the dominance of image force in the contrast. This dominance is due to the protrusion of the highly charged O^{2-} ions above the surface, their image in the conducting tip is also mirrored in the, now proximate, metal substrate, producing a very strong image force. The position of the bridging oxygens above the surface means that there is no compensation from an oppositely charged ion at the same height, as there is for the titanium ions in the surface. This uncompensated interaction produces the strong contrast seen in fig. 6.6. The effect is similar to that seen in the charged step in section 5.3.

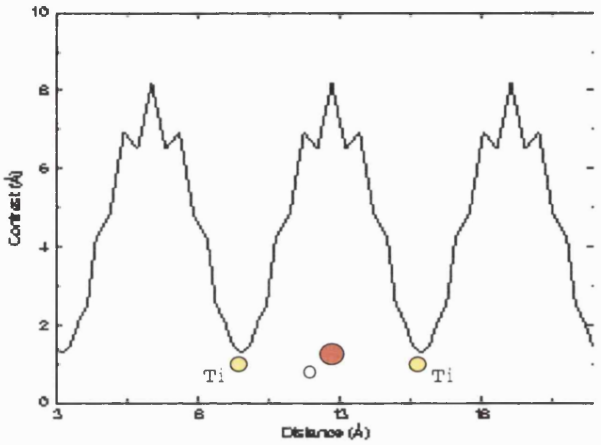

Figure 6.6: Simulated scanlines taken across the TiO_2 (110) surface in the (-110) direction with polarization of surface included. The tip-surface separation of the scanlines is scaled so that zero on the contrast scale represents a tip-surface separation of 4 Å.

6.7 TiO_2 Conclusions

Figure 6.5 shows that this model, given parameters from experiment, reproduces the magnitude of the contrast found in that experiment. This is the only useful indicator that the assumptions made to calculate this model are well justified, and it also allows us to make predictions based on the results from this model. The scanlines predict that the correct contrast is produced at tip-surface distances of 4-5 Å, and at these distances relaxation of the surface ions is negligible and has very little effect on the electrostatic properties of the surface. There is also no possibility of ions jumping from the surface to the tip, or vice versa. This means that the mechanism of contrast in NC-AFM of the TiO_2 surface is dominated by the electrostatic interaction, and unsurprisingly the contrast is produced by the strong attraction between the positive surface Ti ions and the negative O ion at the tip.

The conductivity of the TiO_2 surface has been demonstrated to have a significant effect on the tip-surface interaction. The introduction of the metal substrate close to the surface to model the conductivity demonstrates that the bridging oxygens could be responsible for contrast if the image force is a significant interaction. However, the contrast predicted in this setup is much larger then seen in experiment, suggesting that the conductivity is being overestimated or image force is not involved. In principle by changing the macroscopic radius of the tip and the distance of the metal substrate below the surface, the ratio of van der Waals and image force could be changed until the contrast over the oxygen ions matches experiment. However, this is clearly a very unscientific way to approach interpretation of NC-AFM images of TiO_2. A more thorough analysis requires several more pieces of experimental data. Firstly, a comparison of theoretical and experimental force vs. distance curves over the TiO_2 surface would establish directly the ratio of van der Waals and image forces in the system. Data on the conductivity of the surface of TiO_2 could be used to check any conclusions on the role of image forces. Finally, a systematic theoretical and experimental analysis of adsorption on TiO_2 could conclusively establish the source of contrast in images of TiO_2. In the absence of these key experimental data, it is difficult to proceed further in understanding of

NC-AFM imaging of TiO_2.

Chapter 7

Sodium Chloride on Copper

7.1 Original Motivation

Our collaboration with the group of Ernst Meyer in Basel led to many discussions of the best way to move forward with imaging of insulators in NC-AFM. Since they had already imaged bulk NaCl in atomic resolution, we suggested they try to repeat the study on thin films of NaCl on a metal substrate. This would allow imaging of many low-coordinated sites and also see whether the interaction with the metal substrate would affect the results. When they achieved this, we undertook to try and interpret the features in their images with theoretical modelling.

7.2 Introduction

Although many different classes of surfaces have been imaged in atomic resolution [30, 31], preparation of bulk insulating surfaces still remains difficult and very few examples have been imaged in atomic resolution. These problems prompted several successful studies of thin insulating films grown on conducting substrates [17, 152, 153]. These systems are free from charging problems and allow, in principle, a much better control of the surface chemical structure. However, the film structure depends on the substrate and conditions of growth [152], and the film surface is not generally representative of the surface of a bulk sample of the same material [132]. This, nevertheless, does not make these studies less interesting because by choosing growth and imaging conditions one can focus on different aspects, such as growth mode [153], atomistic structure of films [32], and the mechanisms of growth nucleation [154]. Each of these aspects is of great importance for understanding of the structure and properties of metal-insulator interfaces, mechanisms of film growth, and conditions of NC-AFM imaging of insulators and insulating films on metals with atomic resolution. The prevalence of low-coordinated sites, such as steps, corners and kinks on these thin films makes them of special interest for catalytic studies and NC-AFM offers the possibility of imaging these features in atomic resolution.

Following this approach, properties of NaCl films grown on the Cu (111) surface have recently been studied using a combination of low-energy electron diffraction (LEED) and NC-AFM. Growth modes, orientation and lattice constants of ultrathin films were revealed [155] and atomic resolution at step edges was demonstrated [32]. In this chapter very recent experimental NC-AFM data

produced by R. Bennewitz from Basel University is discussed, this demonstrates high quality atomically resolved images of thin NaCl films on Cu(111). These images show many interesting features which can be modelled theoretically to try and gain more understanding of the mechanisms involved in imaging. By combining experimental data with theoretical modelling, the nature of enhanced contrast observed at step edges and kink sites can be explained. The thickness of the NaCl film can also be estimated by studying the contributions to the tip-surface interaction in the theoretical model.

7.3 Experimental Setup

The experimental data was produced using a NC-AFM, as discussed in chapter 2. The instrument used in this study is a home-built multi-functional ultra-high vacuum scanning force microscope [19]. Oscillation frequency and amplitude, and tip-sample distance are controlled by a fully digitized device [156]. The experiments were performed using a single crystal rectangular silicon cantilever with a spring constant of 26 N/m and a resonance frequency of 158271 Hz. An oscillation amplitude of 1.8 nm was kept fixed during the experiments. The frequency shift was set to $\triangle f$ = -128 Hz while recording topography images. The pyramidal silicon tip carried a native oxide layer. Before recording the images, the tip was several times in contact with the NaCl/Cu(111) sample thereby locally destroying the film. For these reasons the chemical composition of the tip apex is not known exactly. However, it is most probably oxidized silicon possibly with traces of NaCl. The copper substrate exhibits 50-250 nm large atomically flat terraces with single sulphur impurities as only significant contamination. Ultrathin films of NaCl on a clean Cu(111) substrate have been prepared by evaporation of NaCl from a Knudsen cell onto the clean Cu(111) surface. The procedure as well as the growth modes of this system have been described in a recent publication [155].

In NC-AFM experiments the amplitude of the cantilever is kept constant by applying an excitation voltage with an amplitude A_{exc}. Any energy dissipation in the course of the tip-sample interaction, which damps the cantilever oscillation, results in an increase of A_{exc}, therefore, A_{exc} is often referred to as a damping signal. A spatially resolved image of damping of the cantilever oscillation can be measured by recording this damping signal. The excitation amplitude A_{exc} which is needed to compensate the damping should, in principle, be related directly to the dissipated energy. In spite of recent efforts [157, 158, 159, 160, 161, 162, 163] quantitative understanding of A_{exc} measurements is not straightforward due to both technical problems and the absence of clear understanding of the dissipation mechanism.

7.4 Experimental Results

The NC-AFM images presented in fig. 7.1 show a NaCl island on Cu(111) with rectangularly oriented edges. The NaCl has a higher contrast than the Cu substrate, and island edges have a higher contrast compared to the terrace and show an atomically resolved corrugation. In the topography image, the kink sites stick out even more than normal edge sites. The bright dots which appear on the copper substrate are most probably single sulphur impurity atoms.

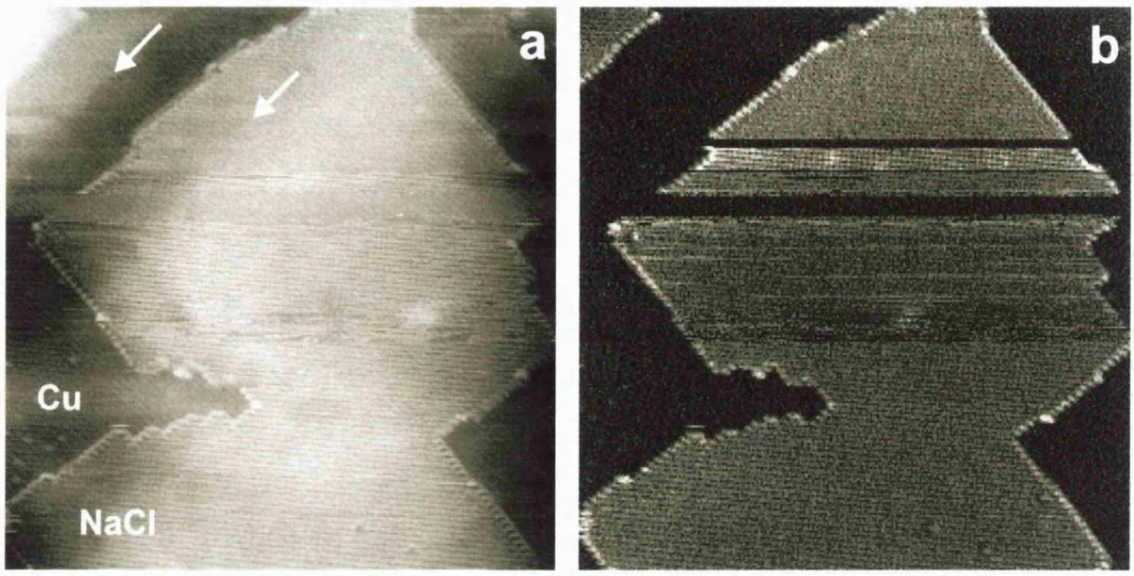

Figure 7.1: (a) Topography and (b) A_{exc} images of a NaCl island on Cu(111). Image size 35×35 nm. The two arrows indicate a weak shadow effect in the topography which is characteristic of a double tip. Note that the double tip does not affect the A_{exc} image.

All images which showed periodicity on the atomic scale were analyzed by means of Fourier analysis. In all cases, a fourfold symmetry was found with a nearest neighbour distance varying between about 0.36 and 0.42 nm. This scattering can be attributed to mechanical and thermal drift of the piezo actuators, as well as to non-linearities in the piezo characteristic when scanning with some offset from the relaxed position. The expected distance between nearest neighbour sodium or chlorine ions in NaCl is about 0.4 nm. Based on this distance correspondence and on the shape of NaCl islands, it is probable that the (001) NaCl surface is exposed. This conclusion is supported by the LEED spectra measured on these islands [155]. However, only one type of lattice site is imaged as a protrusion in NC-AFM, which is confirmed by the modelling presented below. Similar results have been obtained on other binary compounds [39, 17, 164].

Fig. 7.2 shows magnified topographic (a) and A_{exc} (b) images of an area which has been chosen for further discussions. The individually imaged kink sites demonstrate the resolution of NC-AFM. It is impossible to tell whether the maxima in observed contrast really correspond to average positions of the Na or Cl. The kink and corner sites which terminate the island exhibit several characteristic shapes. Since both cation or anion terminated kink sites may occur in the course of the NaCl island growth, such characteristic shapes may act as fingerprints for the identification of kink site types.

Several instabilities in the tip constitution were detected. These show up as contrast changes in the topography, but do not prevent stable regulation of the tip-sample distance. For example, during repeated scanning of the area mapped in fig. 7.2, a tip change occurred which is documented in fig. 7.3. When passing the kink site in the lower left part of the frame, the tip changed resulting in significant change in the contrast in the topography image and contrast enhancement in the A_{exc} image. After scanning 2/3 of the image, the tip again changed its composition and at this time the original contrast in both signals was re-established. Although the characteristic shape

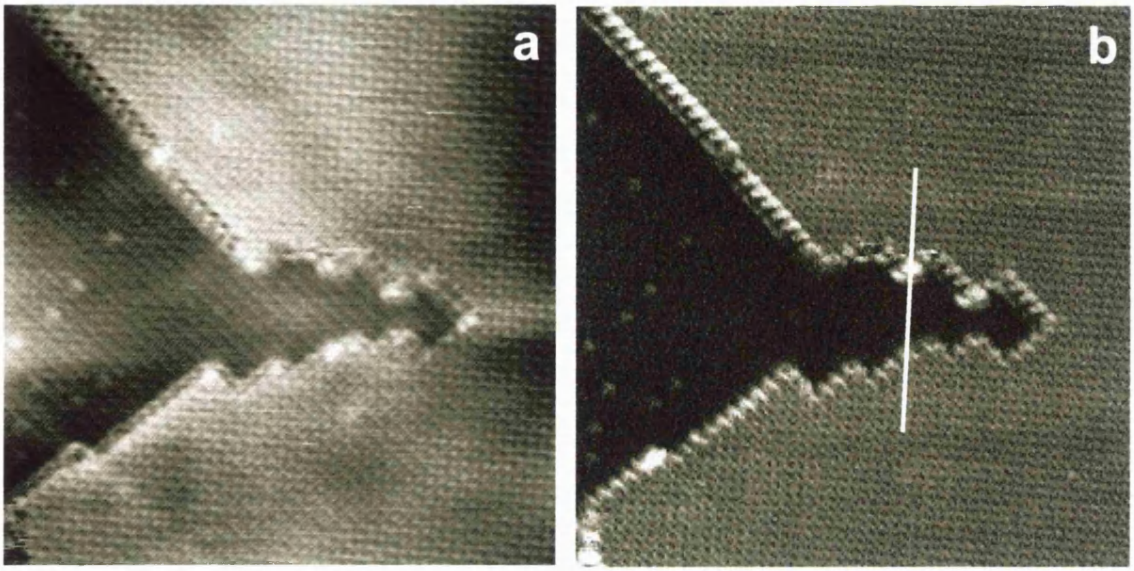

Figure 7.2: (a) Enlarged topography and (b) A_{exc} images of the area mapped in fig.7.1. Image size 18×18 nm.

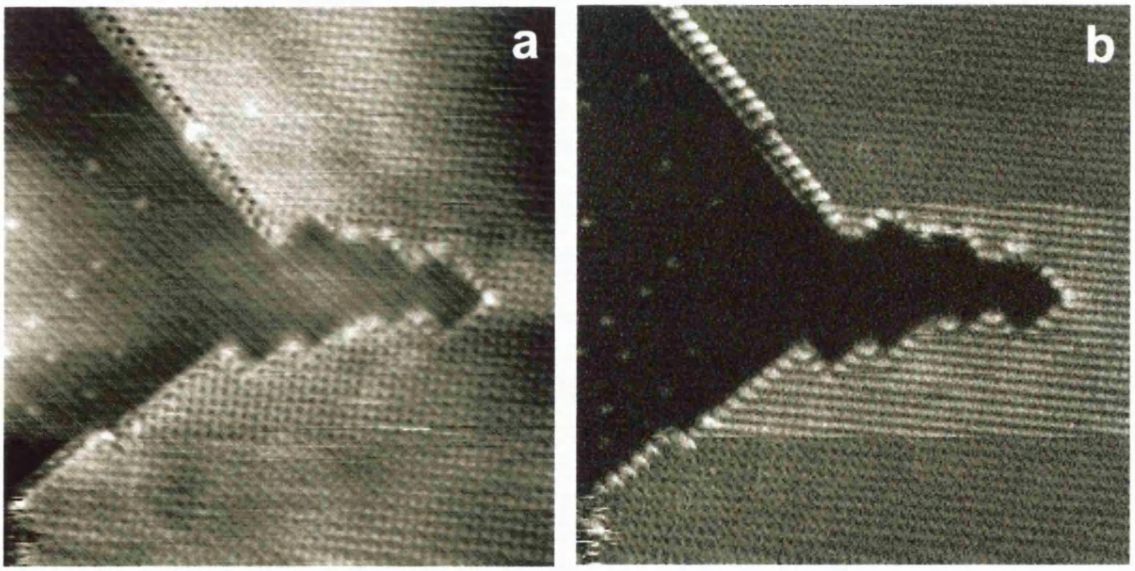

Figure 7.3: (a) Topography and (b) A_{exc} images of a NaCl island on Cu(111). The tip changes after 1/4 of the scan, thereby changing the contrast in topography and increasing the contrast in A_{exc}. After 2/3 of the scan, the contrast from the lower part of the images is reproduced indicating that the tip change was reversible. Image size 18×18 nm.

of the different kink sites was affected by the tip change, each type of the kink site retained a distinguishing appearance.

The average height difference between the Cu substrate and the top of the NaCl island in the NC-AFM images is around 0.07 nm, which is unrealistically small for a distance between an adsorbed NaCl layer and Cu surface. In fact, NC-AFM does not yield real thickness of adsorbed clusters or layers if adsorbed and substrate materials are significantly different, e.g. NaCl on

Cu. This is due to the fact that NC-AFM probes the forcefield, which is very different for ionic materials and metals. Therefore, for given parameters of the cantilever oscillations and frequency change, NC-AFM may record a substrate image at a similar 'height' as that of the adsorbed layer. This means that the detected change in the equilibrium cantilever position as the tip passes over the NaCl cluster edge does not directly reflect the step height [165]. It can correspond to the real height only on a similar substrate.

To further illustrate this point, in fig. 7.4 a topography image of a NaCl island on top of a NaCl terrace [165] is shown. This image was obtained using a different cantilever and a frequency shift of -35 Hz at a cantilever eigenfrequency of 156330 Hz, a spring constant of 24 N/m, and an oscillation amplitude of 2.3 nm. In contrast to the results presented above, the material of the upper and lower terrace in this image is NaCl, and the observed step height is close to the expected value of 0.28 nm. This is seen in the image cross-section shown in fig. 7.4. It exhibits corrugation on the atomic scale on both the upper and lower terraces. In the section over the step sites the corrugation is significantly enlarged, the highest protrusion corresponds to the kink site.

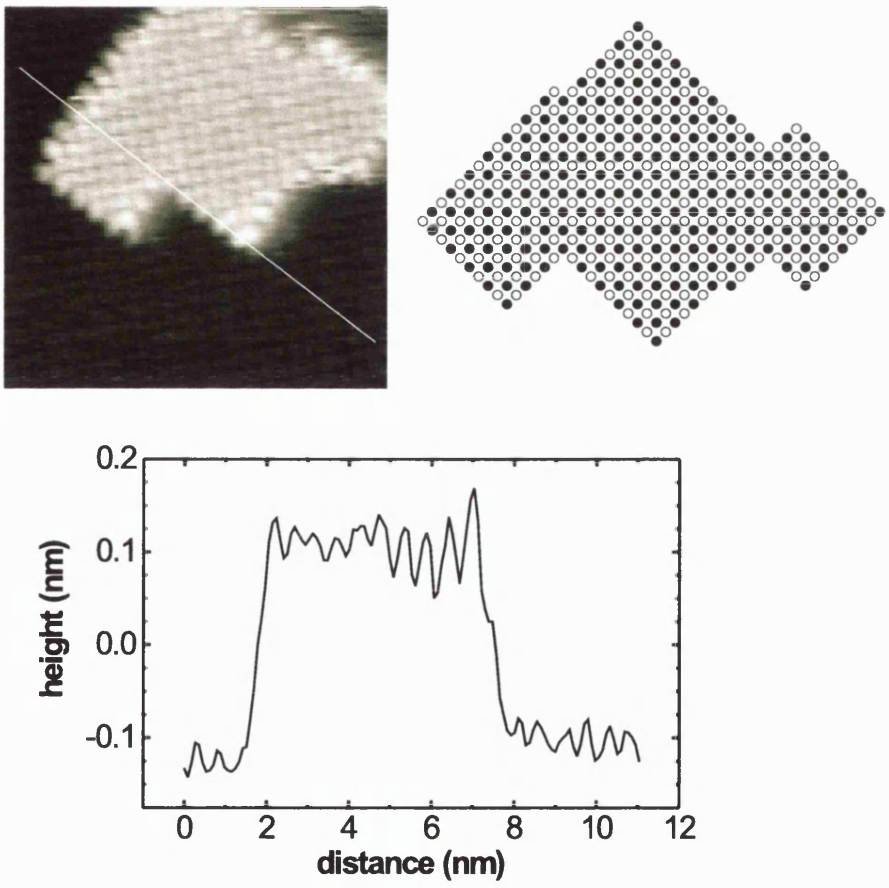

Figure 7.4: Topography image of a monatomic NaCl island, lying on a thin NaCl film grown on Cu(111) (from [165]). The atomic composition of this island is given in the schematic drawing, and a cross section along the indicated line is plotted below. Height in this and subsequent figures represents an arbitrarily shifted measure of contrast, and has no relevance to tip-surface separation.

There is a qualitative agreement between the characteristic features of NC-AFM images of NaCl islands in figs. 7.2, 7.3, and 7.4: island edges in these images look 'brighter' than their inner parts and kink sites seem to be even brighter than edges. This is in spite of the fact that the image in fig. 7.4 has been recorded using a different tip, on a thicker NaCl film, and with a previous version of the instrument. The protrusion of step and kink sites is found to be characteristic rather for NaCl step edges than for the underlying substrate. The observed differences in the corrugation height and in the relative extension and appearance of step and kink sites can be attributed to different tip atomic structures. The dependence of contrast on tip structure has been clearly demonstrated in fig. 7.3.

To characterise the irregular sites of the NaCl film, cross sections of the three-dimensional data represented in experimental images have been analyzed. Fig. 7.5a is another image of the area mapped before. The two parallel cross-sections along the (100) direction across the steps (M and N) are plotted in fig. 7.5b. Two sections M and N were taken through two parallel rows of atoms separated by the nearest neighbour distance which is about 0.28 nm. Section M crosses the step-edge at a site imaged as bright, whereas section N crosses over a site seen as dark. Two different images are compared, the one presented in fig. 7.5a and the one presented in fig. 7.3a where the contrast is significantly improved after the tip change. Sections M and N are made through the same geometric sites in both images. They are aligned in such a way that zero on the abscissa corresponds to the geometrical edge of the NaCl island indicated by the arrow in fig. 7.5a. In spite of the difference in the tip structure the two cross-sections exhibit similar features. The atomic corrugation on the terrace in the image shown in fig. 7.5a. is found to be around 0.015 nm, while the step site in section M protrudes by about one third of the corrugation height. The image shown in fig. 7.3a exhibits a more regular and stronger corrugation which demonstrates only marginal increase at the step. In contrast, the section N exhibits a characteristic dip at the step site in both images.

The three cross sections L shown in fig. 7.5c run along the (110) direction across the same kink site (shown in fig. 7.5a) and are taken from three different images shown in figs. 7.2, 7.3, and 7.5. The image corrugation on the terrace does not differ significantly from that along the (100) direction. This demonstrates the reproducibility of the data even after the tip change in fig. 7.3. These cross-sections across the kink site exhibit wide peaks which have corrugation about three times that on the terrace.

Similar analysis can be made for the damping signal. In fig. 7.6 a cross-section through the A_{exc} data mapped in fig. 7.2b is presented. As indicated in this figure the section runs over two different kink sites. The zero point of the A_{exc} axis has been arbitrarily set to the value measured on the copper substrate. It should be noted that each ion site is imaged by a series of about 3300 oscillation cycles and that the time constant of the amplitude regulator corresponds to about 300 cycles. Therefore, the measurement of A_{exc} averages over hundreds of oscillation cycles but allows detection of variations on the atomic scale. In attempt to establish a direct spatial correspondence between the two signals, the match between topography and A_{exc} on different images and along different directions has been studied. Sometimes topography and A_{exc} are in phase, sometimes shifted a little bit to each other, and in some cases A_{exc} has a minimum where topography has a maximum. One explanation of this behaviour can be that the local contrast formation on the atomic scale depends so much on the atomic tip structure that even the spatial correlation between

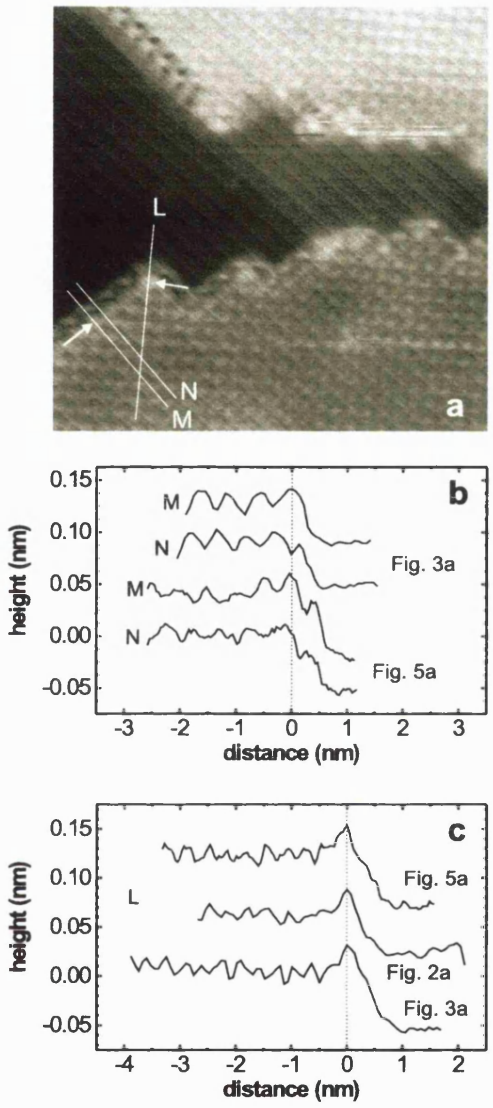

Figure 7.5: (a) Topography image of a detail of the area mapped in fig.7.2. The lines mark the cross sections plotted in (b) and (c), the arrows indicate the distance zero in those cross sections. (b) Parallel cross sections across a step. Section M intersects the step at a protrusion, section N in between two protrusions. Note that both sections run along protrusions on the terrace. The sections are taken from different images as indicated. (c) Three cross sections from different images along the same line L cutting a kink site.

A_{exc} and topography is affected by tip changes.

Finally, it should be noted that although the features in the topography and in the A_{exc} image are quite similar, there are differences which allow some conclusions about the respective imaging mechanism. First, the characteristic appearance of the NaCl island edges running to the upper right differ from that of edges running to the upper left in both figs. 7.2 and 7.3. This difference can be attributed to asymmetry in the atomic shape of the tip apex. The step image is essentially a convolution of the tip apex and the step edge and with the tip being not a perfect pyramid

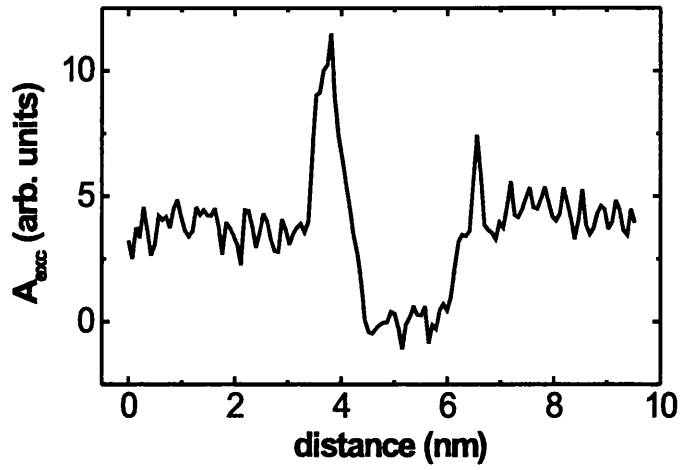

Figure 7.6: Cross-sections from fig. 7.2. A_{exc} given in arbitrary voltage units. The variation of A_{exc} in this cross-section corresponds to a power loss which is of the same order of magnitude as the power loss due to internal friction in the cantilever i.e. 70 meV per oscillation cycle.

but an asymmetric cluster, steps running in different directions will be imaged as having slightly different shapes. Secondly, in the upper right corner of fig. 7.1a one can notice a weak shadow of the island edge which indicates that a double tip was being used, whereby the weak shadow is produced by a tip apex which is less protruding than the one giving best contrast. The distance to the second tip is about 5 nm. Fig.7.1b does not show a corresponding shadow indicating that the double tip does not affect the A_{exc} image. Furthermore, atomic-scale changes of the tip during scanning have a dramatic influence on the contrast of the A_{exc} signal, while stable imaging of the topography is still possible. This suggests that the A_{exc} contrast could be formed by a shorter range interaction than topography. It is also substantially dependent on the composition of the absolute tip apex. The higher quality of A_{exc} images is also owed to the fact that A_{exc} is a measured but not regulated quantity in contrast to the topography signal, which is subject to instrumental drift and regulation noise.

To summarise, the NC-AFM images of NaCl islands demonstrate enhanced tip-surface interaction with step edges and kinks. The image features cannot be directly attributed to Na or Cl ions, the thickness of the NaCl island is impossible to measure with NC-AFM, and the contrast in both topographic and A_{exc} images strongly depends on atomic composition of the end of the tip.

7.5 Theoretical Model

The model used in this study is based on that described in chapter 4 and chapter 5, and only those features which are unique to modelling NaCl will be discussed in detail. Initially the theoretical model assumes that the force can be split into three general components depending on the specific tip/surface combination studied: (i) the *microscopic* chemical force between atoms in the tip and surface, which includes the van der Waals force between ions (ii) the *macroscopic* van der

Waals force between the tip and surface and (iii) bias in the system and image forces due to polarization of conducting materials. It is important to emphasize that this means that the background macroscopic force is composed of the Van der Waals force and image force only.

7.5.1 Theoretical Setup

A schematic diagram of the tip and surface setup used in the calculations is shown in fig. 7.7. Note that this is effectively the same as the setup shown in fig. 4.6, but the 'pyramid' blocks have been added to help clarify some of the discussion presented later in this section. The doped Si tip has a pyramid-like shape at the macroscopic scale with a sphere of effective radius of 10 nm at the end. It is very likely to be contaminated by exposure to air and to be coated by an oxide layer of unknown thickness, therefore its conduction properties are unknown. The temporary change in contrast in fig. 7.3, the dependence of the step image on the scan direction in figs. 7.2, 7.5 and the possibility of a double tip discussed above reinforces the idea discussed previously that there is some sort of nano-asperity at the bottom of the tip which can be contaminated by surface and ambient ions.

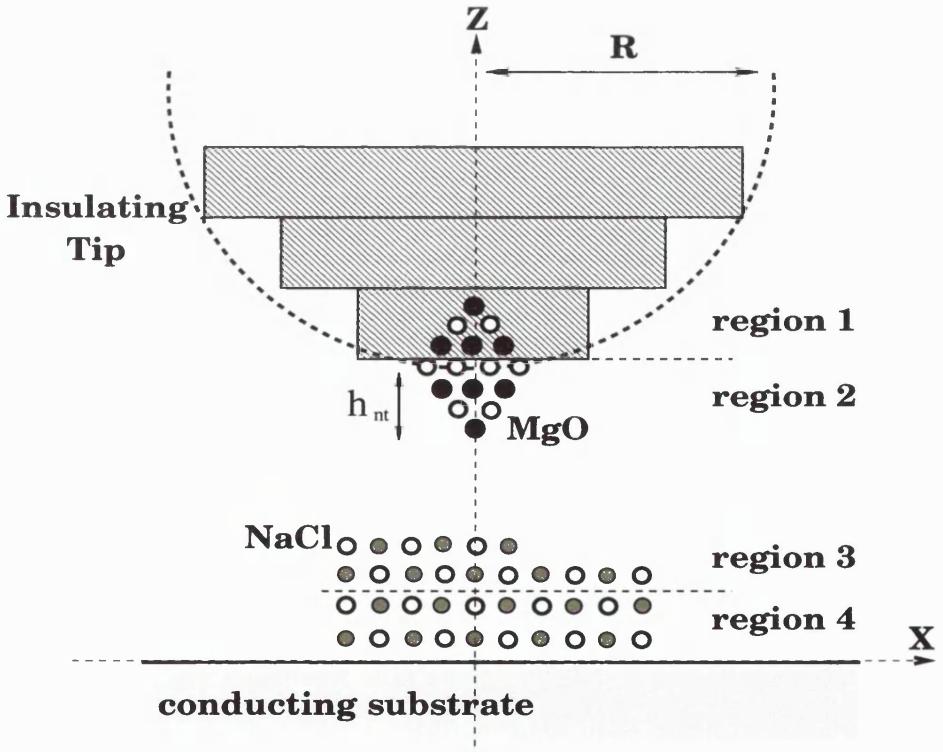

Figure 7.7: Schematic picture of the model used here to simulate the interaction between the tip and the sample. R is the effective radius of the macroscopic tip and h_{nt} is the protrusion of the nano-tip below the macroscopic tip.

To model this nano-asperity a 64-atom MgO cube was used as a 'nano-tip' embedded into the macroscopic tip (see chapter 4). The difference in imaging of opposite step-edges observed in fig. 7.2, can be reproduced by re-orienting the tip so that, for example, one cube edge is nearer to the

surface than the others. However, this z-symmetry tip orientation will reproduce the significant interactions involved in imaging effectively.

In the scanlines shown in the next section the macroscopic force is included by calculating the image force and macroscopic van der Waals, and then adding them to the microscopic force as a function of tip-surface distance to give the total force, as discussed in chapter 3.

7.5.2 Microscopic Forces

The interaction between ions in regions 1 - 4 in fig. 7.7 were calculated using a static atomistic simulation technique and the MARVIN code, as discussed in section 3.2.1. The nano-tip and the NaCl film are each divided into two regions, I and II. In terms of fig. 7.7, region I consists of region 2 and the top two layers of the film (region 3), and region II consists of region 1 and the remaining bottom two layers of the film (region 4). The region I ions are relaxed explicitly, whilst the region II ions are kept fixed. The region II ions represent the interface of the nano-tip with the macroscopic tip and the interface of the film with the Cu substrate, neither of which are included atomistically in the model.

7.6 Theoretical Results

7.6.1 Tip Structure and Film Thickness

To further quantify the theoretical model, the experimentally observed frequency shift can be used to predict the material of the macroscopic tip and estimate the thickness of the NaCl island. By running the model initially with only the chemical interactions between the oxide nano-tip and the island, an additional -0.05 eV/Å background attractive force was found to be needed at characteristic scanning height (h_{sc}~0.47 nm) to reproduce the 128 Hz frequency change observed in experiment. This number can be used to infer the material of the macroscopic tip and the film thickness by directly calculating the macroscopic and image interactions for different possible setups. Fig. 7.1 can be used to estimate the size of the NaCl island on the Cu substrate. For mono-layer coverage it contains about 6000 atoms. The van der Waals and image interaction between the tip and NaCl island/Cu substrate can then be calculated based on this estimate. In these calculations only the macroscopic part of the tip is considered. This is positioned at h_{sc} + h_{nt} from the surface, where h_{nt} is the protrusion of the nano-tip (see fig. 7.7).

To calculate the van der Waals interaction of the tip with the NaCl island, a "pyramid" of square blocks placed on top of each other as shown in fig. 7.7 was used to represent the observed shape of the tip. This was necessary so that the van der Waals interaction between the macroscopic tip and the island can be calculated atomistically. The approximation used in chapter 3 for the van der Waals has no atomistic contribution and the island thickness could not be estimated. Each block of the pyramid consists of atoms arranged in a cubic lattice with a lattice constant of 0.21 nm. The van der Waals interaction is calculated by direct summation of dispersion interactions (C_6/r^6) between the atoms in the blocks and the ions in the NaCl island. The number of square blocks needed in our atomistic calculations to converge the van der Waals interaction was first calculated. This was done by simulating the macroscopic pyramid shape with layers of increasing size. The size of the blocks was chosen to represent the observed effective tip radius of 10 nm. We

found that 3 square slabs (approx. 90,000 atoms) of widths 4 nm, 8 nm and 12 nm, and each of depth 2 nm place on top of each other converged the van der Waals interaction.

In this setup the contribution of the metal substrate to the van der Waals force is negligible [67]. Insulating and conducting tips were modelled by using different dispersion coefficients (C_6). For an insulating/oxidized tip C_6 parameters for MgO-NaCl [117] interactions were used, and for conducting tip parameters for W-NaCl [166] interactions were used. The results are shown in Table 7.1.

Tip Type	NaCl Layers	Force (eV/Å)
Insulator	1	-0.052
	2	-0.074
Conductor	1	-0.138
	2	-0.195

Table 7.1: Comparison of NaCl island contribution to van der Waals force

If these values are compared with the background attractive force needed in the model (-0.05 eV/Å) to reproduce experimental frequency shifts, it is clear that this interaction can provide all of it. In fact this shows that the macroscopic tip is effectively an insulator and that the NaCl island cannot be more than 1 or 2 layers thick or the background force becomes much too large. If this is compared with the image interaction, it is found that for an insulating tip the image force between tip and island/substrate would be less than -0.01 eV/Å compared to about -0.11 eV/Å for a conducting tip. This is again consistent with the prediction that the tip is effectively an insulator due to either a thick oxide layer or the poor conduction properties of silicon. These results show that the major contribution to the background force in the theoretical model is from the macroscopic van der Waals interaction. However, it should be noted that this argument does depend on the radius of the tip used in the experiment, which cannot be known directly. In principle a conducting tip with a smaller radius could produce the force the model predicts at atomic resolution, although a fairly thick oxide layer must still be present otherwise the image forces become too large. The tip cannot have a much larger radius, otherwise the van der Waals force will become too big. The only way to fully establish the real characteristics of the tip is by comparison of theoretical and experimental force vs. distance curves, but unfortunately no experimental curve was available. Nevertheless the results still predict that the NaCl film is not more than 2 layers thick, regardless of the conduction properties of the tip.

Now that the source of the macroscopic interactions involved has been established, the interactions between the small oxide nano-tip and a representative 600 atom unit cell can be calculated and a background force, which we have demonstrated is mainly due to the van der Waals interaction, can be added.

The systems used to calculate the microscopic forces are all setup as shown in fig. 7.7, with only the exact structure of the NaCl cell changing between systems. Now that the island thickness has been estimated, the macroscopic van der Waals force is calculated using the method discussed in chapter 3 for a conical tip, as in other studies. Since the magnitude of the background van der Waals force in experiment has already been established, changing from an atomistic to continuum representation of the macroscopic tip does not affect the results. The cells used consist of four layers of NaCl with the top two layers designated region 3 and the bottom two layers region 4, as

in fig. 7.7. The relaxation of the region 3 ions allows the model to account for the deformation of the NaCl due to the interaction with the tip, which proved to be important for the understanding of the contrast mechanism. The metal substrate is 0.2 nm below the bottom of the layer and does not chemically interact with NaCl. Modelling of the NaCl-Cu interaction directly would require expensive quantum treatment. Instead two fixed layers of NaCl are used to represent the substrate. This is justified by the experimental data presented in figs.7.1 - 7.4 which demonstrate very similar qualitative features for both NaCl islands on Cu and on a NaCl film.

To keep consistency with experimental setup (see also ref. [32]), the bias between tip and substrate was held at 1.0 V in all calculations. All theoretical scanlines were calculated with experimental oscillation amplitude of 1.8 nm, frequency 158 kHz and constant frequency change of 128 Hz. The spring constant of the cantilever was 26 Nm^{-1}. γ_0 (see section 2.3) for these parameters is -1.61.

7.6.2 NaCl Step

This system is identical to that discussed in section 5.3.3, however, the properties being studied are different. A schematic for the calculation cell of this system is shown in fig. 7.8. The upper terrace of the step is a good representation of the ideal (001) surface of NaCl as long as the region studied remains at least 2 rows from the edge, the forces are converged with respect to row choice. This combination allows both the upper terrace and the edge of a NaCl island to be modelled, features which are atomically resolved in experimental images (fig. 7.2).

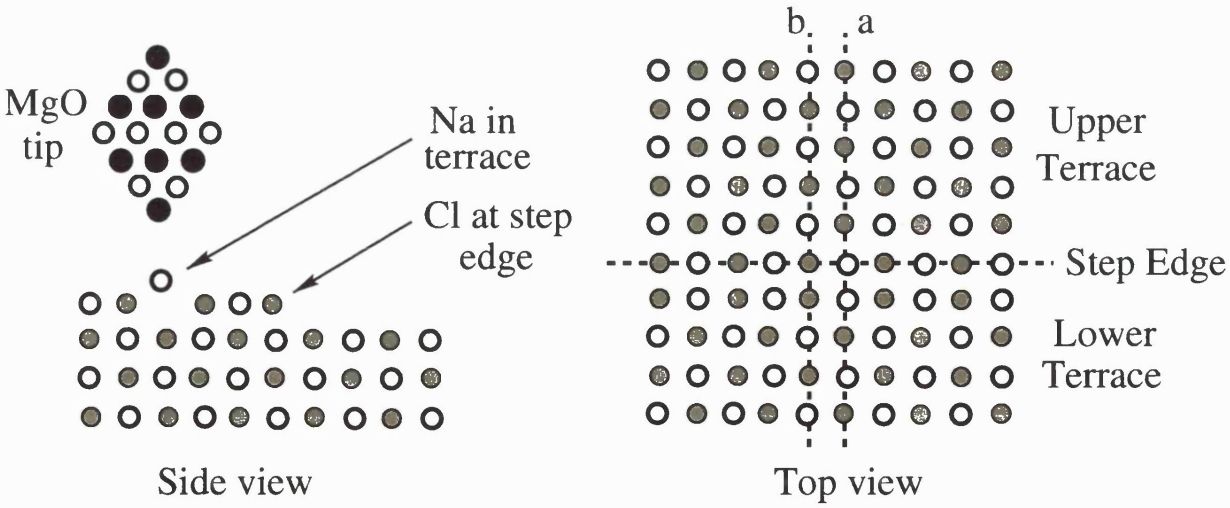

Figure 7.8: System schematic for NaCl step.

Fig. 7.9 shows simulated scanlines along the dashed lines labelled *a* and *b* in fig. 7.8, beginning on the upper terrace. The schematic atoms in fig. 7.9 show the positions of ions in the lattice. The solid scanline *a* in fig. 7.9 crossed the step-edge over a Na ion as shown by fig. 7.8. However, the first two peaks in the scanline are calculated above an unstepped NaCl film, which effectively represents the ideal (001) surface. This is added to the scanline to show how the interaction on the upper terrace converges to the ideal surface away from the step edge. The periodicity of the microscopic calculations means that there is another step edge on the left-hand side of the cell

(looking at the side view in fig. 7.8) and calculating the scanline above atoms close to this edge would be unphysical. The axis labelled height in fig. 7.9 is a measure of how the centre point of the cantilever oscillations changes to keep the frequency change constant. Note that the tip-surface separation in these, and all other, scanlines is measured with respect to the relaxed position of the Na ions in the top layer of the island in the absence of interaction with the tip. The theoretical model predicts that the tip would come to between about 0.43 and 0.47 nm from the surface.

It is immediately evident from scanline *a* in fig. 7.9 that the theoretical model predicts stronger attraction over the Na ions. As shown by the increase in tip-surface closest distance of approach, they would appear bright in an experimental image. It should be noted that the overall interaction is *always attractive* due to the other forces in the system, and the electrostatic repulsion over the Cl ions just reduces the total attractive force. However, the repulsive chemical force between the tip and chlorine ions is resolved in the model, and the fact that they are represented as dark in experimental images is a matter of convention. The difference between the deflection over terrace Na and Cl ions, i.e. contrast, is about 0.032 nm. This shows that contrast in the model is dominated by the electrostatic interaction between the nano-tip and surface ions. The negatively terminated nano-tip is attracted to the surface over Na ions and repelled over the Cl ions.

Displacement of ions also plays an important role in the interaction, as at these tip-surface separations surface ions relax significantly due to the proximity of the tip. Na ions displace by about 0.014 nm towards the tip and Cl ions displace about 0.006 nm away. As discussed in section 5.2, this extends the electrostatic potential over the displaced ion: at scanning height (0.45 nm) the potential from the ideal surface is almost zero and the extended potential from the displaced ion dominates the electrostatic interaction with the surface.

Fig. 7.9 also shows an increase in contrast (and therefore predicted image brightness) over the Na ion at the step-edge, the difference in contrast between the Na ion at the edge and the Cl ion in the terrace along *a* is 0.043 nm. The increase in contrast at the step-edge has two components, (i) the electrostatic potential at the step-edge extends much farther than over the terrace (this effect can also be seen directly for the low-coordinated MgO cube oxygen corner in fig. 4.4) and, (ii) the low coordination of the step-edge ion increases the displacement (step-edge Na displaces by 0.024 nm towards the tip) when the tip is at scanning height, again extending the electrostatic potential.

The dashed line *b* in fig. 7.9 shows a parallel scanline along *b* in fig. 7.8. As expected contrast over the terrace ions is the same, about 0.032 nm. However, now an increase in contrast to about 0.035 nm over the Na ion just before the step edge can be seen and then the tip moves closer to the surface over the Cl ions at the step edge. This means that the model also gives contrast along the step edge itself, in fact the difference between deflection over the Cl and Na ions both at the step edge is about 0.07 nm. The scanline behaviour over the Cl ion at the step edge is again due to the ion's low coordination, which causes a reduction in the attractive force on the tip. The edge Cl ion displaces by about 0.009 nm away from the tip as it passes the step-edge.

The solid scanline *a* over the Na step-edge in Fig. 7.9 seems to decay to a constant height after passing the step-edge, whereas the dashed scanline first dips over the chlorine ion before rising again as it passes the step. In both cases this is due to the interaction of the side of the tip with the step as it passes and is a consequence of the specific nano-tip we use in the model. This also strongly affects the behaviour of the scanlines as the tip passes the step-edge and moves to the

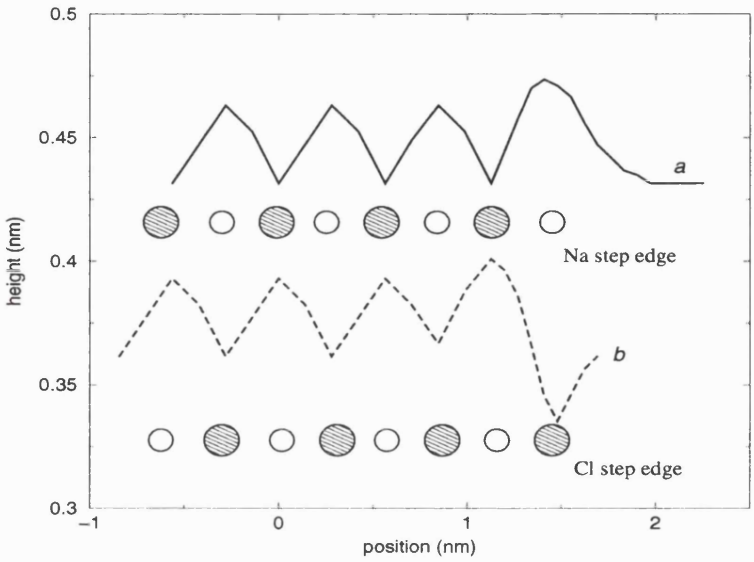

Figure 7.9: Simulated scanlines over NaCl step-edges. Note that both scanlines are at the same height, but b was shifted down for clarity.

lower terrace. The strong tip-side/island-edge interaction means that there are large instabilities of tip and edge ions and the first few rows of the lower terrace cannot be resolved, so they have been omitted from these and all other scanlines. In the current periodic model the island is not large enough to escape the edge interaction and begin to image the lower terrace before the tip starts to interact with the step-edge of the next island image. Since in the specific experiment being modelled here there is no lower terrace of NaCl, we did not perform further calculations with a larger island. However, this type of interaction behaviour near the edge can also be seen in the experimental scanlines in fig. 7.5, where sections M and N both show a shoulder beyond the step-edge due to an interaction with the side of the nano-tip. This confirms our assertion that a protruding nano-tip is a real feature of NC-AFM tips in experiments demonstrating atomic resolution.

Fig. 7.9 demonstrates that the theoretical model predicts an increase in contrast at and near the step edge. This would translate to increased brightness in experimental images along the step edge and along the next row parallel to the edge.

7.6.3 NaCl Kink

To model the interaction of the tip with kink sites a unit cell was produced by removing six atoms from the step edge, creating a double kink site. A schematic diagram of the upper terrace of system is shown in fig. 7.10. The kink atoms have a coordination of 3, as compared to 4 at the step edge and 5 in the terrace itself. This allows the interaction over the kink and corner sites, which can be seen atomically resolved in experimental images (fig. 7.2), to be modelled.

Fig. 7.11 shows simulated scanlines along the dashed lines c and d in fig. 7.10. The schematic atoms in fig. 7.11 show the positions of ions in the lattice. The solid line is a scanline along c over a Na kink as shown in fig. 7.10. Again the contrast on the terrace ions is the same, about 0.032

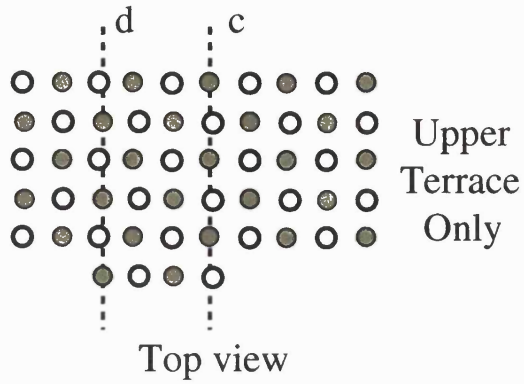

Figure 7.10: System schematic for NaCl kink.

nm. Scanline c also shows an increase in contrast over both the Na ion at the kink site, and the next Na ion along the scanline. Over the kink ion the contrast is about 0.062 nm and over the next Na ion it is about 0.035 nm. This much more de-localized increase in contrast around the kink site is due to the very low coordination of the kink ion.

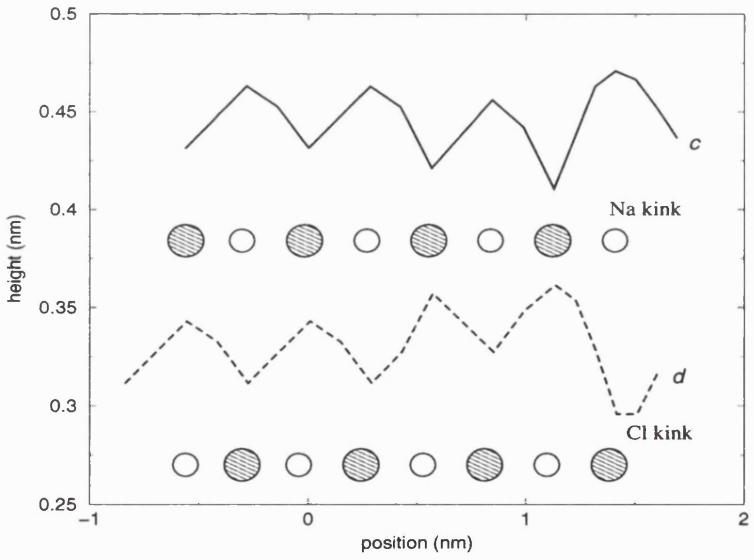

Figure 7.11: Simulated scanlines over different kink sites. Note that both scanlines are at the same height, but d was shifted down for clarity.

This causes both the kink ion itself and its nearest neighbours to be very susceptible to relaxation when the tip is in proximity. The Na ions near the kink site all displace towards the tip much more easily than terrace ions, causing an increase in force on the tip near the kink site. The kink ion itself displaces upwards by 0.025 nm and the nearest Na ion along c by 0.018 nm. A simulation snapshot of the tip passing over the kink site in fig. 7.12 clearly shows the large disturbance of all ions around the kink.

The dashed line d in fig. 7.11 shows a parallel scanline along the line d in fig. 7.10. This allows the interaction over a Cl kink and also the Na ion directly behind the kink site to be seen.

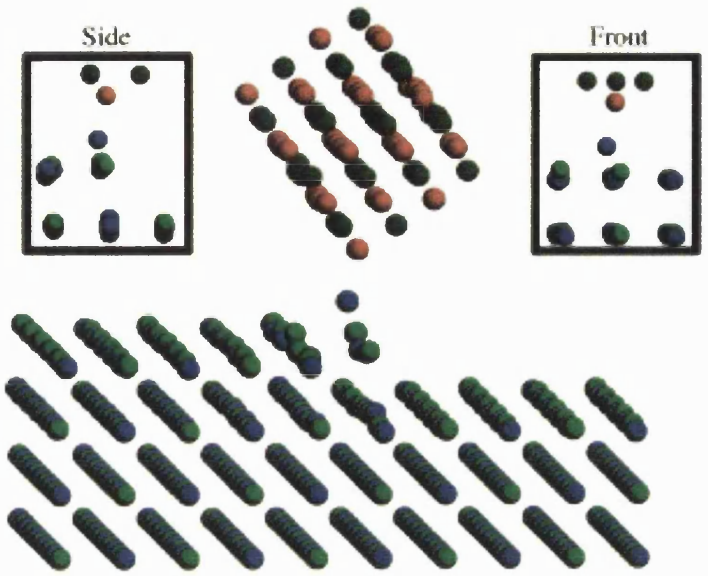

Figure 7.12: Simulation snapshots of atomic displacements as the tip passes the kink site sodium ion. The snapshots are taken from the simulation of scanline *c* in figure 7.10.

The same behaviour as seen in the Na kink scanline is demonstrated, there is a general increase in contrast over Na ions near the kink site. The contrast rises to 0.035 nm over the Na ion directly behind the Cl kink ion, before the deflection falls rapidly as it passes over the kink. The Na ion displaces by 0.024 nm and the Cl ion at the kink site moves 0.009 nm away from the tip, but all the atoms near the kink site experience strong displacements.

It is clear from the kink scanlines that the theoretical model predicts that kink sites would be the brightest feature in a NC-AFM image, and that the Na kink ion would be bright. By comparing several theoretical scanlines it can also be seen that the much less localized interaction predicted by the model over the kink site would produce a wider area of bright contrast in an image than for terrace and step-edge ions. This corresponds well with the experimental images shown in figs. 7.1 - 7.5.

7.6.4 Cation Terminated Tips

To study the effect of the chemical identity of the tip apex on the results, calculations using a tip terminated by a positive Mg^{2+} ion and an OH^{-} group were also performed. This simulates the situation where the original tip has been contaminated by a positive ion from the surface or from the environment, for example, a water molecule could dissociate on the tip. This also simulates the case where the original uncontaminated tip is terminated by a cation, a situation which cannot be ruled out by experimental data at present. Both scans in this section were taken along line b in fig. 7.8.

Mg Terminated Tip

By reversing the orientation of the MgO cube simulating the nano-tip, scanning of the surface with an equally but oppositely charged apex ion can be modelled. All other parameters are kept

the same as previously.

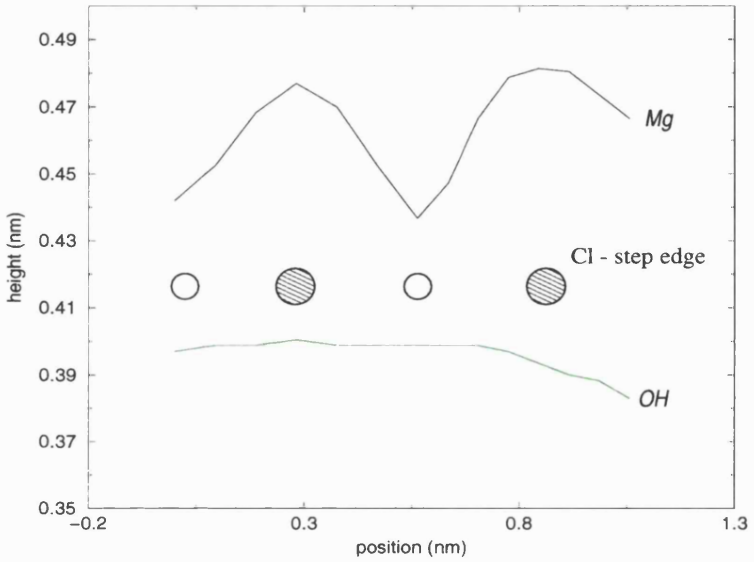

Figure 7.13: Simulated scanline over chlorine step site with Mg and OH terminated tip. As previously scanline *OH* has been shifted down for clarity.

The scanline labelled *Mg* in fig. 7.13 clearly shows that the contrast with an Mg terminated tip is now dominated by the attractive electrostatic interaction between the Mg at the end of the tip and the Cl ions in the terrace. The magnitude of contrast on the terrace is 0.035 nm, which is a slight increase in comparison with the oxygen terminated tip. Again, an increase in contrast to 0.044 nm over the step-edge due to the low-coordination of the edge ion can be seen. However, chlorine ions are more resistant to relaxation, displacing by only 0.019 nm compared to 0.024 nm for the Na ion, so the relative increase in contrast over the step is smaller than scans with the O-tip.

OH Terminated Tip

In this setup the oxygen at the end of the original MgO tip is replaced by a hydroxyl group and another hydroxyl group is added to the opposite side of the tip to keep it neutral. The electrostatic potential gradient from this OH apex is very similar to the potential gradient from a silicon tip contaminated by a hydroxyl group (see fig. 4.4).

The scanline labelled *OH* in fig. 7.13 shows very different behaviour to all the previous tip setups. As for the Mg terminated tip, ostensibly the attractive electrostatic interaction between the hydrogen at the end of the tip and the chlorine ions in the terrace is the source of contrast. However, the magnitude of contrast is only 0.004 nm, almost an order of magnitude less than with the Mg and O terminated tips. This is because at a distance of about 0.48 nm the interaction between the hydrogen and Na and Cl ions is more or less the same, as has been shown in previous studies on C-AFM [54]. There is no contrast at all over the ions near the step edge and the contrast actually decreases rapidly as the tip passes the step-edge. This occurs because at the step-edge the hydrogen atom interacts with less ions for a given radius than over the terrace. Also

the simulation shows no relaxation of the step-edge ion due to the tip.

7.7 Island Formation

The experimental images seen in figs. 7.1, 7.2, 7.3 and 7.4 seem to show a predominance of one type of kink/corner site. Theoretically it has been shown that cation and anion kink/corner sites should appear different in images i.e. one bright, one dark, yet in the experimental images there seems to be more bright than dark kink/corner sites. Although this is only a qualitative observation, it is still interesting to see whether there is any energy preference for kink/corner sites of one particular ion type. The setup for this calculation is the same as in the previous calculations on the NaCl thin film, but now the tip is removed and the cluster is as shown in fig. 7.14. In order to also investigate more thoroughly the role of image forces in island formation, the calculations in this section have been performed using the SCIFI code, as described in section 3.2.1. This means that image forces are now included self-consistently and atoms are relaxed with respect to microscopic and image forces.

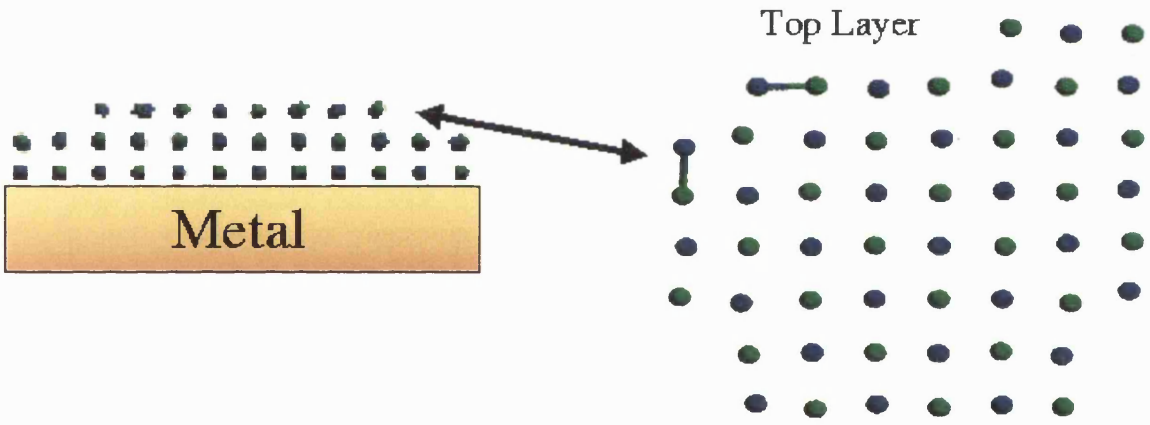

Figure 7.14: Model used to represent an NaCl island on top of a metallic substrate.

The island shown in figure 7.14 has an equal number of anion and cation kink/corner sites, and represents the initial setup. As a first test, a molecule was moved from a kink-forming to a corner-forming position, as shown in fig. 7.15. This reduced the overall energy of the system by 0.3 eV, forming a more stable structure. By turning a kink into a corner, the overall coordination of the island has been increased. This stabilization by increasing coordination can be seen clearly in fig. 7.1, where large regular shaped NaCl islands form on the Cu substrate.

Finally, to test the energy difference of cation and anion corner creation, the initial setup was taken and ions where moved from the second layer to produce an imbalance in number of kink/corner site types. Fig. 7.16 shows a model of the creation of an anion corner site by moving two ions from the second layer. The ions taken from the second layer were chosen so that there would be no significant interaction between the vacancies left after their removal. An extra cation or anion corner can be created by moving the ions to the bottom left or right, in fig. 7.14, of the initial island respectively. The difference in energy for creation of anion and cation corner sites was

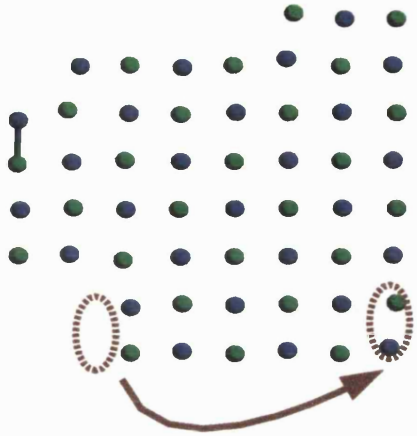

Figure 7.15: Model of corner creation on a NaCl island. A NaCl molecule is moved from a position where it forms a kink to a position where it forms a corner.

found to be only 0.03 eV. This energy is too small for there to be a significant difference, at least in our model, between the number of anion and cation kink/corner sites due to differences in the energy of formation. Note that although there is a contribution to the energy from the vacancy creation, the vacancies are the same for cation and anion corner creation, so their contribution is cancelled when taking the energy difference.

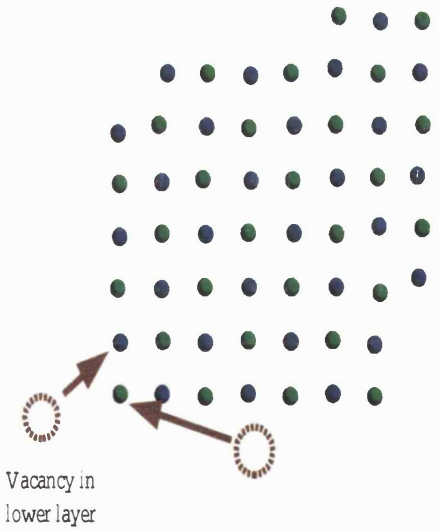

Figure 7.16: Model of anion kink creation. Individual atoms are moved from the second layer (see fig. 7.14), leaving vacancies, and are added to the top layer to create a corner site.

7.8 Conclusions

The results suggest that the tip used in this study is effectively an insulator. The surface of the tip is rough on the nano-scale and one of the features at the tip end serves as a main nano-tip. The

image features suggest that another nano-asperity which serves as a second tip is located about 5 nm away from the main one. To reproduce experimentally observed contrast the nano-tip must have a strong electrostatic field which, as demonstrated in fig. 4.4, could be generated by a polar group at the tip apex or by an oxide. The theoretical results show that a tip terminated by OH^- cannot produce the experimentally observed contrast. The results presented in fig. 7.3 suggest that the tip can also temporarily trap some surface ions.

The theoretical analysis demonstrates that at long-range the tip-surface force is mainly due to the van der Waals interaction. The characteristic scanning tip-surface distance is predicted to be about 0.43 - 0.47 nm (with ion instabilities occurring below about 0.42 nm). The contrast in the image is determined by the chemical interaction between the tip and surface ions at this distance. This interaction dominates the forces at short-range and leads to considerable displacement of surface ions from their ideal sites.

Modelling also predicts that contrast in NC-AFM images corresponds to the average positions of surface ions. Although the tip-surface model is idealised, the contrast mechanism does not allow any other plausible explanation for observed experimental contrast. The increase in contrast (and therefore predicted image brightness) over the step-edges and kinks is due to the lower coordination of the step edge and kink ions. It has two components, (i) the electrostatic potential over the low coordinated sites extends much farther than over the ideal terrace and, (ii) the low coordination of the ions increases their displacements due to the interaction with the tip. These two effects mainly determine the electrostatic interaction with the tip at scanning height.

It is interesting to note that STM experiments on thin films of NaCl on Al(111) by Hebenstreit *et al* [17] have also observed enhanced contrast at step and kink sites. The results presented here suggest that the tip interaction with these sites could be one of the reasons for this enhanced contrast.

Chapter 8

Calcium Difluoride

8.1 Original Motivation

The study of the CaF_2 surface was motivated by our collaboration with the group of Michael Reichling in Munich. They successfully imaged the (111) surface in atomic resolution and even saw evidence of point defects, but were unable to tell much about the chemical identity of the features seen in the images. They then asked us if we could help with interpretation. As a classic bulk insulator with a fairly complex surface termination, CaF_2 seemed a very good candidate for theoretical study, so we begin modelling it.

8.2 Introduction

Difficulties in NC-AFM imaging have so far prevented atomic resolution being achieved on surfaces of many insulators, most notably MgO and Alumina. These difficulties are usually associated with blunt tips, surface charging or surface roughness after cleavage. However, the mechanism behind the imaging instabilities is not well understood and it is not clear how these factors interfere with stable AFM operation. Since the main purpose of NC-AFM is to study insulating surfaces in atomic resolution, it is useful to analyze those insulating surfaces which have been atomically resolved and use that information to try and understand why other surfaces cannot be imaged.

As a wide band gap (12.3 eV [167]), highly ionic material (formal charges $Ca^{2+}$and F^{-}), Calcium Difluoride (CaF_2) represents a classic insulator. It has many applications in optical components due to its high transmission of light in the deep ultraviolet spectral range [168]. These applications have motivated many studies into the properties of the bulk [167, 169, 170, 171, 172] and surface [173, 174], with special regard for degradation of the surface due to air and laser damage. The need for a well-prepared clean surface in optical applications has meant that the techniques for cleaving CaF_2 have improved to such an extent that the production of a well-defined surface along the most stable [173, 174] (111) plane is almost routine. Although fig. 3.4 shows jagged cleavage tips on the CaF_2 surface, these can be reduced by annealing and it is possible to find flat (111) terraces hundreds of nanometres wide. Recent NC-AFM experiments [27] have successfully demonstrated atomic resolution on the (111) surface of CaF_2 and of atomic defects after exposure to oxygen. Therefore the CaF_2 surface represents a good example for

comparison with other, as yet, unimaged insulating surfaces. The γ_0 (see section 2.3) of -38.6 for those experiments also implies that a large macroscopic van der Waals force due to a blunt tip or significant electrostatic forces due to tip and surface charging are present. Both explanations are feasible since AFM studies [79] of CaF_2 have already demonstrated that charging due to cleavage could be significant and tip charging and bluntness due to sputtering is a common preparation problem [96]. By studying theoretically the effects of a blunt tip and charging on NC-AFM imaging of the CaF_2 (111) surface, some general conclusions about the importance of these effects in imaging of other insulators can be made.

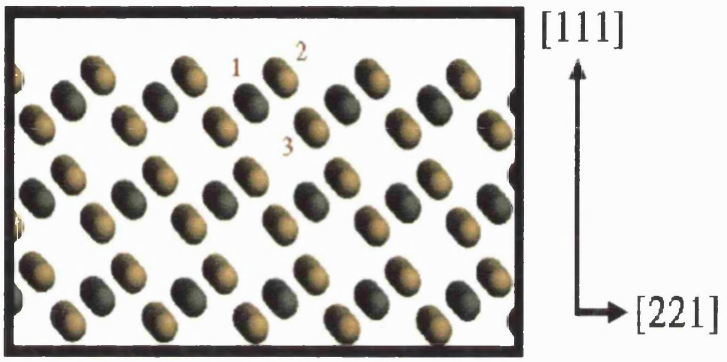

Figure 8.1: Fluorine terminated CaF_2 (111) surface. The calcium layer is labelled 1, the outermost fluorine layer is labelled 2 and the lower fluorine layer is labelled 3. The layers are separated by about 0.08 nm.

Several other factors also make CaF_2 an attractive system to study theoretically. Structurally, the CaF_2 (111) surface offers more interesting physical features than other flat insulators, such as NaCl. The surface has been demonstrated to be fluorine terminated [27] and, as can be seen from fig. 8.1, the outermost fluorine layer protrudes out from surface in a similar manner to the bridging oxygens seen on the TiO_2 surface or As atoms in the InAs surface. A common previous assumption in NC-AFM imaging is that protruding atomic layers are imaged as bright, and it is important to establish whether this "intuition" holds theoretically.

The experimental study itself demonstrated a general problem in NC-AFM imaging, in that they were unable to chemically identify the defect or the sublattice seen as bright in images. They also suffered from a technical problem which exaggerated the apparent contrast measured on the surface. This combination of instrumental problems and lack of information obtained from experimental images motivates the use of theoretical modelling to try and extract more information about the surface and tip-surface interaction, and aid in interpreting experimental images.

After an initial explanation of the method used to model CaF_2, this chapter is effectively split into two parts. The first part deals with the influence of the nature of the background force on imaging. Although this part uses experimental imaging parameters, it focuses on theoretical predictions of imaging of insulating surfaces in general, rather than on a direct comparison with experiment. In the second part, the theoretical model is developed directly from specific experiments on CaF_2 and is then used to aid in interpretting the images from those experiments.

8.3 Method

The model used in this study is the same as that described in chapter 4, so this section will focus on those aspects of modelling that are specific to the study of CaF_2.

The setup of the calculations is the same as in fig. 4.6, with the NaCl cluster replaced by the CaF_2 surface unit cell (shown in fig. 8.1). The distance dependence of the van der Waals force is calculated using a Hamaker constant (H) of 1 eV and the method described in chapter 3. For bulk CaF_2 the sample is so thick (3-5 mm) that the distance between the tip and the conducting substrate makes the image force negligible for neutral systems. However, when the surface is charged there is a strong interaction between the surface charges and their images in the conducting tip, and the image force makes a significant contribution to the background force. The microscopic force is calculated using a periodic static atomistic simulation technique and the MARVIN2 code, as described in section 3.2.1. The bottom of the nano-tip and the top of the CaF_2 surface are relaxed explicitly, in terms of fig. 4.6, region 1 and 2 of the MgO nano-tip are the same, and region 3 now consists of the top three layers of the CaF_2 surface and region 4 the remaining surface layers.

8.3.1 Parameters for CaF_2 Interactions

Several sets of parameters for CaF_2 shell-model interactions exist [171, 175, 176, 177], however none of these studies were interested in the interactions important to NC-AFM, and only one [177] looked at the properties of the CaF_2 surface. In light of this it is important to compare the different parameters to see which, if any, well represent the interactions important for modelling NC-AFM. Obviously it is important to reproduce experimental geometries, but it is also important within the SM method that the electronic polarization of the ions is modelled realistically i.e. the static and high-frequency dielectric constants are reproduced.

Three sets of shell-model parameters were used to calculate relaxed geometries, vibrational and dielectric constants of bulk CaF_2. The first two sets, by Grimes [175] and Gillan [171], are taken from literature, but the third set, called 'opti', (based upon Binks [176]) has been optimized specifically for all the properties shown in table 8.1. For these bulk calculations the General Utility Lattice Program (GULP) [178, 179] code was used. Its operation is very similar to the MARVIN code and differs mainly in that it repeats the unit cell in all three-dimensions to reproduce the bulk rather than the surface. The results of these calculations are shown in table 8.1. The parameter set derived for surface calculations [177] has been neglected since the authors themselves state that it cannot reproduce experimentally observed surface properties. Although initially bulk properties are being compared, it is crucial that the parameters can also reproduce surface properties for NC-AFM modelling.

It is immediately evident from table 8.1 that all the parameter sets well reproduce the bulk lattice constant to within a few percent. This consistency is also seen in the elastic constants, although the opti set gives the best results across all three constants. It is only in the dielectric constants that real improvements of the opti set can be seen. The first two sets underestimate both the static and high frequency dielectric constants, with a 100% error in the high frequency constant. This is not surprising, since neither of these studies were interested in dielectric properties. The opti set reduces the errors to about 10% and gives a much better overall approximation of the six

Parameters	Lattice (Å)	C_{11}	C_{12}	C_{44}	ε_0	ε_∞
Grimes [175]	5.495	16.47	4.05	3.97	5.07	1.00
Gillan [171]	5.445	15.71	4.16	3.96	5.18	1.00
Opti	5.438	16.20	4.28	3.73	5.85	1.82
Exp. [169, 170]	5.465	17.12	4.68	3.62	6.47	2.05

Table 8.1: Comparison of calculated and experimental physical properties for CaF_2. The Opti results are produced using parameters generated in this study and shown in table 8.2.

Ion Type	Ion Type	A (eV)	ρ (1/Å)	C (Å^6)
$Ca^{1.281+}$	$Ca^{1.281+}$	0.00	0.00	0.00
$Ca^{1.281+}$	$F^{1.378-}$	1140.0	0.303	0.00
$F^{1.378-}$	$F^{1.378-}$	911.690	0.2707	13.80
		Spring (eV/Å^2)		
$Ca^{1.281+}$	$Ca^{0.719+}$	34.05	-	-
$F^{1.378-}$	$F^{0.378+}$	24.36	-	-

Table 8.2: Shell-model parameters used in this study.

properties studied.

All further calculations for the surface and the tip-surface interactions have been performed using the opti set to represent CaF_2. Parameters for the interactions between the MgO tip and the CaF_2 surface are taken from Binks [176] and Bush *et al* [149]. The parameters for the tip remain as in the previous systems studied.

8.3.2 *Ab Initio* Modelling of the CaF_2 (111) Surface

It is important to test whether the chosen parameter set from the bulk calculations can also reproduce the properties of the CaF_2 (111) surface. The best method for doing this is by comparing the surface relaxations from shell-model calculations with *ab initio* calculations and experiment. Ultraviolet photoelectron spectroscopy (UPS) experiments [180] have demonstrated that there is no reconstruction at the surface, but unfortunately there is no experimental data on surface relaxations. In the absence of experimental data, *ab initio* calculations are the most reliable source of information. Although *ab initio* calculations have already been performed on the (111) surface [174], these were done with a small number of surface layers and without including the effects of electron correlation. Since electronic polarization has a large influence on the properties of ionic materials it is important to check the surface relaxations with a full DFT calculation including the effects of correlation.

Ab initio calculations of the CaF_2 (111) surface were performed using the VASP code as discussed in section 3.2.1. Specifically, calculations were performed on bulk CaF_2 to converge the total energy of the system with respect to k-point sampling of the Brillouin zone and energy cut-off of the plane waves. The Monkhorst-Pack [56] k-point generation scheme was used and the total energy was converged to 0.1 meV with a $9 \times 9 \times 9$ mesh. The bulk cell was then fully relaxed. The VASP calculations of the bulk predicted a lattice constant of 5.43 Å, which compares well with

the experimental value of 5.47 Å.

The relaxed bulk unit cell from the fully converged calculation was then used to generate the surface unit cell. The total energy of the surface was then converged with respect to the number of surface layers, k-points and the vacuum gap between the periodic slabs. The total energy was converged to 1 meV with a 12 k-point $9 \times 9 \times 1$ mesh. It was found that 9 surface layers with a vacuum gap of 8 Å was sufficient. The relaxed surface geometry was taken from the final fully converged calculation and the relaxed surface unit cell is shown in fig. 8.1. There was no significant relaxation observed for the CaF_2 (111) surface, all relaxations were less than 0.01 Å. This is consistent with the other *ab initio* results from Puchina *et al* [174] and gives a very good basis for testing the shell-model parameters.

The surface calculations were repeated using the MARVIN code, as described in section 3.2.1, and the opti parameter set (see table 8.2). The same 9 layer surface unit cell was used in the shell model calculations and the surface relaxations were again found to be very small, less than 0.02 Å. Although the shell model calculations gave slightly larger relaxations than predicted by *ab initio* calculations, they nevertheless reproduce the qualitative result that there is very little relaxation of the CaF_2 (111) surface. This means that the opti parameter set gives a good representation of the bulk and surface properties of CaF_2, and will reproduce the interactions important for NC-AFM modelling.

8.4 The Influence of the Background Force

In an attempt to understand the effect of the nature of the background force on NC-AFM imaging of CaF_2, this section focuses on theoretical modelling of imaging with different background forces. Although the general setup shown in fig. 4.6 is consistent throughout this study, two different interaction schemes have been used in this section, each representing an extreme model where the entire background force is dominated by one source. Firstly, to model a system with no surface charge where the macroscopic van der Waals interaction dominates the background force, a very blunt tip of radius 400 nm has been used. To model the interaction of charged tip with charged surface, a sharp tip of radius 3.33 nm has been used. The tip held a discreet electric charge of +4e, and the surface a charge of 0.6 e/nm^2. The magnitudes of these charges were chosen so as to reproduce the observed experimental frequency change at scanning height. These charges produce a long-range electrostatic force, which dominates the background force. Note that the surface charge is unrealistically large and represents an extreme limit.

All frequency change vs. distance curves and scanlines were produced with a cantilever amplitude of 23 nm, eigenfrequency of 84 kHz, spring constant of 6 N/m, and a frequency change of -155 Hz, as in experimental images [27]. As stated previously, γ_0 for these parameters is -38.6. It is important to note that although the blunt tip and sharp tip interaction schemes are very different, they both reproduce the magnitude of frequency changes observed at atomic resolution, i.e. -155 Hz. In order to maximize contrast in the theoretical scanlines and therefore more easily see the effect of the background force on imaging, the maximum frequency change, -155 Hz, is assumed to occur at a tip-surface separation at the limit of surface ion stability, about 0.4 nm. Imaging any closer than this causes surface ions to jump to the tip.

In order to demonstrate the differences between the two interactions schemes used, in fig. 8.2

frequency change vs. distance curves have been plotted for both the blunt and charged tips. The blunt tip demonstrates a fast decay, characteristic of a pure van der Waals interaction. The change in oscillation frequency is already less than 10 Hz beyond 7.5 nm. The charged tip shows a much slower decay and the change in frequency is over 30 Hz at 7.5 nm and remains above 10 Hz until around 20 nm. This is characteristic of the electrostatic interaction between the charged tip and surface. The image force due to polarisation of the conductive tip by the ionic sample also makes a significant contribution to the interaction at medium range (< 5 nm). This marked difference in the distance behaviour suggests that by analysing an experimental curve one should be able to determine the dominant force contribution and in this way characterise the tip and surface. However, before comparing directly with experiment it is important to see whether there is any difference in predicted contrast in images due to the different interaction schemes.

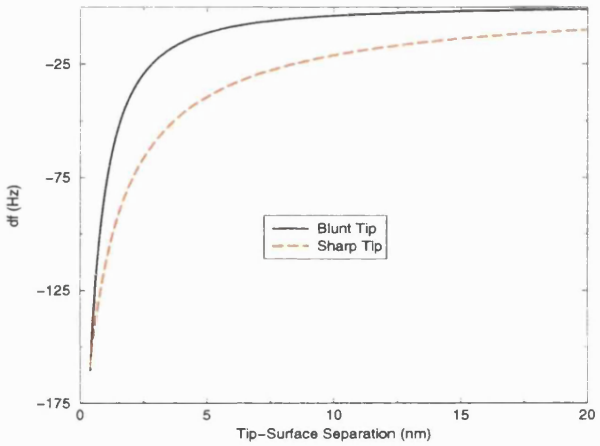

Figure 8.2: Frequency change vs. distance curves over the CaF_2 (111) surface. The blunt tip curve uses a large radius tip and a background force consisting of only van der Waals. The sharp tip curve uses a small radius charged tip and the background force is composed of van der Waals and an electrostatic interaction due to surface charging.

8.4.1 Anion Terminated Tip

The first simulations were performed with the nano-tip oriented so that a negative O^{2-} ion is closest to the surface. This represents the situation were the original silicon tip is oxidized or contaminated by ambient oxygen. The electrostatic potential gradient from an oxygen terminated MgO nano-tip has been shown [3] to be similar to that of an oxygen contaminated silicon tip.

Fig. 8.3 shows simulated scanlines produced over the CaF_2 surface with an O-terminated tip. The overall qualitative behaviour for the sharp and blunt tip scanlines is the same, with contrast dominated by the strong short-range electrostatic interaction between the negative potential from the tip and the positive Ca ions in the surface. Surface relaxation also plays a role in the interaction, with the Ca ions displacing towards the tip by about 0.01 nm during scanning and actually jumping to the tip at tip-surface separations of less than 0.38 nm. The magnitude of contrast is about 0.020 nm for the sharp tip and 0.010 nm for the blunt tip. This contrast is much smaller than the 0.1 nm observed in the original experiments. This is consistent with the assertion made in ref. [27] that AFM electronics exaggerates the experimentally observed contrast. The difference in contrast

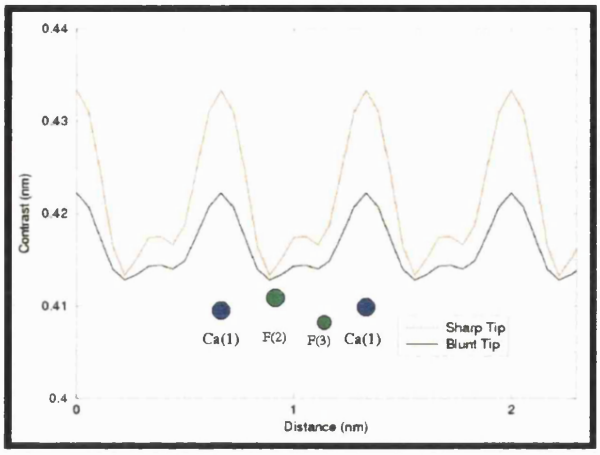

Figure 8.3: Simulated scanlines of the CaF_2 (111) surface along the (221) direction with an oxygen terminated nano-tip. Tip-surface separation is calculated with respect to the Ca layer. The numbers below the schematic atoms refer to the labels in fig. 8.1. The blunt tip scanline is from the simulation with a large radius tip and a background force consisting of only van der Waals. The sharp tip scanline uses a small radius tip and the background force is composed of van der Waals and an electrostatic interaction due to surface charging.

between the two curves is a direct result of the significant difference in the long-range tip-surface interactions for the two systems, as seen in fig. 8.2. Although the interactions are similar at close-range, the van der Waals dominated blunt tip interaction decays much more quickly than the electrostatic dominated sharp tip interaction. This means that the sharp tip must move slightly further from the surface than the blunt tip to feel the same frequency change. In both curves a second maximum can be observed at a distance of 0.33 nm from the main peaks. This is due to a minimum of repulsion from the two fluorine ions when the tip is equidistant between them, producing an increase in the overall attraction.

8.4.2 Cation Terminated Tip

Simulations were also performed using a nano-tip terminated by a positive Mg^{2+} ion. This reproduces the situation where the original tip has been contaminated by a positive ion from the surface or from the environment, and also the case where the original uncontaminated tip is terminated by a cation, a situation which cannot be ruled out by experimental data at present.

Fig. 8.4 shows simulated scanlines over the CaF_2 surface with a magnesium terminated tip. Again the overall qualitative behaviour of the blunt and sharp tip scanlines is the same. For the Mg-terminated tip, the contrast is dominated by the strong short-range electrostatic attraction between the positive potential from the tip and the negative F ions in the surface. The F ions displace by about 0.02 nm towards the tip while scanning and jump to the tip at tip-surface separations of less than 0.40 nm. Note that, as mentioned in fig. 8.3, tip-surface separation is calculated with respect to the Ca layer and the tip is in fact about 0.07 nm closer to the F layer. The magnitude of contrast is about 0.032 nm for the sharp tip and 0.017 nm for the blunt tip. The difference in contrast between the sharp and blunt tips is consistent with that seen for the O-terminated scanlines and is due to same source. However, instead of a second maximum, as seen

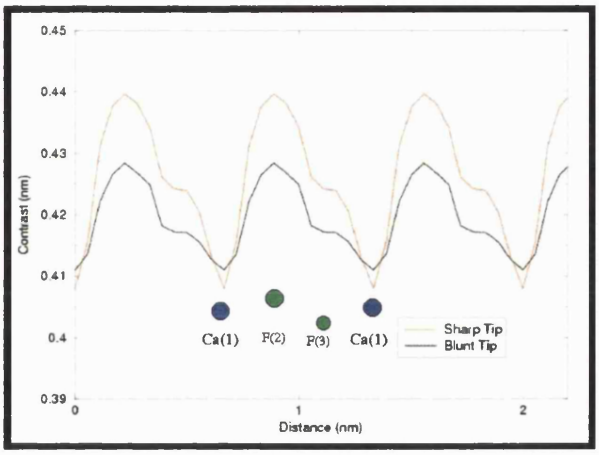

Figure 8.4: Simulated scanlines of the CaF_2 (111) surface along the (221) direction with an magnesium terminated nano-tip.

in fig. 8.3, the scanlines in fig. 8.4 have a shoulder at 0.22 nm to the right of the main peaks. This is due to the attraction of the tip to the fluorine ions in the 3rd layer of the surface, effectively both types of fluorine site are imaged with the Mg-terminated tip.

8.4.3 Summary

This study has shown that the exact nature of the background force does not have a large effect on the contrast mechanism in NC-AFM imaging. The much slower decay of the electrostatic force does not seem to be a significant factor in resolution, and scanlines produced using a van der Waals dominated background force were qualitatively similar to those produced with a background force dominated by long-range electrostatic forces due to tip and surface charging. The balance between van der Waals and electrostatic forces in a real experiment can only be established by comparing directly theoretical force vs. distance curves with experimental curves achieved after atomic resolution.

More generally, the theoretical results show that blunt tips and homogeneous surface charging are not an obstacle to atomic resolution on insulating surfaces. The large forces introduced by these factors can be compensated by the appropriate experimental setup, as was shown in ref. [27]. This implies that it is the roughness of some insulating surfaces after cleavage which causes imaging instabilities. AFM studies on MgO [80] and alumina [181] demonstrate that these surfaces have a very high density of steps and 'nano-debris' compared with the large flat terraces which can be seen in images of NC-AFM atomically resolved systems such as CaF_2 and NaCl [39]. The inhomogeneity of the force field over a rough surface increases tip instability and makes stable imaging much more difficult.

The simulated scanlines with an O-terminated tip demonstrate that it is not necessarily the most protruding surface feature which is imaged as bright in NC-AFM. Even though the Ca ions are in the second surface layer and are shielded by the outer F layer, they are still responsible for contrast with a negative potential tip. In combination with the fact that the second contrast maximum in the O-terminated scanlines is due to the minimum in repulsion between two F ions,

this demonstrates that NC-AFM does not image atoms directly, but images the attraction between the tip and surface electrostatic potential. In general the surface potential will be strongest over atomic positions, but the contrast mechanism also depends crucially on the nature of the tip's electrostatic potential. Displacement of surface ions was shown to be an important effect in imaging of CaF_2 and modelling demonstrated that surface ions would actually jump to the tip at tip-surface separations of less than 0.4 nm. Note that the nature of the scanlines produce in this study are slightly dependent on the orientation of tip. A tilted tip would change the form of potential from the tip and would change the tip-surface interaction. The only way to establish whether the form of the scanlines is physical is by direct comparison with experiment, which is the point of the next section. However, the orientation of the tip is independent of the background force and the conclusions of the influence of the nature of these forces hold whatever the orientation.

The contrast predicted in all theoretical scanlines is much smaller than in the original experiments. This is consistent with the technical problems in the experiment, and also with more recent experiments with improved electronics, which observe smaller contrast (about 0.04 - 0.05 nm) [99]. By the magnitude of contrast alone there is no way of distinguishing whether the Ca or F sublattice is observed experimentally, as the scanlines with cation and anion terminated tips show similar contrast. However, the secondary features in the theoretical scanlines do offer the possibility of identifying the sublattice imaged. Three-dimensional plots of the theoretical image demonstrate that the secondary features are not just artifacts of the scanlines chosen. The difference of 0.11 nm in the position of the secondary features means that if any secondary features are seen in experiments, the sign of the tip potential and the sublattice can be identified by a careful analysis of their position. This possibility will be explored in the next section.

8.5 Comparison with Experiment

Although the previous section made some comparisons with experiment, the main purpose of the study was to see if modelling of NC-AFM on the CaF_2 could help in understanding imaging problems on other insulators. However, several points were highlighted which encourage further analysis. Firstly, fig. 8.2 demonstrated that frequency change vs. distance curves could be used to identify the background forces present in a given experiment. By comparing directly theoretical and experimental curves the tip-surface interaction can be characterized and used to establish a physical setup for the tip and surface. This would allow much more consistency in the modelling process than has been possible in other systems where experimental frequency change vs. distance curves where not available. Secondly, at the atomistic scale, the distance dependence of the features in scanlines can be compared with experiment to give a very good estimate of tip-surface separation during these processes. Finally, a detailed analysis of the secondary features in experimental and theoretical scanlines should offer the possibility of identifying the sublattice imaged.

The method used in this section is exactly the same as discussed in section 8.3, with only the experimental parameters changing. The experimental images and scanlines presented in this section were produced via the 'constant-height' mode of NC-AFM operation, as discussed in chapter 1. This means that simulated images and scanlines are also calculated in the same manner, with an interpolation of the calculated frequency change for a given tip-surface separation generating

the image. All frequency change vs. distance curves and scanlines were produced with a cantilever amplitude of 34.5 nm, eigenfrequency of 77 kHz and a spring constant of 6 N/m, as in all experimental results discussed. In the experiment the electrostatic forces were minimized by applying a bias between the tip and surface.

8.5.1 Macroscopic Characterization

In the first stage of the comparison between theory and experiment, frequency change vs. distance curves have been used to characterize the tip-surface interaction, and hence characterize the macroscopic properties of the tip. Fig. 8.5 shows a comparison of theoretical and experimental curves taken over the surface. For ease of reference all results from this first experiment will be labelled experiment 1. The experimental curve was taken immediately after achieving atomic resolution at 139.5 Hz. This was the largest frequency change used in a series of images of the surface demonstrating increasing contrast, but no evidence of ion jumps. Since the tip moves closer with increasing frequency change, it is reasonable to assume that at 139.5 Hz the tip is close to the theoretical limit for ion jumps given previously, hence the experimental curve has been calibrated so that this frequency change is at 0.4 nm.

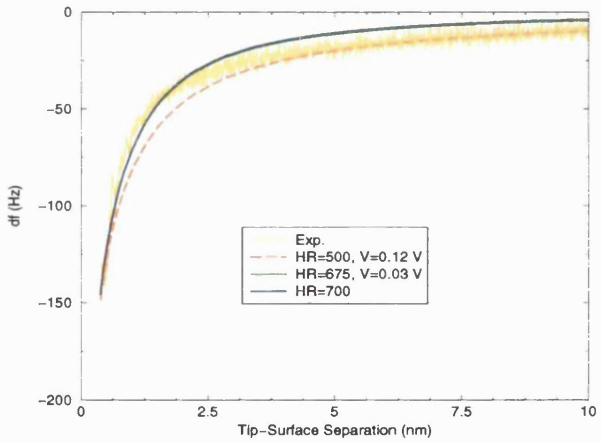

Figure 8.5: Comparison of theoretical and experiment 1 frequency change vs. distance curves over the CaF_2 (111) surface. Note that the legend is given in terms of the product of the Hamaker constant (H) and radius (R), but H is always 1.0 eV and only the radius changes.

Fig. 8.5 contains three theoretical curves produced using different macroscopic tip radii and applied bias. Note that two of the curves, HR=700 and HR=675, are so similar that it is difficult to distinguish them at some tip-surface separations. Varying the tip radii and the applied bias directly changes the background van der Waals and electrostatic forces. Each of the curves reproduces the largest experimental frequency change, 139.5 Hz, at around 0.4 nm. The best fit to the experimental curve is found with a radius in the range 675 - 700 nm and an applied bias in the range 0.0 - 0.03 V, this gives values which are within experimental error at all points and gives very good agreement in the critical 0.4 - 2.0 nm range, the range which most affects atomic resolution (for example, see chapters 6 and 7). Fig. 8.5 shows two theoretical curves at opposite extremes of this range and it is clear that they are practically indistinguishable. This demonstrates that the background force is dominated by the van der Waals force between blunt macroscopic tip and

surface, and is consistent with the fact that the tip was blunted by crashing into the surface before imaging and that the electrostatic force has been minimized by experimentally applied bias. The remaining dashed curve in fig. 8.5 emphasizes the dominance of van der Waals in the experimental curve, as if the radii is reduced to 500 nm and the bias is increased to 0.12 V, there is a large deviation from the experimental curve in the 0.4 - 2.0 nm range even though the theoretical curve still matches experiment at very short and very long range. All further theoretical results are calculated using a macroscopic tip of radius 675 nm and an applied bias of 0.03 V.

8.5.2 Theoretical Images

Anion Terminated Tip

As in previous studies, at present it is impossible to identify the microscopic structure of the tip, so simulations were performed with both an anion and cation terminated nano-tip. The first simulations were performed with the nano-tip orientated so that a O^{2-} ion was at the apex and the tip has an effective negative potential. Fig. 8.6 shows three simulated images taken at different tip-surface separations. The images are orientated such that the white line is along the direction (221) as shown in fig. 8.1, passing over calcium sites and both types of fluorine site. Since their is no way of telling the actual height in experimental images, the average frequency change across the image must be used as a measure of the tip-surface separation. In experiments the tip is held at a constant height and the change in frequency over the surface is measured, but the average frequency change over the whole image is an effective measure of distance. The closer the tip is to the surface the stronger the overall attractive force is and therefore the larger the magnitude of the average frequency change. The tip-surface separations used in the theoretical study were chosen to cover the range of average frequency changes seen in experimental images. The average frequency change in the images in fig. 8.6 was as follows: (A) -120.88 Hz; (B) -129.09 Hz; (C) -138.67 Hz. The images were generated by calculating the frequency change at a large number of points and then using symmetry to create an image of the surface unit cell which can be repeated across the surface. For simplicity only a small section of the simulated image of the surface is calculated. The bright area in the top-right of each image is an artifact and should be ignored.

In fig. 8.6, maximum contrast, i.e. brightness, in the simulated images is over the Ca ions in the surface. An increase in contrast can be seen half-way between bright spots along the direction parallel to the white lines and along other equivalent directions. The images also demonstrate a clear qualitative change in contrast as the tip moves closer to the surface. The bright spots seen at 0.5 nm are non-circular, but as the tip moves closer the spots become more circular until they are almost perfect discs at 0.4 nm. The change in images as a function of tip-surface separation can be analyzed more quantitatively by taking scanlines out of the image.

Fig. 8.7 shows five simulated scanlines taken at different tip-surface separations, along the white line shown in fig. 8.6. Scanlines A, C and E are taken directly from the images in fig. 8.6, and scanlines B and D are added for extra detail. For ease of comparison, each scanline has been calibrated so that the smallest frequency change is at 0 Hz. The average frequency change for each curve was as follows: (A) -120.88 Hz; (B) -124.90 Hz; (C) -129.09 Hz; (D) -133.54 Hz; (E) -138.67 Hz.

As seen in the first part of this chapter, the simulated scanlines with a negative potential tip

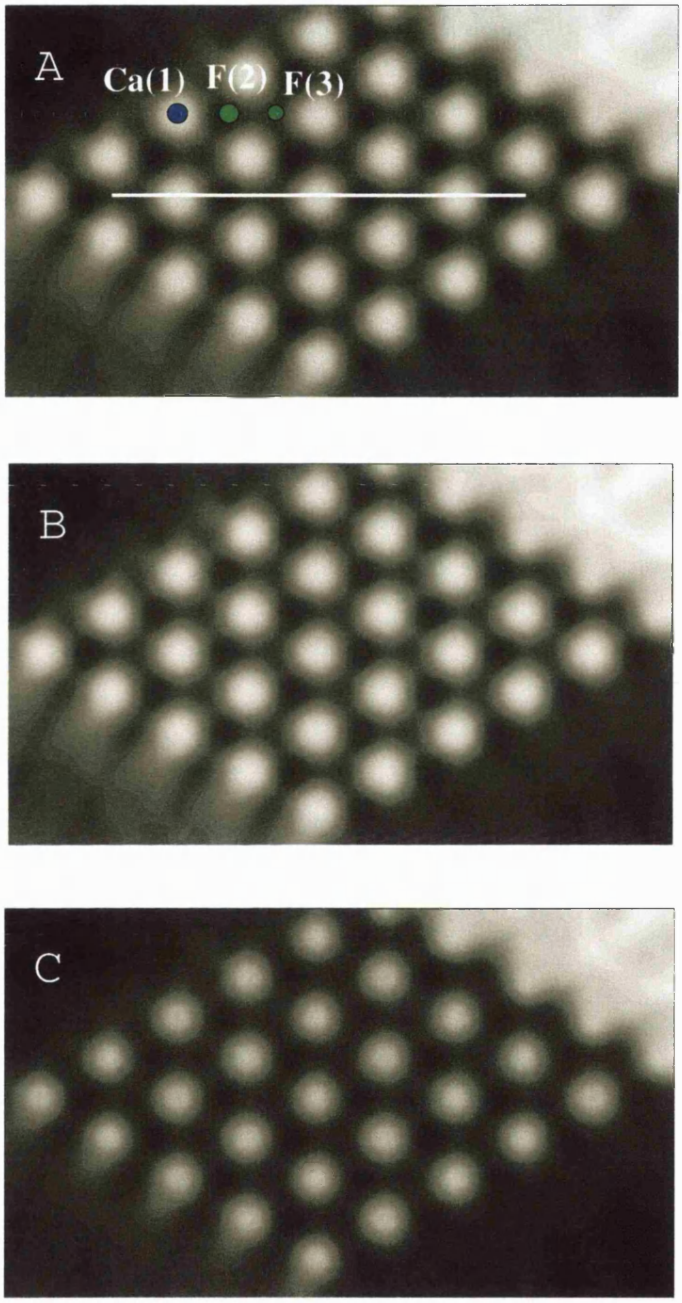

Figure 8.6: Simulated frequency change images at constant height over the CaF_2 (111) surface with an oxygen terminated nano-tip. The images are labelled according to height: A - 0.500nm; B - 0.450 nm; C - 0.400 nm. The numbers below the schematic atoms refer to the labels in fig. 8.1. The white line is along the (221) direction and shows the positions of the scanlines in fig. 8.7.

show a secondary maximum between the two F ions at 0.33 nm from the main peaks, this is a clearer representation of the contrast seen between bright spots in simulated images (fig. 8.6). The weaker repulsion over the deeper F(3) ion compared to the protruding F(2) ions is reflected

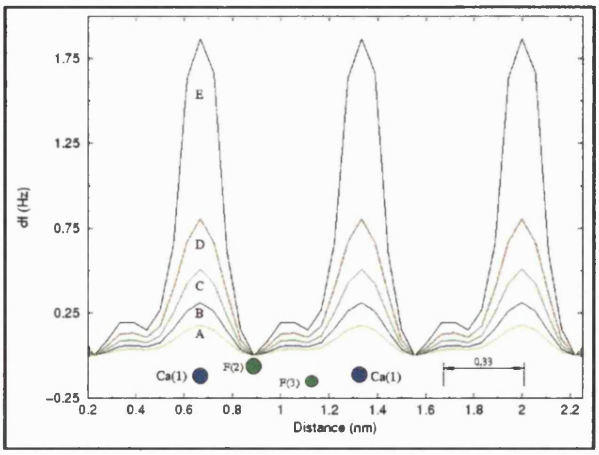

Figure 8.7: Simulated frequency change scanlines at constant height (or tip-surface separation) over the CaF_2 (111) surface along the (221) direction with an oxygen terminated nano-tip. The scanlines are labelled according to height: A - 0.500nm; B - 0.475 nm; C - 0.450 nm; D - 0.425 nm; E - 0.400 nm. The height is measured with respect to the Ca sublattice. The numbers below the schematic atoms refer to the labels in fig. 8.1.

in increased contrast, i.e. shallower scanline minimum, over the deeper ion. This makes the maximum peaks, primary and secondary, asymmetric and translates directly into the simulated images as a slower decay of brightness on one side of Ca ions. This gives the spots over the Ca ions a weak triangular shape at greater tip-surface separations.

Fig. 8.7 clearly shows the dependence of the magnitude of contrast on the tip-surface separation. At 0.5 nm the contrast over the Ca ions is about 0.2 Hz, whereas at 0.4 nm it is about 1.8 Hz. As the tip moves closer to the surface, the chemical forces between the atoms in the surface and the tip increase, producing a corresponding increase in contrast. The scanlines also show an increase in contrast at the secondary maximum as tip-surface separation is reduced. At 0.5 nm it is about 0.05 Hz and at 0.4 nm it is about 0.2 Hz. However, this means that it decreases in significance from about a 0.22 to a 0.11 as a fraction of the contrast over the Ca ions in the same distance range. As the tip is moved closer to the surface the contrast over the Ca ions gets larger, and eventually the difference in contrast over the two F sites is so small compared to contrast over the Ca sites that it is irrelevant. Effectively only the interaction over Ca ions is seen in images and as this is symmetrical, the spots become disk-like. This is because the repulsive interaction with the singly charged F^- ions producing the secondary maximum has a weaker distance dependence than the direct attractive interaction over the Ca^{2+} sites. It should be noted that all the same interactions are present at every tip-surface separation, but it is the change in their relative magnitude as a function of distance which causes a change in the images.

Cation Terminated Tip

Simulations in this section were performed with the nano-tip orientated so that a Mg^{2+} ion was at the apex and the tip has an effective positive potential. Fig. 8.8 shows three simulated images taken at different tip-surface separations. The images are orientated such that the white line is along the direction (221) as shown in fig. 8.1, passing over calcium sites and both fluorine sites.

The average frequency change for each image was as follows: (A) -120.89 Hz; (B) -129.20 Hz; (C) -139.03 Hz. The bright area in the top-left of each image is an artifact and should be ignored.

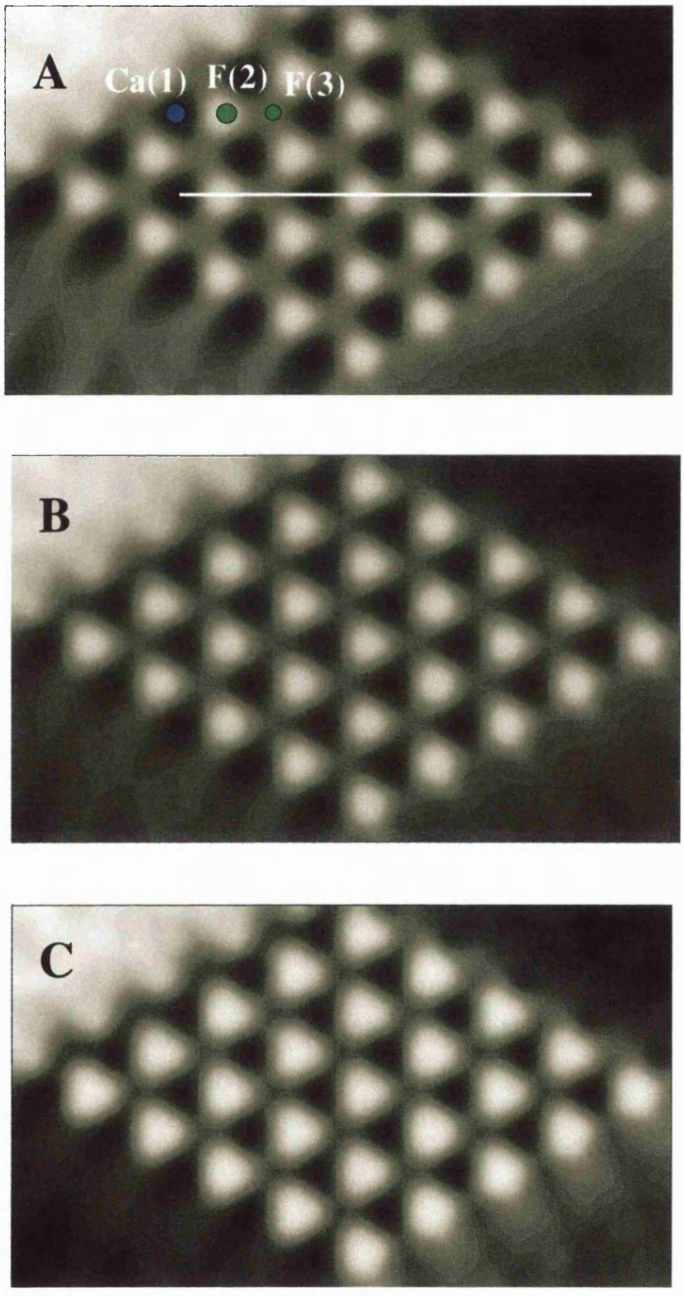

Figure 8.8: Simulated frequency change images at constant height over the CaF_2 (111) surface with a magnesium terminated nano-tip. The images are labelled according to height: A - 0.500nm; B - 0.450 nm; C - 0.400 nm. The numbers below the schematic atoms refer to the labels in fig. 8.1. The white line is along the (221) direction and shows the positions of the scanlines in fig. 8.9.

In fig. 8.8, maximum contrast in the simulated images is over the F(2) (see fig. 8.1) ions in the surface. The contrast pattern in the images is consistently triangular at all tip-surface separations, although a slight change in brightness of the contrast features can be seen. As before this behaviour can be analyzed more quantitatively by taking scanlines from the images.

Fig. 8.9 shows five simulated scanlines taken at different tip-surface separations, along the white lines shown in fig. 8.8. Scanlines A, C and E are taken directly from the images in fig. 8.8, and scanlines B and D are added for extra detail. For ease of comparison, each scanline has been calibrated so that the smallest frequency change is at 0 Hz. The average frequency change for each curve was as follows: (A) -120.89 Hz; (B) -124.90 Hz; (C) -129.20 Hz; (D) -133.81 Hz; (E) -139.03 Hz.

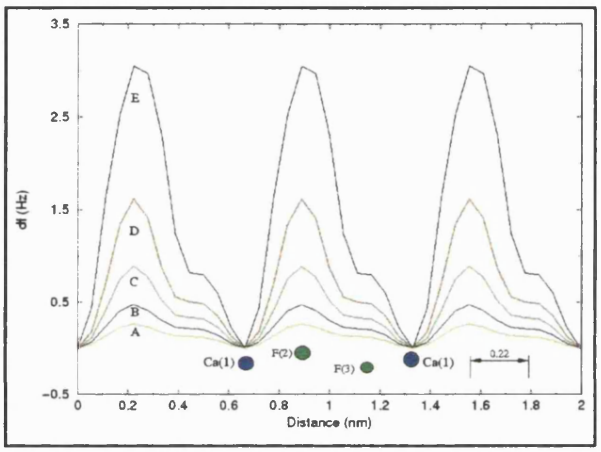

Figure 8.9: Simulated frequency change scanlines at constant height (or tip-surface separation) over the CaF_2 (111) surface along the (221) direction with a magnesium terminated nano-tip. The scanlines are labelled according to height: A - 0.500nm; B - 0.475 nm; C - 0.450 nm; D - 0.425 nm; E - 0.400 nm. The height is measured with respect to the Ca sublattice.

As in the scanlines in the first part of this chapter, a shoulder can be seen at 0.22 nm next to the main peaks in the simulated scanlines and this is responsible for the triangular contrast seen in the simulated images (fig. 8.8). The shoulder elongates the contrast over the F(2) ions in the [221] and equivalent directions, producing the characteristic triangular shape. Again, fig. 8.9 clearly shows the dependence of the magnitude of contrast on the tip-surface separation. At 0.5 nm the contrast over the F ions is about 0.25 Hz, whereas at 0.4 nm it is about 3.0 Hz. The shoulder on the main peaks due to this interaction increases in size as the tip moves closer, at 0.5 nm it is about 0.1 Hz and at 0.4 nm it is about 0.8 Hz. However, unlike the secondary maximum in fig. 8.7, even at 0.4 nm the shoulder is still a significant fraction of the contrast over the F(2) ions. It only decreases from 0.46 at 0.5 nm to 0.27 at 0.4 nm. This is because the primary and secondary features in fig. 8.9 are due to interactions with effectively the same distance dependence, they are both due to the interaction of the tip with the potential from an F^- ion. The images in fig. 8.8 directly reflect the significance of the shoulder at all tip-surface separations, even at 0.4 nm the bright spots are clearly triangular due to the convolution of the interactions of the tip with both F sites. In principle, disk-like bright spots, as in fig. 8.6, would be achieved if the tip-surface separation could be reduced indefinitely, but 0.4 nm is already almost at the limit where ion jumps

begin and the tip cannot move any closer without being contaminated.

8.5.3 Experimental Images

Figures 8.10, 8.11 and 8.12 show a series of constant height experimental images over the CaF_2 surface from experiment 1. The experiment was performed with a cantilever amplitude of 34.5 nm, eigenfrequency of 77 kHz and a spring constant of 6 N/m. The tip used in this experiment was crashed into the surface just prior to producing these images. These images were produced by approaching the surface gradually until periodic contrast was achieved and then the frequency change was increased in magnitude to generate images at closer tip-surface separations. It should be noted that although these images are produced via the constant height mode of NC-AFM operation and frequency change is not constant, the average frequency change across an image will increase in magnitude as the tip-surface separation is reduced. Figure 8.10 is the first image in the series and was generated with an average frequency change of -120.7 Hz. Figures 8.11 and 8.12 show images at smaller tip-surface separations with average frequency changes of -126.7 Hz and -139.5 Hz respectively. The white lines in the images are along the 221 direction.

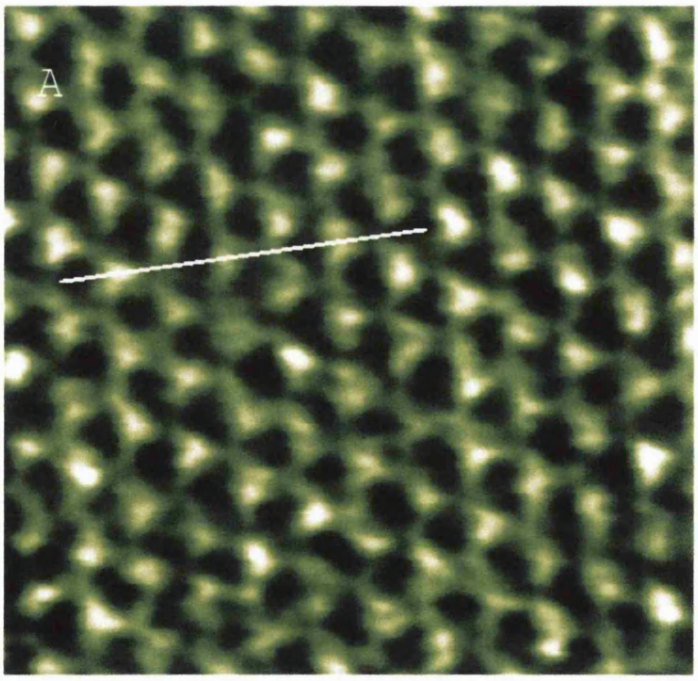

Figure 8.10: Experiment 1 NC-AFM image of the CaF_2 surface taken at constant height with an average frequency change of -120.7 Hz. The white line is along the 221 direction.

The most evident pattern in the series of images is that there is very little change in the nature of the contrast. All the images demonstrate a triangular pattern with apexes along the 221 and equivalent directions on the (111) CaF_2 surface, and this pattern is constant over the tip-surface separation sampled here. Although the nature of the contrast remains the same as the tip-surface separation is reduced, the magnitude of the contrast does not. The average contrast in image A

in fig. 8.10 is 4 Hz, in image B in fig. 8.11 it is 6 Hz and in image C in fig. 8.12 it is 8 Hz.

The behaviour of the contrast features as a function of tip-surface distance can be seen even more clearly in the scanlines shown in figure 8.13. These scanlines are taken directly from the experimental images along the white lines in figures 8.10, 8.11 and 8.12. The scanlines show that the triangular nature of the contrast pattern in images is due to a secondary smaller maximum, or shoulder, next to the largest maximum in the scanlines. By comparing the position of the secondary maximums in the scanlines with the experimental images, it is easy to see that these secondary peaks elongate the contrast in the 221 and equivalent directions away from the bright spots over the primary maximum, giving it a characteristic triangular appearance. This behaviour is consistent at all tip-surface separations as the scanlines show that the magnitude of both the primary and secondary peaks increases with decreasing tip-surface separation. A statistical analysis of 73 pairs of primary and secondary maxima in 15 separate scanlines from the images, gives the average distance of the secondary peak from the primary as 0.247 nm with an error of ± 0.05 nm. Analysis of the scanlines also gives the ratio of the heights of the primary and secondary maxima as 0.55 ± 0.37 in fig. 8.10, 0.51 $\pm$ 0.36 in fig. 8.11 and 0.41 ± 0.13 in fig. 8.12, confirming that they remain relatively consistent as the tip approaches the surface.

If these images are compared with the theoretical results, it is immediately evident that they correspond very well with those images produced with the cation terminated tip with a positive potential. Fig. 8.8 demonstrates that the theoretical model predicts a triangular contrast pattern at all tip-surface separations with a cation terminated tip. The anion terminated tip images in fig. 8.6 demonstrate a much more disk-like contrast pattern. This is also confirmed by a comparison of the theoretical and experimental scanlines. The cation terminated tip scanlines in fig. 8.9 show a secondary peak, or shoulder, next to the primary peaks, as in the experimental scanlines in fig. 8.13. Theory also predicts that the ratio of the size of the primary and secondary peaks in scanlines with a cation terminated tip decreases slightly as the tip-surface separation is reduced. Between 0.5 nm and 0.4 nm tip-surface separation, theory predicts that the ratio of heights changes from 0.46 to 0.27, which compares quite well with the change observed in experiment 1, 0.55 to 0.41, over the same change in image average frequency change. This contrasts with the much smaller ratio seen for modelling with an anion terminated tip. The positions of the shoulders also correspond very well, with theory predicting them at 0.220 nm and experiment at 0.247 ± 0.05 nm.

For comparison, an image from a different experiment is presented in fig. 8.14, for ease of reference this experiment is called experiment 2. This experiment was performed at constant height with a cantilever amplitude of 34.5 nm, eigenfrequency of 84 kHz and a spring constant of 6 N/m. The tip used in this experiment was not crashed before imaging. Images of the surface are taken such that scanning begins at the bottom of fig. 8.14. In this experiment no frequency change vs. distance curve was taken, so the theoretical model cannot be fully characterized for comparison with this data. However, the image demonstrates some interesting features which are important to discuss on a qualitative level.

The image in fig. 8.14 is taken from a series of images, where this image represents the largest average frequency change magnitude and has the smallest tip-surface separation during scanning. The other images at greater tip-surface separation in the series demonstrated contrast across the whole image very similar to that shown in the bottom, below the arrow, of fig. 8.14. This pattern of contrast is different to the triangular pattern seen in figures 8.10, 8.11 and 8.12, and

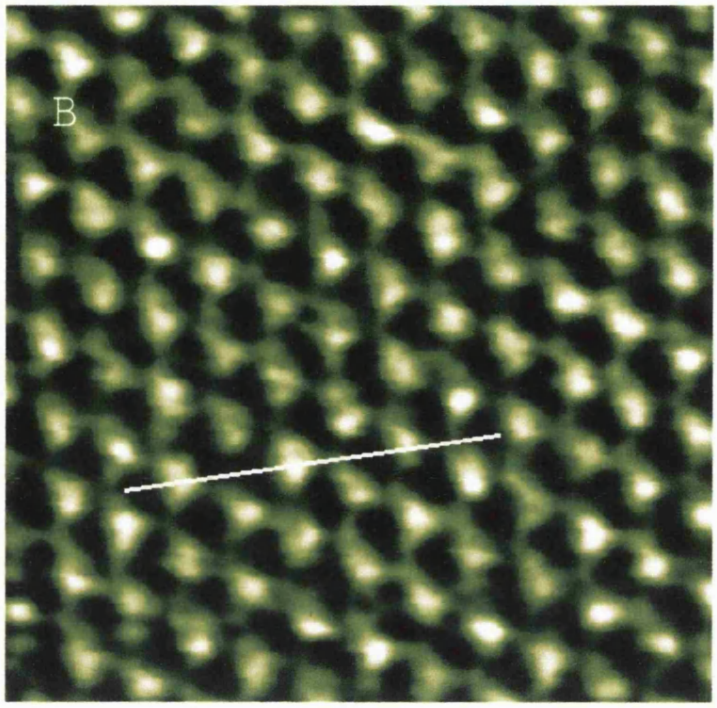

Figure 8.11: Experiment 1 NC-AFM image of the CaF_2 surface taken at constant height with an average frequency change of -126.7 Hz. The white line is along the 221 direction.

demonstrates a much more disk-like contrast. This initial disk-like contrast changes dramatically at about 2/3 through the scan, shown by the arrow in fig. 8.14, where the contrast becomes much more triangular. In fact this change occurs at one pixel in the image i.e. at one point over the surface and is indicative of a change in the nature of the tip at this point. This change in the nature of the contrast can also be seen in the scanlines taken from the image. Before the contrast change, in scanline b, the contrast is dominated by the large primary maximums and the secondary maximums are not large, or close, enough relative to the primary peaks to produce a triangular pattern. However, after the contrast change, in scanline a, the contrast now demonstrates shoulders on the primary peaks, as in fig. 8.13, which elongates the contrast.

If experiment 2 is now compared qualitatively with theory, again the behaviour of the contrast is consistent with theoretical predictions. Before the contrast change, the image and scanlines correspond well with the theoretical predictions for an anion terminated tip with a negative potential. The disk-like bright spots are very similar to those seen in fig. 8.6 and scanline b shows the characteristic domination of the primary maximum in contrast and a small secondary maximum. After the contrast change, the experimental image demonstrates a triangular pattern very similar to that seen in figs. 8.10, 8.11 and 8.12. As discussed previously, this corresponds very well with the theoretical predictions for a cation terminated tip with a negative potential.

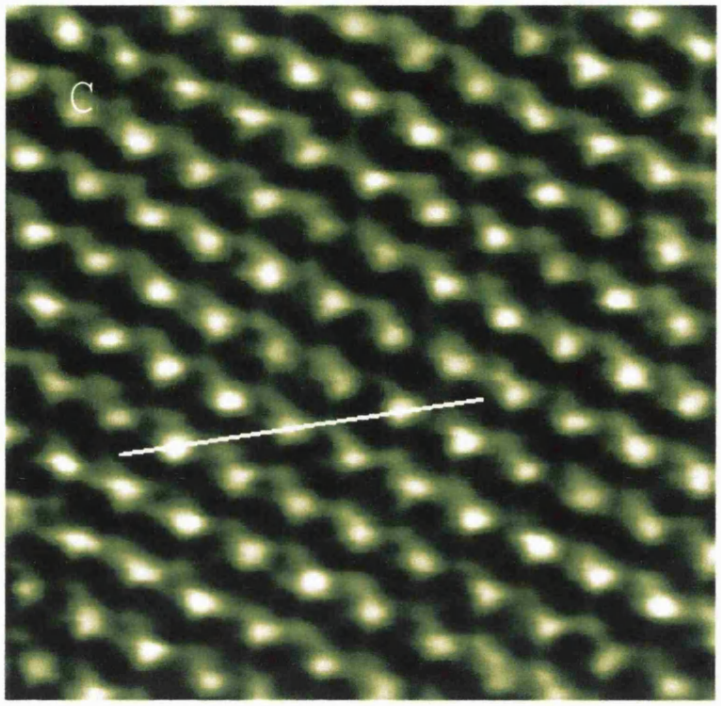

Figure 8.12: Experiment 1 NC-AFM image of the CaF_2 surface taken at constant height with an average frequency change of -139.5 Hz. The white line is along the 221 direction.

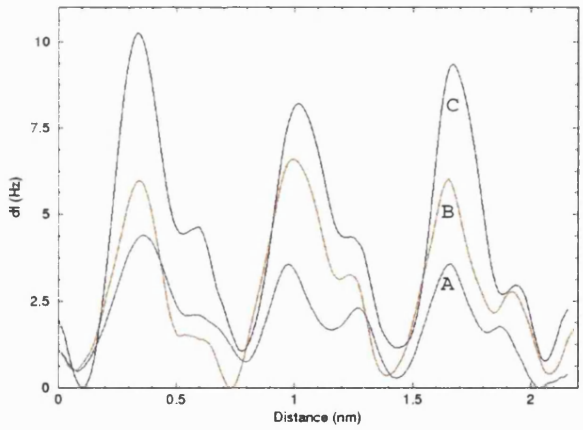

Figure 8.13: Experimental scanlines taken along the white lines in figures 8.10, 8.11 and 8.12. The labels on the scanlines correspond to the labels on the images.

8.5.4 Discussion

The main purpose of comparison between experiment and theory is to extract more information than is available from either field alone. This study has demonstrated that many of the interpretation problems inherent in NC-AFM experimental imaging of the CaF_2 surface can be solved by comparison with a theoretical model of the same system using experimental parameters.

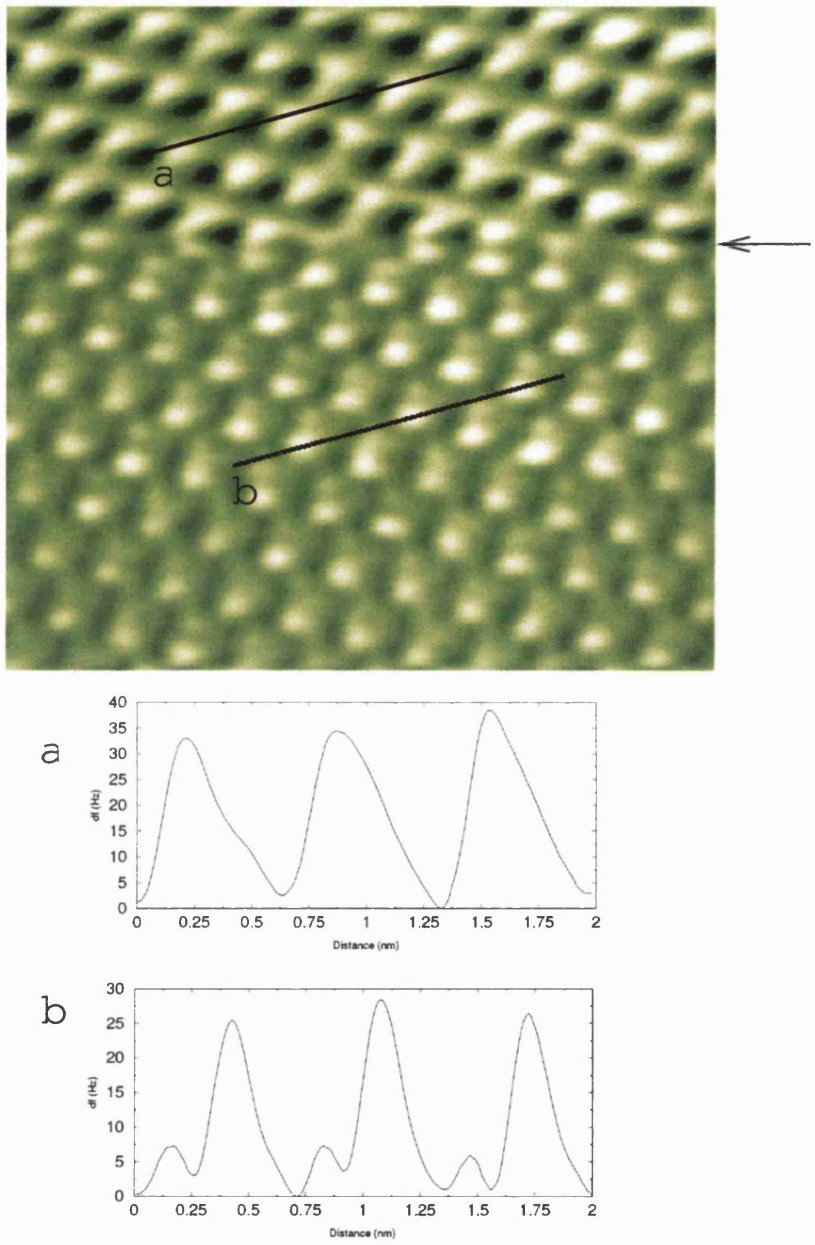

Figure 8.14: Experiment 2 NC-AFM image and example scanlines of the CaF_2 surface taken at constant height with an average frequency change of -146.0 Hz. The scanline is taken along the lines shown in the image. Both lines are long the 221 direction. The arrow indicates where the contrast undergoes a significant change.

A comparison of experimental and theoretical frequency change vs. distance curves showed that the tip-surface interaction in experiment 1 was dominated by van der Waals force and that electrostatic forces due to surface and/or tip charging were negligible. The model predicts that the tip radius was in the range 675 - 700 nm and a residual electrostatic force could be present and

represented by a bias in the range 0.0 - 0.03 V. The general consistency between the theoretical and experimental results as a function of tip-surface separation support the assumption that the tip-surface distance in experimental images is in the range of 0.4 - 0.5 nm. Due to ion jumps the range cannot be closer and it cannot be much greater as contrast very rapidly becomes less than is experimentally detectable as the tip-surface separation is increased.

The magnitude of contrast observed in experiments was larger than that predicted by modelling, suggesting that either contrast is exaggerated in experiments or theory underestimates the strength of the chemical tip-surface interaction. Since it is impossible to be certain of the chemical nature of the tip in experiments, this latter possibility cannot be ruled out, but none of the conclusions in this study depend on the absolute magnitude of the contrast.

Both experiment and theory demonstrated that the contrast in images depends crucially on the nature of the tip. Modelling predicted that an anion terminated tip with a negative potential would image the Ca sublattice as bright and that the pattern of contrast would be more or less disk-like at all tip-surface separations. For a cation terminated tip with a positive potential, modelling predicted that the protruding F sublattice would be imaged as bright with the deeper F sublattice producing a triangular pattern of contrast in images. The latter case corresponds very well with experiment 1 and is supported quantitatively by scanlines taken from the images. The characteristic triangular pattern is due to the interaction of the tip with the deeper F sublattice, which produces a shoulder on the primary scanline peaks due to the protruding F sublattice. The shoulders elongate the contrast producing the triangular pattern. Theory predicts that these shoulders should appear at 0.22 nm from the main peaks and this agrees well with the experiment 1 average position of 0.247 $\pm$0.05 nm. The dependence of scanline features on tip-surface separation is consistent in theory and experiment, both predict that the relative height of the primary and secondary maxima decreases slightly as the tip moves closer. Between 0.5 nm and 0.4 nm tip-surface separation, theory predicts that the ratio of heights changes from 0.46 to 0.27, which compares quite well with the change observed in experiment 1, 0.55 to 0.41, over the same change in image average frequency change.

Overall this strongly suggests that in experiment 1, the tip had a positive potential and that the protruding F sublattice was imaged as bright with the deeper F sublattice producing the triangular contrast pattern. Although most tips are initially oxidized, since the tip in this experiment was crashed before imaging, it could easily be contaminated by surface ions or induced charge to produce an effective positive potential.

The sensitivity of the contrast to the nature of the tip potential was further demonstrated in experiment 2 where a tip change was seen while scanning. The contrast changed from disk-like to triangular at one pixel i.e. one surface point of the image. This implies that the experiment initially began with a negative potential tip imaging the Ca sublattice, but then the tip was contaminated producing a positive potential tip which imaged the F sublattice. This is consistent with the idea of an initially oxidized tip with a negative potential being contaminated by Ca ions from the surface or induced charge, producing a positive potential tip.

8.6 Conclusions

This study of NC-AFM imaging of CaF_2 had two distinct approaches. First, the effect of the nature of the background force on imaging was analyzed and it was found that it does not have a large affect on the contrast mechanism in NC-AFM imaging. The much slower decay of the electrostatic force does not seem to be a significant factor in resolution, and scanlines produced using a van der Waals dominated background force were qualitatively similar to those produced with a background force dominated by long-range electrostatic forces due to tip and surface charging. More generally, the theoretical results show that blunt tips and homogeneous surface charging are not an obstacle to atomic resolution on insulating surfaces and it implies that it is the roughness of some insulating surfaces after cleavage which causes imaging instabilities. Hence, this study predicts that there should be no greater difficulty in imaging insulators such as MgO and alumina in atomic resolution if surfaces of sufficient smoothness can be produced.

The second part of the CaF_2 study focused on a direct comparison of theoretical and experimental imaging of the surface. This showed that, for the first time in NC-AFM imaging of insulating surfaces, very strong conclusions could be made about the identity of the sublattice imaged by comparing theoretical and experimental results. The results also demonstrated the importance of the nature of the electrostatic potential of the tip in imaging, as seen in previous studies (see chapter 7). The comparison was greatly aided by the availability of an experimental frequency change vs. distance curve taken after atomic resolution, which allowed the theoretical model to be fully characterized before simulating scanning.

Chapter 9

Nickel Oxide

9.1 Original Motivation

The group of Roland Wiesendanger in Hamburg has been very successful at studying magnetic properties of surfaces with spin-polarized STM and this developed into an interest in studying similar systems with NC-AFM. They decided to try and measure the difference in exchange force over opposite spin Ni ions in the NiO surface with a metal coated NC-AFM tip. However, the experimental difficulties involved are large and they wanted to get some theoretical backup to try to aid in interpretation if they were successful. They approached us, and we agreed to investigate whether it should be possible to measure the exchange force from a theoretical perspective and the best way to measure it experimentally.

9.2 Introduction

As discussed in chapter 3, very recently attempts have been made to use magnetic tips in NC-AFM to try to image the magnetic structure of materials on the atomic scale. Due to the ease of preparation of an atomically clean surface [2], most of these attempts have tried to measure this phenomenon on the anti-ferromagnetic nickel oxide surface. As yet, no difference in contrast over opposite spin Ni ions has been observed, so it would be useful to study the interactions involved theoretically to establish whether it should be possible. In this chapter a simple model of a magnetic tip has been used to measure the difference in interaction over opposite spin Ni ions in an *ab initio* simulation. The contribution of the exchange force to the tip-surface interaction is calculated and used to predict whether the spin contrast over Ni ions would be observable in NC-AFM experiments.

Nickel oxide is a classic example of one of the class of materials which have excited and perplexed over the past 70 years, first-row transition metal monoxides. In a purely ionic picture of NiO the Ni^{2+} ions have a partially filled d shell in a $3d^8$ ground-state configuration. According to conventional band-theory this should result in metallic behaviour, yet NiO is an insulator with a bulk band gap of 4.3 eV [182]. It crystallizes in the rock-salt structure (as MgO) with a lattice constant of 0.417 nm and a high-spin anti-ferromagnetic spin structure at low temperatures (see fig. 9.1). Its Néel temperature (T_N) is 523 K and it undergoes a magnetic phase transition above

this point.

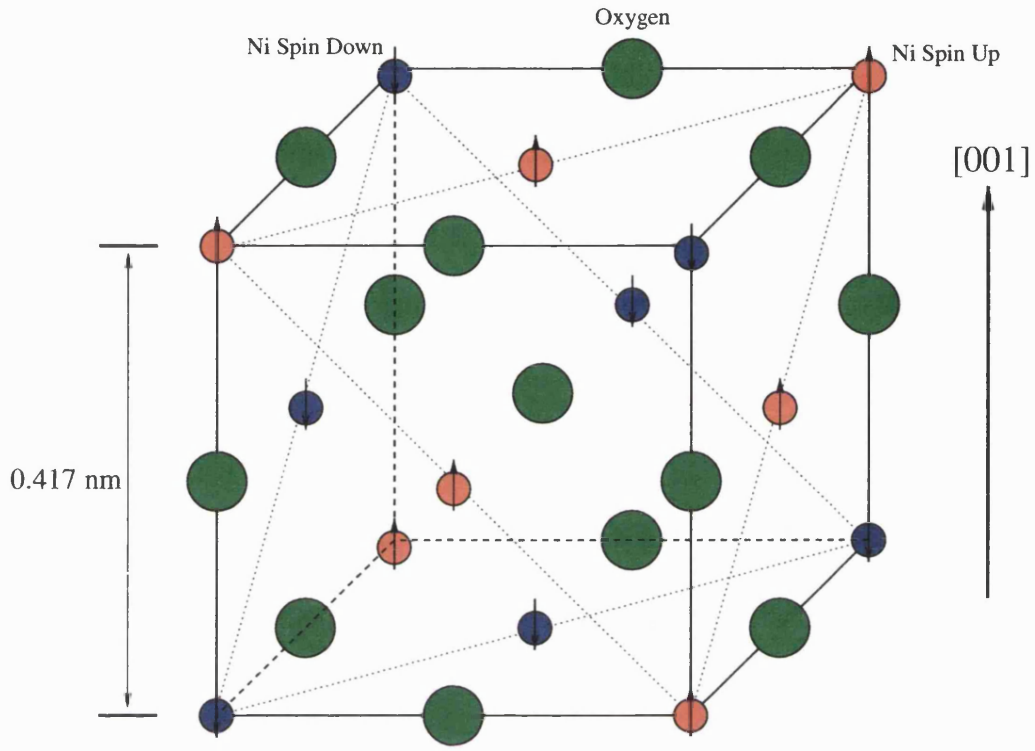

Figure 9.1: Structure of NiO, showing the AF_2 anti-ferromagnetic spin structure with adjacent (111) planes of similar spin Ni ions.

Understanding the electronic structure of NiO, and other transition metal monoxides, has been a topic of great interest for many theorists. Mott [183] proposed that the band gaps in these materials were due to strong on-site repulsion between the d-electrons of the metal ions. Coulomb repulsion between the d-electrons localized on the metal ions increases their effective band volume and produces a pseudo-filled band. Early band theory calculations of NiO based on the local spin density approximation (LSDA) [184] predicted a narrow gap spanned by unoccupied Ni d-states, but underestimation of the repulsion inherent in LSDA methods meant that the antiferromagnetic ordering was required to produce the gap. In the absence of antiferromagnetic ordering, LSDA gives the same one-electron energies for the occupied and unoccupied d-orbitals with the same spin, since they experience the same local effective potential. Unrestricted Hartree Fock (UHF) methods, although by definition including no controlled representation of correlation, have been successfully used to study the structural and magnetic properties of some of these transition metal monoxides [185]. In the HF approximation the effective potential is non-local and occupied and unoccupied d-orbitals have different energies. However, HF methods overestimate the size of the band gap substantially and combinations of LSDA and UHF [186, 187] are needed to provide a more complete picture of NiO's electronic structure. The treatment of correlation in these oxides remains difficult and the role of O($2p$) - Ni($3d$) hybridization in the valence band has proved especially difficult to predict reliably [187]. However, most studies [187, 188, 189] predict that the upper edge of the valence band is of O($2p$) character and that NiO should be classed as a

'charge-transfer' insulator, as opposed to a Mott-Hubbard insulator where the conduction and upper valence edge are of the same character. This consensus can only really be thoroughly confirmed by more calculations with an improved treatment of electron correlation.

In contrast, the magnetic properties of NiO are well known and various techniques have established the antiferromagnetic AF_2 structure as the most stable with each Ni ion having 2 unpaired electrons. The AF_2 structure is shown in fig. 9.1, with adjacent (111) sheets of similar spin Ni ions. This spin configuration has two components, both due to the non-local exchange interaction between Ni electrons. The direct exchange interaction between nearest neighbour Ni ions favours pairing of spins to lower the energy. However, a much stronger interaction comes from the super-exchange between the next-nearest neighbour Ni ions [184, 185, 188]. The hybridization of the O($2p$) and Ni($3d$) states, i.e. covalent bonding between the Ni and O, is stronger than the coupling of the $d-d$ states between nearest neighbour Ni ions and opposite spin next-nearest neighbour ions are energetically favoured. This makes the anti-ferromagnetic spin structure the ground state of NiO.

The (001) surface of NiO has been shown by LEED studies [190, 191] to be an almost perfect bulk termination, with no rumpling and only a 2% relaxation of the outer layer. The surface has also been atomically resolved by NC-AFM [192] and elevated temperature STM [188], clearly demonstrating the stability of the (1×1) reconstruction. Thorough UHF calculations [193] on a monolayer of NiO confirmed the stability of the anti-ferromagnetic phase and also demonstrated the usefulness of HF methods on these systems. Although it cannot model all the subtleties of the surface electronic structure (for discussion of the complexities of NiO surface electronic structure see refs. [194, 195]) of NiO, UHF is an excellent technique for modelling of the structural and magnetic properties of the surface.

9.3 Theoretical Method

Since the interactions of interest for atomic scale magnetic imaging are quantum mechanical in nature, a full *ab initio* treatment of the NiO surface and the tip is required. All calculations on NiO were performed using the periodic Unrestricted Hartree Fock (UHF) method as implemented in the CRYSTAL 98 code (see section 3.2.1). Although the structural properties of an insulator like NiO could be well-represented within the SM, the spin structure can only be modelled by a quantum mechanical technique. As discussed previously, UHF has proven successful in modelling NiO and gives an exact representation of electron exchange, the interaction crucial in atomic scale magnetic imaging.

9.3.1 Setup

All calculations were performed on the (001) NiO surface (see fig. 9.1). The surface is represented by a periodic three layer slab, with a (2×1) surface unit cell, giving a total of 12 atoms in the unit cell. Since the (001) surface of NiO demonstrates no rumpling and very little relaxation, the perfect bulk termination with the experimental lattice constant of 0.417 nm has been used. 10 k-points in the 1BZ were used in all calculations. The Gaussian basis sets for Ni and O were taken from previous studies on NiO [185]. The localized crystal orbitals consisted of 25 atomic orbitals

for Ni and 14 for O:

- Ni : 1s(8)2sp(6)3sp(4)4sp(1)5sp(1)3d(4)4d(1)
- O : 1s(8)2sp(4)3sp(1)4sp(1)

where the numbers in brackets are the numbers of Gaussian functions used to describe the corresponding shell. Test calculations on the surface alone confirmed the anti-ferromagnetic spin structure is more stable than the ferromagnetic by 17 meV/Ni, which is in good agreement with previous UHF studies [193].

The magnetic tip is represented by a single spin polarized atom. In most experiments the silicon NC-AFM tip is coated by a thick layer of iron which is prepared so that the end of the tip is ferromagnetic. Since the exchange interaction between tip and surface is so short-range it is reasonable to approximate the whole tip by one spin polarized atom. A sodium atom and a hydrogen atom were used to represent two possible models of the tip. These models were chosen to represent both a chemically active (with respect to the NiO surface) spin-polarized tip, Na, and inert spin-polarized tip, H. This will demonstrate how different types of tip could affect the measurement of the exchange force. In this initial study relaxation due to the proximity of the tip has also been neglected. The Gaussian basis set for H is from ref. [196] and the Na set is from [197], with 8 orbitals for H and 15 orbitals for Na:

- H : 1s(5)2sp(1)3sp(1)3d(1)
- Na : 1s(8)2sp(5)3sp(1)4sp(1)

All frequency change curves were produced with a cantilever amplitude of 6.7 nm, eigenfrequency of 201 kHz, spring constant of 37 N/m, and a frequency change of 49 Hz, as in experiments on NiO [198]. γ_0 for these parameters is 4.95.

9.4 Results

In an attempt to directly calculate the effect of the exchange force in NC-AFM, adiabatic energy curves were calculated as a function of tip-surface separation over spin up and spin down Ni ions. These energy curves were then fitted and differentiated to get the force as a function of distance. Fig. 9.2 shows the force on a spin up sodium probe, with one unpaired electron, as a function of distance from a spin up Ni ion, a spin down Ni ion and an oxygen ion in the NiO surface. The first thing to notice is the features common to both Ni curves, maximum attractive force at 2.8 Å from the surface and the onset of repulsive force at about 2.4 Å. However, between 2.5 and 4.2 Å there is a clear difference in the force between the interaction over the spin up Ni and the spin down Ni. This is a direct reflection of the change in the exchange force for the spin up Na interacting with the spin up Ni and the spin down Ni. The maximum difference, at 2.8 Å, is about 0.17 eV/Å, but it is still about 0.05 eV/Å at 4.0 Å. The force over the oxygen ion is less than over both types of Ni ion. The adsorption energy of the Na over the Ni ions is about -2.00 eV and over the oxygen ion is -1.40 eV. The difference in adsorption energy is due to the difference in surface potential probed by the Na ion over the two sites. Above the nickel site, the effectively positive

Na probe is repelled by the positive Ni^{2+} ion but is also strongly attracted to the 4 neighbouring O^{2-} ions (see fig. 9.1). Above the oxygen site, the Na is attracted to the negative O^{2-} ion but is repelled by the 4 neighbouring Ni^{2+} ions, making it energetically less favourable than the Ni as an adsorption site. It is this net interaction of the Na probe with the surface potential which gives the Ni as the favoured adsorption site.

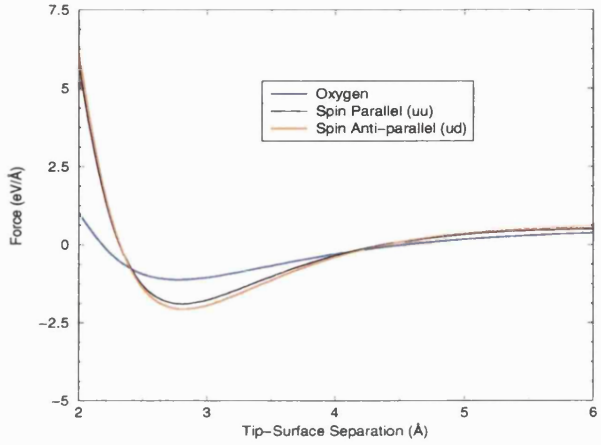

Figure 9.2: Force as a function of tip-surface separation for a spin up Na probe over spin up Ni, spin down Ni and oxygen ions in the NiO surface.

Charge transfer between the Na atom and the surface also plays a role in the interaction. The ionization energy of Na (5.1 eV) is fairly close to the position of the top of the NiO valence band, so as it approaches the surface it transfers charge to the oxygens, at 2.5 Å about 0.25e has been transferred to the surface. However, there is a slight difference in the behaviour of the charge of the Na compared to the spin. The spin of the Na atom is mainly due to the interplay of the spin up $4sp$ orbital and the spin down $3sp$ orbital. As the tip approaches the surface, charge is more easily transferred from the outer $4sp$ orbital producing a slightly faster reduction of spin compared to charge. For the interaction over the oxygen ion the charge transfer is slightly increased, to 0.28 e at 2.5 Å. It is important to note that the values of charge and spin are calculated using Mulliken population analysis [199], and the accuracy of the values is not that high. Therefore small differences cannot be trusted and it is difficult to make a conclusive analysis. Nevertheless, for the purpose of investigating the magnitude of the exchange force, this approach is valid.

In fig. 9.3, the same calculation is repeated, but now with a spin up hydrogen atom, with one unpaired electron, as a probe. The hydrogen atom is much more inert to the NiO surface than the Na atom [200] and this can be seen by the lack of a minimum in the force curves, even over the oxygen ion. There is almost no interaction until about 3.5 Å from the surface when repulsion between the Ni/O and H begins. Again, there is a clear difference in force over the spin up and spin down Ni ions, but it is weighted a little closer to the surface than for the Na probe. At 2.5 Å the difference in force is about 0.17 eV/Å, which is the same magnitude as for the Na probe at 2.8 Å. It increases steadily from that point and is about 1.0 eV/Å at 2.0 Å.

Charge transfer processes do not play a significant role for the interactions of the H probe. The large ionization energy of H (13.5 eV) means that there is very little charge transfer between the probe and surface. Above the Ni ions, only 0.017 e is transferred at 1.5 Å. This amount of

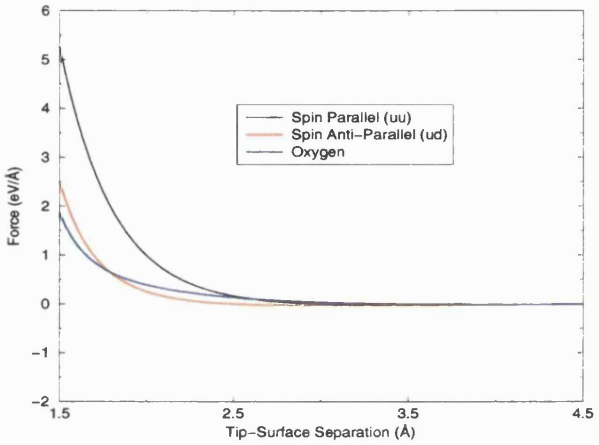

Figure 9.3: Force as a function of tip-surface separation for a spin up H probe over spin up Ni, spin down Ni and oxygen ions in the NiO surface.

charge is much smaller than is meaningful to analyze with the Mulliken method. Even above the oxygen ion only 0.17 e has been transferred at a separation of 1.5 Å and at 2.5 Å, it is already reduced to 0.018 e. For the distances of interest in this study, the hydrogen probe can be effectively considered as neutral. The adsorption energy of the H over the Ni ions is about -0.02 eV and over the oxygen ion is -0.04 eV, effectively zero.

Combining the data from both force curves gives a fairly consistent estimate of the difference in force over the spin up and spin down Ni ions, and its distance dependence. Assuming the tip can scan at around 2.5 Å without ions jumping, then the force needed to be measured is of the order of 0.2 eV/Å. To understand how this would translate to frequency changes of the cantilever oscillations in a real NC-AFM experiment, the model of cantilever oscillations described in chapter 4 must be applied. For this study, there are no background forces and the cantilever oscillations are just simulated in the calculated force field due to the difference in the interaction between the H probe and opposite spin Ni ions in the NiO surface.

Fig. 9.4 shows the frequency change as a function of tip-surface separation for the difference in force over spin up and spin down Ni ions with a hydrogen probe. This effectively shows the magnitude of frequency change as a function of tip-surface separation that must be measured to see a difference over Ni ions. Since the exchange force was very similar in both the H and Na probe, the H probe was chosen for this part as it is more inert to the NiO surface and gives a minimum for exchange force detection. The most advanced low temperature NC-AFM [18], scanning at about 13 K, can measure frequency changes down to 0.05 Hz (an order of magnitude better than room temperature NC-AFM). This value has been marked on fig. 9.4 and it occurs at 3.75 Å. Assuming that a hydrogen atom is a good model of a magnetic tip, the theoretical study of NiO predicts that the difference in contrast over spin up and spin down can be seen with a low temperature NC-AFM when the lowest point of the tip oscillations brings the tip less than 3.5 Å from the surface. For the Na atom, the force decayed more slowly and hence, so would the frequency change, but the larger charge transfer and adsorption energies for the Na probe suggests that ion jumps would be much more of a problem for the Na probe. The effect of ion jumps on measuring the exchange force will be discussed in detail in the next section.

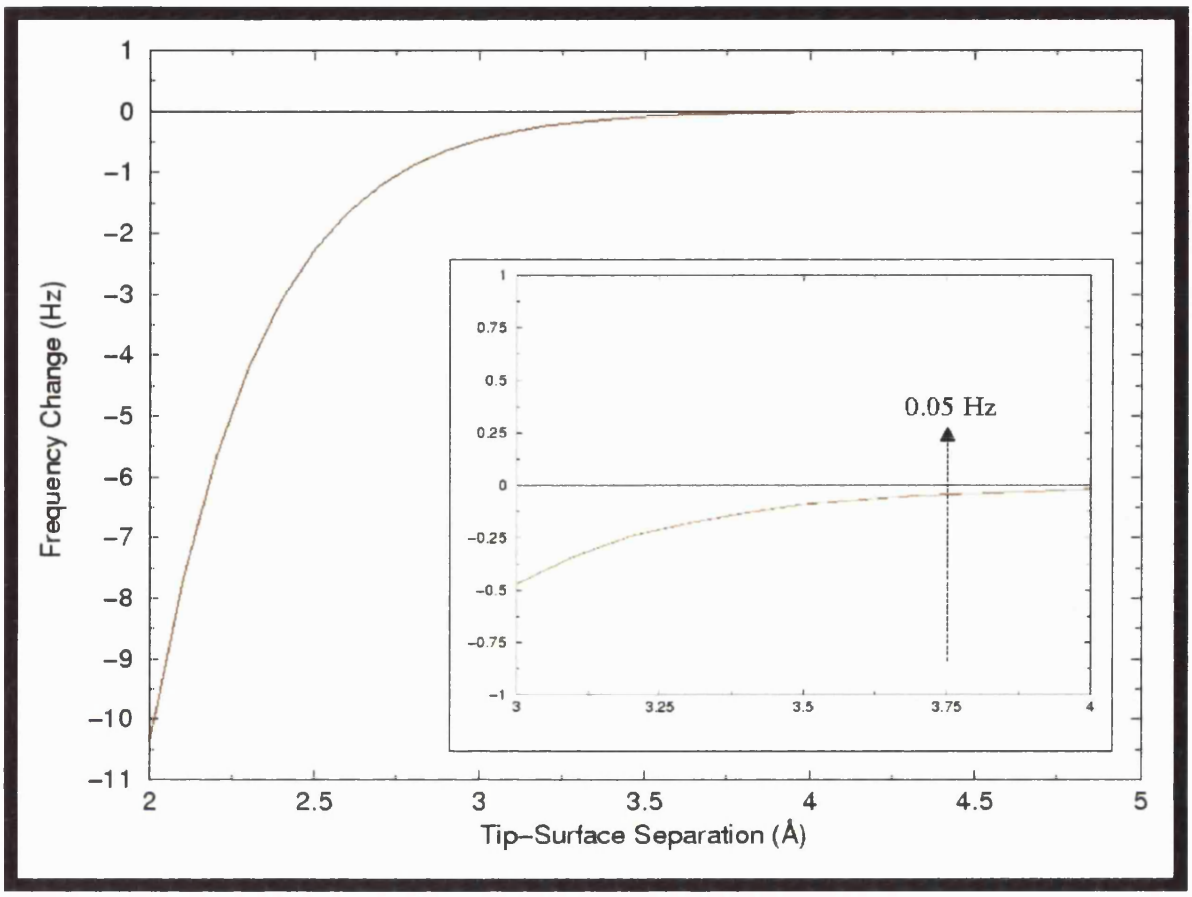

Figure 9.4: Plot of the frequency change due to the difference in force over spin up and spin down Ni ions probed with a Hydrogen atom. The inset shows a blowup of the main curve with the point at which the frequency change is 0.05 Hz labelled.

9.5 Ion Instabilities

The most significant assumption in the calculations in the previous section is that relaxation of surface ions due to interaction with the tip has been neglected. Previous studies (see chapters 7 and 8) demonstrated that surface relaxations for insulators can be of the order of 0.1 Å at tip-surface separations of about 4 Å. Since the exchange force difference is only measurable at 3.5 Å this means that relaxation could play an important role. Also, the onset of surface ion instabilities will be the limiting factor in the tip-surface separation. These instabilities cause large changes or jumps in the tip-surface force and prevent stable imaging. In all the previous systems presented in this study ions jumped to the tip at tip-surface separations greater than 3.5 Å and it is possible that ion jumps will occur before the tip gets close enough to the surface to measure the exchange force difference.

To investigate the effect of ion jumps, in this section the interaction of different metal tips with the MgO surface is used to study the importance of ion jumps to the tip. As an insulating oxide, with very small surface relaxations and little rumpling, MgO represents a good model of the NiO surface and the ion jump ranges for MgO should be a good approximation for the NiO surface.

For most of the metal tips used in experiment, the strongest interaction will be with the oxygen ions in the surface [2], therefore this section will focus on the ion jump limits for oxygen ions only. Despite this, all the arguments presented here would still be valid for jumps of the metal ions, as the main point is to translate adsorption energies of possible tip ions on the NiO surface into ion jump limits. Similar adsorption energies will produce similar ion jump ranges regardless of the chemical identity of the jumping ion.

9.5.1 Method

The setup of the calculations is the same as in fig. 4.6, with the NaCl cluster replaced by a MgO cluster of identical dimensions. A cluster of this size is a good representation of the MgO surface and is a good model for investigating ion jump processes. To model the metal tip at the microscopic and macroscopic scale, the MgO tip is replaced by a four atom metal tip forming a pyramid with its apex towards the surface. The base of the pyramid is at 0.25 nm below the conducting sphere. The interaction between atoms in the tip and surface are calculated using the method described in section 3.2.1 and the SCIFI code. Since the focus of this study is ion jumps, only the forces which influence this process have been considered i.e. microscopic and image forces. For the large forces involved in ion jumps the exchange force due to spin interaction can be neglected completely. The top layer of the cluster is allowed to relax with respect to the microscopic and image forces. The tip is frozen throughout the study.

The potentials for the MgO surface are the same as for the MgO tip used in previous studies. The initial potentials for the the metal tip and its interaction with the surface are taken from HF calculations for the interaction of palladium with the MgO surface [201]. To model tips made from metals other than Pd, the potential between the metal ions of the tip and the oxygen ions in the surface is altered directly to reproduce the adsorption potentials for the specific metal ion on oxygen sites on the MgO/NiO surface. The adsorption energies, equilibrium positions and source of information are given in table 9.1. For this study, calculations have been performed with Pd, Cu, Na and a generic metal, called M*. Pd represents a metal ion which is very weakly adsorbing, although this interaction is still much stronger than the H probe with an adsorption energy of only -0.04 eV. Cu has been shown to adsorb weakly on oxygen sites in the MgO surface [202], but demonstrates a stronger interaction than Pd. Cu is also a spin polarized atom and is therefore of possible interest as a candidate for detecting the exchange force. A Na tip has been included to represent a more strongly interacting tip, although in principle Na prefers to adsorb on Ni in NiO, its interaction with oxygen is still of interest for the purpose of ion jumps. M* represents a metal ion which is strongly adsorbing on oxygen sites in the surface.

9.5.2 Results

Fig. 9.5 shows how the force on different metal tips varies as a function of tip-surface separation over an oxygen ion in the MgO surface. For the Pd tip the force increases very smoothly as the tip-surface separation decreases, to a maximum of 1.19 eV/Å at 2.8 Å. At this distance the oxygen ion displaces by only 0.05 Å. Beyond this point the tip starts to feel a repulsive force from the surface. The force behaviour for the Cu tip is very similar to that of the Pd tip, but as expected the interaction is slightly stronger. The force increases smoothly to a maximum of 1.89 eV/Å

Metal	E_{ad} (eV)	r_{eq} (Å)	Ref.
Pd	-0.48	2.4	[201]
Cu	-0.90	2.1	[202]
Na	-1.40	2.0	This study.
M*	-4.00	2.4	N/A

Table 9.1: Comparison of adsorption energies, E_{ad}, equilibrium positions, r_{eq}, and references for adsorption of metal ions over oxygen in an oxide surface. Pd and Cu are over an MgO surface. The values for Na are taken from the adsorption on NiO from the calculations above and M* represents a generic metal which has a strong adsorption to the surface.

at 2.6 Å and at this distance the oxygen ion displaces by only 0.11 Å. Again beyond this point the tip begins to be repelled by the surface. The Na tip repeats this smooth behaviour with an increase in overall force to a maximum of 2.49 eV/Å at 2.6 Å and a displacement of oxygen by 0.20 Å. The force curve for the strongly interacting M* tip is very different to the previous tips. Although initially the curve is smooth, the force is already much larger than for the other tips. At 3.8 Å there is an abrupt jump in the force, from 5.6 eV/Å to 7.3 eV/Å, this is due to a jump of the oxygen ion below the tip. The oxygen displaces by 0.8 Å towards the tip at this tip-surface separation. This displacement remains fairly constant until at a tip-surface separation of 3.4 Å, the tip and oxygen ion are only separated by 2.6 Å. After this point the force curve becomes smooth again until at 2.4 Å there is another jump. Here the tip is so close to the surface that oxygen ions other than the one directly under the tip start to jump. However, the ion jump at 3.8 Å is of more relevance to this discussion, since this becomes the limit for NC-AFM scanning with a metal tip of M* character.

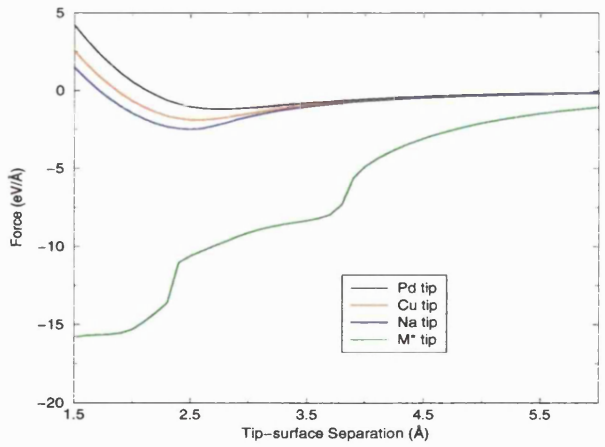

Figure 9.5: Force on the tip as a function of tip-surface separation for different metal tips over an oxygen ion in the MgO surface. Tip-surface separation is measured with respect to the equilibrium position of the oxygen ion without interaction with the tip.

9.6 Conclusions

This study demonstrated that in principle it should be possible to measure the difference in interaction of a magnetic tip over spin up and spin down Ni ions in the NiO surface using NC-

AFM. Using a spin polarized hydrogen atom, the theoretical model predicts that the difference in force would produce a measurable frequency change at tip-surface separations of less than 3.5 Å. Since H was very inert to the NiO surface, this should be considered a minimum limit for detecting the exchange force. However, the real limiting factor in the measurement is the point at which ion jumps begin. The calculations of tip-surface interaction over an oxygen ion in the MgO surface demonstrated the difference in jump behaviour for different tips. The Pd, Cu and Na tips could safely approach the surface beyond the exchange force limit without inducing any ion jumps. However, the more strongly interacting M^* tip induced a jump of the oxygen ion at a tip-surface separation of 3.8 Å. This is before the exchange force limit and tips with this strength of interaction could not image the difference in force over opposite spin Ni ions. These results imply that a successful experimental attempt to detect the exchange force must use a tip that is only weakly interacting with the NiO surface. At present most experimental setups favour iron coated tips for detecting the exchange force, but there is evidence that there is a strong interaction between Fe and oxygen in oxide surfaces [2]. Experiments demonstrate that Fe transfers charge to the surface to form the Fe^{2+} and is then adsorbed on oxygen sites. This implies that ion jumps may prevent imaging of the exchange force with an iron tip. The calculations suggest that copper would be a better choice for the tip coating, it is spin polarized and its weak interaction with oxide surfaces removes the problem of ion jumps. The weakness of interaction also serves to reduce contrast in images due to microscopic forces, making it easier to see any differences in contrast due the exchange force. As the exchange force depends on the spin interaction, its magnitude will not be greatly affected by the chemical nature of the tip. This can be seen clearly in the similarity of the exchange force calculated with the Na and H probe.

The extreme sensitivity of the low temperature NC-AFM means that it can atomically resolve the surface via microscopic forces at distances much farther than normal NC-AFM. The atomic contrast in frequency change predicted over the CaF_2 surface (see chapter 8) was still about 0.2 Hz at 5.0 Å, so a low temperature NC-AFM could potentially measure atomic contrast at tip-surface separations greater than this. This is too far for the difference in exchange force over spin up and spin down Ni ions to be measured and in real low temperature NC-AFM experiments atomic resolution of the difference in microscopic force over O and Ni ions will be achieved before it is possible to measure the difference in exchange force over Ni ions. Successful imaging of the exchange force will require first achieving atomic resolution on the surface of NiO, at distances where opposite spin Ni ions appear identical in images. Then the frequency change should be gradually increased until the exchange force is measured and opposite spin Ni ions appear with different contrast in images. This is extremely difficult, but, as shown in chapter 8, has already been achieved with normal NC-AFM techniques on the CaF_2 surface. Another problem for imaging of the exchange force, is that it is not obvious which sublattice in the NiO surface will be imaged as bright and therefore it is impossible to identify the atom under the tip. Although most metal tips should interact more strongly with the oxygen ions, the study of Na showed that this is not always the case. In light of this, experimentally it would be better to produce frequency change vs. distance curves directly over the whole surface unit cell, so-called Force Spectroscopy. This would be much more thorough way of analyzing the difference in force, rather than trying to tell if certain atoms are 'brighter' in an image. The resultant force map can be easily compared directly with theory to interpret the image and see if the exchange force plays a role.

Although the results discussed above are positive, this initial study has neglected some factors which could be important to the nature of the tip-surface interaction. A basic improvement to the model would be an expansion of the NiO surface unit cell to make sure there are no significant effects from the nearness of the periodic probes. A more thorough analysis of the properties of the tip would also be useful. The magnetization of nano-scale metal clusters is quite complex and it is important to verify both theoretically and experimentally that a single atom probe is an acceptable approximation. A more physical model of the tip itself would also allow more complex spin interactions to be studied. It would be especially interesting to see whether it is possible to flip a Ni ion's spin with the tip and see if it remained 'flipped' when the tip is retracted.

Chapter 10

Conclusions

The main goal of this study was to develop a physical model of Non-Contact Atomic Force Microscopy and use it to aid in interpretting experimental data. This was successfully achieved, a model of NC-AFM which included all the forces relevant to NC-AFM imaging was developed. The model represented the tip on both the macroscopic and microscopic scale, and the necessity of a protruding nano-tip at the end of the tip was demonstrated. Also by including bias and conducting substrate effects in the model, it could be used to study the tip-surface interaction over a wide variety of contrasting systems. In all systems studied, the theoretical modelling increased the amount of information on the tip, surface and tip-surface interaction compared to that from experiment alone.

Studies of TiO_2, NaCl and CaF_2 show that this model, given parameters from experiment, can reproduce the magnitude of the contrast found in experiment. This shows that the model can successfully reproduce the behaviour of the oscillating cantilever under the influence of the tip-surface interaction. The scanlines predict that the contrast in experiments is produced at tip-surface separations of 0.3 - 0.5 nm. The atomic contrast in NC-AFM images was shown to be dominated by the interaction between the electrostatic potential of the tip with the electrostatic potential of the surface. Strongest contrast is observed over atomic sites of largest electrostatic gradient with opposite nature to the tip potential i.e. a negative potential tip is attracted most strongly to sites of largest positive potential gradient in the surface. On the CaF_2 surface similar atomic contrast was generated with widely different macroscopic background forces, emphasizing the dominance of the short-range chemical force. This interaction is also strongly affected by atomic displacements and the coordination of the surface ions. In all the systems studied, the atoms of the surface begin to displace from their equilibrium positions as the tip approaches and at scanning height these displacements can be of the order of 0.01 nm. Atoms that displace towards the tip effectively form a dipole which extends the electrostatic potential above that ion and increases the tip-surface force at a given distance. Loosely bound lower-coordinated ions are also much more easily displaced than normal atomic sites. The study of low-coordinated sites on the edges and kinks of NaCl islands confirmed this and also showed that these sites have higher electrostatic potential gradients even when undisplaced. This combination of factors leads to strong increases in contrast over the edges and kinks of the NaCl islands in theoretical and experimental images.

The dependence of atomic contrast on the interaction of the potential from the tip and surface means that knowing the chemical structure of the nano-tip becomes crucial in understanding images. Modelling of an NaCl thin film and the CaF_2 surface demonstrated that the atomic source of contrast in images could be reversed if the chemical structure of the nano-tip was changed. Modelling of CaF_2 also demonstrated that contrast is not always due to the most obvious atoms or even atoms at all. Even though the F ions protrude from the surface, a negative potential tip still resolves the embedded Ca ions as bright and also resolves a minimum of repulsion between two F ions as a weak bright feature. The dependence of the image contrast on the tip structure is clearly seen in experimental images where contrast changes occur. At a specific point in a scan across a surface the image contrast undergoes a stark change, even reversing completely in some cases. Theoretical modelling shows that ions in the surface can jump to the tip at small tip-surface separations and this would change the potential from the tip, and therefore the contrast, significantly. This is especially evident in the study of CaF_2 where in one image (see fig. 8.14) the contrast changes from that theoretically predicted as due to a negative potential tip, to that of a positive potential tip.

The role of image forces in NC-AFM was analyzed and their importance in conducting or thin film systems was demonstrated. Specifically, modelling of NaCl thin films showed that charged features could be resolved directly in NC-AFM due to the large contribution of the image force to the tip-surface interaction. On the (110) surface of TiO_2 modelling demonstrated that image forces could dominate the simulated contrast, although a physical representation of the conductivity of the TiO_2 surface remains as a future study. On metal surfaces, where the conductivity is more easily defined, image forces proved crucial in understanding the magnitude of forces observed at medium range over a copper surface.

Attempts to compare directly theoretical and experimental results have shown the importance of comparing force vs. distance curves to characterize the tip-surface interactions. The study of the tip-surface interaction over a metal surface demonstrated the ability of frequency change vs. distance curves to differentiate between different tips. This knowledge was applied to characterize the tip used in experiments on the CaF_2 surface and a comparison of theoretical and experimental curves gave a very good estimate of the tip radius and the contribution of long-range electrostatic forces to the tip-surface interaction. This made modelling the imaging process on that surface much more consistent than in previous studies where the tip radius must be estimated from the frequency change while imaging, effectively only one point of a frequency vs. distance curve. Force vs. distance curves should be considered an essential part of any study, theoretical or experimental, as many questions regarding tip radius, tip structure and the components of the tip-surface interaction can be answered immediately.

Direct modelling of a NC-AFM experiment over the CaF_2 (111) surface showed that the experimental results matched very closely with theoretical predictions for a positive potential tip imaging fluorine ions in the surface. On a qualitative level the experimental and theoretical images both demonstrated a clear triangular pattern, and the modelling showed this was due to interaction with the second layer of fluorines in the surface, elongating the contrast. This second feature could also be seen as a shoulder to the main peaks in both experimental and theoretical scanlines. Theory predicted that these shoulders should appear at 0.220 nm from the main peaks and statistical analysis of many experimental scanlines gave the average position of the shoulders

in experiment as 0.247±0.05 nm. Also, over the same range of average frequency change (i.e. same change in tip-surface separation) theory and experiment gave almost the same change in the relative heights of the main peaks and shoulders. This is the first time in NC-AFM imaging of insulators that any strong conclusions about the identity of the sublattice imaged could be made.

A more advanced application of NC-AFM is the study of the atomic scale magnetic properties of surfaces. By applying the theoretical model to the anti-ferromagnetic NiO surface, with a full *ab initio* treatment of atomic interactions, the possibility of measuring the exchange force with NC-AFM was demonstrated. The model predicts that the difference in force between a magnetic tip over spin up and spin down Ni ions can be measured at tip-surface separations of less than 3.5 Å. A study of the effect of ion jumps on measuring the exchange force, demonstrated that it is important to use a tip that is weakly interacting with the NiO surface, otherwise ions will jump to the tip before reaching the exchange force limit.

As can be easily surmised from reading this work, there remain many problems and unknowns in interpretting NC-AFM experiments. However, the first part of any solution is identifying the problem, so this study will end with an analysis of some of the outstanding issues in NC-AFM and some possible methods for overcoming them.

Although image interpretation is a general problem of NC-AFM, it could be made a lot more objective if a more statistical approach is taken. At present experimental images are normally filtered by fourier analysis and then analyzed by eye or by plotting a few scanlines. This approach is very open to prejudice and an approach based more on statistical averages of a large number of images and scanlines would prove much more reliable.

Many of the most technologically important insulating surfaces, such as alumina and MgO, still remain to be imaged successfully in atomic resolution. Theoretical modelling of the interactions over the surface of the classic insulator CaF_2 demonstrated that homogeneous charging is not a problem for imaging, as atomic contrast is not strongly dependent on the nature of the background force. This implies that the roughness of these surfaces after cleavage is the main obstacle to imaging. Nano-debris and localized charge on the surface means that the force field is very inhomogeneous and rapid changes in the force gradient are common. Due to the finite response time of the frequency change modulation electronic loop in NC-AFM electronics, there is a maximum force gradient which can be successfully reacted to without stability problems. Larger force gradients will cause the tip to crash before the loop pulls the cantilever back. However, developments in surface preparation are producing smoother surfaces and many oxides can now be grown as atomically smooth thin films. These techniques should allow the progression of NC-AFM to imaging of any insulating surface.

The most problematic area of NC-AFM interpretation remains the tip, almost all results in this study are dependent on the chemical nature of the nano-tip. It is very difficult to identify the source of contrast in images without knowing the nature of the potential from the tip. Since most insulating surfaces contain more than one atomic species, this is a significant problem. Modelling of the CaF_2 surface revealed one possible technique for identifying clearly both the sublattice imaged and the potential of the tip. The complex nature of the (111) surface meant that it contained 3 different lattice sites, one calcium and two fluorines. The asymmetry of the surface ions translated into differences in images and scanlines taken with different nano-tips, and a comparison between theory and experiment allowed strong conclusions to be made about the sublattice imaged and the

chemical structure of the tip. This type of surface could be used as a benchmark to characterize the tip before imaging on more symmetric surfaces. If experiments could be performed in the same chamber on both the asymmetric and real samples with the same tip, it would be possible to use the asymmetric images to characterize the tip and then use the information on the tip to identify the source of contrast in images of the real sample. Another possible approach to problems with tip identification, is to use a tip which is more easily controlled. Metal tips, such as tungsten, can be cleaned of any contaminants by applying a large voltage to them and they can be made very sharp by ion beams. If NC-AFM was performed with a metal tip prepared correctly, the imaging nano-tip would be almost certainly of pure metal character. The main problem with such tips is that they usually do not demonstrate very strong chemical interactions with the surface and the magnitude of contrast is normally much smaller than with silicon tips. However, the smaller contrast should not be a problem for low temperature NC-AFM, with its greater sensitivity.

NC-AFM has now been established as a powerful technique in surface science, yet reliability and interpretation problems stop it developing into a commonly used and trusted tool. Until a full understanding of the interactions important in imaging is obtained, NC-AFM will remain a specialized technique. This study has demonstrated the power of theory in bridging the gap between experimental data and the physics of surfaces, and with a little more effort from the NC-AFM community there will be no gap at all.

Bibliography

[1] A. Zangwill, *Physics at Surfaces* (University Press, Cambridge, 1988).

[2] V. E. Henrich and P. A. Cox, *The Surface Science of Metal Oxides* (University Press, Cambridge, 1996).

[3] P. V. Sushko, A. S. Foster, L. N. Kantorovich, and A. L. Shluger, Appl. Surf. Sci. **144-145**, 608 (1999).

[4] A. I. Livshits, A. L. Shluger, A. L. Rohl, and A. S. Foster, Phys. Rev. B **59**, 2436 (1999).

[5] A. L. Shluger, A. I. Livshits, A. S. Foster, and C. R. A. Catlow, J. Phys.: Condens. Matter **11**, R295 (1999).

[6] A. S. Foster, L. N. Kantorovich, and A. L. Shluger, Appl. Phys. A (Accepted) (2000).

[7] L. N. Kantorovich, A. S. Foster, A. L. Shluger, and A. M. Stoneham, Surf. Sci. **445**, 283 (2000).

[8] R. Bennewitz, A. S. Foster, L. N. Kantorovich, M. Bammerlin, C. Loppacher, S. Schär, M. Guggisberg, E. Meyer, and A. L. Shluger, Phys. Rev. B **62**, 2074 (2000).

[9] A. S. Foster, A. L. Rohl, and A. L. Shluger, Appl. Phys. A (Accepted) (2000).

[10] A. S. Foster, C. Barth, A. L. Shluger, and M. Reichling, Phys. Rev. Lett.(Submitted) (2001).

[11] C. Barth, A. S. Foster, M. Reichling, and A. L. Shluger, J. Phys.: Condens. Matter (Submitted) (2001).

[12] G. Binnig, C. Quate, and C. Gerber, Phys. Rev. Lett. **56**, 930 (1986).

[13] G. Binnig and H. Rohrer, Helv. Phys. Acta **55**, 726 (1982).

[14] J. Tersoff and D. Hamann, Phys. Rev. B **31**, 805 (1985).

[15] F. Besenbacher, Rep. Prog. Phys. **59**, 1737 (1996).

[16] H. Neddermeyer, Rep. Prog. Phys. **59**, 701 (1996).

[17] W. Hebenstreit, J. Redinger, Z. Horozova, M. Schmid, R. Podloucky, and P. Varga, Surface Science **424**, L321 (1999).

[18] W. Allers, A. Schwarz, U. D. Schwarz, and R. Wiesendanger, Rev. Sci. Instrum. **69**, 221 (1998).

[19] L. Howald, E. Meyer, R. Lüthi, H. Haefke, R. Overney, H. Rudin, and H.-J. Güntherodt, Appl. Phys. Lett. **63**, 117 (1993).

[20] C. F. Quate, Surf. Sci. **299**, 980 (1994).

[21] F. M. Ohnesorge, J. K. H. Hörber, W. Häberle, C. P. Czerny, D. P. E. Smith, and G. Binnig, Biophys. J. **73**, 2183 (1997).

[22] G. Binnig, Ultramicroscopy **42-44**, 7 (1992).

[23] G. Binnig and H. Rohrer, Rev. Mod. Phys. **71**, 543 (1999).

[24] A. I. Livshits and A. L. Shluger, Faraday Discuss. **106**, 425 (1997).

[25] F. J. Giessibl, Science **267**, 68 (1995).

[26] M. Bammerlin, R. Lüthi, E. Meyer, A. Baratoff, M. Guggisberg, C. Gerber, L. Howard, and H.-J. Güntherodt, Probe Microscopy **1**, 3 (1997).

[27] M. Reichling and C. Barth, Phys. Rev. Lett. **83**, 768 (1999).

[28] Y. Iwasawa, Surf. Sci. **402-404**, 8 (1998).

[29] K. Fukui, H. Onishi, and Y. Iwasawa, Phys. Rev. Lett. **79**, 4202 (1997).

[30] S. Morita and M. Tsukada, eds., *Proceedings of the First International Workshop on Noncontact Atomic Force Microscopy*, vol. 140 of *Appl. Surf. Sci.* (1999).

[31] R. Bennewitz, C. Gerber, and E. Meyer, eds., *Proceedings of the Second International Workshop on Noncontact Atomic Force Microscopy*, vol. 157 of *Appl. Surf. Sci.* (2000).

[32] R. Bennewitz, M. Bammerlin, M. Guggisberg, C. Loppacher, A. Baratoff, E. Meyer, and H.-J. Güntherodt, Surf. Interface Anal. **27**, 462 (1999).

[33] H. O. Jacobs and A. Stemmer, Surf. and Int. Anal. **27**, 361 (1999).

[34] M. Gauthier and M. Tsukada, Phys. Rev. B **60**, 11716 (1999).

[35] F. J. Giessibl, H. Bielefeldt, S. Hembacher, and J. Mannhart, Appl. Surf. Sci **140**, 352 (1999).

[36] F. J. Giessibl, Phys. Rev. B **56**, 16010 (1997).

[37] K. Fukui, H. Onishi, and Y. Iwasawa, Phys. Rev. Lett. **79**, 4202 (1997).

[38] Y. Sugawara, M. Ohta, H. Ueyama, and S. Morita, Science **270**, 1648 (1995).

[39] M. Bammerlin, R. Lüthi, E. Meyer, A. Baratoff, M. Guggisberg, C. Gerber, L. Howald, and H.-J. Güntherodt, Probe Microscopy **1**, 3 (1997).

[40] S. H. Ke, T. Uda, R. Pérez, I. Stich, and K. Terakura, Phys. Rev. B **60**, 11631 (1999).

[41] J. Tóbik, I. Stich, R. Pérez, and K. Terakura, Phys. Rev. B **60**, 11639 (1999).

[42] M. P. Seah, S. J. Spencer, P. J. Cumpson, and J. E. Johnstone, Appl. Surf. Sci. **144-145**, 151 (1999).

[43] B. W. Reed, J. M. Chen, N. C. MacDonald, J. Silcox, and G. F. Bertsch, Phys. Rev. B **60**, 5641 (1999).

[44] N. Burnham, R. Colton, and H. Pollock, Nanotechnology **4**, 64 (1993).

[45] B. G. Dick and A. W. Overhauser, Phys. Rev. **112**, 603 (1958).

[46] K. Ohno, K. Esfarjani, and Y. Kawazoe, *Computational Materials Science* (Springer, Berlin, 1999).

[47] P. Hohenberg and W. Kohn, Phys. Rev. **136**, B864 (1964).

[48] W. Kohn and L. J. Sham, Phys. Rev **140**, A1133 (1965).

[49] D. C. Langreth and J. P. Perdew, Phys. Rev. B **21**, 5469 (1980).

[50] D. C. Langreth and M. J. Mehl, Phys. Rev. B **28**, 1809 (1983).

[51] J. P. Perdew and Y. Wang, Phys. Rev. B **33**, 8800 (1986).

[52] J. P. Perdew, Phys. Rev. B **33**, 8822 (1986).

[53] D. Gay and A. Rohl, J. Chem. Soc. Faraday Trans. **91**, 925 (1995).

[54] A. Shluger, A. Rohl, D. Gay, and R. Williams, J. Phys.: Condens. Matter **6**, 1825 (1994).

[55] A. L. Shluger and A. L. Rohl, Topics in Catalysis **3**, 221 (1996).

[56] G. Kresse and J. Furthmüller, Comp. Mat. Sci. **6**, 15 (1996).

[57] G. Kresse and J. Furthmüller, Phys. Rev. B **54**, 11169 (1996).

[58] R. Car and M. Parrinello, Phys. Rev. Lett. **55**, 2471 (1985).

[59] J. Perdew, in *Electronic Structure in Solids '91*, edited by P. Ziesche and H. Eschrig (Academie Verlag, Berlin, 1991).

[60] J. P. Perdew, J. A. Chevary, S. H. Vosko, K. A. Jackson, M. R. Pederson, D. J. Singh, and C. Fiolhais, Phys. Rev. B **46**, 6671 (1992).

[61] D. Vanderbilt, Phys. Rev. B **41**, 7892 (1990).

[62] G. Kresse and J. Hafner, J. Phys.: Condens. Matter **6**, 8245 (1994).

[63] V. R. Saunders, R. Dovesi, C. Roetti, M. Causà, N. M. Harrison, R. Orlando, and C. M. Zicovich-Wilson, *CRYSTAL98 User's Manual* (University of Torino, Torino, 1998).

[64] J. Israelachvili, *Intermolecular and Surface Forces* (Academic Press, London, 1991).

[65] F. London, Trans. Faraday Soc. **33**, 8 (1937).

[66] H. C. Hamaker, Physica **4**, 1058 (1937).

[67] C. Argento and R. H. French, J. Appl. Phys. **80**, 6081 (1996).

[68] L. N. Kantorovich, A. I. Livshits, and A. M. Stoneham, J. Phys.: Condens. Matter **12**, 795 (2000).

[69] J. A. Stratton, *Electromagnetic Theory* (McGraw-Hill, N. Y., 1941).

[70] L. D. Landau, E. M. Lifshitz, and L. P. Pitaevskii, *Electrodynamics Of Continuous Media*, vol. 8 (Pergamon Press, Oxford, 1993).

[71] J. D. Jackson, *Classical Electrodynamics* (John Wiley, N. Y., 1999).

[72] M. W. Finnis, Surf. Sci. **241**, 61 (1991).

[73] M. W. Finnis, R. Kaschner, C. Kruse, J. Furthmüller, and M. Scheffler, J. Phys.: Condens. Matter **7**, 2001 (1995).

[74] M. García-Hernández, P. S. Bagus, and F. Illas, Surf. Sci. **409**, 69 (1998).

[75] W. R. Smythe, *Static and Dynamic Electricity* (McGraw-Hill, N. Y., 1968).

[76] S. Hudlet, M. S. Jean, C. Guthmann, and J. Burger, Eur. Phys. J. **2**, 5 (1998).

[77] M. S. Jean, S. Hudlet, C. Guthmann, and J. Berger, J. Appl. Phys. **86**, 5245 (1999).

[78] N. Burnham, R. Colton, and H. Pollock, Phys. Rev. Lett. **69**, 144 (1992).

[79] J. B. Engelhardt, H. Dabringhaus, and K. Wandelt, Surf. Sci. **448**, 187 (2000).

[80] K. Sangwal, F. Sanz, and P. Gorostiza, Surf. Sci. **424**, 139 (1999).

[81] M. Luna, F. Rieutord, N. A. Melman, Q. Dai, and M. Salmeron, J. Phys. Chem. A **102**, 6793 (1998).

[82] L. B. Harris and J. Fiasson, J. Phys. C: Solid State Phys. **18**, 4845 (1985).

[83] H. J. Wintle, Meas. Sci. Technol. **8**, 508 (1997).

[84] Y. Martin, C. C. Williams, and H. K. Wickramasinghe, J. Appl. Phys. **61**, 4723 (1987).

[85] K. Fukui, H. Onishi, and Y. Iwasawa, Phys. Rev. Lett. **79**(21), 4202 (1997).

[86] R. Pérez, M. Payne, I. Stich, and K. Terakura, Phys. Rev. Lett. **78**, 678 (1997).

[87] J.C.Bean, G.E.Becker, P.M.Petroff, and T.E.Seidel, J. Appl. Phys. **48**, 907 (1977).

[88] J.H.Comfort, L.M.Garverick, and R. Reif, J. Appl. Phys **62**, 3388 (1987).

[89] L.M.Garverick, J.H.Comfort, T.R.Yew, R.Reif, F.A.Baiocchi, and H.S.Luftman, J. Appl. Phys. **62**, 3398 (1987).

[90] Y.Z.Hu, P.P.Buaud, Y.Wang, L.Spanos, and E.A.Irene, Appl. Phys. Lett. **64**, 1233 (1994).

[91] P.Raynaud and C.Pomot, J. Vac. Sci. Tech. **B11**, 699 (1993).

[92] K.Uesugi, M.Yoshimura, T.Yao, T.Sato, T.Sueyoshi, and M.Iwatsuki, J. Vac. Sci. Tech. **B12**, 2018 (1994).

[93] Y.Z.Hu, J.W.Andrews, M.Li, and E.A.Irene, Nucl. Instr. and Meths. Phys. Res. **59**, 76 (1991).

[94] Y.Z.Hu, M.Li, J.W.Andrews, K.A.Conrad, and E.A.Irene, J. Electrochem. Soc. **139**, 2023 (1992).

[95] T.Bekkay, E.Sacher, and A.Yelon, Surf. Sci. **217**, L377 (1989).

[96] S. W. Downey and A. B. Emerson, Nuc. Instr. and Methods in Phys. Res. B **93**, 252 (1994).

[97] M. A. S. Kalceff, G. J. Thorogood, and K. T. Short, J. Appl. Phys. **86**, 205 (1999).

[98] C. Loppacher, M. Bammerlin, M. Guggisberg, S. Scär, R. Bennewitz, A. Baratoff, E. Meyer, and H. J. Güntherodt, Phys. Rev. B (accepted) (2000).

[99] C. Barth and M. Reichling, Private Communication (2000).

[100] K. Fukui and Y. Iwasawa, Surf. Sci. **441**, 529 (1999).

[101] E.Kaxiras, Phys. Rev. Lett **64**, 551 (1990).

[102] K.Jug and M.Krack, Chem. Phys. **173**, 439 (1993).

[103] X.G.Gong, Phys. Rev. **B52**, 14677 (1995).

[104] E.Kaxiras and K.K.Jackson, Phys. Rev. Lett **71**, 727 (1993).

[105] U.Rothlisberger, W.Andreoni, and M.Parrinello, Phys. Rev. Lett. **72**, 665 (1994).

[106] I.Lee, K.J.Chang, and Y.H.Lee, J. Phys. Condens. Matter **6**, 741 (1994).

[107] M.Menon and K.R.Subbaswamy, Phys. Rev. **51**, 17952 (1995).

[108] J.C.Grossman, Phys. Rev. Lett. **74**, 1323 (1995).

[109] M.V.Ramakrishna and J.Pan, J. Chem. Phys. **101**, 8108 (1994).

[110] M.Krack and K.Jug, Chem. Phys. **192**, 127 (1995).

[111] D.A.Jelski, B.L.Swift, T.T.Rantala, X.Xia, and T.F.George, J. Chem. Phys. **95**, 8552 (1991).

[112] J.L.Gavartin and C.C.Matthai, Materials and Science Engineering **B35**, 459 (1995).

[113] X.G.Gong, Q.Q.Zheng, and Y.He, J. Phys. Con. Mater. **7**, 577 (1995).

[114] K.Takayanagi, Y.Tanishiro, M.Takahashi, and S.Takahashi, J. Vac. Sci. Technol. **A3**, 1502 (1981).

[115] M. Zaibi, J. Lacharme, and C. Sebenne, Surf. Sci. **377**, 639 (1997).

[116] A. L. Shluger, A. L. Rohl, D. H. Gay, and R. T. Williams, J. Phys.: Condens. Matter **6**, 1825 (1994).

[117] R. Grimes, C. Catlow, and A. Stoneham, J. Phys.: Condens. Matter **1**, 7367 (1989).

[118] M. A. Lantz, H. J. Hug, P. J. A. van Schendel, R. Hoffman, S. Martin, A. Baratoff, A. Abdurixit, H. J. Güntherodt, and C. Gerber, Phys. Rev. Lett. **84**, 2642 (2000).

[119] H. Hölscher, A. Schwarz, W. Allers, U. D. Schwarz, and R. Wiesendanger, Phys. Rev. B **61**, 12678 (2000).

[120] T. Uchihashi, Y. Sugawara, T. Tsukamoto, M. Ohta, and S. Morita, Phys. Rev. B **56**, 9834 (1997).

[121] M. Guggisberg, M. Bammerlin, C. Loppacher, O. Pfeiffer, A. Abdurixit, V. Barwich, R. Bennewitz, A. Baratoff, E. Meyer, , and H.-J. Güntherodt, Phys. Rev. B **61**, 11151 (2000).

[122] M. S. Jean, S. Hudlet, C. Guthmann, and J. Berger, J. Appl. Phys. **86**, 5245 (1999).

[123] S. Sounilhac, E. Barthel, and F. Creuzet, Appl. Surf. Sci. **140**, 411 (1999).

[124] R. Wyckoff, *Crystal Structures* (Interscience, New York, 1963).

[125] M. Guggisberg, M. Bammerlin, R. Lüthi, C. Loppacher, F. Battiston, J. Lü, A. Baratoff, E. Meyer, and H.-J. Güntherodt, Appl. Phys. A **66**, S245 (1998).

[126] W. Hebenstreit, J. Redinger, Z. Horozova, M. Schmid, R. Podloucky, and P. Varga, Surf. Sci. **424**, L321 (1999).

[127] R. Bennewitz, M. Bammerlin, M. Guggisberg, C. Loppacqher, A. Baratoff, E. Meyer, and H.-J. Güntherodt, Surface and Interface Analysis **27**, 462 (1999).

[128] C. Loppacher, M. Bammerlin, M. Guggisberg, F. Battiston, R. Benewitz, S. Rast, A. Baratoff, E. Meyer, and H.-J. Güntherodt, Appl. Surf. Sci. **140**, 287 (1999).

[129] D. M. Duffy, J. H. Harding, and A. M. Stoneham, Phil. Mag. **67**, 865 (1993).

[130] R. H. French, R. M. Cannon, L. K. DeNoyer, and Y. M. Chiang, Solid State Ionics **75**, 13 (1995).

[131] A. L. Shluger, L. N. Kantorovich, A. I. Livshits, and M. J. Gillan, Phys. Rev. B **56**, 15332 (1997).

[132] S. Street, C. Xu, and D. W. Goodman, Annu. Rev. Phys. Chem. **48**, 43 (1997).

[133] V. Henrich, Rep. Prog. Phys. **48**, 1481 (1985).

[134] G. Charlton, P. Howes, C. Nicklin, P. Steadman, J. Taylor, C. A. Muryn, S. Harte, J. Mercer, R. McGrath, D. Norman, T. Turner, and G. Thornton, Phys. Rev. Lett. **78**(3), 495 (1997).

[135] B. Maschhoff, J.-M. Pan, and T. Madey, Surf. Sci. **259**, 190 (1991).

[136] P. Murray, N. Condon, and G. Thornton, Phys. Rev. B **51**(16), 10 989 (1995).

[137] M. Sander and T. Engel, Surf. Sci. **302**, L263 (1994).

[138] H. Onishi and Y. Iwasawa, Surf. Sci. **313**, L783 (1994).

[139] J. Purton, D. Bullett, P. Oliver, and S. Parker, Surf. Sci. **336**, 166 (1995).

[140] M. Ramamoorthy, R. King-Smith, and D. Vanderbilt, Phys. Rev. B **49**(11), 7709 (1994).

[141] M. Ramamoorthy, D. Vanderbilt, and R. King-Smith, Phys. Rev. B **49**(23), 16721 (1994).

[142] P. Lindan, J. Muscat, S. Bates, N. Harrison, and M. Gillan, Faraday Discuss. **106** (1997).

[143] P. Lindan, N. Harrison, M. Gillan, and J. White, Phys. Rev. B **55**(23), 15919 (1997).

[144] N. M. Harrison, X. G. Wang, J. Muscat, and M. Scheffler, Faraday Discussions **114** (1999).

[145] P. Oliver, G. Watson, E. Kelsey, and S. Parker, J. Mater. Chem **7**(3), 563 (1997).

[146] K. Fukui, H. Onishi, and Y. Iwasawa, Chem. Phys. Lett. **280**, 296 (1997).

[147] M. Matsui and M. Akaogi, Mol. Sim. **6**, 239 (1991).

[148] C. R. A. Catlow, C. M. Freeman, M. S. Islam, R. A. Jackson, M. Leslie, and S. M. Tomlinson, Phil. Mag. A **58**, 123 (1988).

[149] T. S. Bush, J. D. Gale, C. R. A. Catlow, and P. D. Battle, J. Mater. Chem. **4**, 832 (1994).

[150] D. McKie and C. McKie, *Crystalline Solids* (J. Wiley, New York, 1974).

[151] J. Muscat, Private Communication (1999).

[152] S. Fölsch, A. Helms, S. Zöphel, J. Repp, G. Meyer, and K. Rieder, Phys. Rev. Lett. **84**, 123 (2000).

[153] K. Glöckler, M. Sokolowski, A. Soukopp, and E. Umbach, Phys. Rev. B **54**, 7705 (1996).

[154] J. Venables, G. Haas, H. Brune, and J. Harding, Epitaxial Growth - Principles and Applications **57**, 570 (1999).

[155] R. Bennewitz, M. Bammerlin, M. Guggisberg, C. Loppacher, A. Baratoff, E. Meyer, and H.-J. Güntherodt, Surface Science **438**, 289 (1999).

[156] C. Loppacher, M. Bammerlin, F. Battiston, M. Guggisberg, D. Müller, H. Hidber, R. Lüthi, E. Meyer, and H.-J. Güntherodt, Appl. Phys. A **66**, 215 (1998).

[157] C. Loppacher, M. Bammerlin, M. Guggisberg, F. Battiston, R. Bennewitz, S. Rast, A. Baratoff, E. Meyer, and H.-J. Güntherodt, Appl. Surf. Sci. **140**, 287 (1999).

[158] M. Gauthier and M. Tsukada, Phys. Rev. B **60**, 11716 (1999).

[159] A. Abdurixit, T. Bonner, A. Baratoff, and E. Meyer, Appl. Surf. Sci. **157**, 355 (2000).

[160] W. Denk and D. W. Pohl, Appl. Phys. Lett. **59**, 2171 (1991).

[161] U. Dürig, Surf. and Interface Analysis **27**, 467 (1999).

[162] T. D. Stowe, T. W. Kenny, D. J. Thomson, and D. Rugar, Appl. Phys. Lett. **75**, 2785 (1999).

[163] B. Gotsmann, C. Seidel, B. Anczykowksi, and H. Fuchs, Phys. Rev. B **60**, 11051 (1999).

[164] A. Schwarz, W. Allers, U. D. Schwarz, and R. Wiesendanger, Phys. Rev. B **61**, 2837 (2000).

[165] M. Bammerlin and et al., In preparation (2000).

[166] C. Girard, D. V. Labeke, and J. M. Vigoureux, Phys. Rev. B **40**, 12133 (1989).

[167] J. Szajman, R. C. G. Leckey, J. G. Jenkin, and J. Liesegang, Phys. Rev. B **12**, 5872 (1975).

[168] M. Reichling, M. Huisinga, S. Gogoll, and C. Barth, Surf. Sci. **439**, 181 (1999).

[169] C. R. A. Catlow and M. J. Norgett, J. Phys. C: Solid State Phys. **6**, 1325 (1973).

[170] P. W. M. Jacobs and S. H. Ong, J. Physique Colloq. **37**, 331 (1976).

[171] M. Gillan, J. Phys. C: Solid State Phys. **19**, 3391 (1986).

[172] M. Gillan, J. Phys. C: Solid State Phys. **19**, 3517 (1986).

[173] B. Stankiewicz and P. Modrak, Surf. Sci. **331-333**, 1441 (1995).

[174] A. V. Puchina, V. E. Puchin, M. Huisinga, R. Bennewitz, and M. Reichling, Surf. Sci. **402-404**, 687 (1998).

[175] A. Dornford-Smith and R. W. Grimes, Phil. Mag. B **72**, 563 (1995).

[176] D. J. Binks, *PhD Thesis* (University of Surrey, 1994).

[177] A. Jockisch, U. Schröder, F. W. de Wette, and W. Kress, J. Phys.: Condens. Matter **5**, 5401 (1993).

[178] J. D. Gale, JCS Faraday Trans. **93**, 629 (1997).

[179] J. D. Gale, Phil. Mag. B **73**, 3 (1996).

[180] M. Riechling, M. Huisinga, D. Ochs, and V. Kempter, Surf. Sci **402-404**, 145 (1998).

[181] J. R. Heffelfinger, M. W. Bench, and C. B. Carter, Surf. Sci. Lett. **370**, L168 (1997).

[182] G. A. Sawatzky and J. W. Allen, Phys. Rev. Lett. **53**, 2339 (1984).

[183] N. F. Mott, *Metal-Insulator Transitions* (Taylor and Francis, London, 1974).

[184] K. Terakura, A. R. Williams, T. Oguchi, and J. Kübler, Phys. Rev. B **40**, 4734 (1984).

[185] M. D. Towler, N. L. Allan, N. M. Harrison, V. R. Saunders, W. C. Mackrodt, and E. Aprà, Phys. Rev. B **50**, 5041 (1994).

[186] M. Arai and T. Fujiwara, Phys. Rev. B **51**, 1477 (1995).

[187] S. L. Dudarev, G. A. Botton, S. Y. Savrasov, C. J. Humphreys, and A. P. Sutton, Phys. Rev. B **57**, 1505 (1998).

[188] M. R. Castell, P. L. Wincott, N. G. Condon, C. Muggelberg, G. Thornton, S. L. Dudarev, A. P. Sutton, and G. A. D. Briggs, Phys. Rev. B **55**, 7859 (1997).

[189] F. Aryasetiawan and O. Gunnarsson, Phys. Rev. Lett. **74**, 3221 (1995).

[190] F. P. Netzer and M. Prutton, J. Phys. C **8**, 2401 (1975).

[191] C. G. Kinniburgh and J. A. Walker, Surf. Sci. **63**, 274 (1977).

[192] H. Hosoi, K. Sueoka, K. Hayakawa, and K. Mukasa, Appl. Surf. Sci. **157** (2000).

[193] C. Noguera and W. C. Mackrodt, J. Phys.: Condens. Matter **12**, 2163 (2000).

[194] S. L. Dudarev, A. I. Liechtenstein, M. R. Castell, G. A. D. Briggs, and A. P. Sutton, Phys. Rev. B **56**, 4900 (1997).

[195] M. R. Castell, S. L. Dudarev, G. A. D. Briggs, and A. P. Sutton, Phys. Rev. B **59**, 7342 (1999).

[196] R. Dovesi, C. Ermond, E. Ferrero, C. Pisani, and C. Roetti, Phys. Rev. B **29**, 1984 (1984).

[197] R. Dovesi, C. Roetti, C. Freyriafava, M. Prencipe, and V. R. Saunders, Chem. Phys. **156**, 11 (1991).

[198] W. Allers, Private Communication (2000).

[199] R. S. Mulliken, J. chim. Phys. **49**, 497 (1949).

[200] J. Freitag and V. Staemmler, J. Elec. Spectrosc. and Rel. Phen. **69**, 99 (1994).

[201] J. A. Venables and J. H. Harding, J. Cryst. Growth **211**, 27 (2000).

[202] N. Lopez, F. Illas, N. Rösch, and G. Pacchioni, J. Chem. Phys. **110**, 4873 (1999).